Two-particle interferometry for quantum signal processing

Arthur Marguerite

THÈSE DE DOCTORAT
DE L'UNIVERSITÉ PIERRE ET MARIE CURIE

Spécialité :

Physique Quantique

présentée par

Arthur MARGUERITE

Pour obtenir le titre de
DOCTEUR de l'Université Pierre et Marie Curie

Sujet de la thèse :

Two-particle interferometry for quantum signal processing

Dirigée par : **Gwendal FÈVE** et soutenue le 3 juillet 2017
devant le jury composé de :

Mme.	**Janine Splettstösser**	**Rapportrice**
M.	**Masaya Kataoka**	**Rapporteur**
Mme.	**Maura Sassetti**	**Examinatrice**
M.	**Chrisopher Bauerle**	**Examinateur**
M.	**Michel Brune**	**Président**
M.	**Gwendal Fève**	**Directeur de thèse**

Remerciements

Avant de lire une thèse, j'aime beaucoup lire les remerciements. C'est la partie qui permet d'entrevoir l'aventure humaine derrière l'aventure scientifique de la thèse mais la place qui y est allouée est maigre comparée à ce que cela représente réellement et c'est donc souvent un exercice impossible. C'est maintenant à mon tour d'écrire ces remerciements qui je l'espère ne seront ni trop longs, ni trop réducteurs; ni trop gênants, ni trop vexants.

I would like first to thank Janine Splettstößer and Masaya Kataoka for accepting to review this manuscript and carefully reading and commenting it. I thank them also, together with Maura Sassetti, Christopher Bauerle and Michel Brune for doing me the honour to be my jury. It was a pleasure to defend in front of them and I was delighted to see their interest for this work during the questions.

Un énorme merci à Gwendal Fève qui a accepté de me prendre en thèse et avec qui j'ai pris grand plaisir à travailler (en chantant). J'aurais difficilement pu rêver meilleur encadrement, Gwendal a été pour moi un modèle autant scientifique qu'humain : grand pédagogue, travailleur acharné, excellent physicien mais aussi optimiste, bon vivant, généreux de son temps et toujours de bonne humeur. Encore souvent les mains sur la manip', il a aussi réussi à trouver le bon équilibre entre encadrement et autonomie. On dit dans les couloirs que j'ai pris certains de ses traits, j'espère que ce mimétisme ira plus loin qu'une barbe, des lunettes et quelques expressions.

Mon second mentor fut Vincent Freulon. Merci d'avoir pris la patience de me montrer les subtilités et les exigences des mesures de bruit et de la cryogénie. Ce fut un plaisir d'apprendre à tes cotés à maîtriser le frigo et l'analyseur de spectre et aussi de découvrir ensemble les premiers résultats de l'expérience. Ce fut tout autant un plaisir d'enseigner ensuite ~~tout~~ le maximum de ce que j'avais appris sur la manip à Clément Cabart puis Rémi Bisognin. Travailler avec eux fut très agréable et ils m'ont eux même beaucoup appris. J'espère que Clément a gardé un bon souvenir de cette période avant de se plonger dans la physique théorique. Je suis sûr que Rémi, personnification de la zen attitude, réussira sereinement et calmement à faire fonctionner le nouveau frigo et en faire sortir de beaux résultats. Je lui souhaite tout la réussite possible pour sa thèse et la suite quelle qu'elle soit. Thanks also to Manohar, it was a pleasure to work with him and to benefit from his long experience. I wish him good luck for the future and hopefully not too much time on the bonding machine.

Merci à Bernard Plaçais qui a suivi d'un peu plus loin mais avec constance et intérêt nos travaux. Merci aussi pour nos nombreuses discussions scientifiques ou non (même si on n'est pas souvent d'accord) et son inépuisable stock de subtils jeux de mots. Merci à Jean-Marc Berroir qui au début de ma thèse a pu prendre un peu de son temps de direction pour faire de la physique avec nous. Merci aussi d'avoir été un bon directeur de laboratoire et pour le soucis constant qu'il a eu que l'on travaille dans de bonnes conditions (même pendant les travaux). Merci à Jérôme Tignon qui a pris sa relève et notamment avec qui nous avons pu relancer le "foot du LPA" qui j'espère aura été apprécié. Merci à Bouygues de m'avoir appris à être encore plus résiliant, à ne pas toujours pouvoir contrôler mon agenda et à gérer les imprévus.

Un grand merci à mes théoriciens préférés, Pascal Degiovanni et deux de ses Daltons : Benjamin Roussel et Clément Cabart. Ensemble ils forment un trio détonnant et foldingue mais équilibré et intelligent. Sans eux, je n'aurais jamais rien compris à la

décohérence et aux fonctions de Wigner. Ce fut toujours un plaisir d'interagir avec eux à Lyon, Paris, Aussois, Pékin ou la Nouvelle-Orléans de même que d'écouter Pascal, grand penseur de la fin du monde, de la sobriété heureuse (surtout acteur de la partie heureuse) et du calcul quantique, prédire la prochaine crise boursière ou la nouvelle épidémie de virus à la mode. Sa capacité d'abstraction a pu nous emmener loin, à des vitesses pas toujours très contrôlées. Heureusement que Benjamin et Clément étaient là pour s'assurer que Gwendal et moi suivions toujours. Merci encore à Benjamin d'avoir pris le temps de nous expliquer comment se servir des ses codes. Au début de ma thèse, la frénésie du trio était tempérée par la présence d'un autre grand pédagogue Etienne Thibierge, merci à lui, je lui souhaite un bel avenir dans l'enseignement.

Merci aussi à Dario Ferraro et à l'équipe du CPT : Thierry Martin, Jérôme Rech, Thibaut Jonckheere et Claire Wahl. Merci de nous avoir éclairé sur l'effet Hall quantique fractionnaire, la supra-induite dans les canaux de bords et surtout de nous avoir permis d'aller au bout de l'analyse de la décohérence électronique. Cette thèse n'aurait bien sûr pas pu être possible sans les échantillons fabriqués par Yong Jin, Antonella Cavanna et Ulf Gennser. Merci à eux aussi pour avoir été à l'écoute de nouvelles attentes et d'avoir su gérer nos fichiers gds pas toujours compatibles. Merci aussi pour la qualité et la robustesse des amplis HEMTs. Merci à Michele Filippone pour m'avoir fait découvrir et si bien expliqué ses résultats sur les effets d'interaction dans le quantum-dot. Ces travaux sont venus au bon moment et je pense nous ont permis de comprendre la totalité des figures d'interférences HOM, repoussant les derniers éléments d'incompréhension (ou d'explications un peu trop *ad hoc*).

Pour les aspects non-physiques mais tout autant indispensables à la réalisation de cette thèse j'ai bénéficié de l'aide de nombreux services du département de physique et du laboratoire. Merci en particulier à Anne Matignon pour son efficacité et son énorme travail de gestion. À chaque fois que l'on fait quelque chose de travers, elle réussi à s'énerver juste ce qu'il faut dans ses remontrances et explications pour nous rappeler à quel point, sans elle, nous serions vite perdu dans le maelstrom administratif du CNRS. Merci aussi à Olga, et Fabienne avant elle, pour les gestions des cartes, des accès (et sûrement tout un tas de chose dont je ne suis pas au courant). Un grand merci aussi au travail de l'équipe du service cryogénie : Olivier Andrieu, Aurélien Sabatié et Florent Perrin. Même dans les moments les plus difficiles, ils ont toujours pu faire en sorte que nous ayons droits à notre dose régulière d'helium liquide. Qu'ils soient remercié pour la constance de leur engagement. Merci au service électronique. En particulier, merci à Anne Denis pour le design des nouveaux PCB, à Phillipe Pace pour le design des nouveaux filtres et des pistes de thermalisation. Merci à David Darson pour l'aide et les explications sur les sources Bilt, merci aussi pour son intérêt et sa volonté de partager nos connaissances pour constamment améliorer nos circuits. Merci aussi pour ses belles illustrations. Merci aussi à Pascal Morfin et Anaelle Pascal pour le design et la fabrication du nouveau puck et du nouveau porte échantillon pour la bondeuse. Merci à Jules Silembo et Mathieu Sardin pour les sauvetages de visses grippées sur le frigo et les nombreuses pièces qu'on a pu leur demander. Merci infiniment à toute l'équipe de Didier Courtiade, notamment Catherine Gripe et Célia Ruschinzik grâce à qui le bâtiment ne s'écroule pas. Merci aussi pour leur aide lors du déménagement induit par les travaux et les petites réparations qui ont suivies. Merci aussi aux électriciens Jean-Marc Jusseau, Franck Bouchereau et Philippe Rousseau qui, toujours avec humour, ont pu répondre à nos besoins croissants de puissance électrique et limiter au mieux les coupures de courant. Merci aussi à Claude Dodray pour l'entretient de la bondeuse. Merci beaucoup à Yann Colin pour son expertise informatique, sa disponibilité et l'assistance efficace qu'il a pu

nous fournir pour régler nos nombreux bugs, notamment avec Matlab ou Labview et trouver de nouveaux ordinateurs pour nous moderniser un peu.

Au sein du labo j'ai pu profiter des conseils éclairés et de l'attention du débordant Takis Kontos (qui m'a vu grandir depuis que je suis "bébé"). J'ai bien aimé écouter ses histoires "*about life in the big city*". Merci aussi à Sukhdeep Dhillon, parrain pétillant et très attentif au bon déroulement de ma thèse. Merci aussi aux autres permanents avec qui j'ai pu interagir scientifiquement ou non : Benjamin Huard, Zaki Leghtas, Audrey Cottet, François Mallet, Gabriel Hetet et les autres. Merci à l'UFR de physique de l'UPMC d'avoir accepté de me confier une charge de moniteur. J'ai vraiment bien apprécié cette opportunité et je me suis rendu compte de l'importance et la complémentarité d'une activité modérée d'enseignement. Merci notamment à Sophie Hameau, Sandra Ninet et Jocelyne Quellier d'avoir si bien organisé et pensé l'UE "énergie et entropie".

L'ambiance de travail en P13 (est ce qu'un jour on dira vraiment L175 ?) a été incroyablement joviale et plaisante. Cela je le dois à tout ceux qui y sont passés. Je remercie particulièrement Quentin, Andreas et Holger. Nous avons réalisé nos thèses presque en même temps et donc partagé beaucoup de nos moments de doutes et de joie. Avec eux, j'ai pris beaucoup de plaisir à boire des bières à la Montagne ou des café au balcon, à partager nos vie, discuter de la physique, de la vie, de politique, de cuisine et de musique. Bien sûr l'esprit P13 ne serait pas le même sans tous les autres thésards, postdocs, jeunes chercheurs et stagiaires qui ont fait vivre cette équipe : Vincent, Rémi, Clément, Manohar, Wei (xièxie), Mohamed, Badih, Pablo, Anshu, Dora, Baptiste, Margaux, Hugo, Clément, Jake, Taylor, Erwann.

Bien évidement le reste du labo n'est pas épargné par cet entrain et cette bonne ambiance juvénile. C'est la partie des remerciements qui n'a plus grand chose à voir avec la thèse en soit et qui commence à être très réductrice, ne vous en fâchez pas : je vous aime tous ! Un merci tout particulier mais insuffisant à Sarah (qui mériterait bien plus qu'une page de remerciement pour toutes ses qualités), il s'en est passé des choses depuis nos premiers cours d'amphi à Lyon et je ne crois pas que la diffusion par postdocs soit un mécanisme suffisant pour arrêter tout ça. Il en va de même pour Adrien que j'ai appris à connaître un peu plus tardivement, merci pour sa bonne humeur et son implication politique, son humour et ses invitations à "Science Debout". Merci à Lauriane de défendre si sérieusement nos droits de thésards et postdocs. Merci à Danijela pour les soirées Parisiennes. Merci à Matmat pour les sorties Fontainebleau. Merci Michael a.k.a. docteur love et potins. Merci à Quentin F. pour sa pêche et son implication dans la vie du labo. Merci Matthieu Baillergeau pour les séminaires jeunes. Merci à Loïc pour son bureau et son ventilateur pendant la rédaction. Merci aux "anciens" : Jérémie, Laure, Benjamin, Jean, Raphaël, Ombline, Landry, Manu et Philippe. Merci à Madar, Federico, Tino, Nathanaël, Raphael, Théo, Sébastien, Thanya, Simon, Romaric, Théo, Christophe, Louis, Tom et son échelle, Sylvain. Merci évidement à tous ceux que j'ai oublié.

On ne passe pas toute sa thèse enfermé au labo et j'ai pu me reposer l'esprit et avoir le soutient et l'attention de nombreuses autres personnes et amis. Merci Simon pour nos aventures chinoises. Merci Xavier pour m'avoir appris à grimper. Merci à la team Belette, la team New-Orleans, la team Sherbrooke et à Cyril, la team "Le Rayon" et à Maxime. Un énorme merci à tous mes amis de Lyon. Merci à Olivier et Marine, Augustin, Clément et Fanny. Merci à Antonin et la team ArtDeco. Merci à mes amis de lycée (et d'avant) Martin et Paul et enfin un grand merci à ma famille qui me soutient depuis toujours.

Contents

Résumé en Français - Summary in French

0.1 Introduction

La fin du XXe siècle a vu la naissance et le perfectionnement des techniques de cryogénie et de nano-fabrication permettant ainsi l'émergence de la physique mésoscopique. Ce domaine de la physique qui attire aussi bien des expérimentateurs que des théoriciens, étudie des systèmes intermédiaires allant de quelques particules à des matériaux faisant quelques micromètres. En cela, elle permet de faire le lien entre l'échelle microscopique et l'échelle macroscopique. Les systèmes d'études privilégiés en physique mésoscopique sont par exemple les conducteurs cohérents. Dans ces conducteurs de taille micrométrique, on mesure les effets de la cohérence de phase sur le transport du courant électrique, c'est à dire des interférences d'ondes électroniques.

Le système sur lequel j'ai travaillé durant ma thèse est un gaz bi-dimensionnel d'électrons dans lequel on peut contrôler la trajectoire des électrons en travaillant sur l'architecture de l'échantillon. Les très basses températures (quelques dizaines de mK) permettent en outre d'atteindre des régimes où la longueur de cohérence et le libre parcours moyen des électrons sont grands devant la taille de l'échantillon, c'est à dire que l'on est dans un régime où on peut négliger non seulement les chocs inélastiques mais aussi les chocs élastiques. La phase de l'électron est conservée tout au long de son parcours dans l'échantillon. On a ainsi un transport d'électrons cohérent et balistique, et on peut appliquer une description ondulatoire aux électrons. Il est alors possible de réaliser des expériences analogues à celles d'optique comme l'expérience des fentes d'Young ou des interféromètres. Grâce à la source d'électron unique réalisée au laboratoire Pierre Aigrain (LPA) [1], on pousse l'analogie à des expériences d'optiques avec des particules uniques mais dans la matière condensée.

Cette thèse est dédiée à l'analyse de signaux électriques quantiques. En particulier, j'ai utilisé l'analogue électronique de l'interféromètre de Hong, Ou et Mandel pour réaliser

des expériences d'interférométrie à deux particules. En entrée de l'interféromètre sont placées des sources d'électrons uniques qui permettent l'injection contrôlée d'excitation ne contenant qu'une seule particule. Ces excitations sont guidés par des fils unidimensionnels jusqu'à l'interféromètre qui, en soit, est un contact ponctuel quantique agissant comme une lame semi-réfléchissante pour les électrons. On mesure en sortie les fluctuations aux basses fréquences du courant. Cela nous permet de mesurer le recouvrement entre les fonctions d'onde à un électron émises à chaque entrée. Grâce à cette mesure de recouvrement, j'ai pu caractériser à des échelles de temps sub-nanoseconde, le rôle des interactions Coulombienne sur la propagation de l'électron unique. J'ai pu montrer que ces interactions étaient la source principale de la décohérence du paquet d'onde mono-électronique et qu'elles décomposent l'électron sur des modes collectifs. C'est une manifestation de la fractionalisation de l'électron qui apparaît dans les systèmes unidimensionnel en interactions. Grâce à cet interféromètre, j'ai pu aussi implémenter un protocole de tomographie qui permet de reconstruire toute l'information à une particule de n'importe quel signal émis dans le fil.

0.2 L'interféromètre

0.2.1 Réalisation de l'interféromètre

0.2.1.1 Le gaz d'électron bidimensionnel

Le système sur lequel j'ai travaillé est un gaz bidimensionnel d'électrons à l'interface entre une couche d'Arséniure de Gallium (GaAs) et une couche de AlGaAs dopé au silicium. La différence de *gap* entre les deux matériaux permet le confinement d'électrons à l'interface sur une épaisseur de l'ordre de 10 nm. Ce type de gaz 2D a une très grande mobilité électronique ($\simeq 10^6\,\mathrm{cm}^2.\mathrm{s}^{-1}.\mathrm{V}^{-1}$) car il ne contient quasiment aucune impureté. L'échantillon sur lequel j'ai travaillé a été fabriqué au laboratoire de photonique et de nanostructures à Marcoussis par Y. Jin et A. Cavanna. Les densités électroniques mesurées sur ces échantillons sont de l'ordre de $10^{11}\,\mathrm{cm}^{-2}$ et les libres parcours moyen mesurés de l'ordre de $10-20$ μm ce qui est intéressant si on veut manipuler des électrons balistiques. On peut augmenter encore le libre parcours moyen en se plaçant en régime d'effet Hall quantique entier.

L'effet Hall quantique, découvert en 1980 par von Klitzing, se caractérise par une dépendance particulière de la conductance d'un échantillon avec le champ magnétique transverse au gaz 2D : pour des champs suffisamment intenses (supérieurs au Tesla), on observe que la conductance diminue en passant par des paliers. Les hauteurs de ces paliers sont des multiples de e^2/h où e est la charge de l'électron et $h = 2\pi\hbar$ la constante de Planck.

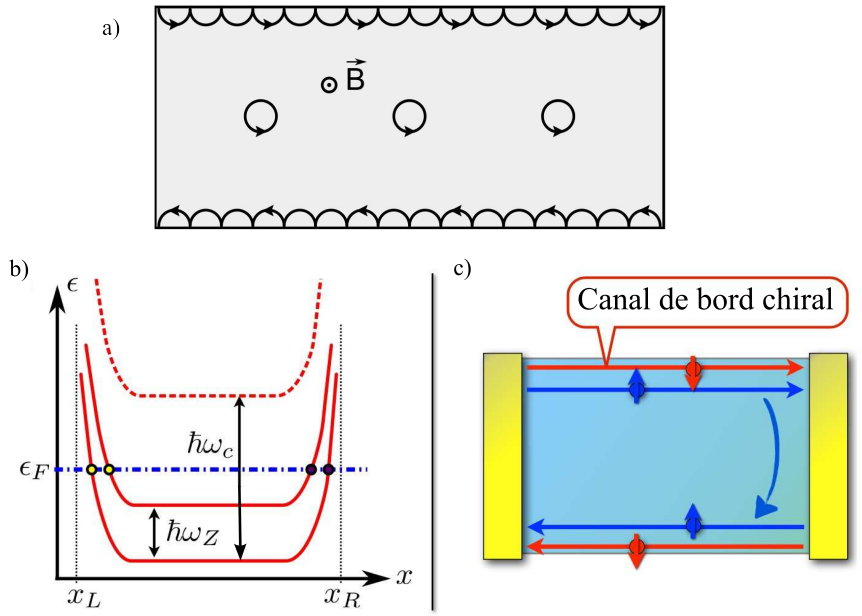

FIGURE 1: **a)** Description semi-classique de l'effet Hall quantique. Au milieu du gaz, les orbites cyclotrons sont restreintes spatialement et ne participent pas au transport d'électron. Au contraire, les orbites aux bords "rebondissent" et s'étendent d'un bout à l'autre du gaz : elles participent donc au transport. **b)** Spectre en énergie à taux de remplissage $\nu = 2$ en fonction de la position, x_L et x_R correspondent aux bords de l'échantillon. $\hbar\omega_Z$ correspond à l'énergie de Zeeman. **c)** Schéma des canaux de bords à taux de remplissage $\nu = 2$. Parce que les bords sont suffisamment espacés, l'effet tunnel d'un bord à l'autre est très peu probable et donc les événements de rétrodiffusion (flèche bleue) sont très limités.

Chaque électron occupe (à une dégénérescence de spin près) un niveau dit de Landau. Un niveau de Landau peut contenir un grand nombre d'électron. Le nombre d'électron du système fixe le niveau de Fermi ϵ_F et donc ainsi le nombre de niveau de Landau remplis ν. Dans le cœur de l'échantillon (ou *bulk*), les électrons occupent des niveaux de Landau qui se localisent du fait du désordre et ils ne participent pas à la conduction. En effet, l'écart entre deux niveaux vaut $\hbar\omega_c$ (où ω_c est la pulsation cyclotron) ce qui correspond à une température de $\sim 200K$ interdisant toute conduction à basse température.

En revanche, du fait du travail de sortie (*work function*), les électrons ressentent sur les bords du matériaux un potentiel variable qui les maintient à l'intérieur du gaz 2D. Ce potentiel courbe les niveaux de Landau qui remontent jusqu'à croiser le niveau de Fermi (voir figure 1-b). Les électrons localisés sur les bords ont donc un spectre d'excitations sans *gap* et participent ainsi à la conduction électronique à basse température. En outre, le champ magnétique brise la symétrie de renversement en temps ce qui impose une chiralité au système et les électrons d'un bord ne peuvent donc se propager que dans un seul sens (voir figure 1-c).

Ce dernier phénomène est particulièrement intéressant puisqu'il bloque la rétrodiffusion

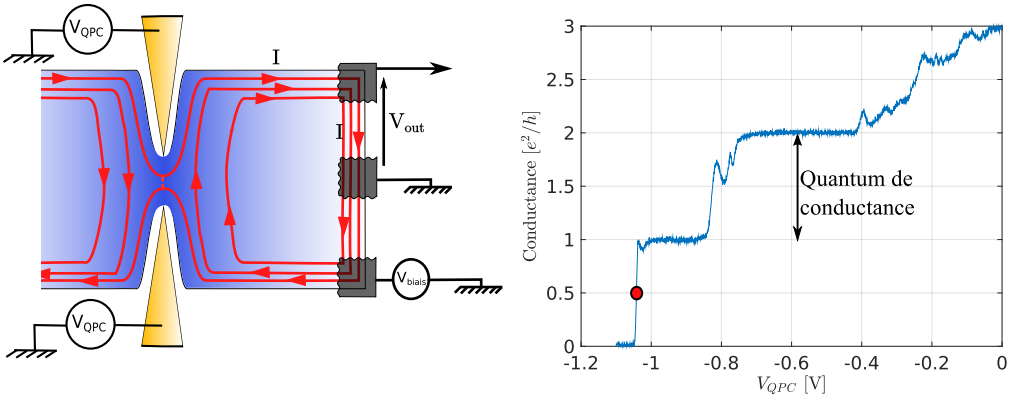

FIGURE 2: **a.** Schéma de la répartition des canaux de bords dans la situation qui correspond au point rouge sur la figure **b** qui représente la conductance à travers le QPC en fonction de la tension V_{QPC}. Pour $V_{\mathrm{QPC}} = -1.05$ V, le canal externe est transmis avec une probabilité de 50%.

des électrons. À facteur de remplissage entier, la rétrodiffusion ne peut se faire qu'en passant d'un bord de l'échantillon à l'autre, les 2 bords étant suffisamment espacés la résistance longitudinale s'annule. Cette absence de rétrodiffusion augmente encore le libre parcours moyen des électrons (jusqu'à ~ 100 μm). En outre, de grandes longueurs de cohérence ont pu être observées dans ces systèmes (~ 20 μm à 20 mK [2]). On peut raisonnablement approximer chaque canal de bord par un conducteur unidimensionnel chiral parfait avec une conductance égale au quantum de conductance : $e^2/h = 1/R_K$ où $R_K \simeq 25.8k\Omega$ est la résistance de von Klitzing. Ainsi, un gaz 2D à taux de remplissage ν entier a une impédance de R_K/ν.

0.2.1.2 Le contact ponctuel quantique comme lame séparatrice

Avant de pouvoir faire des expériences d'optique, il faut pouvoir réaliser l'analogue de la lame semi-réfléchissante présente dans de nombreux interféromètres et notamment celui de Hong, Ou et Mandel.

Pour réaliser une lame semi-réfléchissante, on utilise un contact ponctuel quantique (QPC). Le QPC est constitué d'électrodes métalliques déposées au dessus du gaz 2D dont on peut varier le potentiel. En portant ces grilles à un potentiel négatif on peut, par influence électrostatique, repousser la partie du gaz d'électrons qui se situe autour des électrodes et ainsi créer une constriction dans le gaz (voir figure 2). En appliquant un potentiel suffisamment négatif, on réfléchit tous les canaux de conduction et la conductance du QPC est nulle. À partir de là, en ramenant peu à peu le potentiel vers 0 on transmet progressivement les canaux un par un. On peut ainsi choisir combien de canaux sont transmis au niveau de la constriction et on voit la conductance varier par plateaux de e^2/h. Plus finement, on peut ouvrir partiellement un canal en sélectionnant

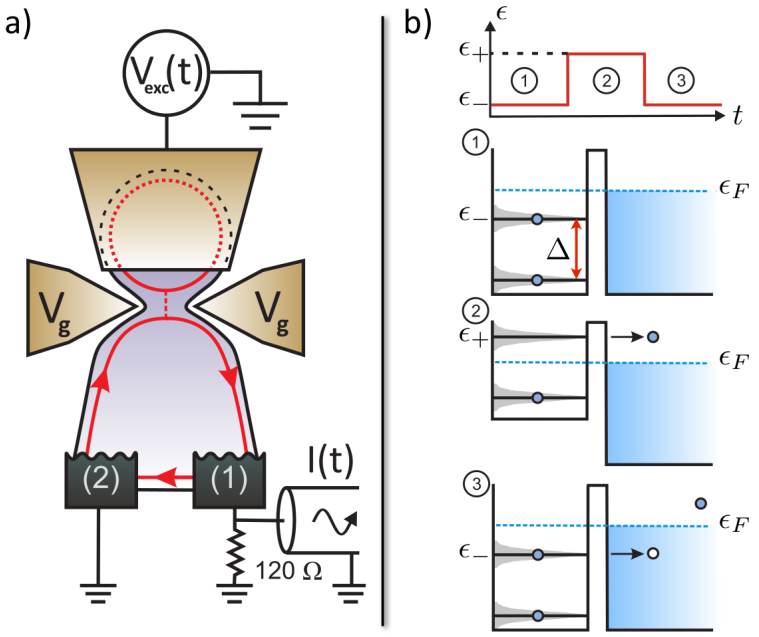

FIGURE 3: a)-**Schéma de la source d'électrons uniques.** Une boîte quantique de niveau discret suffisamment espacés est couplée au gaz 2D par un QPC. b)-**Principe de l'émission d'électrons et de trous uniques.** Le premier schéma représente l'évolution dans le temps du potentiel appliqué à la boîte ; les trois phases correspondantes sont représentées en dessous. ① la boîte est à l'équilibre. ② un fort potentiel est appliqué ce qui décale les niveaux vers le haut permettant à un d'entre eux de passer au dessus du niveau de Fermi ce qui déclenche l'émission d'un électron. ③ le potentiel est ramené à sa valeur initiale ce qui ramène un niveau vide sous le niveau de Fermi et permet l'émission d'un trou dans le gaz 2D. L'extension en énergie des niveaux est représentée par la zone grise. (Schémas extraits de [3]).

une valeur de potentiel intermédiaire entre canal ouvert et canal fermé (point rouge sur la figure). On va pouvoir ainsi contrôler la transmission par effet tunnel d'une charge sur un canal d'un côté de la constriction vers le canal correspondant de l'autre côté de la constriction. On peut ainsi choisir la tension qui correspond à une transmission $\mathcal{T} = 1/2$ et obtenir l'équivalent d'une lame semi-réfléchissante.

0.2.1.3 Source d'électrons uniques

Je vais présenter dans cette partie la source d'électrons uniques que j'ai utilisée pendant ma thèse. Elle a été extensivement étudiée par le passé [4–7]; je me concentrerai sur les points essentiels à la compréhension de l'expérience.

La source est constituée d'une boîte quantique couplée au gaz 2D (voir figure 3). La boîte a une largeur de l'ordre du μm ce qui crée un fort confinement dans les trois dimensions et discrétise les niveaux d'énergie. Les niveaux sont régulièrement espacés en

énergie avec un écart Δ[1]. On peut contrôler le potentiel dans cette boîte à l'aide d'une grille (ou *top-gate*) couplée capacitivement à la boîte. Du fait que l'on applique un fort champ magnétique à tout l'échantillon, il n'y a pas de dégénérescence de spin et chaque niveau occupé de la boîte ne contient qu'un seul électron. La boîte est reliée au reste de l'échantillon à travers un autre QPC. En contrôlant la tension de grille V_g de ce QPC, on joue sur le couplage par effet tunnel entre la boîte quantique et le reste de l'échantillon.

Lorsque la boîte est complètement fermée et isolée du gaz 2D (V_g très négatif), le confinement dans la boîte est important, les niveaux électroniques sont bien définis et peu étendus en énergie. À l'inverse, lorsque la boîte est complètement ouverte sur le gaz 2D on peut la décrire comme une simple extension du gaz 2D et les niveaux de la boîte sont tellement élargis en énergie qu'ils forment un continuum.

Le principe de fonctionnement de la source (résumé sur la figure 3-b) est le suivant. Partant d'une situation d'équilibre, on applique une marche de potentiel sur la *top-gate* de la boîte quantique de façon à promouvoir un niveau occupé au dessus de l'énergie de Fermi du gaz 2D. Cet électron peut traverser par effet tunnel la barrière de potentiel électrostatique créée par les électrodes du QPC. La barrière a une transmission D. La probabilité de rester dans la boîte est exponentiellement décroissante en temps. On associe à cette décroissance un temps de sortie $\tau_e \simeq h/(D\Delta)$[8]. On applique le potentiel suffisamment longtemps par rapport au temps de sortie pour faire tendre la probabilité d'avoir émis un électron vers 1. Ensuite on redescend le potentiel à son niveau initial. Le niveau électronique qui s'est vidé de son électron passe sous le niveau de Fermi. On peut alors adopter une description symétrique à l'étape précédente en considérant qu'un électron à une énergie inférieure au niveau de Fermi est absorbé par la boîte ce qui revient à émettre dans la mer de Fermi un trou d'énergie opposée (en prenant le niveau de Fermi comme origine des énergies). On répète ensuite le processus à la fréquence f de l'ordre du GHz.

0.2.2 L'expérience de Hong, Ou et Mandel avec des particules uniques

Maintenant que toutes les briques élémentaires ont été présentées, je vais introduire ici le principe de l'interféromètre de Hong, Ou et Mandel (HOM). On peut voir sur la figure 4 une image en fausse couleur prise au microscope électronique de la partie centrale de l'interféromètre. Cet interféromètre est placé dans un réfrigérateur à dilution He3/He4 qui permet d'atteindre des températures électroniques $T_{el} \approx 90$ mK. Dans les entrées 1 et 2 on injecte deux particules (électron ou trou) identiques et donc indiscernables (même énergie, même spin *i.e.* même état quantique). On peut contrôler précisément

[1] Il s'agit d'un Δ effectif qui prend en compte les énergies d'addition de charge dues aux interactions Coulombiennes.

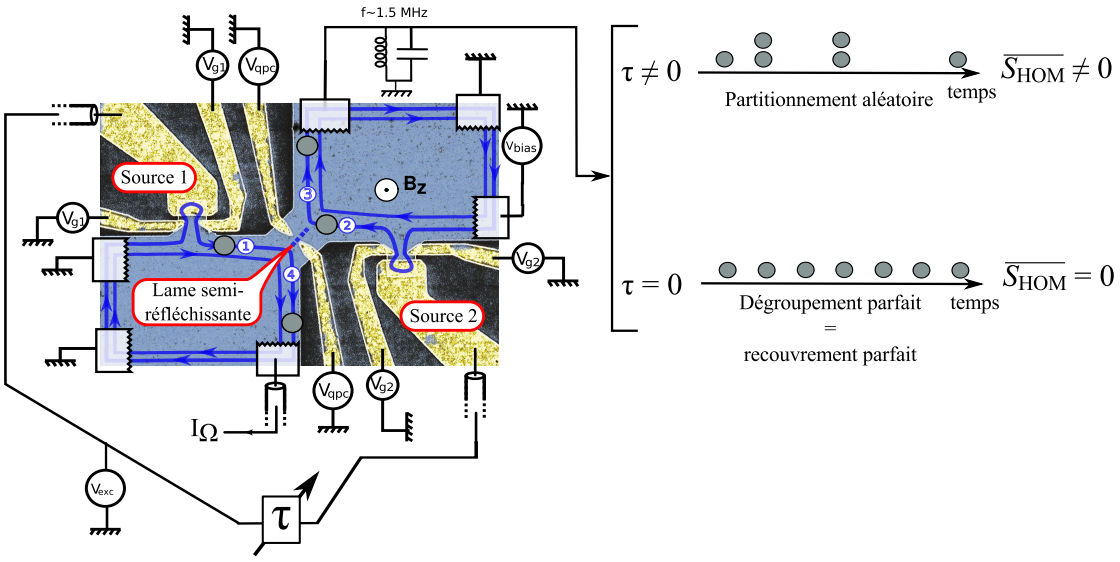

FIGURE 4: **Schéma de l'interféromètre HOM** à taux de remplissage 2. Les lignes bleues représentent les canux de bords de l'effet Hall. Le canal externe guide les électrons depuis la source vers le QPC qui est fixé à transmission $0,5$. On mesure le bruit de courant dans la sortie 3 dans une bande de fréquence proche de $1,5$ MHz. Sur la droite sont schématisés les deux cas limites : avec interférence à deux particules ($\tau = 0$) et sans ($\tau \neq 0$).

le décalage τ entre l'émission de la source 1 et la source 2 jusqu'à ± 7 ps. Sur la droite de la figure sont schématisés deux résultats possibles de l'expérience. Quand le retard τ entre les sources est nul, les deux particules indiscernables arrivent en même temps sur le QPC et il y a donc un recouvrement parfait des deux fonctions d'onde. Parce que les électrons sont des fermions, il va y avoir un effet de dégroupement (ou anti-bunching en anglais) : les électrons ne peuvent pas occuper le même états donc ils vont prendre chacun une sortie différente (3 ou 4), c'est le principe d'exclusion de Pauli. Ainsi, si on excite les sources à haute fréquence pour répéter l'expérience un grand nombre de fois par unité de temps, on observe un train d'électron unique dans chaque bras de sortie. Dans la sortie 3, il y a toujours une seule particule par (demi-)période, c'est un signal qui ne fluctue pas (à basse fréquence). Au contraire, quand τ est suffisamment grand pour que les particules ne "se voient pas" au niveau du QPC, cet effet d'interférence à deux particules disparaît et chaque particule prend aléatoirement une des deux sorties. On parle de partitionnement aléatoire. Cette fois on obtient donc un signal fluctuant en sortie 3 avec aléatoirement aucune, une ou deux particules par demi-période.

Pour observer si il y a des fluctuations à basse fréquence ou non, on mesure le bruit de courant. En pratique, on mesure la densité spectrale du courant intégrée dans une bande de $78,125$ kHz centrée à $1,48$ MHz. On peut montrer qu'une partie du bruit du courant que l'on appellera $\overline{S_{\mathrm{HOM}}}$ est sensible à ces fluctuations. C'est la mesure de cette quantité qui est au cœur de l'expérience d'interférométrie. Quand $\tau = 0$, si les particules

sont parfaitement indiscernables, on a $\overline{S_{\mathrm{HOM}}} = 0$ et au contraire pour $|\tau|$ suffisamment grand $\overline{S_{\mathrm{HOM}}} = \overline{S_{\mathrm{HBT1}}} + \overline{S_{\mathrm{HBT2}}}$, la somme des bruits créés indépendamment par chaque source. $\overline{S_{\mathrm{HBT}i}}$ correspond au bruit de courant créé par la source i lorsque elle seule est allumée, on peut donc aussi le mesurer facilement, il suffit d'éteindre l'autre source. On ne présentera pas les valeurs de bruit absolues mais seulement le bruit normalisé :

$$\Delta q(\tau) = \frac{\overline{S_{\mathrm{HOM}}}}{\overline{S_{\mathrm{HBT1}}} + \overline{S_{\mathrm{HBT2}}}} \tag{0.1}$$

qui est une quantité qui vaudra 1 lorsqu'il n'y a aucun effet d'interférence et 0 quand il y a recouvrement parfait entre les deux paquets d'onde. On a vu plus haut que les paquets d'onde avaient une certaine extension temporel τ_e donc quand $|\tau| < \tau_e$ il y a un recouvrement partiel entre les paquets d'onde et Δq peut prendre donc des valeurs intermédiaires entre 0 et 1. Globalement, en mesurant le bruit normalisé Δq en fonction du retard entre les sources τ, on s'attend à un creux vers $\tau = 0$ qui va jusqu'à 0 quand les particules qui se rencontrent sont parfaitement indiscernables. On appellera ce trou le trou de Pauli.

Cette expérience permet donc de sonder l'indiscernabilité des particules mais aussi de mesurer l'extension temporelle de leur paquet d'ondes. Plus généralement, on voit que c'est un outil puissant pour mesurer le recouvrement entre deux fonctions d'onde. Il est à noter qu'il faut faire appel à l'indiscernabilité et à la statistique (bosonique ou fermionique) des particules pour comprendre complètement le résultat, une interprétation purement corpusculaire ou purement ondulatoire ne suffit pas.

Sur la figure 5, on voit l'évolution de la profondeur du trou de Pauli en fonction de l'extension temporelle (ou temps de sorti) τ_e du paquet d'onde. On appelle visibilité γ cette profondeur. Une visibilité de 1 correspond à une interférence parfaite alors que pour $\gamma = 0$ il n'y a pas d'interférence du tout et les particules se comportent comme des billes classiques. Ces mesures ont été réalisées à deux taux de remplissage ($\nu = 2$ et 3). On voit une diminution des effets d'interférence en fonction du temps de sortie, on parle de décohérence. Plus les paquets d'onde s'étendent temporellement plus ils subissent cette décohérence de façon importante. De cette dépendance, on peut extraire, par une modélisation phénoménologique, un temps de cohérence caractéristique τ_c (98 ps pour $\nu = 2$ et 59 ps pour $\nu = 3$). Au delà, de ces temps là, le paquet d'onde ne peut pas maintenir sa cohérence. Les paquets d'onde dépassant cette extension temporelle sont en quelque sorte découpés en brique de cohérence plus petite mais incohérente entre elles et c'est pourquoi l'effet d'interférence est dramatiquement réduit.

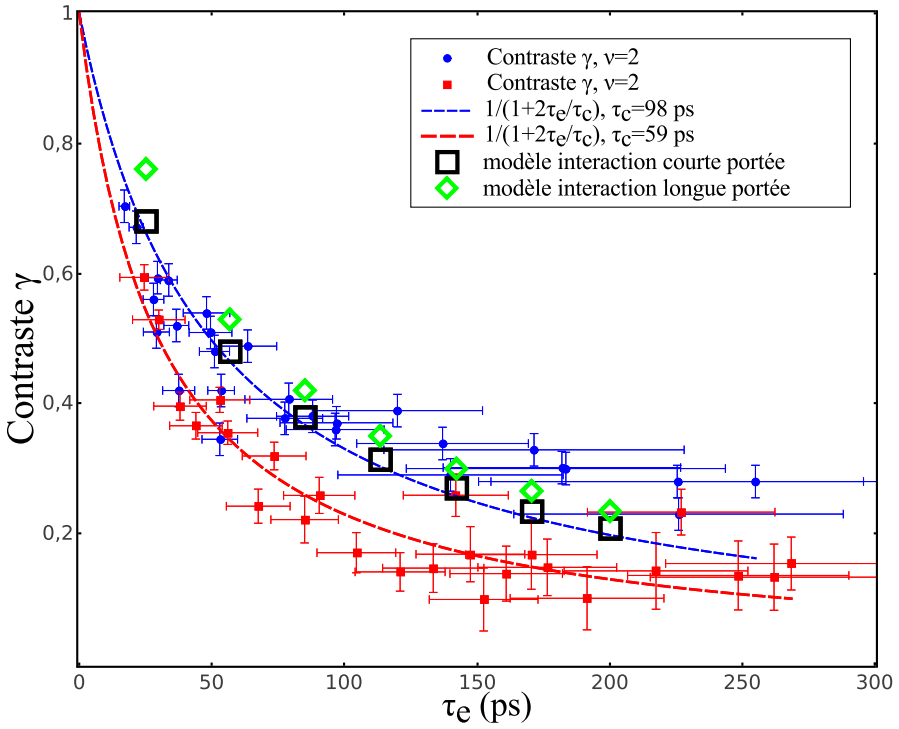

FIGURE 5: Évolution de la visibilité γ en fonction du temps de sortie τ_e à taux de remplissage $\nu = 2$ (points bleus) et $\nu = 3$ (carrés rouges). Les lignes correspondent à un fit qui permet d'extraire les temps de cohérence suivant le modèle $\gamma(\tau_e) = (1+2\tau_e/\tau_c)^{-1}$. Les carrés noirs et losanges verts correspondent aux prédictions théoriques (explications dans le texte principal).

0.3 Effet des interactions sur la cohérence d'un électron dans un fil

On remarque sur la figure 5, qu'en ajoutant un troisième canal co-propageant (en passant de $\nu = 2$ à $\nu = 3$), le temps de cohérence est encore plus faible. Il semble donc que c'est l'interaction entre ces canaux qui est à l'origine de cette décohérence. C'est un phénomène connu qu'on appelle *fractionalisation* et qui apparaît dans tous les systèmes électroniques à une dimension dès qu'il y a des interactions (même très faibles). Dans ces systèmes, ce n'est plus l'électron qui est la bonne particule élémentaire pour décrire les excitations de basse énergie du système mais plutôt des ondes acoustiques de charge que l'on appelle ici magnéto-plasmons de bord. Ces excitations sont des modes collectifs de charge et c'est la décomposition de l'électron sur ces modes collectifs qui va entraîner sa perte de cohérence. Le phénomène dans le cas particulier à $\nu = 2$ est schématisé sur la figure 6 pour des interactions Coulombiennes fortes. Dans ce régime, les nouveaux modes propres du système sont les distributions de charge symétrique (mode de charge) et anti-symétrique (mode neutre). Par rapport au mode neutre, le mode de charge a une plus forte répulsion Coulombienne donc une plus haute énergie et donc dans notre cas,

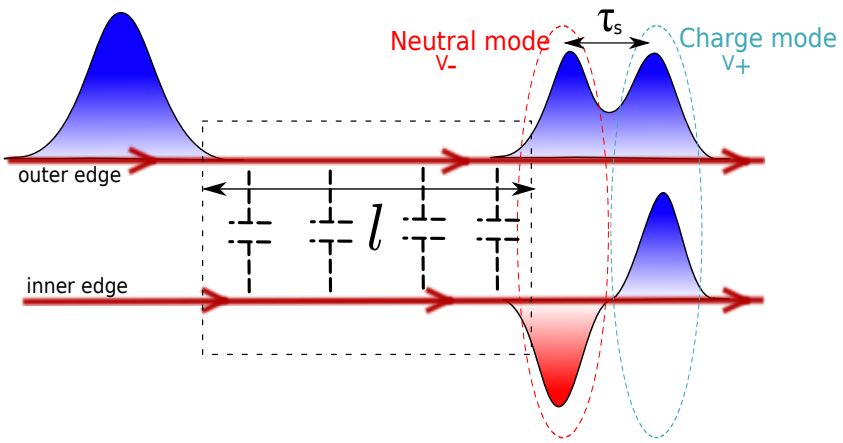

FIGURE 6: Schéma de la fractionalisation d'un pulse de courant à $\nu = 2$. La charge se décompose sur un mode symétrique (de charge) et un anti-symétrique (neutre). Ces deux modes n'ont pas la même vitesse. Une zone bleue correspond à un excès d'électron et une zone rouge à un excès de trou. l est la longueur de propagation entre l'injection et le QPC.

une plus grande vitesse. Cette différence de vitesse va entraîner, après une longueur de propagation l une séparation en deux du paquet d'onde sur le canal externe et la création d'une distribution dipolaire sur le canal interne.

Pour quantifier la force de l'interaction, on définit le temps de séparation $\tau_s = \frac{l}{v_-} - \frac{l}{v_+}$. On va voir qu'avec l'interféromètre on peut accéder à ce temps τ_s mais aussi observer directement la distribution dipolaire créée par la fractionalisation à $\nu = 2$. Pour cela, on va remonter la valeur de la tension appliquée sur les électrodes qui définissent le QPC central pour qu'il transmette parfaitement le canal externe mais agisse comme une lame semi-réfléchissante pour le canal interne. Ainsi on réalise l'expérience HOM avec le canal interne. C'est ce qui est représenté sur la figure 7. Puisque l'on veut sonder un phénomène qui implique des échelles de temps courtes, on va utiliser les paquets d'onde les plus courts possibles c'est à dire que l'on se place à $D = 1$ pour les deux sources pour émettre des pulses de charge avec un temps de sortie $\tau_e = 17$ ps. En orange est représentée la figure HOM complète pour le partitionnement du canal externe et en noir les données pour le canal interne. Les lignes pleines sont des simulations faites en utilisant une approche de type matrice de diffusion de plasmons. En effet, à $D = 1$ on n'émet pas réellement un électron unique et il est donc assez simple d'avoir une description de l'état de sortie en terme de magneto-plasmons de bord directement, ce qui facilite les calculs.

Les deux mesures ont en commun d'avoir un creux central à $\tau = 0$ ce qui montre que les excitations induites sur le canal interne sont cohérentes elles aussi. Une autre similarité est l'excès de bruit normalisé au dessus de 1 à $\tau = \pm T/2$. Ceci est dû au fait qu'on a des collisions entre des excitations de charge opposée [9]. En effet, les créneaux qui excitent les sources sont en opposition de phase. On retrouve des valeurs $\Delta q > 1$ pour le canal

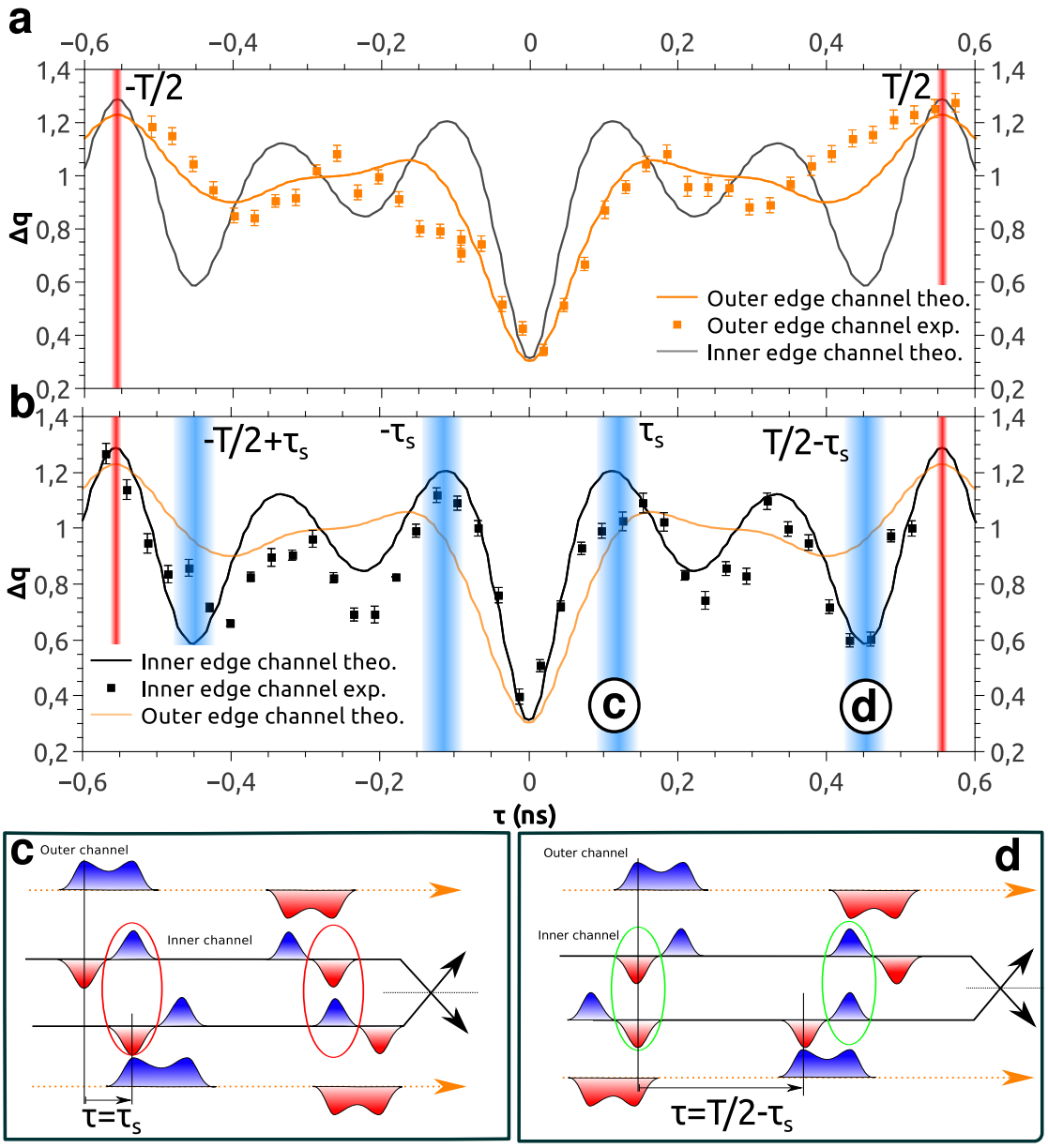

FIGURE 7: **a.** $\Delta q(\tau)$ à $D = 1$ pour le canal externe (points orange). **b.** Idem pour le partitionnement du canal interne (points noirs). Les lignes correspondent à des simulations. Les barres verticales rouges correspondent à des retards τ égaux à une demi-période de l'excitation carrée sur les sources $\tau = \pm T/2$. Les cercles c et d font références aux schémas **c** et **d**. **c** Schématisation des pulses de courant sur le canal interne quand $\tau = \tau_s$. **d** Même schématisation mais à $\tau = T/2 - \tau_s$.

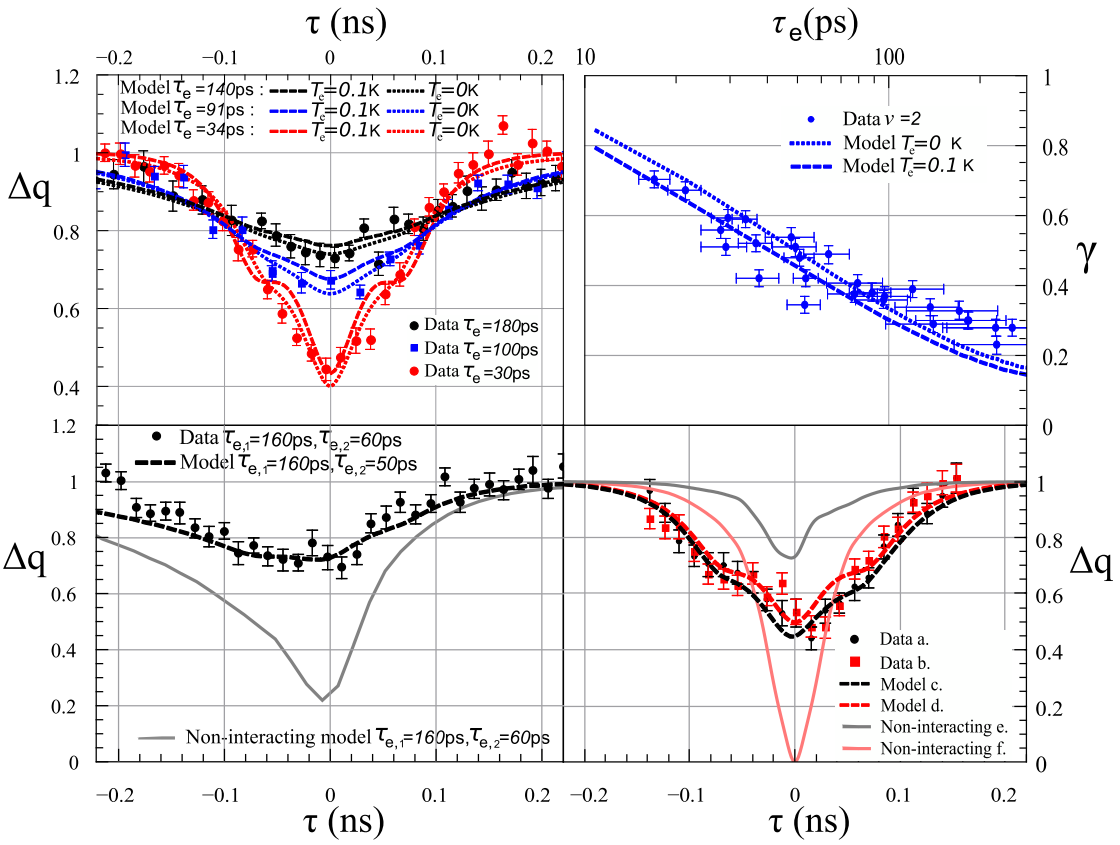

FIGURE 8: Comparaison entre prédictions et mesures à $\nu = 2$. **Haut-gauche** $\Delta q(\tau)$ pour différent temps d'émission τ_e. La théorie prenant en compte les interactions Coulombiennes est représentée en ligne pointillée ($T = 0$ K) et en tirets ($T = 0.1$ K). **Bas-gauche**, $\Delta q(\tau)$ pour des temps de sortie asymétriques. Théorie avec interactions ($T = 0.1$ K) en tiret et sans interactions en noir flou. **Haut-droit** Contraste γ en fonction du temps d'émission τ_e (en échelle log-linéaire). Les pointillés ($T = 0$) et tirets ($T = 100$ mK) représentent les prédictions théoriques avec interactions. **Bas-droit** (a) mesures, $\tau_e = 40$ ps, avec un bruit sur l'électrode de la source 2 équivalent à 400 mK; (b) mesures, $\tau_e = 40$ ps sans bruit rajouté; (c) théorie, $T = 0.1$ K, $\omega_{e1} = 0.7$ K, $\omega_{e2} = 0.3$ K, $\tau_e = 40$ ps; (d) théorie, $T = 0.1$ K, $\omega_{e1} = \omega_{e2} = 0.7$ K; (e) modèle sans interaction, $\omega_{e1} = 0.7$ K, $\omega_{e1} = 0.3$ K, $\tau_e = 40$ ps; (f) modèle sans interactions, $\omega_{e1} = \omega_{e2} = 0.7$ K, $\tau_e = 40$ ps.

interne essentiellement au niveau des zones bleues marquées c. Comme schématisé sur la figure, c'est parce qu'on a décalé les pulses de $\tau = \pm\tau_s$ et donc on retrouve partiellement des collisions avec des distributions de charge opposées. À l'inverse, on retrouve un creux supplémentaire à $\tau = \pm(T/2 - \tau_s)$. Comme schématisé sur la figure 7-d, c'est parce que ce décalage permet de retrouver des collisions avec des distributions de même charge. On ne retrouve pas ces deux dernières caractéristiques (c et d) sur la figure d'interférence du canal externe. Cette figure révèle bien que les interactions créent une distribution dipolaire sur le canal interne et permettent en outre de mesurer le paramètre $\tau_s \simeq 70$ ps ce qui est compatible avec une hypothèse d'interaction forte.

Grâce à ce paramètre τ_s, on peut complètement prédire l'effet des interactions pour n'importe quel état propageant. C'est ce qu'on pu faire deux équipes théoriques avec

qui j'ai beaucoup collaboré. Grâce à la mesure de τ_s, ils peuvent prédire pour n'importe quel régime d'émission (pas seulement $D = 1$) la forme de la figure d'interférence HOM, et ce quelque soit le temps de sortie τ_e et l'énergie d'injection ω_e dans les deux bras. On peut accéder à ces paramètres indépendamment, donc c'est un modèle sans paramètre ajustable. Ces prédictions ont pu être testées expérimentalement et les différents résultats sont présentées sur la figure 8. Les prédictions théoriques du panneau en haut à droite sont les mêmes que les carrés noirs et verts de la figure 5.

Sur les deux panneaux supérieurs on peut voir que l'accord est satisfaisant à la fois sur l'évolution de la forme du trou de Pauli (gauche) mais aussi pour toutes les visibilités qu'on avait mesurées (droite et voir aussi figure 5). Sur le panneau inférieur gauche, on voit que le modèle peut prédire assez bien ce qui se passe dans le cas d'une interférence entre des paquets asymétriques ($\tau_{e1} \neq \tau_{e2}$). On peut même voir que le modèle prédit une relaxation en énergie des particules vers le niveau de Fermi (panneau inférieur droit). La faible différence entre les points rouges et noirs montre que l'interférence est quasiment insensible à l'énergie d'injection initiale (ou au fait qu'elle fluctue). C'est confirmé par le modèle avec interaction. Cela s'explique par le fait que le modèle prédit une forte relaxation en énergie qui ramène tous les paquets d'ondes proche du niveau de Fermi quelque soit leur énergie d'injection initiale.

Le bon accord entre nos mesures et les prédictions de nos collaborateurs montre que l'on a une bonne compréhension du mécanisme de décohérence d'un électron unique. Nous avons pu tester d'autres potentiels mécanismes de décohérence et montré qu'ils étaient complètement négligeables, dis autrement, l'interaction Coulombienne entre canaux est tellement forte qu'elle masque complètement les autres sources de décohérence.

0.4 Tomographie d'électron

Durant la seconde partie de ma thèse, j'ai utilisé l'interféromètre HOM pour implémenter un protocole de tomographie afin de reconstituer la fonction d'onde à un corps de n'importe quel signal électronique se propageant dans les canaux de bords. Ce protocole a été imaginé et décrit par C. Grenier *et al.* en terme de mesure de fonction de Wigner [10].

0.4.1 Fonction de Wigner

La fonction de Wigner d'un état quelconque ρ est définie comme suit :

$$\mathcal{W}(t,\omega) = \int d\tau \left\langle \hat{\Psi}^\dagger \left(t - \frac{\tau}{2}\right) \hat{\Psi} \left(t + \frac{\tau}{2}\right) \right\rangle \; e^{i\omega\tau}, \tag{0.2}$$

où $\hat{\Psi}(t)$ est l'opérateur de champ qui annihile un électron à l'instant t et $\langle ... \rangle$ est la moyenne quantique calculée sur l'état ρ. $\mathcal{W}(\omega, t)$ est une fonction du temps et de l'énergie qui contient toute l'information à un corps sur l'état. C'est donc un bon outil lorsque l'on travaille avec des particules uniques notamment parce qu'on peut séparer la contribution de la mer de Fermi de celle de la particule additionnelle :

$$\mathcal{W}(t,\omega) = \mathcal{W}_F(\omega) + \Delta\mathcal{W}(t,\omega) \tag{0.3}$$

mais cela reste vrai quelque soit l'état. En revanche, cette distribution ne dit rien des corrélations à plusieurs particules qui peuvent exister notamment quand il y a des interactions. Cette fonction permet d'avoir une représentation en énergie et en temps de l'état quantique et a l'avantage de prendre des valeurs réelles uniquement (dans $\mathbb{R}$). La fonction de Wigner n'est pas rigoureusement une distribution de probabilité en temps/énergie car elle peut prendre des valeurs non-classiques pour un état fermionique (négative ou supérieure à 1). L'apparition de ces valeurs est un indicateur que l'état en question n'a pas d'équivalent classique *i.e.* c'est un état quantique. De cette fonction, on peut calculer toute les grandeurs physique à un corps comme le courant I ou la distribution moyenne en énergie $f(\omega)$ sur un intervalle de temps T :

$$I(t) = -e \int \frac{d\omega}{2\pi} \, \Delta\mathcal{W}(\omega, t) \tag{0.4}$$

$$f(\omega) = \frac{1}{T} \int_0^T dt \; \mathcal{W}(\omega, t). \tag{0.5}$$

Le protocole de tomographie va permettre de reconstruire la fonction de Wigner de n'importe quel état électronique.

0.4.2 Principe de la tomographie

Comme on l'a vu dans la partie 0.2.2, le bruit de courant que l'on mesure en sortie de l'interféromètre est relié au recouvrement des fonctions d'onde des deux particules qui arrivent à chaque entrée. En fait on peut généraliser cette assertion et montrer que le bruit contient un terme proportionnel au recouvrement entre les fonctions de Wigner (en

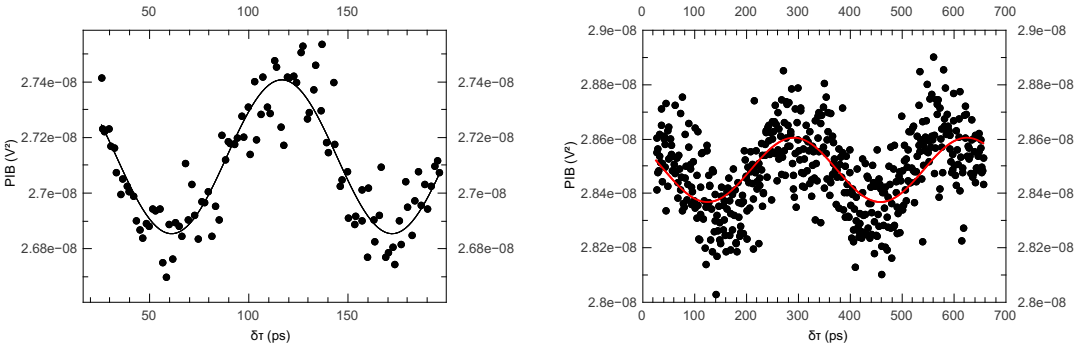

FIGURE 9: **Gauche**- Bruit intégré sur la bande de mesure avec une excitation en sinus à 9 GHz dans les deux entrées en fonction du déphasage entre ces sinus. Un biais DC de $3,65\ \mu$V est appliqué sur l'entrée 2. Cela permet de mesurer à $-3,65\ \mu$eV l'harmonique à 9 GHz de la fonction de Wigner (soit $\Delta\mathcal{W}_{1,1}(-3,65\mu eV)$) créée par l'excitation sinus à 9 GHz en entrée 1. **Droite**- Même chose mais avec d'un côté une excitation à $1,75$ GHz et de l'autre une excitation à $3,5$ GHz et un biais DC à 34 μV. Cela permet de sonder à $-34\ \mu$eV la deuxième harmonique (à 3,5 GHz) de la fonction de Wigner (soit $\Delta\mathcal{W}_{1,2}(-34\mu eV)$) créée par une excitation sinus à $1,75$ GHz.

excès) de l'entrée 1 et l'entrée 2:

$$\overline{S_{\mathrm{HOM}}} - \overline{S_{\mathrm{HBT1}}} - \overline{S_{\mathrm{HBT2}}} = -4R(1-R)e^2 \int \frac{d\omega}{2\pi}\ \overline{\Delta\mathcal{W}_1(\omega,t)\Delta\mathcal{W}_2(\omega,t)}^t \tag{0.6}$$

où R est la transmission du QPC central et $\overline{...}^t$ est la moyenne temporelle.

Le principe du protocole est d'utiliser à notre avantage cette mesure *in situ* de recouvrement de fonction de Wigner : pour mesurer la fonction de Wigner $\Delta\mathcal{W}_1$ d'un état inconnu injecté en entrée 1, on va mesurer son recouvrement avec une famille de n fonctions de Wigner parfaitement connues $\Delta\mathcal{W}_2^n$. La seule hypothèse que l'on va faire sur notre connaissance *a priori* du signal inconnu, c'est qu'il est périodique de période $T = 2\pi/\Omega$. Ainsi on peut décomposer la fonction de Wigner en harmoniques de Fourier :

$$\Delta\mathcal{W}_1(\omega,t) = \sum_{n=-\infty}^{\infty} \Delta\mathcal{W}_{1,n}(\omega)\ e^{in\Omega t}. \tag{0.7}$$

Un choix judicieux de famille de fonctions pour $\Delta\mathcal{W}_2^n$ est donc la famille des signaux créés en appliquant, sur un contact Ohmique, une tension sinusoïdale de faible amplitude et de pulsation $n\Omega$. En effet, on peut montrer ainsi que, pour un n donné, $\Delta\mathcal{W}_2^n(\omega,t)$ va permettre de mesurer l'harmonique de Fourier $\Delta\mathcal{W}_{1,n}(\omega)$. Comme pour l'expérience HOM, on va varier le retard $\delta\tau$ entre les deux signaux sur des petites échelles de temps. On obtient donc un bruit qui va osciller en fonction de ce retard, à la pulsation $n\Omega$. Deux exemples d'oscillations de ce bruit en fonction de $\delta\tau$ sont montrés sur la figure 9.

De ces oscillations, on extrait deux quadratures (ou un module et une phase) qui permettent d'accéder (à une déconvolution près) aux parties réelles et imaginaires de $\Delta\mathcal{W}_{1,n}(\omega)$. Finalement pour retrouver la dépendance énergétique en ω de ces coefficients de Fourier, il suffit de changer le niveau de Fermi dans l'entrée 2 avec un biais DC, d'ailleurs pour sonder $n = 0$ c'est la seule chose que l'on fait : il n'y a pas d'excitation sinusoïdale. L'harmonique $\Delta\mathcal{W}_{1,0}$ correspond à la distribution moyenne en énergie. Une fois qu'on a obtenu toutes les harmoniques $\Delta\mathcal{W}_{1,n}(\omega)$, on les recombine selon les formules 0.3 et 0.7 pour reconstruire la fonction de Wigner totale.

0.4.3 Fonctions de Wigner reconstituées

J'ai d'abord testé ce protocole sur des signaux simples à analyser : des excitations créées par une tension sinusoïdale sur un contact Ohmique (ou de façon équivalente sur la source à $D = 1$) pour différentes fréquences. À l'aide de simulations, on peut montrer que ces fonctions de Wigner sont plus simples et rapides à reconstruire car elles ne se construisent que sur quelques harmoniques ($n \leq 3$). Si on ne connaît rien *a priori* du signal, on doit mesurer toutes les harmoniques. Plus on mesure une haute valeur de n plus on accède à des dynamiques de temps courtes.

Les mesures des 3 premières harmoniques d'une excitation sinusoïdale à 10 MHz et les deux premières d'une à 9 GHz (ainsi que la distribution moyenne en énergie $\Delta\mathcal{W}_{1,0}(\omega)$) sont présentées sur la figure 10 et les reconstructions déduites sur la figure 11. Ces deux fréquences permettent de tester deux régimes : une excitation classique (ou adiabatique, avec $\hbar\Omega < k_B T_{el}$) et une excitation photo-assistée ($\hbar\Omega > k_b T_{el}$). Contre-intuitivement, c'est le signal non-classique qui a besoin de moins d'harmoniques pour être reconstruit ou, de façon équivalente, qui a des harmoniques plus faibles pour $n > 1$.

On peut comparer nos reconstructions aux prédictions théoriques et voir que l'accord est plutôt bon, surtout proche du niveau de Fermi ($\omega = 0$). Les écarts à plus hautes et plus basses énergies (typiquement $|\hbar\omega| > 33$ μeV) sont dus, d'une part aux effets de bords lors de la déconvolution, mais aussi aux non-linéarités de notre QPC qui sont activés pour des biais de cet ordre de grandeur là. Cela rend l'interprétation des mesures de bruits en terme de recouvrement de fonction de Wigner moins licite et plus compliquée. Néanmoins, on peut observer des négativités et des valeurs au dessus de 1 très significatives pour le signal à 9 GHz. Des effets quantiques non-négligeables, tels que l'absorption de photons à 9 GHz, sont à l'origine de la non-classicitée de cet état et on peut clairement les observer. Au contraire, la fonction de Wigner reconstruite à 10 MHz peut, à quelques erreurs près, s'interpréter comme une mer de Fermi avec un potentiel chimique

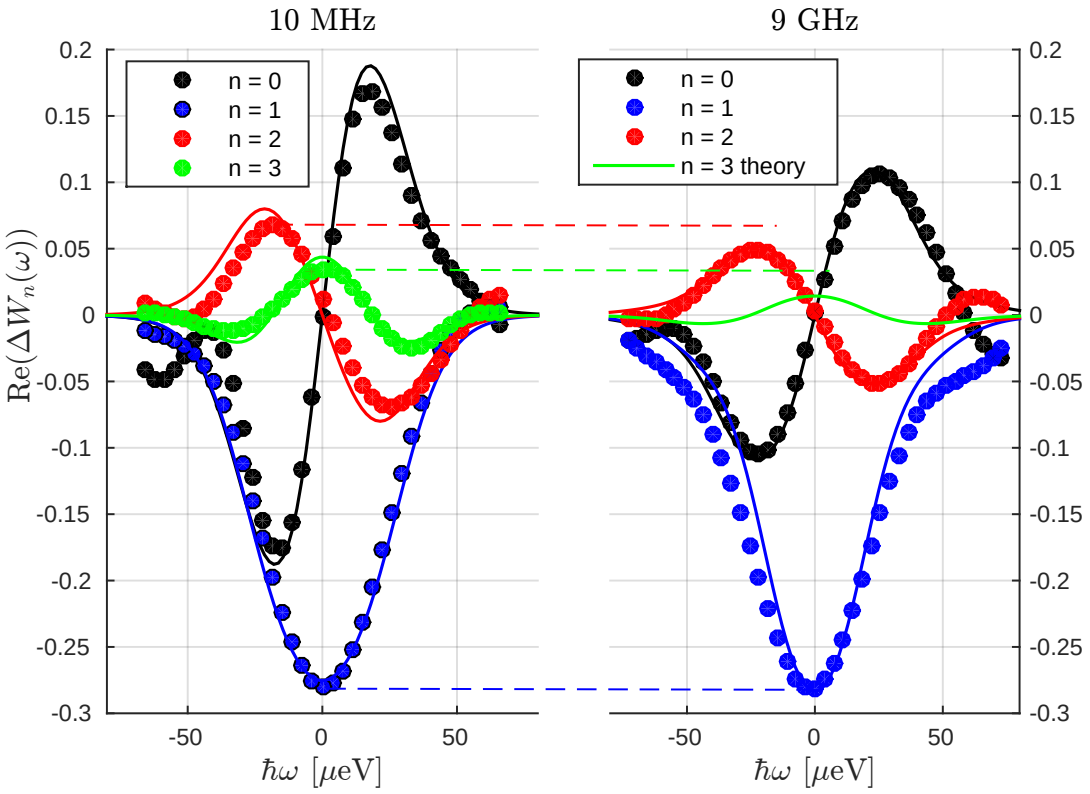

FIGURE 10: **Gauche**- $Re(\Delta W_n(\omega))$ (après déconvolution) pour n de 0 à 3 pour une excitation sinusoïdale à 10 MHz d'amplitude $33 \pm 2\mu V$. **Droit**- *Idem* pour une excitation à 9 GHz d'amplitude $V_{exc} = 31 \pm 1\mu V$. Les lignes correspondent aux prédictions théoriques. Les lignes horizontales sont des guides pour l'œil qui permettent de comparer les niveaux relatifs des harmoniques. Les poids à $n = 1$ sont comparables mais on voit qu'il faut en fait plus d'harmoniques pour reconstruire une harmonique basse fréquence que haute fréquence.

qui varie sinusoïdalement en fonction du temps. C'est donc une excitation complètement adiabatique et classique.

Avec cet interféromètre, nous pouvons donc quantitativement distinguer une excitation classique d'une excitation quantique. Durant la fin de ma thèse, j'ai donc commencé à utiliser ce protocole pour mesurer des états sortant de la source pour $D < 1$. Les résultats sont pour l'instant préliminaires et prennent plus de temps car il faut mesurer plus d'harmoniques et être plus vigilant aux fluctuations de la source lors de la mesure.

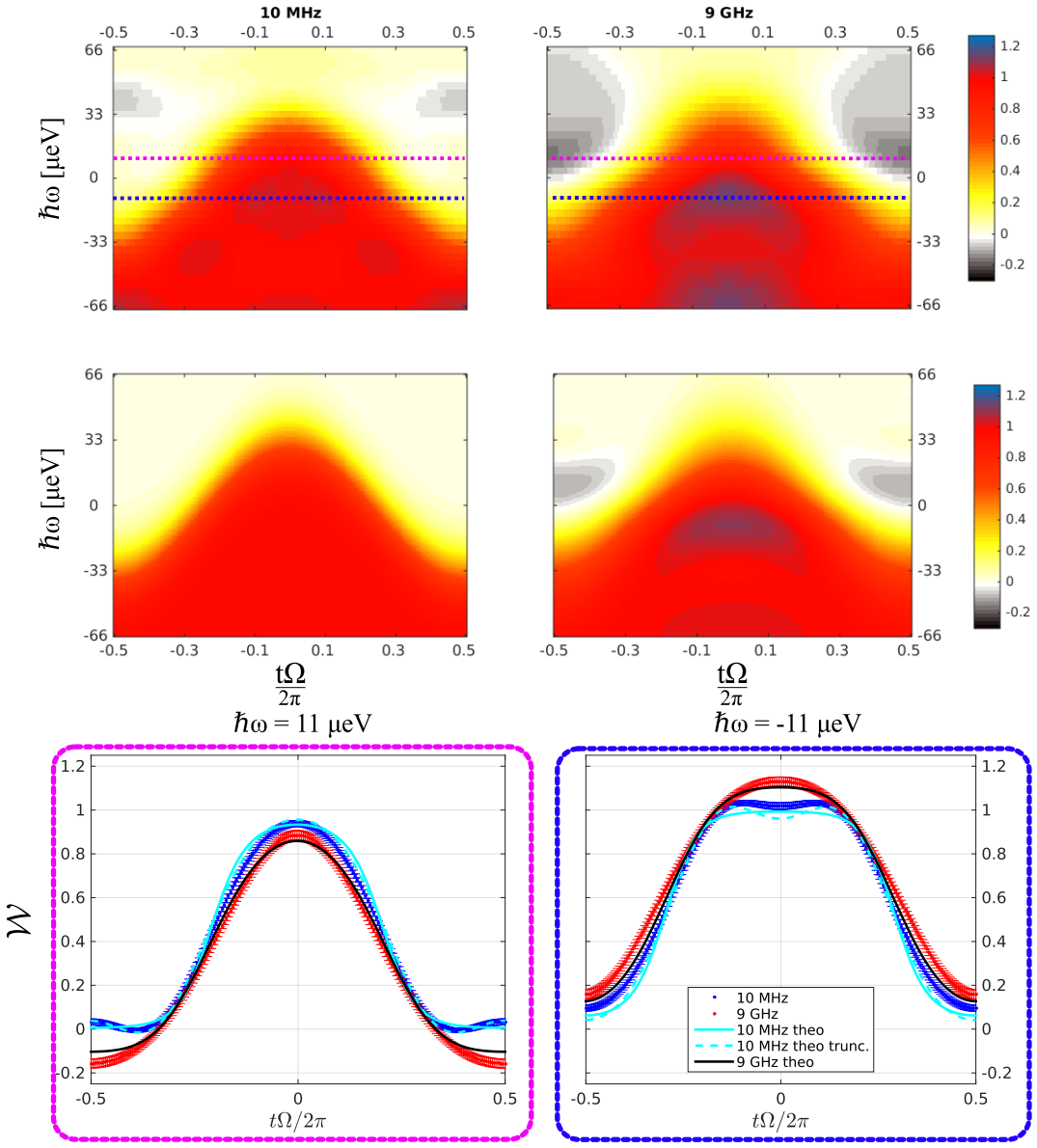

FIGURE 11: **Haut**- Fonctions de Wigner reconstruites pour une excitation à 10 MHz (à gauche) et à 9 GHz (à droite). **Milieu** Prédictions théoriques correspondantes **Bas**- Coupes en énergie des données et des prédictions. Pour 10 MHz, on peut voir qu'une part de la différence avec le modèle vient du fait qu'il manque des harmoniques supérieures ($n \geq 4$) dans la reconstruction.

0.5 Perspectives

Il reste à finir les mesures d'états émis pour une source en régime $D < 1$. Cependant, on sait que les interactions vont fortement influencer la fonction de Wigner finale. Nous avons donc aussi réfléchi à des stratégies pour limiter l'effet des interactions. Par exemple, nous avons cherché, pour l'instant sans succès, à séparer spatialement les canaux externe et interne pour réduire la force des interactions. Nous avons aussi commencé à réfléchir à ce que donnerait ce genre d'expérience dans le régime d'effet Hall quantique fractionnaire.

Chapter 1

Introduction

"[...] nous ne faisons que nous entregloser. Tout fourmille de commentaires ; d'auteurs, il en est grand cherté. Le principal et plus fameux sçavoir de nos siecles, est-ce pas sçavoir entendre les sçavans ? Est-ce pas la fin commune et derniere de tous estudes ? Nos opinions s'entent les unes sur les autres. La premiere sert de tige à la seconde, la seconde à la tierce. Nous eschellons ainsi de degré en degré. Et advient de là que le plus haut monté a souvent plus d'honneur que de mérite ; car il n'est monté que d'un grain sur les espaules du penultime."

Montaigne *Essais* partie III, chap. 13 (« De l'expérience »).

"If I have seen further, it is by standing on the shoulders of giants."

Sir Isaac Newton.

This works settles in the ever evolving and fascinating field of mesoscopic physics. It is a branch of physics one could vaguely define as the interface between condensed matter physics and quantum physics. Actually the term is broad enough to cover subjects that are now quite different, that we could call daughter branches of mesoscopic physics. For instance, the superconducting qubits community does not address the same problematics than the topological insulator community. However different they are, these branches share common methods: they benefited from the important development of nano-fabrication technology as well as the growth of the cryogenic industry. They also share the same long term (perhaps naive) goal that from these researches will emerge ground breaking and practical quantum technologies that will revolutionize computers and information industry. Recently, this has appeared a bit less like a dream with the interest showed by many companies or institutions to invest massively on these projects.

For instance, Google bought a D-wave machine, Thales is looking for applications of topological insulators for new spintronics devices, Microsoft started to develop its own quantum research lab "Station Q", IBM launched "IBM Q", NSA invested in a $79.7 million quantum based cryptography research program titled "Penetrating Hard Targets" and even a few start-ups were created on those ideas (*e.g.* Rigetti). Whatever the consequences of these projects, it cannot hide the fact that mesoscopic physics is essentially driven by basic research and has been a formidable platform for fundamental physics, in particular in its ability to create or manipulate new states of matter or exotic quasi-particle excitations rivaling with particle physics. In this thesis, I have studied the propagation of a single electron and how its quantum coherence is affected by the quantum circuit in which it propagates. This circuit is created in a bi-dimensional electron gas. I have also implemented a protocol that aims at fully characterizing such excitations in quantum circuits.

In this general introduction chapter, I will specify the achievements of mesoscopic physics on which this very work relies on. I will also place this work in its current scientific context, presenting other recent works related to this one. Some particularly important points will be discussed in more detail in the following chapters.

1.1 Bi-dimensional electron gas

The systems I worked with are tiny circuits created at the interface between two semiconductors, one of which is made of GaAs, the other of AlGaAs. Because these two semiconductors do not have the same gap (the energy needed to bring an electron from the valence band to the conduction band), bands will rearrange so as to create a bi-dimensional potential trap at the interface (or quantum well). A silicium (Si) doping layer is added above the interface and the excess electrons they bring will be trapped in this well (for temperatures lower than 150 K) with an electronic density of the order of 10^{11}cm^{-2}. Because the interface between the 2 semiconductors is really thin, there will be quantum confinement *i.e.* the excitation along the axis perpendicular to the gas will be quantized by energy gaps, this gap is of the order of ≈ 300 K. This means that below 150 K we can safely consider the gas of electron has formed and it has no possible excitation in the perpendicular direction *i.e.* it is bi-dimensional. A sketch of this heterostructure is shown on figure 1.1.

This sample can then be designed and shaped both with chemical etching and by depositing golden electrode gates on top of the heterostructure. Thanks to these gates we can change the local density beneath it through a voltage control. Indeed, compared to a conventional metal, this gas has an electron density much lower ($n \approx 10^{15}\text{cm}^{-2}$ for a one

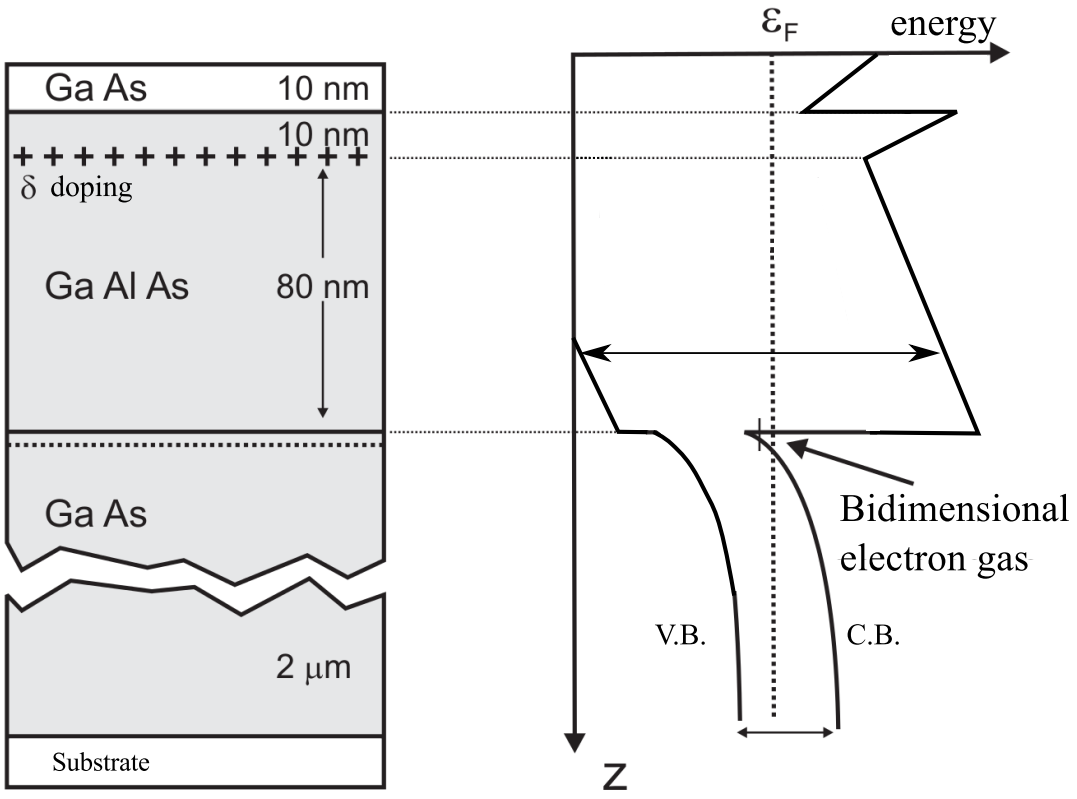

FIGURE 1.1: Figure adapted from [4] **Left.** Vertical cut of a GaAs/AlGaAs heterostructure. + signs represent Si dopants and horizontal double arrow is a gap. **Right.** Corresponding energy diagram. V.B. stands for valence band and C.B. for conduction band.

atom thick layer of copper) which makes it easier to deplete (even completely) a defined area by imposing an electrostatic gate voltage. Finally, the gas is electrically connected to other electrical components (measurement apparatus or generators) through Ohmic contacts. They are made of an alloy of gold, nickel and germanium that can diffuse from the top of the structure down to the electron gas.

The design of the two dimensional gas I used for this work will be presented in section 2.2. Most of the results I will present were obtained on gas with density $n = 1.9 \times 10^{11}\text{cm}^{-2}$, however, we also used gas with halved electron density (see end of chapter 4).

1.2 Ballistic transport

Thanks to the development of molecular beam epitaxy technology and its increasing precision, it is now possible to make a really clean interface with deposition of layers of atomic precision. This, combined with the fact that Si impurities are way above the interface, implies that there is a very low impurity density in the proximity of the gas.

The mobility μ is high enough so that the mean distance between two successive elastic collisions l_e is around $\approx 10\mu$m at 4 K; for our samples μ is around $2 \times 10^6 \text{cm}^2.\text{V}^{-1}.\text{s}^{-1}$. This means that we can design circuits of a few μm size that will not have a diffusive transport but rather a ballistic one.

What is even more interesting is that the number of inelastic and dephasing processes is also reduced and therefore the wave-like behavior of electrons cannot be neglected over distances $l_\varphi \simeq 20\mu$m at 20 mK [2, 11](or a few μm at 1K [12, 13]). We can thus define a phase to an electronic wave which stays coherent over distance l_φ.

1.3 Quantization of conductance

This phase coherence radically imposes to change how we describe the motion of electrons in these systems. We can no longer view electrons as colliding hard spheres. Waves can interfere and we now have to talk about transmission or reflection of modes. This formalism was first developed by Rolf Landauer in 1957 [14]. One of the main predictions of this formalism is that each mode has a quantized conductance of e^2/h. This was confirmed by the measurements of van Wees *et al.* [15] and Wharam *et al.* [16] who created the first quantum point contacts. It consists of two golden electrodes deposited on top of the GaAs heterostructure so as to design a slit (see inset of figure 1.2). This circuit enables to control how many electronic modes one can transmit through the slit by changing the voltage applied on the electrodes. On figure 1.2 we show their main result. On the right panel we see the quantization of conductance as multiple of $2e^2/h$ (modes are spin degenerate here) as a function of the gate voltage. Each step corresponds to the additional transmission of one (spin degenerate) electronic mode. In this work, we also used a quantum point contact and its functioning is detailed in section 2.2.1.

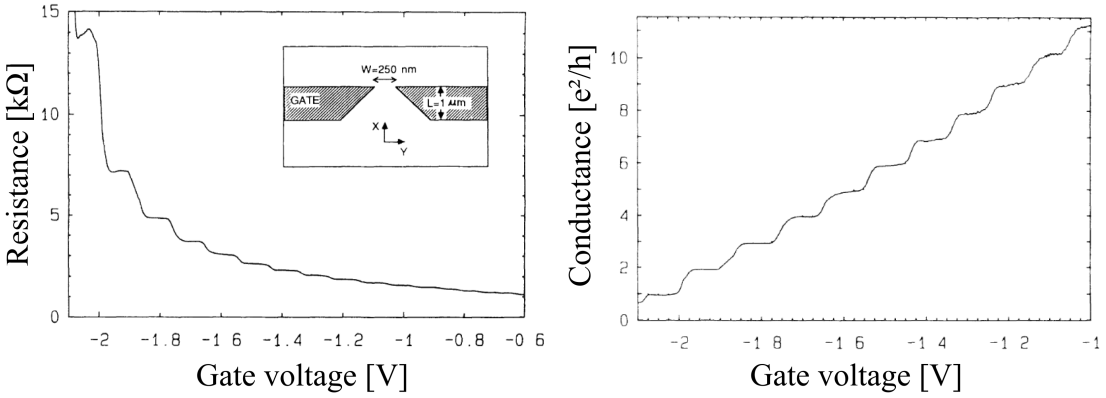

FIGURE 1.2: **Left.** Resistance through the point-contact constriction versus gate voltage at 0.6 K. Inset: point-contact layout **Right.** Point-contact conductance versus gate voltage obtained from left data without lead resistance. Plateaus at multiple of $2e^2/h$ are clearly visible. Figures extracted from [15].

1.4 Coherent transport

The development of high mobility electron gases enabled to create circuits smaller than the coherence length and thus to design electronic interference experiments analogous to optics. The first experiment of this kind is the double slit Young's experiment that was reproduced by Yacoby *et al.* [17]. On the left panel of figure 1.3, we see a micrograph of the GaAs/AlGaAs heterostructure they used with the additional top gates to design the double slit geometry. Current is injected in area C and a voltage measured in E. An additional top gate in front of one slit enables to change the phase difference (N_V here) between the two paths. On the right panel, we clearly see oscillations in the voltage measured in E with respect to this phase difference at 2 different magnetic fields. These oscillations are a clear sign that the current has a wave-like behavior and that electrons can interfere with themselves. Depending on the phase difference between paths going through one slit or the other, the probability amplitude for an electron to go from C to E will either interfere constructively or destructively which will change the total transmission from C to E. This is essentially a one-particle interference experiment in the sense that an electron wave function can interfere with itself; as we will see in the next chapter our works mainly concern two-particle interference.

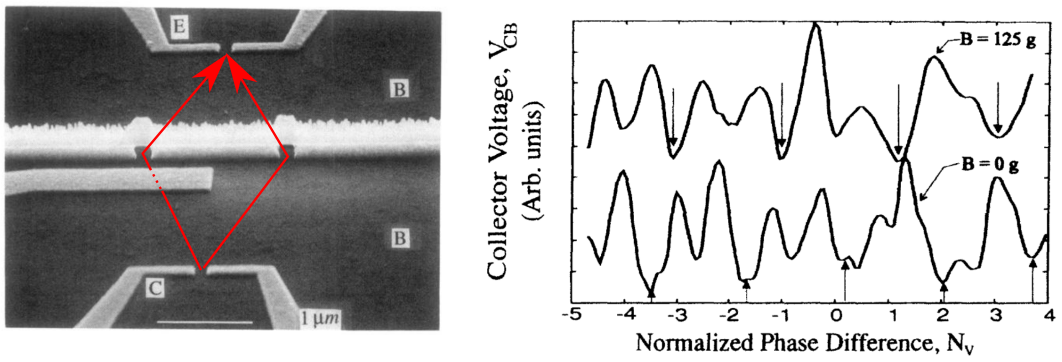

FIGURE 1.3: **Left.** Top view scanning electron microscope picture of the sample. Light area correspond to top gates. **Right.** Voltage measured in E versus phase difference between the two path at 2 different magnetic fields. Figures extracted from [17].

1.5 Single electron sources

Another major achievement of mesoscopic physics is the realization of single charge and single electron sources (see [18] for a review) and in particular *on demand* single electron sources *i.e.* sources that can be triggered at will and that deliver only one particle in a circuit with a defined energy. They are of great interest for several reasons. First, they enable to get a clearer picture of what happens in a circuit at the microscopic level. Indeed, single particle representation is often more intuitive. Another interest in the generation of single electron sources is their potential application for metrology and the redefinition of the Ampere unit [18]. Finally, combined with coherent transport, they are essential for the implementation of electron quantum optics experiments and the implementation of quantum information processing protocols [19–23]. For this work, I used an AC driven mesoscopic capacitor to emit a single particle [1]. I will describe its working principle more in details in section 2.2.2.1. Here, I will briefly present other possible realizations of such single particle sources.

1.5.1 Quantum turnstile and quantum pumps

Both based on the same principle, single charge pumps and turnstile were implemented at the beginning of the 1990s [24–26] and strongly improved at the end of the 2000s [27, 28]. The idea is to use electrodes to define a quantum dot well isolated both from the input reservoir and the rest of the circuit. It can either use 3 electrodes for turnstile [29] or only two for pumps [30, 31]. Figure 1.4 is extracted from [30] and illustrates the working principle of these pumps. We see on the left panel that the two electrodes above the GaAs heterostructure define a small area which will be confined enough to create a quantum dot. The left gate is driven at radio frequencies ($\approx$ 300 MHz) whereas the right

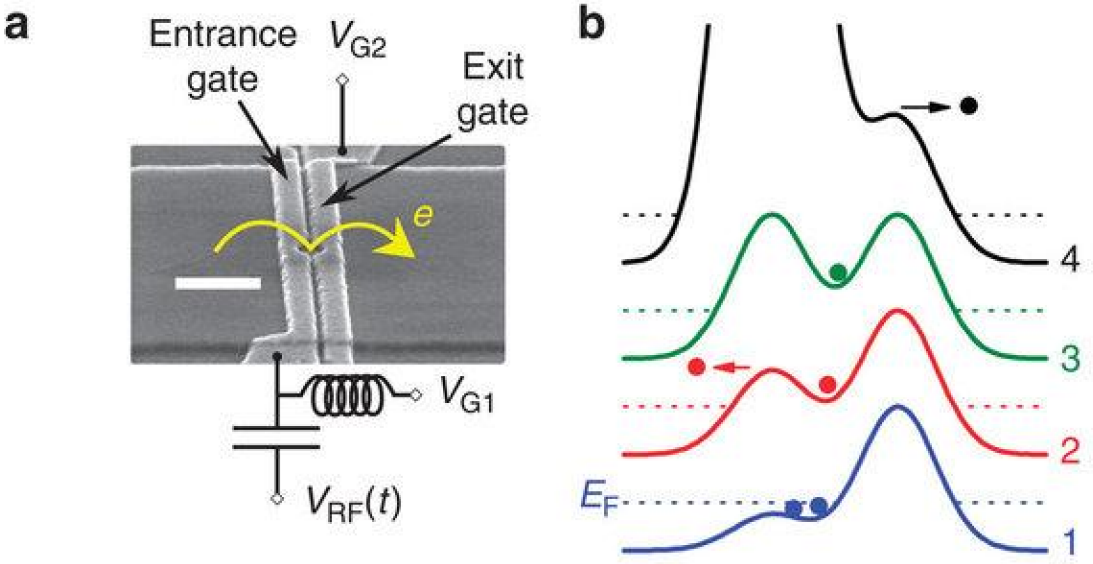

FIGURE 1.4: **Left.** Scanning electron microscope image of the setup. The lighter areas correspond to gate electrodes. White scale bar indicates 1 μm. **Right.** Schematic diagrams of the potential along the channel during four phases of the pump cycle: (1) loading, (2) back-tunneling, (3) trapping and (4) ejection. One cycle transports an electron from the left (source) to the right (drain) lead.

one is kept constant. First, the voltage on the left one is lowered so that one or several electrons are captured from the left part and put in the small dot. When the left gate potential starts to rise, there are possible back tunneling events. Because of Coulomb energy, back tunneling events are a few orders of magnitude larger for all electrons but the least energetic one. Therefore, there is a probability converging quickly to one that, going from event 1 to 3, only one electron remains in the dot. Then in 4, the left potential is raised again so that the energy of the electron reaches a level comparable to that of the right barrier and then can tunnel in the right part of the circuit. The height of the right barrier imposes the energy at which the electron is released. With this system the electron is emitted with good precision at a few hundreds meV above the Fermi sea. This is high enough to avoid thermally activated states or co-tunneling processes. Another advantage of these sources, is that they can be driven quickly (GHz range) and the temporal size of the wave packets can be as low as a few tens of picoseconds [32].

Such quantum pumps were also realized in silicon systems with drive frequencies in the GHz range with charge quantization accurate to better than 0.92 ppm [33]. Another remarkable recent realization was done with a single level quantum dot at the interface between two superconducting leads [34]. Benefiting from the sharp energy filter induced by superconducting gaps in the lead, they could reach an energy width of around 1 % the average emission energy ($\approx 260\mu$eV). This precision could be enhanced with a lower rise time for the square voltage sequence used to drive the pump.

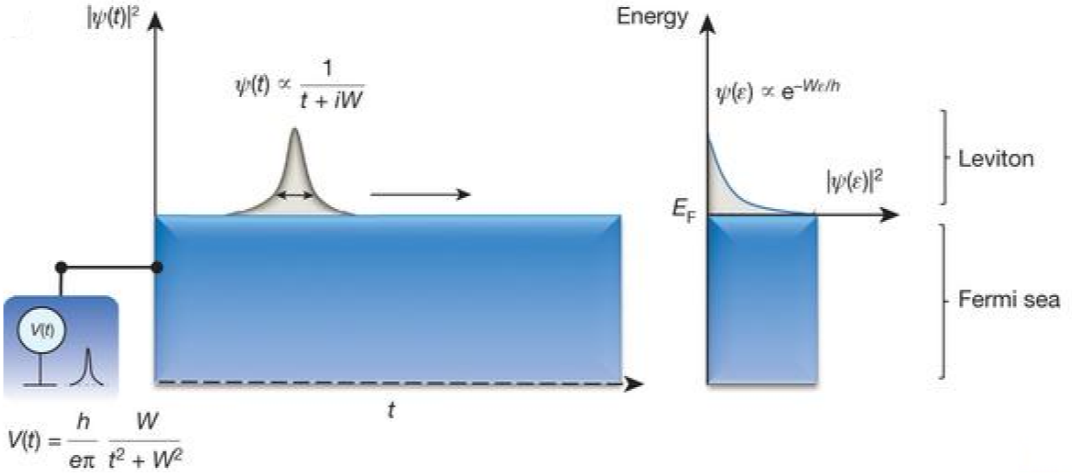

FIGURE 1.5: Schematic representation of the wave function ψ of a leviton in time (left) and energy domain (right). (Extracted from [36].)

1.5.2 Leviton excitation

Another approach to realize single electron injection in a circuit is to directly excite the whole many-body state of the Fermi sea in a very particular way so that the resulting many-body state is exactly a Fermi sea with a single electron excitation on top of it. To do so, one has to apply a Lorentzian shape voltage $V(t)$ on the Ohmic contact. This excitation is called a leviton after Levitov who predicted which shape to apply [35]. More precisely, to emit only one electron with this pulse, the Lorentzian of width $2W$ writes:

$$eV(t) = \frac{h}{\pi} \frac{1}{1 + (t/W)^2}, \tag{1.1}$$

where $-e$ is the elementary charge of an electron and h the Planck constant. This was realized (also in GaAs heterostructures) by Dubois *et al.* [36] where they realized a periodic train of leviton excitations. They showed with shot noise measurements that indeed the number of additional electron-hole pairs generated by this drive is very small compared to a sine drive or a square drive and that the remaining excess particles could almost all be explained by finite temperature and heating effects. This minimal excitation property seems to hold also for more complex ground state like the Laughlin fractional states [37].

For the leviton, W governs both the temporal extent and the (inverse of the) energy width. As sketched on figure 1.5, the distribution in energy of the wave function goes like $\exp(-2W\epsilon/\hbar)$ ($\hbar = h/2\pi$ is the reduced Planck constant). In [36], Dubois *et al.* created excitations with width $2W$ of 30 and 75 ps with a repetition rate respectively of 6 and 4.8 GHz. This implies excitation very close to the Fermi level with characteristic

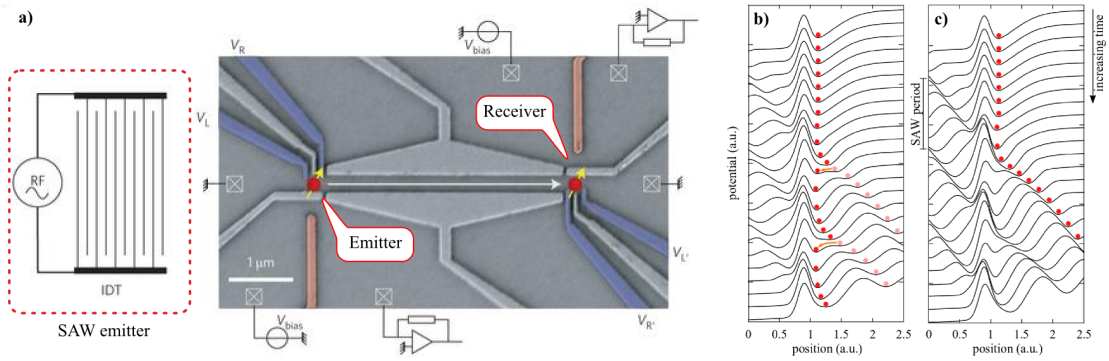

FIGURE 1.6: Figure extracted from [40, 41] **a).** Scanning electron microscope image of the device. **b) and c).** Time evolution of the dot potential for two different amplitudes of SAW excitation. The time increases going from top to bottom traces. In c) the amplitude of SAW drive is large enough and deeper moving quantum dots are defined compared to b). Tunneling back of the electron to the source dot is negligible in c) so probability to transfer exactly one electron converges to one.

exponential energy scale of respectively $\hbar/2W = 11\mu$eV and 4 μeV, when at 35 mK $k_B T_{el} = 3\mu$eV (where k_B is the Boltzmann constant).

By construction, this type of excitations have the advantage to behave as a coherent state *i.e.* they are not sensitive to decoherence contrary to electrons well defined in energy, higher above the Fermi level as we will discuss in chapter 4. However, it is a many-body state *i.e.* the additional electron cannot really be separated from the rest of the Fermi sea as if it was an individual quasi-particle.

1.5.3 Electrons surfing on surface acoustic wave

Another way to create and transfer single electrons in GaAs heterostrucutres is to use surface acoustic waves. Indeed, there is a non negligible piezoelectric effect in GaAs that enables to change the electric potential through a mechanical stress. Using an electro-acoustic transducer to create propagating surface acoustic waves (SAW), two groups managed to create moving arrays of quantum dots. Each of this dot is confined enough to contain mainly one electron. This SAW propagates from one static quantum dot filled with one electron toward another static empty dot. Therefore an electron can be transferred from the former to the latter [38, 39] (see figure 1.6).

Furthermore, since this array of quantum dots affects identically both spin components of the electron, it is expected to be a good way to implement coherent transfer of electron spins. Indeed, with this method, Bertrand *et al.* demonstrated an electron spin transfer over 4 μm with high fidelity, on a time scale shorter than spin coherence time in GaAs [40]. They predict that with the current state of technology, they should be able to coherently transfer electron spins over distances larger than 100μm.

1.6 Quantum Hall effect

To guide electrons in our circuit, we did not use surface acoustic waves but rather one dimensional chiral wires defined at the edges of the sample when a sufficiently strong perpendicular magnetic field is applied to the bi-dimensional electron gas. This phenomenon is called the (integer) quantum Hall effect.

The quantum Hall effect was discovered in 1980 by v. Klitzing, Dorda and Pepper [42]. Once again, this discovery would not have been possible without the development of high mobility electron gases. Indeed, the higher the mobility, the more pronounced is this effect. Nevertheless, now that this effect is well known it has been possible to identify it in more "dirty" samples with a mobility of only $\mu = 10\text{cm}^2.\text{V}^{-1}.\text{s}^{-1}$ but at 45 T [43].

The integer quantum Hall effect arises when the magnetic field is high enough; the Hamiltonian of the system can be rewritten as the one of an harmonic oscillator [44]. Electrons in the bulk have a spectrum in energy $E_n = \hbar\omega_c(n + 1/2)$, with $\omega_c = |eB/m^*|$ the cyclotron frequency and m^* the renormalized effective mass of the electron which, in GaAs, is 0.067 times the bare electron mass. The quantized levels are called Landau levels. This effect appears for particular values of the magnetic field such that:

$$B = \frac{hn}{e\nu} \tag{1.2}$$

where n is the electron density, h/e is the quantum flux and ν is the filling fraction. In the case of integer quantum Hall effect, ν is an integer number. It can be interpreted either as the number of electrons in the sample per quantum flux or the number of filled spin polarized Landau levels or equivalently the number of conductive edge channels. Indeed in our case, we will work with magnetic fields high enough so that spin degeneracy is lifted by Zeeman effect (see sketch b of figure 1.7). Actually, thanks to disorder this effect appears over a wider range of magnetic field around these defined values. These regimes are identified by plateaus in the off-diagonal (or Hall) resistance at values matching $R_K/\nu = h/(e^2\nu)$ where R_K is the von Klitzing resistance.

On these plateaus, transport only occurs at the edges. Indeed, in the bulk electrons occupy flat band Landau levels that localize because of disorder and do not contribute to transport (when $k_bT_{el} < \hbar\omega_c \sim 7$ meV~ 80 K at $B = 4$ T, for instance). However, because of the confining potential near the edge (that prevents electrons from going out of the sample), Landau levels will bend and cross the Fermi level (see Figure 1.7-b). Electrons at the edges thus have a gap-less excitation spectrum *i.e.* they have a metallic behavior and participate to low temperature electron transport. Besides, the transverse

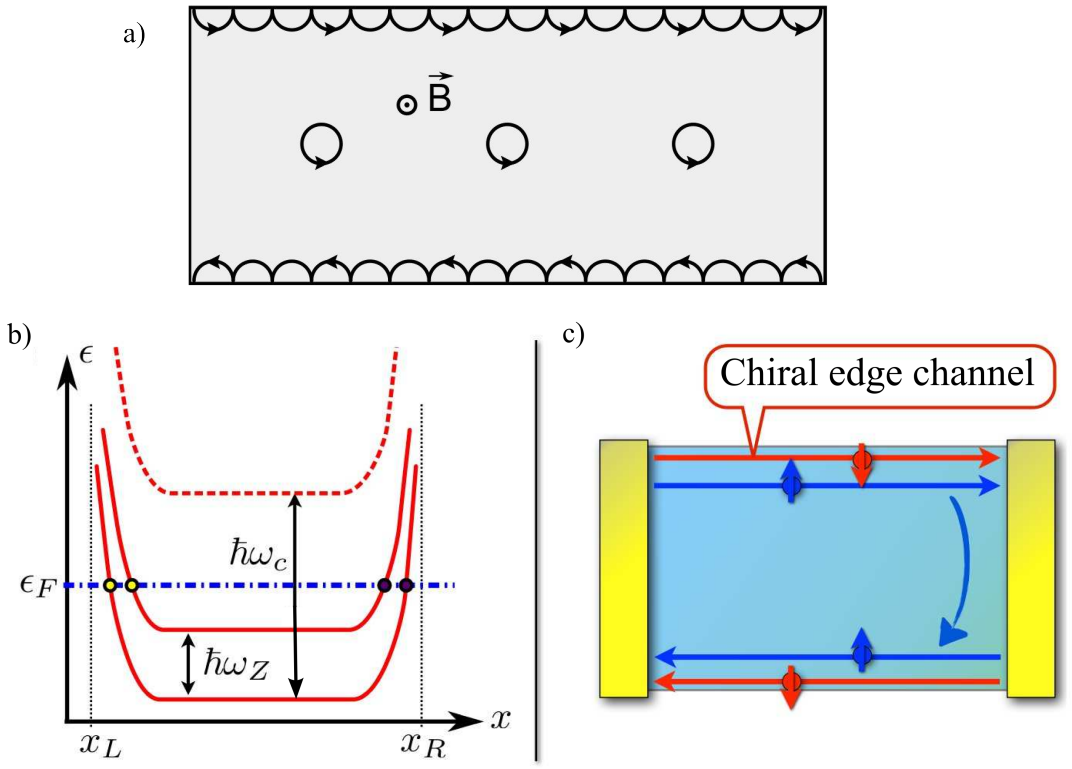

FIGURE 1.7: **a)** Semi-classical picture of the quantum Hall effect. Cyclotron orbits are localized in the bulk and do not contribute to transport whereas orbits close to the interface are reflected and then propagate from one edge to another. They are called skipping orbits and contribute to transport. **b)** Energy spectrum at filling factor 2 along one spatial direction, x_L and x_R correspond to limits of the sample. $\hbar\omega_Z$ corresponds to Zeeman splitting. Landau levels are bent toward the edges and cross the Fermi level allowing gap-less excitations. **c)** Edge channel picture at filling factor 2. Because of Zeeman splitting, they are spin polarized and because of large spatial separation, tunneling from one side to the other is extremely unlikely so backscattering (curved blue arrow) is almost forbidden.

magnetic field breaks time reversal symmetry imposing a chirality. Electrons on one edge can only propagate in one way (see Figure 1.7-c).

This has the advantage to forbid backscattering events. Indeed, for an electron to be backscattered, it has to tunnel through the other edge of the sample which is extremely unlikely for wide enough samples. This absence of backscattering enhances the elastic mean free path (until $\approx 100\mu$m). Therefore, we can safely approximate each channel by a one dimensional chiral dissipationless wire with quantized conductance e^2/h. Because they follow the boundaries of the sample and back scattering is topologically suppressed, they behave as good electron wave guides. Thanks to these waveguides, electronic analogs of the Mach-Zehnder interferometer [45–49] were implemented in which single particle interferences are predominant. Therefore, depending on the phase difference between two electron paths, the current amplitude can be modulated by 100% of its value. As a comparison, it is much more pronounced than the modulation presented in section 1.4.

1.7 Analysis of quantum signals

In section 1.5, we have introduced various ways to create single electron sources. Electron particles are indivisible (at least below 130 GeV [50]) thus signals generated by these sources are quantum by construction. To analyze such a signal, one can measure the current it produces but it cannot give information on the total number of particle (an electron-hole pair does not contribute to current). To do so, one can analyze the signal in energy and count excess excitations with respect to the Fermi sea, however it will not give access to the phase relation between these excitations. Moreover, these sources work at high speed (radio or GHz frequencies) hence the need for fast signal analysis methods beyond the simple averaging of energy distribution (spectroscopy) or time distribution (current measurement), that not only enable to measure the high speed dynamics of these excitations but also to recover the phase terms and statistics, essential to understand the quantum transport properties of these excitations. Another issue is that, contrary to photons, there exists for the moment, no single electron detector. Here I introduce some recent proposals or realizations in this direction and motivate the need for a quantum tomography protocol.

1.7.1 Average current and energy distribution

To measure the average current created by small electronic excitations, one needs to work both with high frequencies (radio-frequencies or even GHz), because of the fast dynamics of electrons, and low noises to be able to detect a small number of particles (typically at $f = 100$ MHz, $ef = 16$ pA). Both time domain or frequency domain approaches were used. For instance, in reference [1], a fast acquisition card was used to measure the average current $I(t)$ going out of the mesoscopic capacitor single electron source and homodyning techniques were used to measure the source first harmonic response to the drive so as to characterize its variation with the gate parameters or the drive amplitude.

Since then, commercially available oscilloscopes and acquisition cards have been significantly improved. The available bandwidth is around 80 GHz [51], however measuring small signals containing only a few electrons still requires a lot of averaging. There has been an attempt in this direction to design single-shot detection of single flying electrons based on double quantum dot qubit. In reference [52], a few propagating electrons have been detected but it is predicted that single-shot single particle detection should be experimentally accessible essentially by improving the sample design and using more sophisticated qubit operations.

For periodic sources, or experiments repeated and triggered at high speed, averaging is not an issue; fast signal sampling can be achieved through fine clock controlled synchronization of the trigger and a tunnel barrier that acts as a time controlled energy filter at a given point in the circuit. With this technique, Kataoka *et al.* have been able to simultaneously characterize the average time and energy distribution of single electron wave packets with great precision [31, 32]. Their single electron source is accurate enough so that they can implement precise, energy resolved, time of flight experiments in quantum Hall edge channels to deduce the dispersion relation of electrons in these edges [53]. In some sense the problematic has changed, single electron sources are not the object of study but the tool to study the circuit in which they propagate (see figure 1.8). In the very same spirit, in chapter 3 and 4, we are going to rely on the good control of our single particle sources to study the circuit they are injected into and how Coulomb interactions affect electron propagation. Such sources are also used to sample voltage drives incoming on the sample (at the bottom of the cryostat). In reference [54], an *in-situ* voltage arbitrary waveform analyzer with bandwidth up to possibly 100 GHz was realized.

Energy distributions were measured before that, in a similar way, in the group of F. Pierre. An energy resolved quantum dot instead of a tunnel barrier was used to measure the energy distribution of out-of-equilibrium stationary states [55–57].

1.7.2 Noise is the signal

To go further in the characterization of these sources, various theoretical proposals have been made. For instance, low frequency[1] current noise measurements were proven to reveal true quantized pumping (and not just average). This was verified in surface acoustic waves electron pumps [58] and gate defined single electron pumps in [59].

Low frequency noise after partitioning through a QPC or a tunnel barrier enables to count the number of particles and not just charges. Thus it can be used to probe the emission of additional electron-hole pairs accompanying the emitted single electron that could not have been detected with current measurement [60]. This enables to check how clean a single electron source is. It was used to count additional electron-hole pairs created by drives on Ohmic contacts [36, 61] and by the mesoscopic capacitor [62].

Furthermore, study of high frequency noise enables to determine the degree of imperfection of single electron sources [63–66]. In references [67, 68], finite frequency current noise was measured to check that the mesoscopic capacitor indeed emitted a single particle at each (half-)period of the drive and not just on average and without spurious electron-hole

[1] Low frequency refers to frequencies smaller than the inverse of the typical escape time of the sources ($\lesssim$ 10 MHz).

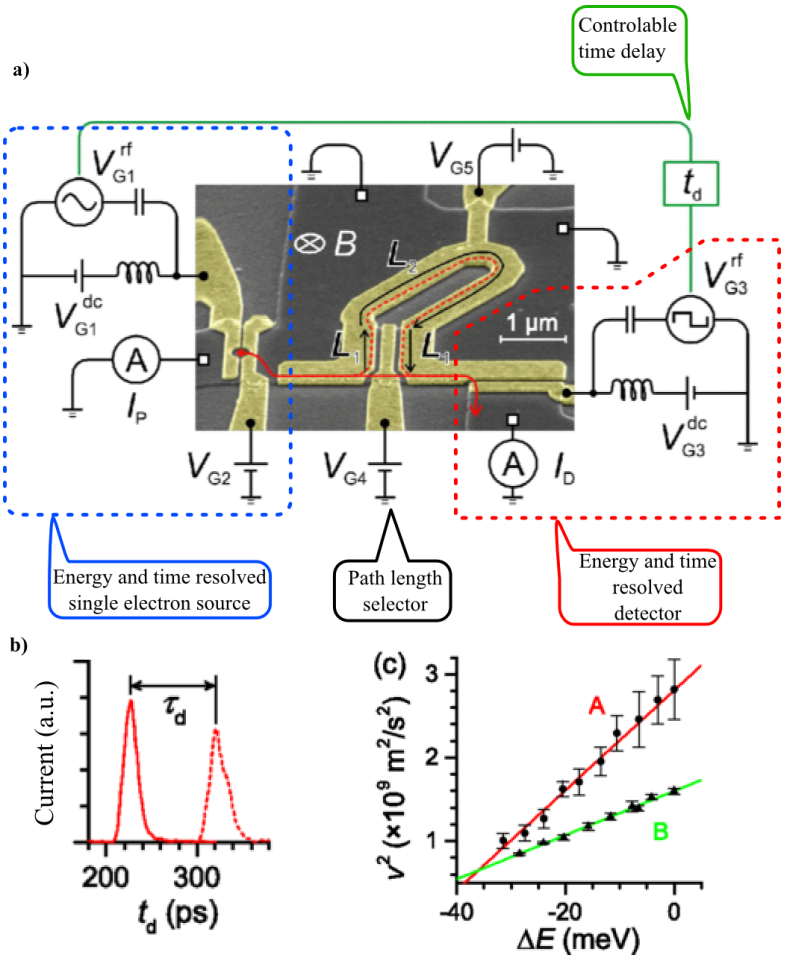

FIGURE 1.8: (Adapted from [53]) **a)** Scanning electron microscope image of the sample. In the dashed blue area is the energy resolved quantum pump that is synchronized with a time delay t_d with the square sequence applied on the energy filter (red area). Gate V_{G4} enables to change the path length taken by the single electron. **b)** Response of the detector versus time delay for the two possible paths. This experiment is reproduced for different emission energy and with an estimate of the 2 path lengths they manage to recover **c)** the velocity of the electron versus its energy *i.e.* its dispersion relation (for two different samples A and B).

pairs. Heat current noise measurements were also proposed but not yet realized either to study quantum fluctuations of the electron wave function [69–71] or correlations between electron and hole excitations [72].

In fractional quantum Hall system (when ν is no longer an integer) the low frequency partition noise created by a biased QPC unraveled the fractional charge carried by the elementary quasi-particle of these strongly correlated phases [73, 74]. Charge $e/3$ [75, 76], $e/5$, $e/7$ [77] and even $e/4$ [78] were observed so as multiple of these fractions [77, 79]. Often, depending on energetics and disorder, several excitation mechanisms occur at the same time with possible grouping of excitations [80, 81] which renders the low frequency measurement difficult to interpret [82]. To circumvent this issue the idea to measure

high frequency shot-noise was proposed. The frequency dependence should discriminate between different excitation mechanisms and bunching of excitations at 2/3, 2/5 [83, 84] and 5/2 [85, 86].

1.7.3 New theoretical tools

On a more fundamental level, theoretical formalisms have been invented or renewed to better picture the coherence of electronic excitations and their quantum fluctuations. Different quasi-probability distributions have been developed such as first [10, 87, 88] and second order [89] coherence functions (details in section 2.3.1), first order Wigner function [90] or full counting statistics (FCS) [91–95]. FCS is suitable to study fluctuations of a quantity integrated over time (*e.g.* charge which is an integral of current over time). Because it is integrated, it is not really suited to this work where we study the short time dynamics of elementary excitations. To study random time processes occurring in nano-scale circuits, a complementary approach to average current and current fluctuations measurement was developed: waiting time distributions [96–103]. It corresponds to the statistical distribution of waiting times between successive charge transfers between two given parts of a conductor. Contrary to FCS, it is not integrated and thus gives access to short-time dynamics which is crucial in electron quantum optics experiments. In some sense, this formalism gives a more intuitive reformulation of the information given by finite frequency noise but is, for the moment, still experimentally challenging to access. In this work, we are going to use two formalisms more suited to study short-time dynamics and easier to access experimentally: first order coherence function and Wigner functions. The first order coherence function is a complex valued function depending on two variables (either two times t, t' or two energies ω, ω'). It is related to the single body density matrix, its diagonal elements ($t = t'$ or $\omega = \omega'$) give access to population terms *i.e.* current or energy distribution and the off-diagonal elements give access to interference terms enabling for instance to distinguish a statistical mixture from a pure quantum state. It is essential to measure it because it contains all single particle information on the state and is thus suitable to describe single particle excitations and single particle sources. The Wigner function formalism is an equivalent but more convenient theoretical framework. It also gives all the single particle information necessary to understand single particle interferences occurring in any coherent circuit however it it has the advantage to look like a time/energy representation. With it we can clearly distinguish electron like excitations occurring at $\omega > 0$ from hole like excitations occurring at $\omega < 0$ while at the same time keeping a time line visualization of these excitations. Details will be given in section 2.3.2.

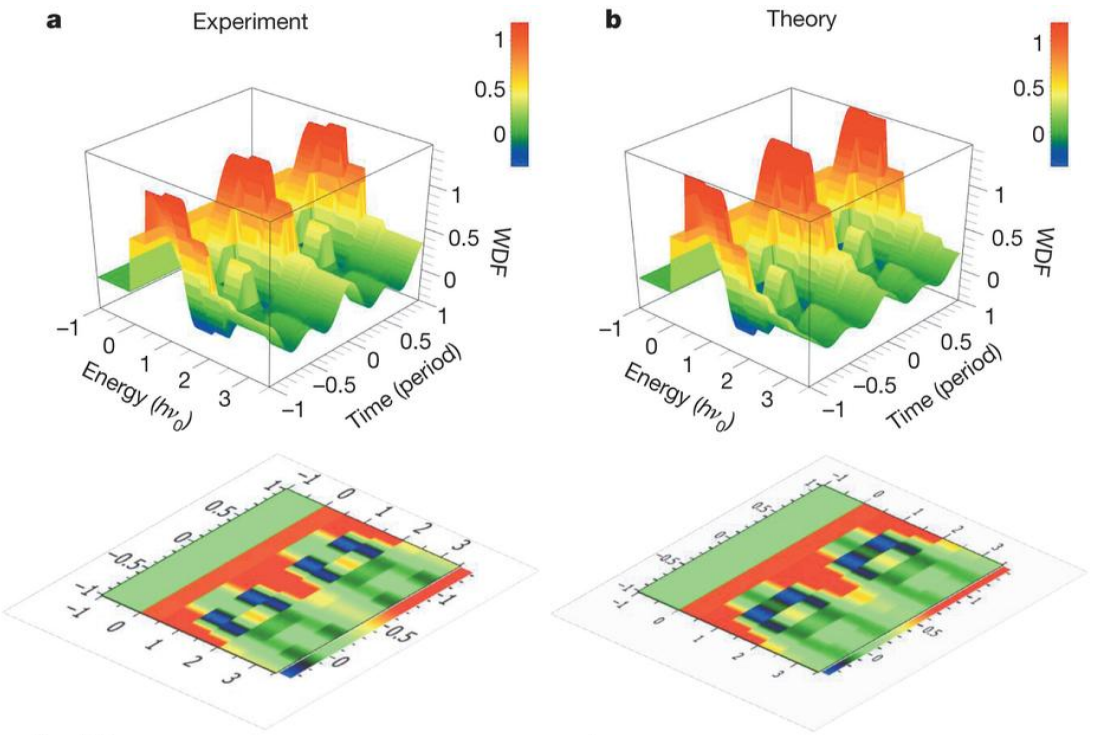

FIGURE 1.9: Reconstructed experimental (left) Wigner function compared to theoretical expectations at 0 K (right) for a Lorentzian drive at 6 GHz with a full width at mid-height of 30 ps. For energies lower than 0 (the Fermi level) $W = 0$ because the Fermi sea contribution has been removed. Negative values and values above one in the Wigner function are signs of non-classical states. Extracted from [104].

1.7.4 Tomography

However accurate the aforementioned measurements may be, they can only recover population terms (either in energy or time) and do not give access to off-diagonal coherence terms of the single particle wave packet. These terms are essential to understand quantum phenomena and interferences in transport experiments. To do so, one needs to reconstruct the whole wave function of the particle. Of course in quantum mechanics measurements affect the quantum state and therefore it is not possible to recover a full wave function in only one measurement. We actually mean that we rely on the stability and fidelity of single particle sources to be able to create N independent and identical copies of the same state on which we are going to apply a sequence of different complementary measurements *i.e.* a tomography protocol, to extract their unique common wave function. In mesoscopic systems, a tomography protocol to probe orbital entanglement has been proposed [105] but only to probe orbital state populated by stationary sources. To probe non-stationary states the protocol proposed by Charles Grenier *et al.* [10] relying on the Hong Ou Mandel interferometer is more suited. We will present the interferometer in chapter 2 and the implementation of the tomography in chapter 5. This protocol has been realized in the group of Christian Glattli [104] for the Leviton

source. Their main result is presented on figure 1.9. The Wigner function W (a time energy representation that will be introduced in details in section 2.3.2) of a Leviton at zero temperature was reconstructed. This realization represents a particular case of the protocol that will be presented in the last chapter of this thesis. In section 5.3.4 we will emphasize the important differences and show the broader universality of our protocol.

Beyond Wigner function reconstruction, one could envision to image the full many-body state. Indeed, the tomography analysis might be applied to probe any arbitrary electronic system, not only a single particle flying on top of a Fermi sea. In this case, the excitation is accompanied by several electron-hole pairs which might have a defined phase relation, or on the contrary be a statistical mixed state. How to probe it? How to probe electron-hole pairs wave functions? A first attempt in this direction is described in [106]. They theoretically predicted the many-body state created by sine drives on an Ohmic contact in a regime close to one charge per period, at zero temperature. In this regime other spurious excitations were approximated by only one dominant electron-hole pair and its impact on noise measurement in a Hong Ou Mandel like setup was computed. Predictions agree well with measurements (at finite temperature). However, the measurement in itself has no predictive power, it is only *a posteriori* verification of the initial assumption. With this in mind, the group of Pascal Degiovanni is currently developing a signal analysis procedure based also on the Hong Ou Mandel setup to analyze and reconstruct possibly any arbitrary many-body state with minimal *a priori* knowledge of the state. However this approach is also limited by the fact that the Hong Ou Mandel interferometer only probes single particle coherence overlap. To measure higher order coherence terms, one has to design new experimental tools. For instance, in reference [19], is proposed to recover two particle coherence through the measurement of low-frequency noise at the output of a Franson interferometer. Measuring two-particle coherence would for instance enable to distinguish between a time-bin entangled pair of electrons and a statistical mixture of electron pairs [89].

1.8 Outlook and results of this thesis

In section 1.6, I briefly mentioned that the long coherence length available in ballistic edge channels of the quantum Hall effect enabled the implementation of electronic interferometer such as Mach-Zehnder. In chapter 2 of this thesis, I will present another kind of electronic interferometer: the Hong Ou Mandel interferometer. The goal of this thesis is to use this interferometer to probe electronic coherence and process quantum signals.

Part of this work addresses the issue of interactions in between edge channels with a focus at filling factor 2 (only two co-propagating edge channels). At the beginning of chapter

3, I give a more specific review on the state of the art concerning this issue and then show how I used the Hong Ou Mandel interferometer to probe the effect of inter-edge Coulomb interactions on charge propagation. I show also that the measurement is precise enough so as to give information on the shape of the current pulse. This precision enables to probe the effect of Coulomb interactions not only during propagation in edge channels but also during the emission process in the source itself. We indeed observed that the pulse generated by the source cannot be described by a non-interacting theory of the dot. We successfully compared our measurements with existing interaction models.

In chapter 4, I used again two-particle interferometry and the Hong Ou Mandel setup to study the effect of inter-channel interactions on the propagation of a single particle. I measured the decoherence of the Landau quasi-particle for different wave packet sizes and show that interactions between neighboring channels is indeed the main source for decoherence. Comparing our results with theoretical models, we could show the relaxation and decoherence of a single electron and its decomposition into collective modes.

Finally, in chapter 5, I show the first results of the implementation of a universal tomography protocol introduced in section 1.7.4. This protocol aims at reconstructing all the single particle coherence of any propagating electronic signal. I tested first this protocol on simple signals created by sine drives. We were able to quantitatively compare and distinguish an adiabatically driven Fermi sea (*i.e.* a state described by a time dependent electronic distribution) and one with photo-assisted quantum effects which can no longer be described by a mere time dependent electronic distribution. We then started to implement this protocol to reconstruct a more complex signal coming out of the mesoscopic capacitor.

Chapter 2

The Hong Ou Mandel interferometer as a quantum signal processor

"This is how we do..., do, do ..., do, do."

Katy Perry, "This is how we do".

In this chapter, I give a comprehensive description of all the essential building blocks of the Hong Ou Mandel (HOM) interferometer together with important quantities and formalisms needed to understand and interpret its results. I then show how this interferometer is a good tool to measure electronic first order coherence and therefore a good tool to analyse a quantum signal. In the following chapters, I will then present 3 different uses of this tool relevant to electron quantum optics. This work benefits from previous ones done in the LPA mesoscopic group. The single electron source was developed and realized during Julien Gabelli's and Gwendal Fève's PhD thesis [4, 5], sources were characterized extensively during Adrien Mahé's and François Parmentier's thesis [6, 7]. Finally the first realization of the Hong Ou Mandel experiment with single electron was achieved by Erwann Bocquillon and Vincent Freulon [3, 107].

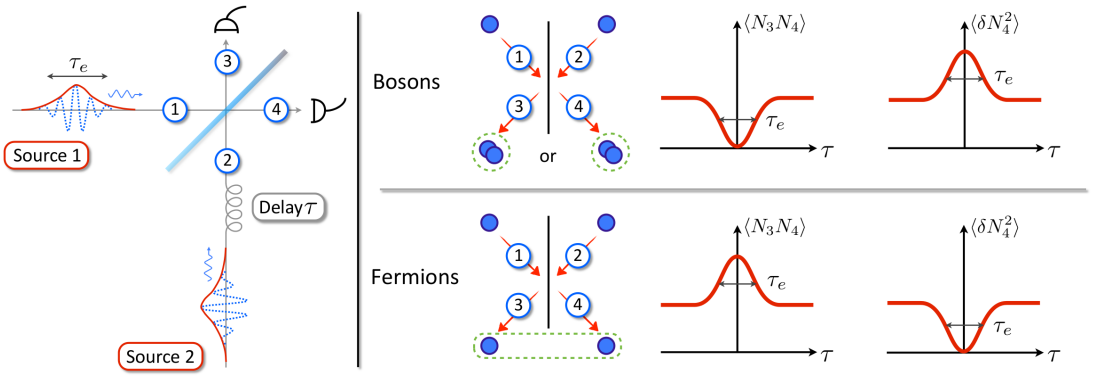

FIGURE 2.1: Sketch of the experiment. Two indistinguishable single particle wave packets arrive in each input of a beam splitter. One can either measure the average coincidence counts between outputs 3 and 4 $\langle N_3 N_4 \rangle$ or the fluctuations of number of particle in one output $\langle \delta N_4^2 \rangle = \langle N_4^2 \rangle - \langle N_4 \rangle^2$. See main text for explanation.

2.1 Principle of the experiment

2.1.1 Description

The experiment was originally done with photons by Chung Ki Hong, Zhe Yu Ou and Leonard Mandel in 1987 [108]. It is not an amplitude interference setup like Fabry-Pérot, Michelson or Mach-Zehnder interferometers but relies on intensity interference like the Hanbury Brown and Twiss interferometer. It consists of a simple 50/50 beam splitter where the two input states can be time delayed with high precision. The principle is sketched in figure 2.1. At each realization of the experiment, we are interested in the exit taken by the two particles. The measurement of interest is therefore either the average coincidence count in the two outputs 3 and 4: $\langle N_3 N_4 \rangle$, or the fluctuation of number of particles in one output $\langle \delta N_4^2 \rangle = \langle N_4^2 \rangle - \langle N_4 \rangle^2$. These quantities are averaged over a high number of iterations of the collision. When the delay $\tau = 0$, and if the wave packets are indistinguishable, bosons will tend to bunch together in the same output, reducing thus $\langle N_3 N_4 \rangle$ (and on the contrary increasing $\langle \delta N_4^2 \rangle$). When the delay $|\tau|$ is larger than the temporal width of the wave packet τ_e, there is no more overlap and the two particle interference disappears [109]. We recover random partitioning at each realization of the experiment. On the contrary, indistinguishable fermions will have a tendency to anti-bunch *i.e.* to take systematically a different output at $\tau = 0$. This can be understood as a manifestation of Pauli's exclusion principle, fermions will not exit in the same state. Thus, as sketched on figure 2.1 the trends for $\langle N_3 N_4 \rangle$ and $\langle \delta N_4^2 \rangle$ are opposite to bosons.

2.1.2 Interest of the experiment

This experiment was originally done with photons but has also been realized with other particles and quasi-particles like surface plasmons or surface plasmons polaritons [110–112], Rubidium atoms [113], Helium 4 atoms [114], phonons [115], collective excitations in atomic clouds [116] with continuous streams of electrons [117] and single electrons [118] (with the setup I will present). The global interest of this experiment is many-fold. As the seminal paper of Hong, Ou and Mandel indicates, it was first thought of as a way to probe, on short time scales, the time interval between two photons and by implication the photon wave packet length. Indeed, the overlap, and so the interference, occurs, even partially, for time delay τ smaller than the temporal width of the wave packet τ_e. Thus, probing the total shape of the dip gives a quantitative access to τ_e. However, the interest can be much more fundamental, indeed this experiment is one of the few that need a real quantum formalism that reconciles both the wave and particle physics in order to be understood completely and in particular must integrate the quantum statistics. The experiment measures the degree of indistinguishability between two particles and also between independent sources by extension. Finally, and more fundamentally, the experiment enables to test if a particle is a boson or a fermion. This is useless for already known elementary particles but is of great interest for quasi-particles that emerge as a result of correlations or hybridization. For instance it has been possible to prove the bosonic character of surface plasmon polaritons which are a mix of electrons (fermions) and photons (bosons) [111]. It would be interesting to transpose this experiment to test the quantum statistics of anyons or non-Abelian quasi-particles arising at some fraction of the quantum Hall effect [119] or at the interface of quantum Hall edges and topological superconductors *i.e.* Majorana fermions [120].

2.2 Building blocks of the electronic interferometer

Figure 2.2 represents the active part of the sample. It mainly consists in a bi-dimensional electron gas created at the interface between GaAs and AlGaAs semiconductors. All our samples were fabricated by Y. Jin and A. Cavanna at LPN in Marcoussis. On figure 2.3 is presented the sample at different scales and how it is integrated in our setup.

2.2.1 Quantum Point Contact

The first important element to reproduce in the interferometer is the central beam splitter. To do so we use a quantum point contact (QPC) [15, 16]. It consists in two top

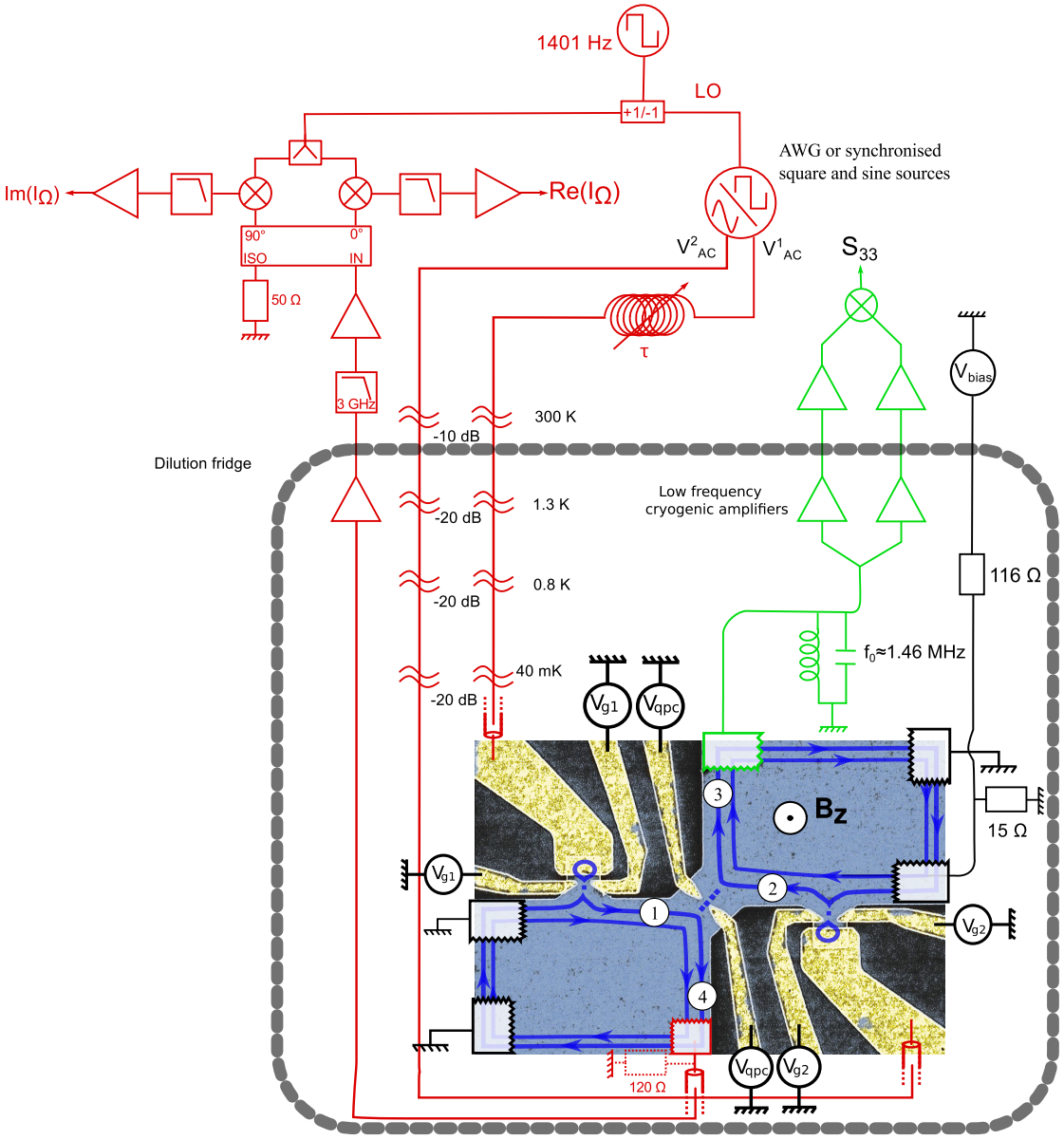

FIGURE 2.2: False color SEM picture of the active part of the sample and the electric setup. In blue is the bi-dimensional electron gas. Ohmic contacts (white saw toothed square) are actually further away. The central quantum point contact defined by the two central electrodes defines a beam splitter. Two edge channels are pictured in dark blue. Each source consists in one top gate (V_{exc}) and two side gates (V_{g}). The output 3 is sent to low-frequency cryogenic amplifiers (green part) whereas the output 4 is connected to a radio-frequency 50 Ω impedance circuitry (red part) with in some cases a 120-50 Ω impedance matching.

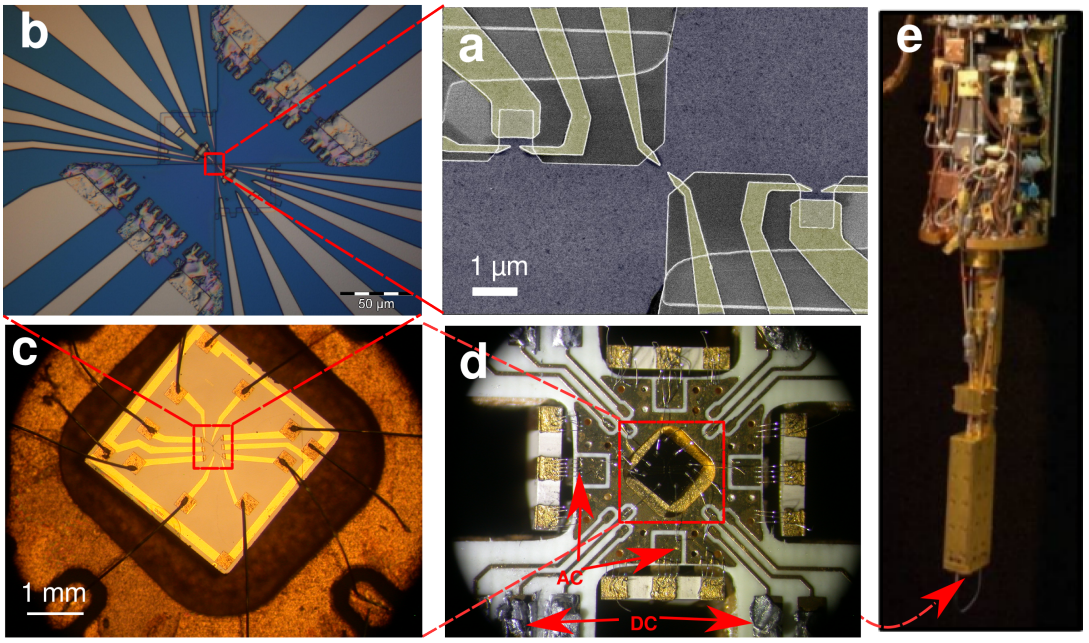

FIGURE 2.3: **a.** SEM picture of the active part of the sample. Yellow parts are gates. The electron gas is in light gray. **b.** Optical image of the sample on which we can see the integrity of the gas that has a butterfly shape. The darker crenelated area are Ohmic contacts (AuNiGe). **c.** Optical image of the whole chip. Here is actually a sample developed at the end of my PhD that is not an electronic HOM interferometer. **d.** Optical image of the printed circuit board (PCB) designed by Anne Denis on which the sampled is glued. **e.** The PCB is placed at the bottom of a He_3/He_4 cryostat and at the center of a 14 T superconducting coil.

gate electrodes (AuCr) deposited above the gas' central constriction. Applying a negative voltage on this electrode will deplete the gas beneath it. It is possible to control the number of transmitted modes through the QPC. Each mode transmits electric current with a quantized conductance of e^2/h. In the integer quantum Hall regime, each mode correspond to an edge channel. On the left panel of figure 2.4 this variation of the conductance is shown with the voltage applied on the gates at different filling factor. We clearly see that at filling factor ν, there are ν resolved steps that correspond to the successive reflection of the ν modes. Notice how the QPC always seems to fully close and fully open at roughly the same gate voltages.

To measure the conductance, we inject a small current on the Ohmic contact related to V_{bias} (see figure 2.2) and then we measure the backscattered current in output 3 of the beam splitter. To do so we use a *Zurich instrument HFLI* lock-in amplifier with a drive at ≈ 1.4 MHz to go through the resonating tank circuit. The drive voltage is converted into current in the edges through their conductance $I = V\nu e^2/h$ *i.e.* for a voltage V applied on the Ohmic contact, the current in only one edge is Ve^2/h. Because the Ohmic contact in output 3 is connected to high impedance amplifier, the current

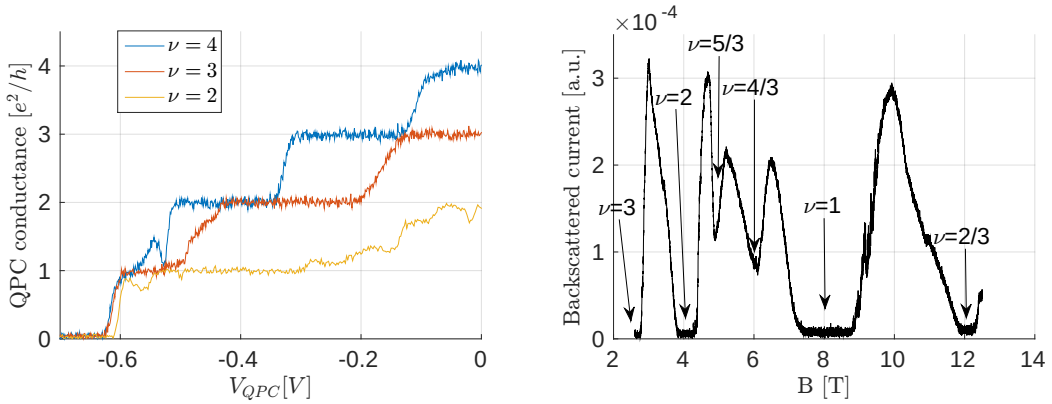

FIGURE 2.4: **Left.** Conductance of the central QPC versus gate voltage applied on the electrodes for different filling factor (same cool down). **Right.** Backscattered current when the QPC is fully open, versus magnetic field. Plateau of (almost) zero backscattering correspond to the integer quantum Hall effect and most well defined fractional quantum Hall states. We can only resolve $\nu = 2/3$ here.

is actually dissipated in the next Ohmic contact (grounded) therefore, in the integer quantum Hall regime, the voltage V_{out} read by the amplifiers on the Ohmic contact right after the QPC is $V_{out} = \frac{h}{\nu e^2} I_{out}$, where I_{out} is the backscattered current. This is actually a simplified model that is not valid when we take into account the impedance of the resonating tank circuit. We postpone to section 2.4 the discussion on the exact role of the resonating tank circuit and the low frequency amplifiers.

With this same method, we check what is the filling fraction. On right panel of figure 2.4 is plotted the backscattered current I_{out} when the QPC is fully open as a function of the magnetic field. The back-scattering minima correspond to well defined quantum Hall phases. We only resolve one fractional plateau (2/3). The relative center positions of each plateaus with respect to each other enable to determine filling fractions. We can plot filling fractions as a function of $1/B$ to obtain a linear relation. If the filling fractions are correct, the slope goes through the origin. Then, we can also check that the number of steps observed varying V_{QPC} is coherent with our determination.

The result presented on the left panel of figure 2.4 demonstrates that we can control precisely the transmission of the central QPC (up to the precision of the gate voltage value). The total conductance of the QPC is:

$$G = \frac{e^2}{h} \sum_{\alpha=1}^{\nu} D_\alpha = \nu \frac{e^2}{h} \left(1 - \frac{V_{out}}{V_{in}}\right) \tag{2.1}$$

where D_α is the transmission probability of mode α, V_{out} is the voltage measured on output 3 and V_{in} the voltage imposed on the ohmic contact connected to V_{bias}. This formula is often refered as the Landauer formula [14, 121, 122]. The QPC enables not only to choose to transmit or not a mode but also to control the exact transmission D_α.

Indeed, if we set ourselves a little bit below $V_{\mathrm{QPC}} = -0.6$ V we can, for instance, choose to transmit the outer edge channel with probability $D = 0.5$. Hence, an electron in the outer edge channel coming toward the QPC will have a 50/50 probability to be reflected or transmitted. This is the realization of an electronic beam splitter. We can address the exact transmission of any channel individually, however we cannot set every edge channel to half transmission. This is because edges are spatially separated thus when we address the transmission of one of them, all the inner one will be reflected perfectly ($D = 0$) and the outer one transmitted perfectly ($D = 1$). To conclude this part let us point out that the exact relation between V_{QPC} and D can vary significantly from a cool down to another. A positive bias cooling (applying a voltage on QPC during the cool down) can also shift the closure point toward more positive values of V_{QPC} however it also changes the overall stability of the electrostatic environment (sometimes better, sometimes worse). The $G(V_{\mathrm{QPC}})$ relation can also drift a bit at base temperature and has to be checked from time to time during long run measurements.

2.2.2 Single electron source

2.2.2.1 Working principle

The single electron sources are quantum dots defined by chemical etching of the gas and partly by electrodes (V_g on figure 2.2). Applying a negative voltage on V_g creates a confined area that is tunnel coupled with transmission D to the outer edge channel of the rest of the gas. Hereafter, so as to limit confusion, we are going to call D the transmission of the QPC associated to the dots (D_1 and D_2) and $R = 1 - D$ the reflexion probability of the central QPC (T will usually refer to a temperature). This confinement creates a quantization in energy with level spacing Δ. We apply a magnetic field high enough to have Zeeman splitting thus there is only one electron for each energy level. The chemical potential of the dot μ_{dot} is controlled capacitively by the top gate with V_{exc}. This realizes a mesoscopic quantum capacitor. A simplified version of its functioning principle, extracted from [3], is shown on figure 2.5. In the single particle injection regime, the top gate is driven with a square pulse sequence with a peak-to-peak amplitude equal to Δ (we call this amplitude the injection amplitude) and of mean value equal to the Fermi level in the outer edge *i.e.* the average dot chemical potential is equal the one of the outer edge. This level is governed by the DC part V_{DC} applied on the top gate. In this regime, during the first half of the square sequence, an electron is emitted at an energy $+\Delta/2$ above the Fermi sea and in the second half, a hole is emitted at an energy $-\Delta/2$ below the Fermi sea (see figure 2.5-b). During this cycle, only one level takes part in the emission. The escape time τ_e only depends on the transmission of the QPC and is

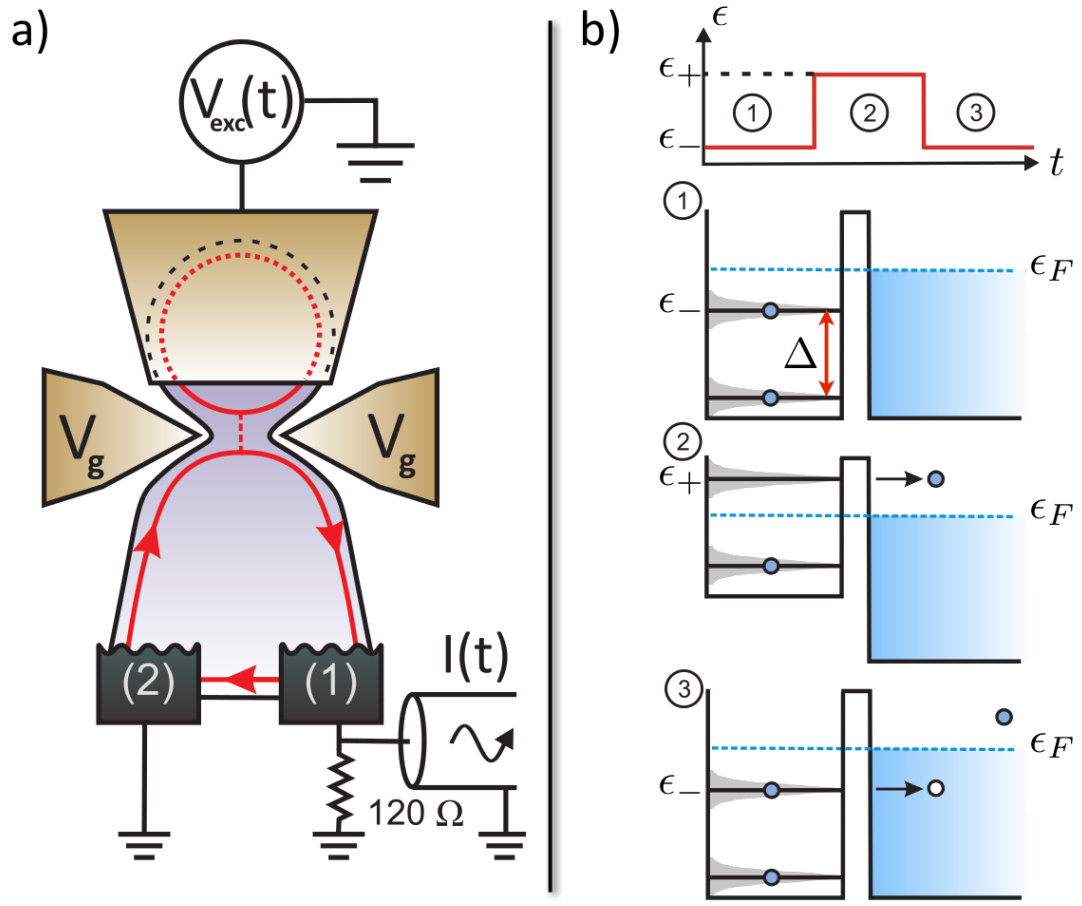

FIGURE 2.5: **Left a).** Sketch of the source. A quantum dot with a large level spacing is coupled to the reservoir through a QPC (gate voltage V_g). The potential in the dot is tuned using the top gate (voltage $V_{\rm exc}$) , and the emitted current is collected on contact (1). **Right b).** Principle of single charge emission with the mesoscopic capacitor. The upper graph represents the evolution of the potential of the dot during the emission cycle. ① The dot is at equilibrium, for an initial value of $V_{\rm exc}$. ② the application of a large voltage step to the dot top-gate shifts the energy levels upwards with respect to the Fermi energy, promoting a single occupied level above the Fermi energy. A single electron is emitted. ③ the excitation voltage is switched back to its original value: the emptied level is shifted back below the Fermi energy, and can absorb an electron from the reservoir. A single hole is emitted.

related to D and Δ through the Nigg formula [8]:

$$\tau_e = \frac{h}{\Delta}\left(\frac{1}{D} - \frac{1}{2}\right). \tag{2.2}$$

This time will govern the temporal width of the emitted wave packet. τ_e is actually the escape RC time associated to the density of state *i.e.* the quantum capacitance of the dot. At $D = 1$, when the coupling is perfectly capacitive between the top gate and the outer edge, τ_e does not converge to zero but to $h/2\Delta$ which actually corresponds to half the transit time of an electron in the dot. In full generality, one has to consider the effect of Coulomb interaction which manifests in the geometrical capacitance C_g. The

total charge relaxation time τ_{RC} is a combination of τ_e and τ_c the RC time associated with the geometrical capacitance only. However, it has been showed by G. Fève and F.D. Parmentier [5, 7] that Δ and Coulomb energy $E_c = e^2/C_g$ are of the same order of magnitude. In this regime, we can approximate the effects of interactions as a simple renormalization of $\Delta \to \Delta^* = \Delta + e^2/C_g$. Hereafter, we will call Δ the renormalized dot spacing. The effect of interactions within the dot and the relation between τ_{RC}, τ_e and τ_c will be rediscussed in section 3.4.2.2.

2.2.2.2 High frequency current measurement and determination of emission time

To characterize the sources and find the good parameters V_{exc}, V_{DC} and V_g to emit a given train of electrons and holes at energies (resp.) ω_e and ω_h and escape time τ_e, we rely on the measurement of the averaged complex first harmonic of the current I_Ω. The setup is described on (the red part of) figure 2.2. Here Ω corresponds to the pulsation of the AC drive on the top gate. Its measurement is enough to access those parameters and is less time consuming than a real time measurement of $I(t)$.

To measure I_Ω coming from a source we first need to transmit completely the signal to the Ohmic contact dedicated to RF measurements. This means closing fully the QPC to calibrate source 1 and opening completely for source 2. Then the signal is sent through a 120 Ω resistor and a $120 - 50$ Ω matching impedance strip line (see [6] for details). This resistor was removed in the middle of my PhD when we changed the whole PCB. This enabled us to have a better PCB but at the price of a higher impedance mismatch between the gas and the RF line. This lowered a bit (but not dramatically) the signal-to-noise ratio on RF measurements. The impedance matching circuit was used for measurements presented until section 4.3.1 included. Then the signal is amplified a first time with a cryogenic high frequency amplifier (*Miteq AMFK-2F-001-020*) anchored at 4 K, with a gain $\approx 33dB$ and then amplified again at room temperature with a *Miteq AMF-3F-00500400S* ($\approx 23dB$). The whole amplification setup bandwidth is limited by the first stage ($0.1 - 2$ GHz) but works well enough until 3GHz. Then the two quadratures are measured with standard homodyning method. To do so we either implemented our own set up (bandwidth 0.9 GHz to 3 GHz) or used a monolithic IQ mixer *MLIQ0218L* ($2-18$ GHz). The local oscillator (LO) signal is modulated with square drive through a phase modulator *Miteq DM0104LA1* to perform a lock-in measurement (≈ 1 kHz) on the two quadratures X and Y.

With this procedure we get a complex number $X + iY$ which is related but not quite exactly the same as I_Ω. Indeed, there are a lot of parasitic signals added to the signal of

interest. We have to take into account the phase rotation induced by propagation and the unavoidable direct parasitic coupling between input and output RF connectors; we must also take care of phase drifts between LO and V_{exc}. A second important point to notice is that because of the amplifiers and mixers, the signal is successively multiplied, attenuated and phase shifted in an untraceable way. All this considered, shows us that we actually measure:

$$Z = \kappa(I_\Omega + I_p) \tag{2.3}$$

where κ and I_p are of arbitrary modulus and phase (and can fluctuate on long time scales). This pleads for the use of a calibration to remove I_p. To any measure Z, we subtract, whenever possible, the same measure Z' but with V_g sufficiently negative to be sure the dot QPC is closed ($D = 0$) thus $Z - Z' = \kappa(I_\Omega + I_p - (0 + I_p)) = \kappa I_\Omega$.

Then to access the emission time we use the relation [7]:

$$\Omega\tau_e = \frac{\text{Re}(I_\Omega)}{\text{Im}(I_\Omega)}, \tag{2.4}$$

however, κ can have non zero complex phase. So we have to make another calibration measurement at V_g sufficiently high so as to be sure the dot is fully open ($D = 1$). Indeed, in this regime, we know that $\tau_e = h/2\Delta$ (see following section to know how to measure Δ) which enables us to fix the ratio of real and imaginary part measured and thus the complex phase of κ. More specifically, we rotate the two measured quadratures of $Z - Z'$ until the ratio of real and imaginary part equals $\Omega h/2\Delta$. This fixes a rotation in the complex plane that we apply to any measure $Z - Z'$.

Let us here be more specific about what we call V_g sufficiently negative or high enough. On figure 2.6 is presented a color map of I_Ω versus V_{exc} (amplitude of the drive) and V_{g1} (voltage on the QPC of source 1). Characteristic white diamond-shaped areas appear when $I_\Omega = 2ef = e\Omega/\pi$. The canonical *injection regime* correspond to the horizontal dashed line when $eV_{\text{exc}} = \Delta/2$. If we set ourselves to a different drive amplitude, we observe oscillations in I_Ω versus V_{g1}. This is because the latter not only controls D_1 but also influences the dot DC potential. Not being in a white diamond area correspond to a situation where energy levels of the dot are not symmetric with respect to the Fermi level in the edge channel as sketch on the right inset of figure 2.6. Now let us come back to the two steps calibration to access I_Ω. For the first subtraction, we need a point where we are sure $I_\Omega = 0$, this is exactly the left blue area on figure 2.6. More specifically we do not have to measure the whole 2D plot but simply to measure I_Ω versus V_{g1} at a finite V_{exc} and reach the minimum plateau which corresponds to no current emission. Then we needed a value of V_{g1} high enough to have $D = 1$. This correspond to perfect capacitive coupling between dot and edge *i.e.* there is no quantization in energy. We can observe

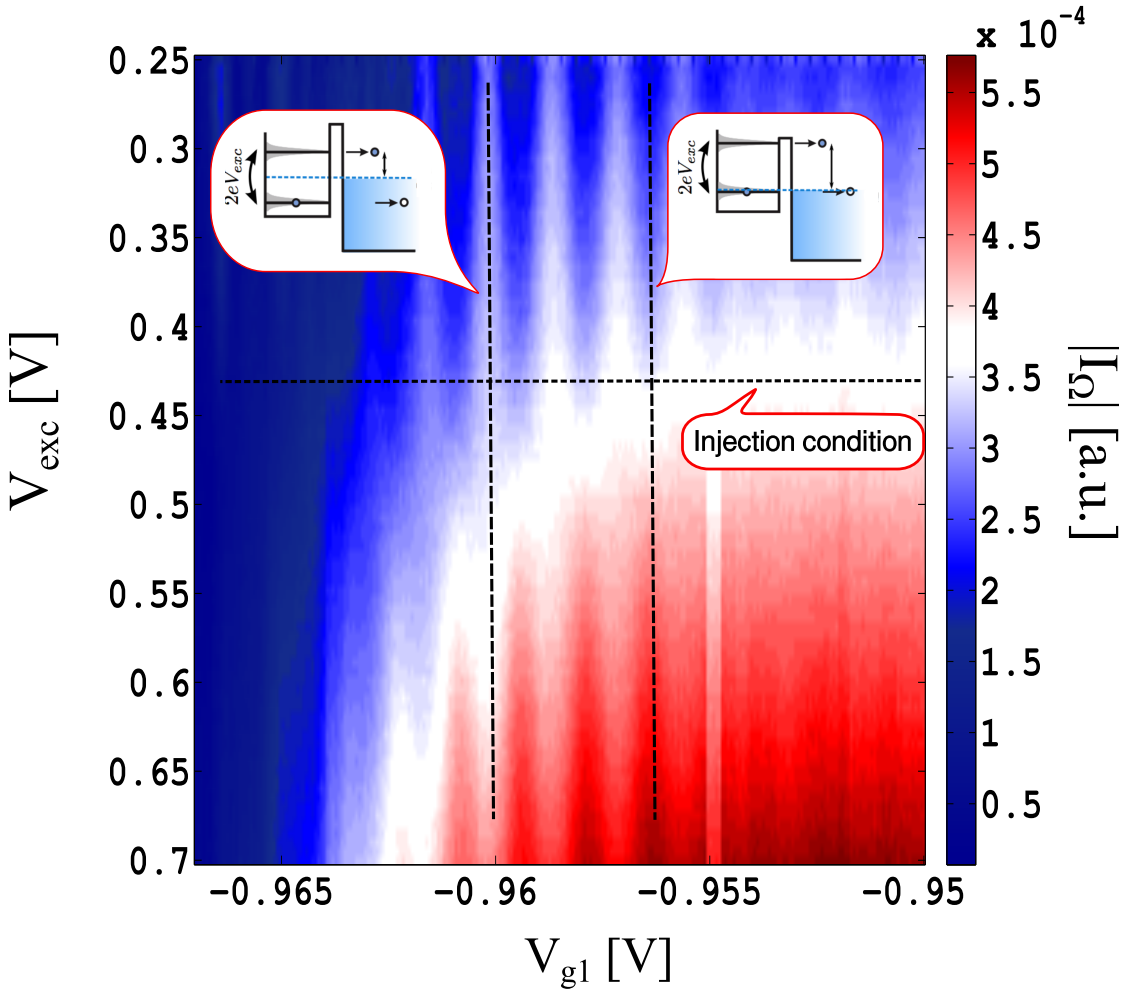

FIGURE 2.6: First harmonic of current measured on lock-in when source 1 is excited with a square drive at $f = 1.2$ GHz versus amplitude of the drive V_{g1}. Blue region corresponds to no emission and white region to the emission of a current $I_\Omega = 2ef$. Because, V_{g1} acts both on transparency D and on the inner chemical potential μ_{dot} we can see oscillation of this white region. Centers of a white diamond correspond to a region where the averaged in time DC potential of the dot equal the Fermi level of the rest of the circuit as sketched on the left inset. Theoretically, in this regime, any drive amplitude enables the emission of current at $2ef$ with electrons and holes at opposite energy $\omega_e = -\omega_h = eV_{\text{exc}}$. On the contrary, in between white diamonds the situation is not favorable for emission and $I_\Omega = 2ef$ only when $eV_{\text{exc}} = \Delta/2$.

this loss of quantization in the dot on the right side of the figure where diamonds are more and more blurred. Thus to be sure to measure $I_\Omega(D = 1)$, we set $eV_{\text{exc}} \neq \Delta/2$ and increase V_{g1} until the oscillations in I_Ω disappears.

2.2.2.3 Calibration of dot spacing Δ

Here I am going to present the calibration used to determine the dot spacing Δ (or more precisely the renormalized spacing Δ^*). We first apply a square voltage drive on the source we want to calibrate with a small amplitude and in a regime where we can see

name	**S434**	**S902**
nominal density n	$1.9 \times 10^{15}\mathrm{m}^{-2}$	$1.4 \times 10^{15}\mathrm{m}^{-2}$
mobility μ	$2.4 \times 10^{6}\mathrm{cm}^{2}\mathrm{V}^{-1}\mathrm{s}^{-1}$	$1.4 \times 10^{6}\mathrm{cm}^{2}\mathrm{V}^{-1}\mathrm{s}^{-1}$
dot spacing Δ	1.4 K$\leftrightarrow$ 120μeV	5.6 K$\leftrightarrow$ 483μeV

TABLE 2.1: Summary of the characteristics of the two different batch used during this thesis.

the previously mentioned current oscillations. We then record the evolution of I_Ω versus V_{DC} applied on the top gate; we expect to see a succession of peaks when the potential of the dot crosses the Fermi level. The conditions mentioned insure that the width of these peaks will be as thin as possible so as to be mainly governed by thermal blurring. Indeed, in a good quantization regime and with a small drive amplitude, there are very few values of inner potential allowing for particle emission. We typically record a few of these peaks and look at the evolution of their width while we increase the electron temperature.

Such a calibration is presented on figure 2.7 for a sample of batch *S902* (not the same one as samples which gave main results of this work). We fit each peak with $a/\cosh^2((V - V_i)/2W)$ where V_i is the position of peak i and W the peaks width in Volts (see [7]). This gives us an evolution of the width of peaks with temperature plotted on the right part. We fit this evolution with $\beta\sqrt{T^2 + T_0^2}$ where β^{-1} is the coupling between top gate and the energy level. Indeed, the relation is linear at high temperature but saturates at low temperature both because there is not enough thermalisation of electrons and because the peak has a finite minimum width imposed by the emission time $\tau_e = 20$ ps (deduced afterward from the calibration of Δ). The level spacing is simply the inverse of these slope multiplied by the spacing between peaks in Volts. Averaging on the three spacings, we get $\Delta = 5.6 \pm 0.2$ K which gives an emission time at $D = 1$ of $\tau_e = 4.3$ ps (and data taken at $\tau_e = 20$ ps correspond to $D = 0.35$).

This value of Δ is a bit higher to what was measured during V. Freulon thesis for a sample from batch *S434*. He found $\Delta \approx 1.4$ K. Most results I will show in this manuscript were obtained on this *S434* sample (C16L25A). Summary of the characteristics of the two different batch used during this thesis can be found in table 2.1.

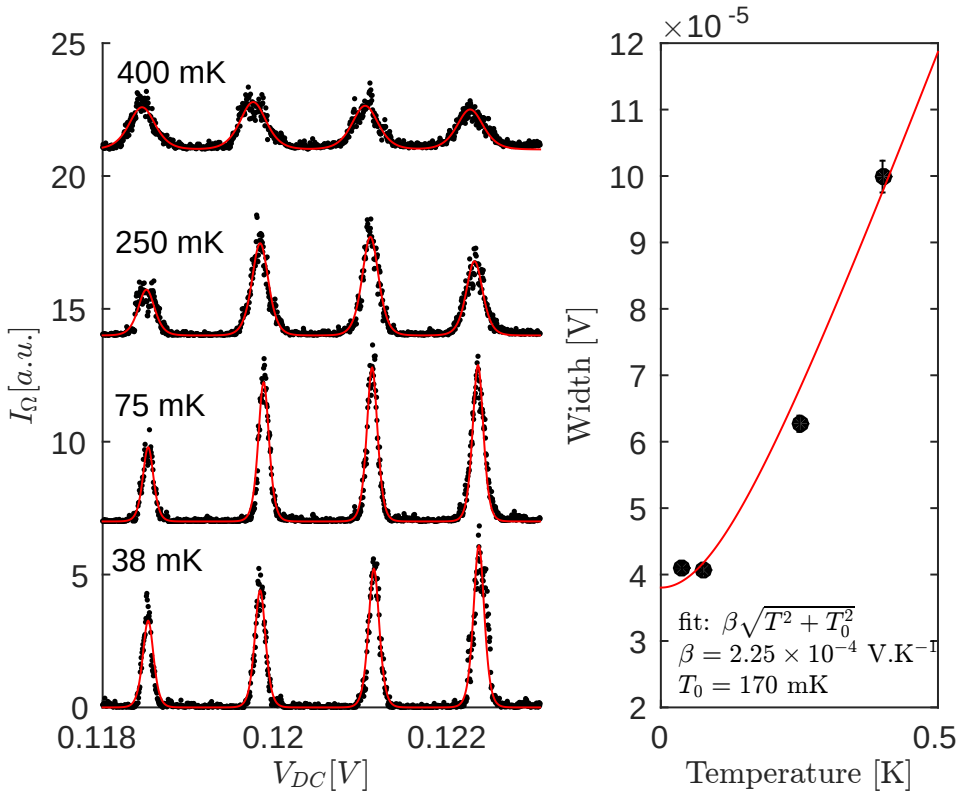

FIGURE 2.7: **Left.** I_Ω versus V_{DC1} for different electronic temperatures. Drive frequency: 1.2 GHz, amplitude around $eV_{\mathrm{exc}} = \Delta/8$. After estimation of Δ we can recover that $\tau_e = 20$ ps (or equivalently $D = 0.35$). Following [7], we fit each peak with $a/\cosh^2((V - V_i)/2W)$ where V_i is the position of peak i and W the peaks width in Volts. Each curve is shifted upward for clarity. **Right.** Width W extracted from fits as a function of temperature. We fit this with $\beta\sqrt{T^2 + T_0^2}$ where β^{-1} is the coupling between top gate and the energy level.

2.3 What do we measure?

The last important element to implement the HOM experiment is the equivalent of a photocounter. In our case, we will not measure the coincidence counts but rather the fluctuating number of particle in one output $\langle \delta N_3^2 \rangle$, more precisely we measure the low frequency current noise which indeed has units of a fluctuating number of charge per unit of time ($\mathrm{A}^2.\mathrm{Hz}^{-1} \sim \mathrm{C}^2.\mathrm{s}^{-1}$). In this section, I will also introduce the first order electronic coherence function [10, 87, 123] and the electronic Wigner function [90] defined in analogy with Glauber's theory of optical coherence [124]. These functions enable to describe efficiently the propagation of wave packets containing one particle. I will also show how the current noise at the output of the HOM interferometer enables to probe overlap of coherence functions or Wigner functions.

2.3.1 Coherence function $\mathcal{G}^{(e)}$

These theoretical tools rely on the formal analogy between the electric field operator $\hat{E}^{+}(x,t)$ (that annihilates photons at time t and position x), and the electron field operator $\hat{\Psi}(x,t)$ (that annihilates electron at time t and position x[1]).

$$\hat{\Psi}(t) = \int \frac{d\omega}{\sqrt{2\pi}}\, e^{-i\omega t}\hat{c}(\omega), \tag{2.5}$$

where $\hat{c}$ is the electron annihilation operator that annihilates an electron at energy ω and the integral goes over all real ω (in this manuscript, unless specified, integration intervals are $\mathbb{R}$). We have the anti-commutator $\left\{\hat{c}(\omega), \hat{c}^{\dagger}(\omega')\right\} = \delta(\omega - \omega')$ and $\left\langle \hat{c}^{\dagger}(\omega)\hat{c}(\omega)\right\rangle = f(\omega)$.

The coherence function (of degree one) is defined for electrons as:

$$\mathcal{G}^{(e)}(t,t') = \left\langle \hat{\Psi}^{\dagger}\left(t'\right)\hat{\Psi}\left(t\right)\right\rangle, \tag{2.6}$$

and with the Fourier transform convention:

$$\tilde{\mathcal{G}}^{(e)}(\omega,\omega') = \int\int \frac{dtdt'}{2\pi}\, \mathcal{G}^{(e)}\left(t,t'\right) e^{i\omega t}e^{-i\omega' t'} = \left\langle \hat{c}^{\dagger}\left(\omega'\right)\hat{c}\left(\omega\right)\right\rangle, \tag{2.7}$$

where $\langle ... \rangle$ is the quantum average on the state of interest. Coherence functions are a good tool to express temporal observable such as average total current:

$$\langle I_{\text{total}}(t)\rangle = -e\left\langle \hat{\Psi}^{\dagger}(t)\hat{\Psi}(t)\right\rangle = -e\ \mathcal{G}^{(e)}(t,t). \tag{2.8}$$

In the same spirit, density in energy is simply $f(\omega) = \tilde{\mathcal{G}}^{(e)}(\omega,\omega)$. More generally, diagonal terms of the coherence function ($t = t'$ or $\omega' = \omega$) give information on the population of state and off-diagonal terms give access to coherence terms or phase relations.

This formalism can be simplified for our system owing to the time periodicity of our drive. Indeed, all the out-of-equilibrium quantities we are going to study (apart from DC calibration) are created by a time periodic drive with periodicity $T = 2\pi/\Omega$. When the quasi-stationary regime is established (after a few μs) all these quantities will also be periodic in time. The most appropriate formalism in this regime has been developed by Gaston Floquet in 1883 [125] and can be transposed to our case [126, 127]. It can be seen as a Bloch decomposition but in time rather than space coordinates. The coherence

[1] Actually, we will assume ballistic propagation on the edge channel at a finite velocity so we drop the $x-$dependence. Everything depends on $t - x/v$ and we set $x = 0$ and, contrary to [10] for instance, $\hat{\Psi}$ is in unit of $\mathrm{s}^{-1/2}$ and not $\mathrm{m}^{-1/2}$.

function rewrites:

$$\mathcal{G}\left(t,t'\right)=\sum_n \mathcal{G}_n\left(t-t'\right)\, e^{-in\Omega\frac{t+t'}{2}}=\sum_n \mathcal{G}_n(\tau)e^{-in\Omega\bar{t}}. \tag{2.9}$$

Contrary to its photon counterpart, our "vacuum" here is a many-body state: the Fermi sea $|F_\mu\rangle$ at equilibrium and chemical potential μ whose coherence function is non-zero. Because the Fermi sea is a stationary state, its coherence function $\mathcal{G}^{(e)}_{F_\mu}$ only depends on time difference $t-t'$. One can then decompose any state as:

$$\mathcal{G}^{(e)}(t,t')=\mathcal{G}^{(e)}_{F_\mu}\left(t-t'\right)+\Delta\mathcal{G}^{(e)}\left(t,t'\right). \tag{2.10}$$

The current that is really measured in quantum Hall edge channels is always an excess current $\langle I(t)\rangle=-e\Delta\mathcal{G}^{(e)}_1(t,t)$. In energy domain, we have:

$$\begin{aligned}\tilde{\mathcal{G}}^{(e)}(\omega,\omega')=&\tilde{\mathcal{G}}^{(e)}_\mu(\omega,\omega')+\Delta\tilde{\mathcal{G}}^{(e)}(\omega,\omega')\\ \tilde{\mathcal{G}}^{(e)}(\omega,\omega')=&f_\mu\left(\frac{\omega+\omega'}{2}\right)\delta(\omega-\omega')+\Delta\tilde{\mathcal{G}}^{(e)}(\omega,\omega')\end{aligned} \tag{2.11}$$

where $f_\mu(\omega)$ is the Fermi distribution at chemical potential μ. The excess coherence function of a single electron state with wave function φ_e on top of a Fermi sea

$$|\varphi_e\rangle=\int d\omega\,\varphi_e(\omega)\hat{c}^\dagger(\omega)|F_\mu\rangle \tag{2.12}$$

is easily expressed as (see A.2 or reference [10]):

$$\Delta\mathcal{G}^{(e)}(t,t')=\varphi_e(t)\varphi_e^*(t') \tag{2.13}$$

$$\Delta\tilde{\mathcal{G}}^{(e)}(\omega,\omega')=\tilde{\varphi_e}(\omega)\tilde{\varphi_e}^*(\omega'). \tag{2.14}$$

We see here the interest of measuring first order coherence functions: for a single particle state it contains all the information on the state. The diagonal elements ($t=t'$ or $\omega=\omega'$) give access to the square modulus of the wave function and thus to population terms, whereas off-diagonal elements enable to recover the phase of the wave function. More generally, first order coherence functions contain all single particle physics and even all the physics of non-interacting many-body systems.

In appendix A are recalled a few properties of coherence functions and how they are computed with Floquet theory from the parameter of the dot. From there, I show how the HOM outputs are computed with coherence functions. All current and noise simulations (without interaction) presented in this work are based on a Matlab code whose main calculation steps are explained in this appendix. The code was first developed by F.D.

Parmentier and E. Bocquillon. I used it extensively and brought some corrections. I also developed all the numerical functions related to coherence functions created by a drive on an Ohmic contact and Wigner distributions calculation and representation (with and without Coulomb interactions).

2.3.2 Wigner function

2.3.2.1 Definitions

Coherence functions $\mathcal{G}^{(e)}$ are the good functions to use and compute to understand and describe the behavior of observables in such an interference experiment. However it is difficult to develop a pictorial and intuitive representation of it. To circumvent this issue we introduce the Wigner functions.

First introduced in 1932 by Eugene Wigner [128] to give a quantum formulation of the low temperature statistical mechanics so as to be able to compute thermodynamical quantities of a quantum system, it is defined for a density matrix ρ:

$$W(x,p) = \frac{1}{h}\int dy\ \left\langle x+\frac{y}{2}\right|\hat{\rho}\left|x-\frac{y}{2}\right\rangle e^{\frac{iyp}{\hbar}} = \frac{1}{h}\int dy\ \hat{\rho}\left(x+\frac{y}{2},x-\frac{y}{2}\right)e^{\frac{iyp}{\hbar}}, \quad (2.15)$$

so for a pure state ψ:

$$W(x,p) = \frac{1}{h}\int dy\ \psi^*\left(x+\frac{y}{2}\right)\psi\left(x-\frac{y}{2}\right)e^{\frac{ipy}{\hbar}}, \quad (2.16)$$

and can be generalized to $n-$dimensional phase spaces. Its use has been extended to signal analysis by Jean Ville [129] so that it is sometimes referred as the Wigner-Ville distribution. It has proven to be an essential tool for time-frequency representation [130]. In quantum mechanics it is a good tool to represent quantum states[131]. It is only one of the possible quasi-probability distributions but compared to other possible representations (P [132, 133] or Q functions [134, 135] for instance) it has the advantage to keep the intuitive classical phase space representation and also to highlight clearly quantum phenomena such as superposition of states. A more practical advantage is that it only takes real values so it is easier to represent.

Such a Wigner function was first successfully measured by Smithey *et al.* [136] that reconstructed the Wigner function of vacuum and squeezed states of the optical field with homodyning methods. After that, the method has been widely used in quantum optics to measure various kind of state of light (squeezed state or Fock state) [137–140]. A noticeable milestone was achieved with the measurement of the Wigner function of

a Schrödinger cat state of microwave light in a superconducting cavity [141]. Then the progress in the superconducting qubit community enabled to measure more complex state of light [142–145]. Wigner functions were also measured in other systems like vibrational state of a molecule [146], motional state of trapped ion [147], atomic wave packets [148], and more recently on propagating electronic state in a metal [104].

Apart from the last reference, one can notice that they are all Wigner functions of single mode harmonic oscillators which can mapped to a single particle in a harmonic trap. A lot of effort was put forward to extend the definition of a Wigner function to other kind of states, for instance finite dimensional Hilbert space [149] so as to define Wigner functions of spin ensembles. Another approach that will be of great interest to us, is the definition of a Wigner function of systems with an arbitrary number of particles, in particular Wigner function of electronic systems. The Wigner function of an electron in a semiconductor was used successfully several times [150–153] but more to compute stationary transport quantities than to study single electron coherence. The latter was done in reference [90] by Ferraro *et al.* and motivated by the need for a time/frequency representation of electronic excitations in quantum conductors with a finite extension both in time and energy. Indeed, as pointed out in this reference, it contains the same information as the coherence function but is easier to visualize. The time domain representation of coherence functions is suitable to analyze time-dependent phenomena or observables but one has to look at the complex phase of $\mathcal{G}(t,t')$ to infer about the electron or hole nature of excitations. Conversely, this is really clearly pictured in the frequency representation of $\tilde{\mathcal{G}}(\omega,\omega')$. Weights in the quadrant $(\omega,\omega'>0)$ correspond to electron excitations whereas the quadrant $(\omega,\omega'<0)$ corresponds to hole excitations. The two other quadrants $(\omega\times\omega'<0)$ correspond to coherent electron-hole pairs excitations. However, $\tilde{\mathcal{G}}$ is not well suited to describe time dependent phenomena. The Wigner function has the advantage of the two representations (in addition to all the other previously mentioned).

The electronic[2] Wigner functions writes:

$$W(\omega,\bar{t}) = \int d\tau\ \mathcal{G}^{(e)}\left(\bar{t}+\frac{\tau}{2},\bar{t}-\frac{\tau}{2}\right)e^{i\omega\tau} \tag{2.17}$$

where $\tau = t-t'$ and $\bar{t} = (t+t')/2$. Similarly to the coherence function, we can isolate the mere Fermi sea at chemical potential μ, $|F_\mu\rangle$ and define the excess Wigner function:

$$\Delta W(\omega,t) = W(\omega,t) - W_{F_\mu}(\omega) \tag{2.18}$$

$$W_{F_\mu}(\omega) = f_\mu(\omega). \tag{2.19}$$

[2]We could also define a hole Wigner function but we will not use it in this manuscript, so we drop the (e) notation.

2.3.2.2 Properties and Floquet decomposition

Another advantage of the Wigner representation is that we can recover probability distribution thanks to marginal distributions:

$$\Delta\rho(\omega) = \frac{1}{T}\int_0^T dt\ \Delta W(\omega, t) \tag{2.20}$$

$$I(t) = -e\int \frac{d\omega}{2\pi}\ \Delta W(\omega, t) \tag{2.21}$$

where $\Delta\rho(\omega)$ is the electronic distribution over the time period T which is the period of the source or the total measurement time. Integrating $\Delta\rho(\omega)$ over all energies gives access to the average excess electron number per unit of T. $\Delta\rho(\omega)$ can also be seen as an average energy distribution per unit of T. Unless specified, all our signals are time periodic therefore $\Delta\rho(\omega)$ is also the total average energy distribution. As a misuse of language we will sometimes mix electronic distribution and energy distribution.

The main advantage of the Wigner function representation is that it pictures well the classical-quantum transition. For a classical state, the Wigner function can simply be interpreted as a time/energy electronic distribution $W(\omega, t) = f(\omega, t)$ with $0 \leqslant f(\omega, t) \leqslant 1$. This is the case for stationary distributions or electronic distribution with a chemical potential varying adiabatically with time. In this regime we can write:

$$W(\omega, t) = f(\omega, t) = f_{\mu(t)}(\omega). \tag{2.22}$$

In this classical regime, all AC properties can entirely be derived from DC ones. However, this is no longer the case for non adiabatic driving of the chemical potential or more generally for non-classical (quantum) states. This regime can easily be identified by the values taken by the Wigner distribution which can become negative or rise above one. When $W < 0$ or $W > 1$, the function can no longer be interpreted as an electronic distribution, $W(\omega, t) \neq f(\omega, t)$: the state has no classical description. This can serve as a criteria to distinguish a classical state from a quantum one.

One important remark must be made here. There is usually a normalization relation that fixes to one the integral of the Wigner function over the whole phase space. This is no longer true here in general. Indeed, we deal with a many-body state and the total number of particle depends on the excitation. If we remove the Fermi sea and focus on the excess Wigner function, its integral over energy and over a time period T should give the

number of net charge present in this time period. It gives zero if we only have electron-hole pairs and one if we managed to inject a single electron but this number is not fixed *a priori* and does not have to be an integer. This is an important difference with the usual Wigner function of a one mode harmonic oscillator. Indeed, this problem can be mapped to the one of a *single* particle trapped in a quadratic potential. For those systems, it is true to say the Wigner function contains all the physical information on the system. This is because it is constructed with single particle operators. This is particularly clear when one looks at the definition 2.17 which uses the *first* order coherence function. In electronic conductors, the number of particle is not fixed to one so the Wigner function does not *a priori* contain all the information on the system but only the single particle one. Nonetheless, single particle knowledge is enough to understand and predict the HOM interferences as we will see in equation 2.39. To fully characterize a many-body state, one needs to access higher order coherence functions especially when these many-body correlations are predominant *e.g.* in the fractional quantum Hall effect. Based on the definition of an electronic second order coherence function [89] one can define a two-electron Wigner function [154] that can give for instance information about entanglement between two particles.

Here again, we can benefit from $T-$periodicity to decompose Wigner functions on Floquet coefficients:

$$\Delta W(\omega, t) = \sum_{n\in\mathbb{Z}} \Delta W_n(\omega) e^{-in\Omega t}, \tag{2.23}$$

it appears that the Wigner Floquet coefficient $\Delta W_n(\omega)$ are equal to the coherence function Floquet coefficient defined as the Fourier transform of $\Delta\mathcal{G}^{(e)}(\tau)$

$$\Delta W_n(\omega) = \Delta\mathcal{G}_n^{(e)}(\omega). \tag{2.24}$$

2.3.2.3 Illustrations

On figure 2.8 and 2.9 are plotted examples of Wigner functions with their marginal distributions. Figure 2.8 represents Wigner functions created by a sine drive applied on an Ohmic contact or on the top gate of the dot when $D = 1$ only. Figure 2.8-**a** is in a regime where the electronic temperature is higher than the frequency drive ($T_{el} = 100$ mK, $f = 1.5$ GHz $\rightarrow hf/k_B = 72$ mK) so the Wigner function can be interpreted as a classical time energy probability distribution. The function can be described as a Fermi sea with an oscillating chemical potential. Going from figure 2.8-**a** to 2.8-**b** the temperature is decreased to 20 mK but everything else is kept constant. Because hf becomes higher than $k_B T_{el}$ there starts to be photon assisted effects which are quantized by nature. This non-classicality is manifested in the appearance of negative values of

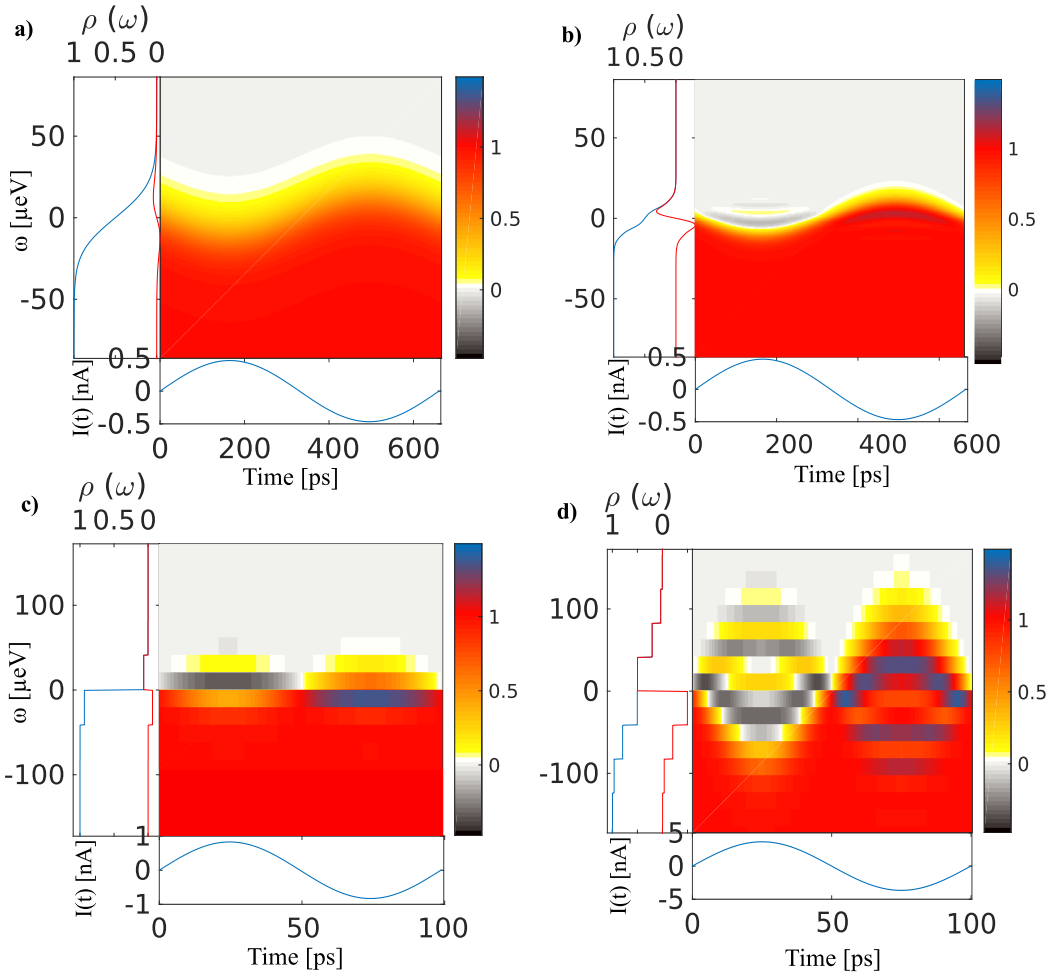

FIGURE 2.8: Wigner function created by a sine drive on an Ohmic contact calculated with Floquet theory. The bottom marginal distributions correspond to current and the left one to $\rho(\omega)$ the energy probability distributions. The red curve corresponds to the excess occupation whereas the blue represents the same to which we add Fermi sea. **a)** Frequency drive $f = 1.5$ GHz, $T_{el} = 100$ mK, $V_{\text{exc}} = 12\mu$eV. **b)** Frequency drive $f = 1.5$ GHz, $T_{el} = 20$ mK, $V_{\text{exc}} = 12\mu$eV. **c)** Frequency drive $f = 10$ GHz, $T_{el} = 0.1$ mK, $V_{\text{exc}} = 21\mu$eV. **d)** Frequency drive $f = 10$ GHz, $T_{el} = 0.1$ mK, $V_{\text{exc}} = 95\mu$eV.

the Wigner function. However, contrary to its bosonic equivalent the electronic Wigner function has another non-classicality criteria: it is when the values taken by the Wigner function are above unity. Indeed such a value cannot be interpreted as a probability for a fermionic system (whose occupation number are bounded between 0 and 1). This values above 1 are visible on figure **b** but the effect is much stronger on figure 2.8-**c**. When temperature is negligible (0.1 mK on 2.8-**c** and **d**) we clearly see a quantization of the Wigner function which also appears in $\rho(\omega)$ but not in the current which is always a sine function. The Wigner functions are quantized by steps of size $hf/2$ whereas the energy distribution is by steps hf. This really illustrates the fact that the excitation of the Fermi sea is no longer adiabatic but governed by absorptions and emissions of photons (here at $f = 10$ GHz) that can create electron-hole pairs of energy hf, this is a manifestation

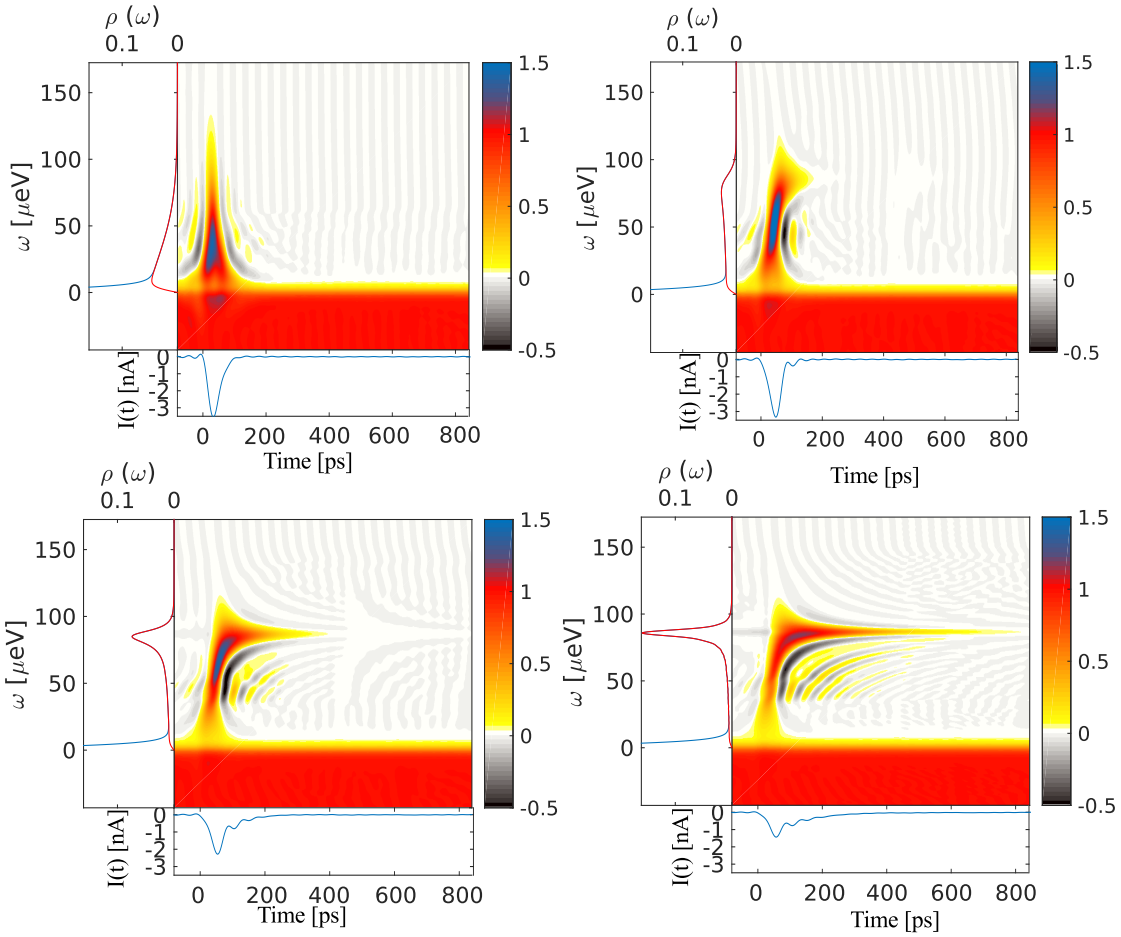

FIGURE 2.9: Wigner functions calculated with Floquet theory at the exit of the dot. We zoomed in the the half period on which the electron is emitted and removed the other half period. The drive frequency is at 0.5 GHz with an amplitude of 86μeV and a rise time of 30 ps. Dot spacing Δ is 170μeV. The Wigner functions are plotted with their marginal distributions (all with same scale for the sake of comparison). The bottom marginal distributions correspond to current and the left one to $\rho(\omega)$ the energy probability distributions. The red curve corresponds to the excess occupation whereas the blue represents the same to which we add Fermi sea which goes to 1 for energies below Fermi level. The electronic temperature is 25 mK. **a)** $D = 1$, $\tau_e = 12$ ps. **b)** $D = 0.65$, $\tau_e = 25$ ps. **c)** $D = 0.35$, $\tau_e = 57$ ps. **d)** $D = 0.2$, $\tau_e = 108$ ps.

of the famous photon-assisted transport [155–157] which creates a complex many-body system that is a superposition of electron-hole pairs [106]. For those excitations, non-classical values are more pronounced. To create electron-hole pairs with higher energies, one has to rely on multi-photon processes whose probability increase with the number of photon *i.e.* with the amplitude of the drive. We can observe this transition between **c** and **d**. In the last figure, we clearly observe more than one step and the Wigner function extends to higher energies both for electrons ($\omega > 0$) and holes ($\omega < 0$).

On figure 2.9, the Wigner function of the excitation created by the single electron source for different transparencies D is shown. All the marginal distributions are plotted at the same scale. For all but **d**, we observe a strong region of values above one that

comes from the fact that the wave packet is strongly localized in time on a time scale τ_w such that $h\tau_w^{-1} > k_B T_{el}$[3]. As illustrated on the previous figure 2.8, this regime leads to non-classical values of the Wigner function. Going from **a** to **d** (to lower and lower transparency D) we start from a wave packet localized in the time domain with a high peak of current and a broad energy distribution with main weight around the Fermi level and finish with a wave packet with a long temporal extension whose maximum of current is lowered but the distribution in energy is much more peaked around $\Delta/2 = 86$ μeV. For the lower transparency, $D = 0.2$, at $t = 0$ the emission is initiated but the energy not yet resolved as manifested by the broadening of the Wigner function in energy. As time evolves, the distribution is narrower and narrower and energy of the electron more resolved. This is a direct manifestation of Heisenberg uncertainty principle.

Let us here stress the important difference between two regimes for the source. When $D = 1$, the top gate has perfect capacitive coupling with the outer edge channel and driving this top gate will directly excite low energy collective modes called edge-magneto plasmons. By tuning the amplitude of the drive one may reach a regime where these collective modes appear as one net charge per period but this charge will be accompanied by several electron-hole pairs. It is a many-body state. On the contrary, when $D < 1$, coupling to the edge is no longer purely capacitive and the state at the exit of the source tends toward a *single particle* on top of a Fermi sea, with probabilities of having additional electron-hole pairs going to zero. As we will see in section 4.2, both cases can always be described as a sum of edge magneto-plasmons.

To compute this Wigner function we assumed that the transparency D was independent of energy but we could imagine other kind of wave packet emission with different dot to edge coupling. There is a proposal by Kashcheyevs and Samuelsson [158] to structure the barrier such that the tunneling transparency depends on energy, enabling creation of different wave packets. They showed that for a given $D(\epsilon)$, a change from classical to quantum wave packet emission can be observed by changing the rapidity of the drive. In our case, this classical-to-quantum crossover can be observed by tuning the transparency D from 1 to 0. On figure 2.9-**a** the state already shows negativities and values above one but we can recover a purely classical state with a longer rise time and still observe (not shown) a transition with the appearance of values $W < 0$ and $W > 1$ while decreasing D.

[3] τ_w is related to the emission time τ_e but also to the finite rise time of the square sequence.

2.3.2.4 Computation

In this section, I detail the method used to calculate numerically Wigner functions of excitation either from an Ohmic contact as on figure 2.8 or from the mesoscopic capacitor as on figure 2.9. All relevant observables (current, HOM interferences, distribution in energy) can then be computed from it.

Excitation of an Ohmic contact To compute numerically a Wigner function in this regime, we use results from reference [159]. An electron traveling in the Ohmic contact experiences a potential $V(t)$ thus its wave function $\varphi(t)$ acquires an extra term $\exp\left(-\frac{ie}{\hbar}\int_{-\infty}^{t} V(\tau')d\tau'\right)$. Thus the coherence function emitted by an Ohmic contact driven by a voltage $V(t)$ is:

$$\mathcal{G}^{(e)}(t,t') = \exp\left(\frac{ie}{\hbar}\int_{t'}^{t} V(\tau')d\tau'\right)\mathcal{G}_{\mu}^{(e)}(t'-t). \tag{2.25}$$

Thanks to Floquet theory, this can easily be computed through the calculation of the c_n coefficients (see also appendix A) defined as the Fourier coefficient of:

$$\exp\left(-i\frac{e}{\hbar}\int_{0}^{T} V_{\mathrm{AC}}(t')dt'\right) = \sum_{n=-\infty}^{+\infty} c_n \exp\left(-i2\pi n f t\right) \tag{2.26}$$

which correspond to the probability amplitude for an electron to absorb ($n > 0$) or emit ($n < 0$) n photons, with T the period of the drive. They enable us to compute the coherence out of the contact but we can also use them for the computation of the Wigner function [90]:

$$W(\omega,t) = \sum_{(n_+,n_-)\in\mathbb{Z}^2} c_{n_+}[V_{\mathrm{AC}}]c_{n_-}[V_{\mathrm{AC}}]^* e^{2\pi i(n_- - n_+)ft} f_{\mu}\left[\omega - \pi\left(n_+ + n_-\right)f\right]. \tag{2.27}$$

In the case of a simple sine drive $V_{\mathrm{AC}}(t) = V_0\cos(2\pi f t)$, it can be computationally a little bit quicker to directly use the expressions of c_n in terms of Bessel functions of the first kind, $c_n = J_n\left(\frac{eV_0}{hf}\right)$ so to have:

$$W(\omega,t) = \sum_{n\in\mathbb{Z}} \frac{J_n\left(\frac{2eV_0}{hf}\cos(\Omega t)\right)}{\exp\left(\frac{h(\omega+n\Omega/2)}{2\pi k_B T_{el}}\right)+1}. \tag{2.28}$$

Excitation out of the mesoscopic capacitor For this kind of injection we have to rely on the formalism developed in [7] and recalled (up to minor modifications) in A.3

to compute the Wigner Floquet coefficient $\Delta W_n(\omega)$ and then sum them up according to equation 2.23 to recover $\Delta W(\omega, t)$.

One might realize, that we never calculate "directly" Wigner functions but almost always go through the step of calculating first order coherence function. Indeed, it is easier to compute and although the two representations are mathematically equivalent, Wigner functions will always have the advantage of a better representation of the system and a more straightforward interpretation.

2.3.3 Application to HOM

In the electronic realization of HOM we use two independent but identical sources labeled 1 and 2. In appendix A.3, we show how to compute the output modes $\hat{\Psi}_{out,1}$ and $\hat{\Psi}_{out,2}$ and coherence function out of these sources from Floquet formalism. This model does not take into account any Coulomb interaction but still provides a solid theoretical predictions to guide us in our interpretation.

In a first non interacting description of our setup, $\hat{\Psi}_1$ and $\hat{\Psi}_2$ will propagate toward the input of the beam splitter. The effect of the QPC on this modes can be modeled with the following scattering matrix:

$$\begin{pmatrix} \hat{\Psi}_3 \\ \hat{\Psi}_4 \end{pmatrix} = \begin{pmatrix} \sqrt{1-R} & i\sqrt{R} \\ i\sqrt{R} & \sqrt{1-R} \end{pmatrix} \begin{pmatrix} \hat{\Psi}_1 \\ \hat{\Psi}_2 \end{pmatrix}, \tag{2.29}$$

where R is the reflection of the QPC, and $\hat{\Psi}_3$ and $\hat{\Psi}_4$ are the output modes of the QPC. From it we can compute the output current operators:

$$\hat{I}_3 = e\,\hat{\Psi}_3^\dagger\hat{\Psi}_3 = (1-R)\hat{I}_1 + T\hat{I}_2 + ie\sqrt{R(1-R)}(\hat{\Psi}_1^\dagger\hat{\Psi}_2 - \hat{\Psi}_2^\dagger\hat{\Psi}_1) \tag{2.30}$$

$$\hat{I}_4 = e\,\hat{\Psi}_4^\dagger\hat{\Psi}_4 = (1-R)\hat{I}_2 + R\hat{I}_1 - ie\sqrt{R(1-R)}(\hat{\Psi}_1^\dagger\hat{\Psi}_2 - \hat{\Psi}_2^\dagger\hat{\Psi}_1). \tag{2.31}$$

$\hat{\Psi}_1^\dagger\hat{\Psi}_2 - \hat{\Psi}_2^\dagger\hat{\Psi}_1$ is the exchange term responsible for 2 particle interference. This two particle interference term is at the heart of the HOM interference and is important to explain all our results and the interest of this experiment. However, measuring this exchange term is not straightforward. Indeed it disappears when we try to measure any single particle quantity such as energy occupation or the average current which is simply the sum of transmitted and reflected currents:

$$\langle\hat{I}_3\rangle = (1-R)\langle\hat{I}_1\rangle + R\langle\hat{I}_2\rangle. \tag{2.32}$$

To access this exchange term, we will actually need to measure fluctuations of this operators either by measuring current cross correlations between the two outputs $S_{34}(t,t') = \langle(\hat{I}_3 - \langle\hat{I}_3\rangle)(t)(\hat{I}_4 - \langle\hat{I}_4\rangle)(t')\rangle$ or by measuring autocorrelation of current in one output $S_{33} = \langle(\hat{I}_3 - \langle\hat{I}_3\rangle)(t)(\hat{I}_3 - \langle\hat{I}_3\rangle)(t')\rangle$. As we will see, this quantities are of great interest because they give access to off-diagonal elements of coherence functions and thus to quantum coherence. Applying Wick's theorem we get after a bit of algebra:

$$\begin{aligned} S_{33}(t,t') =& (1-R)^2 S_{11}(t,t') + R^2 S_{22}(t,t') + R(1-R)Q(t,t') \\ S_{34}(t,t') =& R(1-R)\left(S_{11}(t,t') + S_{22}(t,t') - Q(t,t')\right) \end{aligned} \tag{2.33}$$

Where we removed $S_{12}(t,t')$ because the two sources are independent so it is reasonable to assume no correlation between them. S_{11} and S_{22} correspond to output autocorrelations from both sources before partitioning by the QPC. The last remaining term labeled $Q(t,t')$ corresponds to quantum interferences created by the partitioning. It is also called exchange term as it contains coherence products of both inputs:

$$Q(t,t') = e^2\left[\mathcal{G}_1^{(e)}(t,t')\left(\delta(t-t') - \mathcal{G}_2^{(e)^*}(t,t')\right) + \mathcal{G}_2^{(e)}(t,t')\left(\delta(t-t') - \mathcal{G}_1^{(e)^*}(t,t')\right)\right]. \tag{2.34}$$

What is really measured is the power spectrum density in output 3 $S_{33}(\Omega_M)$, with Ω_M the measurement frequency, but Wiener-Khintchine theorem shows it enables to access:

$$\overline{S_{33}}(\Omega_M) = 2\int d\tau e^{i\tau\Omega_M}\overline{S_{33}(t,t')}^{\bar{t}}, \tag{2.35}$$

where $\tau = t - t'$, $\overline{S_{ij}(t,t')}^{\bar{t}}$ is the average on $\bar{t} = (t+t')/2$ and factor 2 comes from an engineer convention where $\overline{S_{33}}(\Omega_M)$ is defined for positive frequencies only.

Looking back at equation 2.33, we realize the additional noise created by both sources S_{11} and S_{22} can blur the measurement. However, focusing on the low frequency limit $\Omega_M \to 0$ of the noise removes these contributions. Indeed, at low frequency, the noise created by the source is zero [67] and this can be extended to a drive applied on an Ohmic contact. As long as Ω_M^{-1} is larger than time scales at which random process starts to manifest for the source, the input noise reduces to thermal noise $S_{ii} = 2e^2 k_B T_{el,i}/h$. Therefore, at low frequency, $\overline{Q}$ can be decomposed as the sum of the 4 following terms:

$$\overline{Q_{\mathrm{eq}}} = 2e^2\int\frac{d\omega}{2\pi}\left(f_{\mu 1}(\omega)\left(1 - f_{\mu 2}(\omega)\right) + 1 \leftrightarrow 2\right) \tag{2.36}$$

$$\overline{Q_{\mathrm{HBT},1}} = 2e^2\int\frac{d\omega}{2\pi}\Delta\mathcal{G}_{0,1}^{(e)}(\omega)\left(1 - 2f_{\mu 2}(\omega)\right) = 2e^2\int\frac{d\omega}{2\pi}\Delta W_{0,1}(\omega)\left(1 - 2f_{\mu 2}(\omega)\right) \tag{2.37}$$

$$\overline{Q_{\mathrm{HBT},2}} = 2e^2\int\frac{d\omega}{2\pi}\Delta\mathcal{G}_{0,2}^{(e)}(\omega)\left(1 - 2f_{\mu 1}(\omega)\right) = 2e^2\int\frac{d\omega}{2\pi}\Delta W_{0,2}(\omega)\left(1 - 2f_{\mu 1}(\omega)\right) \tag{2.38}$$

$$\begin{aligned}\overline{Q_{\mathrm{HOM}}} =& -2e^2\sum_n\int\frac{d\omega}{2\pi}\left(\Delta\mathcal{G}^{(e)}_{n,1}(\omega)\Delta\mathcal{G}^{(e)*}_{n,2}(\omega)+\Delta\mathcal{G}^{(e)}_{n,2}(\omega)\Delta\mathcal{G}^{(e)*}_{n,1}(\omega)\right)\\ =& -4e^2\int\frac{d\omega}{2\pi}\overline{\Delta W_1(\omega,t)\Delta W_2(\omega,t)}^t.\end{aligned} \tag{2.39}$$

$\overline{Q_{\mathrm{eq}}}$ corresponds, when $\mu_1=\mu_2$, to the equilibrium noise. It is measured while both sources are off. In equations 2.37 and 2.38, HBT stands for Hanbury Brown and Twiss. Indeed, these terms can be obtained by turning on only the corresponding source and off the other one. Then the setup is the electronic equivalent to the original experiment developed by Hanbury Brown and Twiss [160] and which is now routinely done to characterize single particle sources. We have expressed $\overline{Q_{\mathrm{HBT}}}$ and $\overline{Q_{\mathrm{HOM}}}$ both in terms of an overlap of coherence functions and overlap of (excess) Wigner function. We see that we can measure $\overline{Q_{\mathrm{HOM}}}$ when both sources are on. In appendix A.4.2 we also show that $\overline{Q_{\mathrm{HOM}}}$ can be interpreted as a single particle wave packet overlap for states well defined above Fermi level. $\overline{Q_{\mathrm{HOM}}}$ can be interpreted as a Wigner (or equivalently first order coherence) overlap and from 2.39 we see that this term contribute to noise with a minus sign because of fermionic statistics. Therefore any single particle overlap between the two input states will decrease noise or conversely any decrease of noise (compared to a reference we will soon define) will be interpreted as an overlap, even partial, between Wigner functions sent to the QPC.

To remove thermal contribution and $\overline{Q_{\mathrm{eq}}}$, we simply measure $\overline{S_{33}}(0)$ when both sources are off ($\overline{S_{33}^{(\mathrm{off,off})}}$) to get the excess low frequency noise:

$$\Delta\overline{S_{33}}=\overline{S}_{33}^{(\mathrm{on,on})}-\overline{S}_{33}^{(\mathrm{off,off})}=R(1-R)\overline{\Delta Q} \tag{2.40}$$

where

$$\overline{\Delta Q}=\overline{Q_{\mathrm{HBT},1}}+\overline{Q_{\mathrm{HBT},2}}+\overline{Q_{\mathrm{HOM}}}. \tag{2.41}$$

Following the same idea, we can obtain only HBT contributions measuring the excess noise when only one source is on. For example for HBT of source 1:

$$\overline{S}_{33}^{(\mathrm{on,off})}-\overline{S}_{33}^{(\mathrm{off,off})}=R(1-R)\overline{Q_{\mathrm{HBT},1}}, \tag{2.42}$$

thus we can access independently each HBT noise and subtract them from $\overline{\Delta Q}$ to recover only $\overline{Q_{\mathrm{HOM}}}$. We can combine the last 3 formula to get:

$$R(1-R)\overline{Q_{\mathrm{HOM}}}=\overline{S}_{33}^{(\mathrm{on,on})}-\overline{S}_{33}^{(\mathrm{on,off})}-\overline{S}_{33}^{(\mathrm{off,on})}+\overline{S}_{33}^{(\mathrm{off,off})}. \tag{2.43}$$

One might question the interest of such a strategy compared to the simple measurement of $\overline{S}_{33}^{(\mathrm{on,on})}$ while varying the time delay τ between the two sources. Indeed, according to 2.43 this strategy is 4 times longer and the uncertainty is increased by a factor 2 so to get

to the same precision on a value of $\overline{Q_{\mathrm{HOM}}}$ than on a value of $\overline{S}_{33}^{(\mathrm{on,on})}$ it is 16 times longer ! However $\overline{Q_{\mathrm{HOM}}}$ is only a small part of $\overline{S}_{33}^{(\mathrm{on,on})}$ in terms of magnitude and we have to deal with the fact that the other contribution to $\overline{Q_{\mathrm{HOM}}}$ are actually not really stable in time. We have observed on long time scales, random small fluctuations of the base noise small compared to $\overline{S}_{33}^{(\mathrm{on,on})}$ but large compared to $\overline{Q_{\mathrm{HOM}}}$ rendering impossible any interpretation of the raw $\overline{S}_{33}^{(\mathrm{on,on})}$. The subtraction strategy is thus a good one provided we measure those differences on time scales shorter than typical drifts of the base noise ($\approx 1-2$ minutes) [161]. It of course comes with the need to increase measurement time to have decent signal-to-noise ratio.

One can show (appendix A.4 or references [9, 109] for more details) that by normalizing $\overline{\Delta Q}$ by the sum of the 2 HBT noises, we construct a quantity Δq easy to interpret in terms of single particle wave packet. In a regime where each source emits a well define wave packet φ_i above the Fermi sea *i.e.* with an average energy high compare to $k_B T_{el}$, we have:

$$\Delta q(\tau) = \frac{\overline{\Delta S_{33}}(\tau)}{\overline{\Delta S_{33,\mathrm{HBT1}}} + \overline{\Delta S_{33,\mathrm{HBT2}}}} = \frac{\overline{\Delta Q}(\tau)}{\overline{\Delta Q_{\mathrm{HBT1}}} + \overline{\Delta Q_{\mathrm{HBT2}}}} = 1 - |\langle \varphi_1(t) | \varphi_2(t+\tau) \rangle|^2 . \tag{2.44}$$

For perfect overlap ($\varphi_1 = \varphi_2$ and $\tau = 0$), we have $\Delta q = 0$. This shows that perfect interference cancels out perfectly the sum of the independent partition noise $\overline{Q_{\mathrm{HBT,1}}} + \overline{Q_{\mathrm{HBT,2}}}$. In chapter 3 and 4 most of the results will be presented with $\Delta q(\tau)$. Note also that because of the modulus squared in expression 2.44, we really deal here with an intensity interference and not an amplitude interference. We are not sensitive to incoherent elastic dephasing that usually limits amplitude interference experiments such as Michelson or Mach-Zehnder interferometers.

2.4 Low frequency noise measurements

2.4.1 Setup

As sketched on the left panel of figure 2.10 (see also green part of figure 2.2), our low frequency setup dedicated to QPC characterization, determination of filling factor and more importantly to noise measurement is constituted first of a LC tank circuit, then the signal is split in two and amplified with two independent amplifying chain. The amplification at 1K is done by high electron mobility transistors (HEMT) fabricated by Yong Jin. This amplifiers have remarkable performances in terms of added noise [162]. There implementation in our setup together with the 4 *Coilcraft* 33 μH inductances was done by V. Freulon. An extensive study of HEMTs property can be found in chapter 3 of

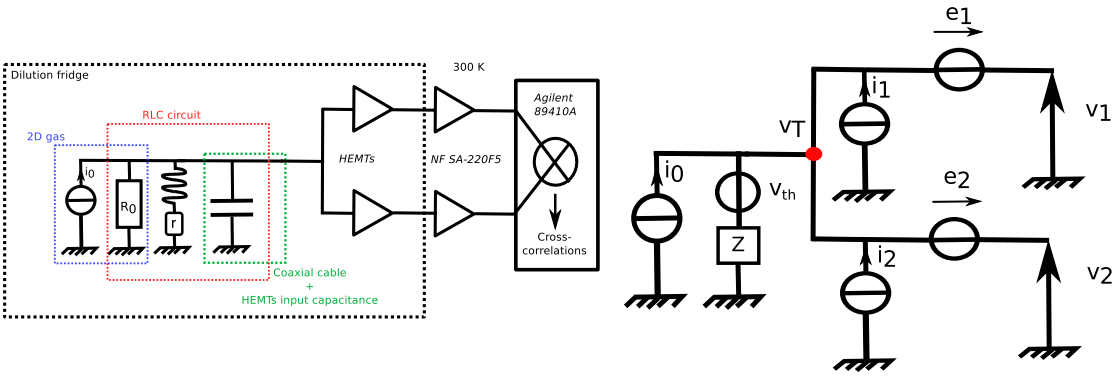

FIGURE 2.10: **Left.** Sketch of the equivalent circuit modeling the low frequency noise measurement setup. i_0 represent the backscattered current or noise current in output 3 of the QPC. $R_0 = h/(\nu e^2)$ is the impedance of the bi-dimensional electron gas. Then there is an imperfect coil of total inductance $L = 132\mu$H at room temperature and of internal resistance $r \approx 11\ \Omega$ at room temperature. The following capacitance C comes from linear capacitance of coaxial cables and input impedance of HEMTs. **Right.** Equivalent circuit with all source of fluctuating voltage and current. Z is the total impedance of the RLC circuit of the left panel. i_0 the current coming out of output 3 of the QPC. V_{th} is the Johnson-Nyquist noise generated by Z. i_k and e_k are respectively the current noise and voltage noise added by HEMT amplifier k.

his manuscript [107]. Then, there is a second stage of amplification at room temperature done with *NF SA-220F5* amplifiers after which the two outputs are then connected to a spectrum analyzer *Agilent 89410A* which can calculate, almost in real time, cross correlations between these two signals. We integrate the cross-spectrum on 1601 points in a 78.125 kHz bandwidth centered on the maximum of the lorentzian function defined by the LC circuit (1.4 MHz typically). This integrated noise defines a power in band (PIB) in V^2. To be able to access absolute current noise value with this PIB, one has to find a way to calibrate the total gain of the amplification chain. Because the inductance and capacitance of the LC components may change with temperature and more importantly, because HEMTs do not work at room temperature, this calibration has to be done when the fridge is running and the sample cold. Moreover, there are other sources of noise in the setup; they all are summarized on right panel of figure 2.10. All this considered, the signal we want to extract is at best of a few $10^{-29}\text{A}^2.\text{Hz}^{-1}$ on top of a ground base noise around $10^{-27} - 10^{-28}\text{A}^2.\text{Hz}^{-1}$.

2.4.2 Two chains of amplification

Doubling the chain of amplification enables to reduce this base noise. Indeed, the HEMT amplifiers, although quite efficient, add some noise to the signal. As modeled on figure 2.10, it adds a current noise $\langle i_k^2 \rangle$ and a voltage noise $\langle e_k^2 \rangle$ $(k = 1, 2)$. We will show later how to access these quantities. If we assume they are white Gaussian noise and that there is no correlation between the two HEMT amplifiers, then we can show that

measuring cross-correlations between the two path of amplifications enables to remove the voltage noise of each amplifier (but not the current one). As sketched on figure 2.10, we separate the thermal noise of the circuit response v_{th} from the partition noise i_0. We have:

$$\langle v_1 v_2 \rangle = \langle v_{th}^2 \rangle + |Z|^2 \left(\langle i_0^2 \rangle + \langle i_1^2 \rangle + \langle i_2^2 \rangle \right), \tag{2.45}$$

but,

$$\langle v_1^2 \rangle = \langle v_{th}^2 \rangle + \langle e_1^2 \rangle + |Z|^2 \left(\langle i_0^2 \rangle + \langle i_1^2 \rangle + \langle i_2^2 \rangle \right). \tag{2.46}$$

In the following sections, we are going to evaluate these noise contributions but already from these equations we guess that it is a good strategy to lower the base noise that contributes to $\overline{S}_{33}^{(\text{off,off})}$. However, this does not solve everything. One can show [107] that the "noise of the noise" that comes into the evaluation of the signal-to-noise ratio depends on $\langle e_1^2 \rangle$ and $\langle e_2^2 \rangle$ so it will always matter to have low noise amplifiers.

As mentioned before, we actually measure an integrated power spectrum density (in $[V^2]$) in the measured band $[f_c - \Delta f/2; f_c + \Delta f/2]$. Replacing $\langle v_{th}^2 \rangle$ by its Johnson-Nyquist expression [163, 164], we have:

$$P = G^2 \left(4 k_B T \int_{f_c - \frac{\Delta f}{2}}^{f_c + \frac{\Delta f}{2}} df' \mathrm{Re}\left(Z(f') \right) + \left(\langle i_0^2 \rangle + \langle i_1^2 \rangle + \langle i_2^2 \rangle \right) \int_{f_c - \frac{\Delta f}{2}}^{f_c + \frac{\Delta f}{2}} df' \left| Z(f') \right|^2 \right), \tag{2.47}$$

where G is the total voltage gain of the two added amplification stages.

From formula 2.47, we see that we not only need to know about G but also about $\mathrm{Re}(Z)$ and $|Z|$. We do not want to measure in the kHz range because there is a dominant $1/f$ noise that induces low frequency random variations of the background noise that are not negligible and cannot be eliminated by increasing the time average. It is thus interesting to measure in the MHz range which is still low compared to $k_B T_{el}$ but much less sensitive to this flicker noise. This is why we use a LC circuit resonating around 1.5 MHz. However it makes the variation of Z with f less trivial and we need to study more in detail what will be the effect on the measured total power in band.

2.4.3 The RLC circuit

2.4.3.1 Model

From the circuit model on the left panel of figure 2.10 we infer that the impedance Z seen by the amplifier is:

$$Z(\omega) = \frac{R_0\,(r + i\omega L)}{r + R_0 + i\omega\,(L + CR_0 r) - \omega^2 R_0 LC}. \tag{2.48}$$

In the regime where the inductance is perfect ($r = 0$) we recover a simple Lorentzian band pass filter with resonance pulsation $\omega_0 = 1/\sqrt{LC}$ and quality factor $Q = R_0\sqrt{C/L}$. However, as calibrations will reveal later, we are not quite in this regime and to be as accurate as possible we decided to study $Z(\omega)$ in full generality. In general, $Z(\omega)$ deviates from a standard Lorentzian function. The resonance is at:

$$\omega_0 = \sqrt{\frac{L - Cr^2}{L^2 C}} \tag{2.49}$$

at which the total impedance is not R_0 but:

$$Z(\omega_0) = Z_0 = \frac{R_0}{1 + \frac{rR_0C}{L}}. \tag{2.50}$$

We see that it is not enough to be in the regime $r \ll R_0$ to neglect the imperfection of the inductance. Doing so we would overestimate the impedance seen by the amplifier and thus underestimate the total amplifiers gain G (see formula 2.47). We can roughly estimate the ratio $\frac{rR_0C}{L}$ with room temperature measurement. For $R_0 = h/(2e^2)$, $r \approx 11\Omega$, $L \approx 120\mu$H and $C \approx 100$ pF we have $\frac{rR_0C}{L} \approx 0.2$.

2.4.3.2 Calibration with current response

To test this hypothesis, we used the lock-in Zurich instrument to sweep in frequency the excitation sent to the input Ohmic contact. For this calibration, we wire-bonded the RF line usually connected to dot 2 to the Ohmic contact on the same side of the noise measurement Ohmic contact. Because we used signal below 10 MHz, we can safely trust the room temperature calibration of the RF line that gives an attenuation of $-60dB$ and we should expect a flat behavior in frequency. The signal is then completely reflected by the closed QPC and all the signal will go through the LC circuit. We swept frequency between 1 and 2 MHz at different filling factor (6,4,3 and 1) during the same cool down.

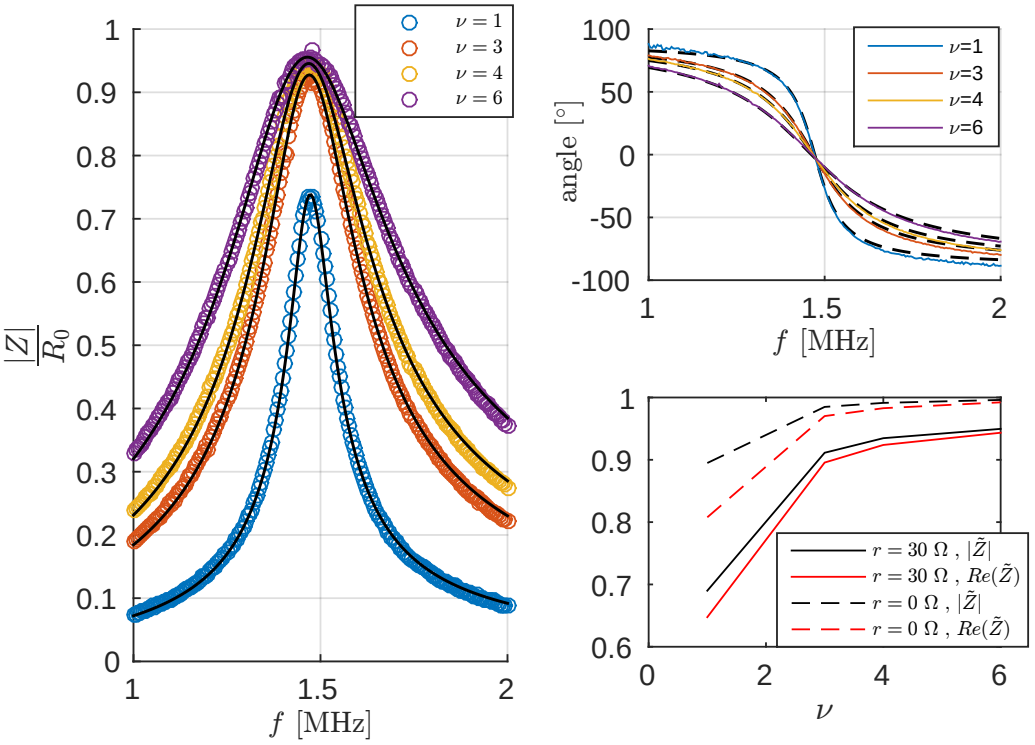

FIGURE 2.11: **Left.** Measured $|Z(\omega)|/R_0$ at 4 different filling factors between 1 and 2 MHz. Black lines correspond to fits. **Right upper.** Phase in degree (corrected by a linear shift so as to be zero at resonance) measured (colored lines) and predicted from the fit of the modulus (black dashed line). **Right lower.** Averaged $|Z|$ (black) and Re(Z) (red) divided by R_0 calculated for any filling factor with the rLC fit parameters obtained at $\nu = 1$ (full line) and when r is set to zero (dashed lines).

More precisely we measure the modulus of the outgoing signal:

$$|V_{out}(\omega)| = \frac{|Z(\omega)|}{R_0} G |V_{in}(\omega)|, \tag{2.51}$$

where G is the voltage gain of the two amplifiers and V_{in} the voltage applied on the Ohmic contact (amplitude $V_{0,in}$). We drive the contact with a $1\mu V$ amplitude sine voltage. The frequency response are then fitted with the modulus of equation 2.48 where r, C and G are left as free parameters (with some constraints to help convergence and L is fixed to a value that makes the fit compatible with thermal calibration presented in section 2.4.3.3). On the left panel of figure 2.11 is plotted $|V_{out}(\omega)|/GV_{0,in} = |Z|/R_0$. Results of the fit parameters (when L is fixed by hand) are presented in the following table:

ν	L (μH,fixed)	r (Ω)	C (pF)	G
1	161	30.4 ± 0.6	72.61 ± 0.02	2004 ± 6
1	140	36.2 ± 0.5	83.52 ± 0.03	2305 ± 7
3	139	14.92 ± 1	84.47 ± 0.05	2325 ± 8
4	132	13.2 ± 1.3	89.17 ± 0.07	2411 ± 9
6	125	14.25 ± 1.75	94.7 ± 0.1	2543 ± 10

A value of C around 90 pF is coherent with a coaxial cable ($\approx$ 100 pF.m^{-1}) of length a bit less than 1 meter between the sample and the amplifier, we also have to take into account the entrance capacitance of the HEMTs. The variation of r and L with magnetic field is a bit more surprising since the inductance is not suppose to contain ferrite. We tried various constraints on the fitting parameters and different approaches to try to reduce the number of fitting parameters. For instance, in the first two lines of the table, we did not imposed the same value for L. Imposing $L = 140$ μH, seems closer to the other inductance values at other filling factors but it gives a total gain higher than the one obtained with thermal calibration (see next section). $L = 161$ μH is higher but gives a gain closer to the one given by thermal calibration. Other fitting methods give roughly the same kind of results. However, none of these methods gave a better agreement with data and tends to overestimate gains ($G \simeq 3000$) which are not compatible with the temperature dependence presented in the next section so we decided to keep results from the table above. Looking in details at figure 2.11 the fit seems to slightly overestimate the current modulus above resonating frequency and underestimate for frequencies below. This may come from the small low pass RC filtering happening between the room temperature amplifiers and the lock-in which are separated by $\simeq 2$ m of coaxial cables.

On the right lower panel, we show the evolution of the integration of $|Z|$ or Re(Z) in the integration band $[f_0 - \Delta f/2; f_0 + \Delta f/2]$ (with $\Delta f = 78.125$ kHz) divided by $R_0 = R_K/\nu$ (where R_K is the Von Klitzing constant). This integral appears in the expression of noise. As we see, the imperfection of the inductance is critical at low filling factor where there is more and more dissipation in the resistance of the inductance. If we had a dissipation-less (superconducting) inductance, this issue would appear at lower filling factor and we would recover almost all the signal in the amplifiers.

The consistency of this calibration of the setup can be checked with the two calibration relying on noise measurement. They will be the subject of the two following sections. The first one is a measurement of the thermal Johnson-Nyquist noise the second relies on shot noise.

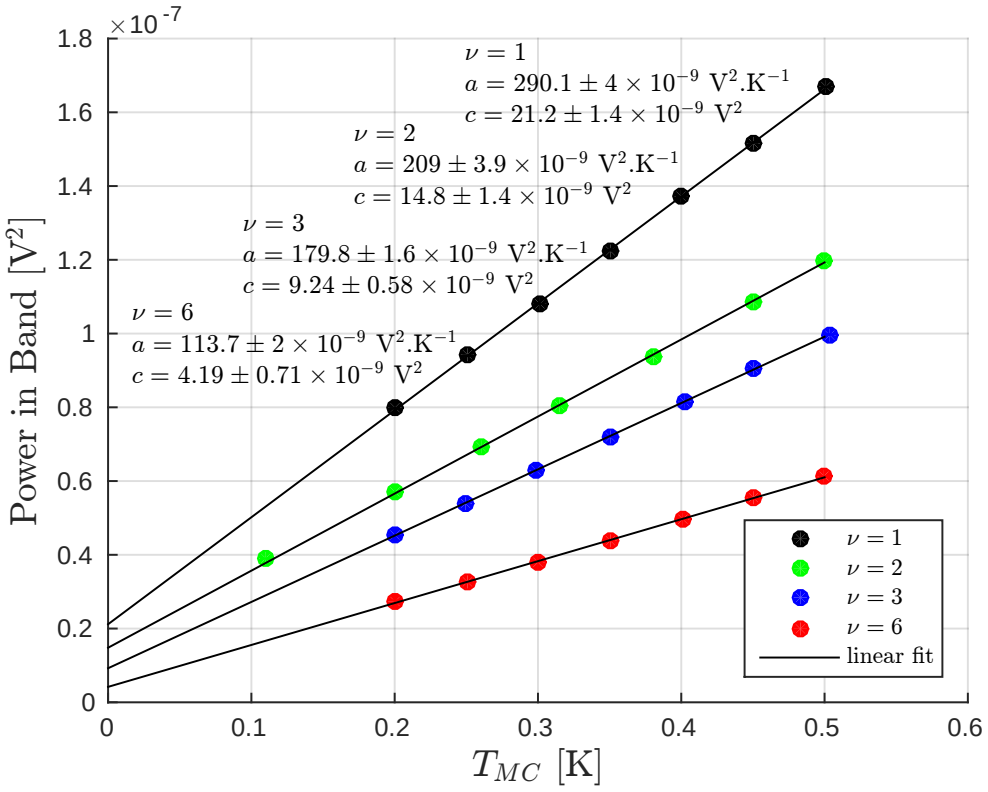

FIGURE 2.12: Power in band of the cross-spectrum versus mixing chamber temperature at filling factor 1,2,3 and 6 (different cool down for $\nu = 2$). From the value of noise at $T = 0$ we can extract the current noise of the amplifiers.

2.4.3.3 Calibration with temperature and estimation of noises from the amplifiers

This calibration is easier to implement and frequently used to calibrate noise setup measurement. It relies on thermal noise (or Johnson-Nyquist noise). Indeed, this noise is flat in frequency until a few GHz at base temperature and only depends on the impedance of the sample and temperature. On a plateau of the integer quantum Hall effect, this impedance is well known (R_K/ν) and it is easy to change the temperature of the mixing chamber up to 500 mK without risking to boil all He^3. Finally, we do not have to inject any calibrated signal.

There is no partitioning during this calibration so $i_0 = 0$. On figure 2.12 is presented such a calibration at filling factor $\nu = 1, 2, 3$ and 6. We focused on high temperatures to recover a linear dependence as expected. Data stops following the linear regime at low temperature (typically below 100 mK). This is because of a lack of phonons at these temperature which makes thermalisation of electrons less efficient. From the slope a is:

$$a = G^2 4 k_B \int_{f_c - \frac{\Delta f}{2}}^{f_c + \frac{\Delta f}{2}} df' \mathrm{Re}\left(Z(f')\right). \tag{2.52}$$

In the previous section, we finely tuned the inductance L so that the computed $\mathrm{Re}(Z)$ and G gives a prediction for the slope within the error bars of what was measured[4]. Using the previous results to compute $\mathrm{Re}(Z)$ in the previous section we can deduce G from the slope a and compare it to the gain obtained from the Lorentzian fits. Results are summarized in the following table. For $\nu = 2$ we used the average r, L and C parameters from $\nu = 1$ ($L = 140\mu$ H) and $\nu = 3$, this enhances the uncertainty.

ν	L (μH,fixed)	G (with Lorentzian)	G (with thermal noise)
1	161	2004 ± 6	2004 ± 14
1	140	2305 ± 7	2149 ± 15
2	140	not measured	2187 ± 200
3	139	2325 ± 8	2318 ± 10
4	132	2411 ± 9	not measured
6	125	2543 ± 10	2546 ± 22

In principle one could suspect the rLC parameters to change at each cool down and thus this double calibration should be down at each cool down for each sample. In practice, for every new sample we only remeasured the noise versus temperature calibration and observed that for a given filling factor, it did not vary significantly therefore we could assume the that rLC parameters did not change.

From the offset c, we have:

$$c = \left(\langle i_1^2 \rangle + \langle i_2^2 \rangle\right) G^2 \int_{f_c - \frac{\Delta f}{2}}^{f_c + \frac{\Delta f}{2}} df' \left|Z(f')\right|^2 \tag{2.53}$$

which gives access to the current noise of both amplifiers. We can linearly fit values of c versus predicted "LC+gain" response. The slope gives $\langle i_1^2 \rangle + \langle i_2^2 \rangle = 1.7 \times 10^{-28} \mathrm{A}^2.\mathrm{Hz}^{-1}$ and the offset gives a spurious amount of parasitic noise $3.5 \times 10^{-9} \mathrm{V}^2$ that does not depend on the impedance of the tank circuit. This last term is negligible in our measurement. However, as could already be seen on the offset contribution on figure 2.12 the current noise of the amplifier is low but comparable to thermal noise below 100 mK and larger than the typical excess noise we want to measure in the HOM interferometer.

Using the same kind of calibration but with a 50 Ω load instead of our sample we can significantly reduce both the contribution of amplifier current noise and total thermal noise of the impedance. Thus we can expect to have a noise dominated by voltage fluctuations of the amplifier. Of course to measure it we need to measure directly each amplified outputs and not their cross-correlations as done usually. Results for the two amplification output are presented on figure 2.13 at 3 different temperatures. Because

[4] For filling factor 4 we choose an average inductance between the one from 3 and 6.

the 50 Ω is completely negligible compared to the impedance of the LC circuit $\sqrt{L/C}$, we can safely assume that the impedance $Z(\omega)$ seen by the HEMT amplifiers is really 50 Ω and that it is flat in the integration band. What is more, we can measure independently the gain of each room temperature amplifier G_{rt} which is around 400. From the two slopes a we can then simply calculate the gain of HEMT amplifiers:

$$a = G_{rt}^2 G_{\text{HEMT}}^2 4 k_B R \Delta f \tag{2.54}$$

which gives $G_{\text{HEMT1}} = 7.2 \pm 0.2$ (red curve) and $G_{\text{HEMT2}} = 7.4 \pm 0.1$. This gives a total gain $G_{rt}G_{\text{HEMT1}} = 2890$ and $G_{rt}G_{\text{HEMT2}} = 2940$. These values are higher than what the fitting with a Lorentzian gives. Actually, the latter measurement was done at the beginning of my PhD at least one year before the LC measurements, the HEMTs probably got deteriorated over this period. With a 50 Ω load, the impedance has been divided by at least 80 so the current noise from the amplifiers is negligible. Therefore we can assume that the offset c corresponds to voltage noise of the amplifiers. Dividing by the total gain and the integration band we recover a noise power spectrum at the input of HEMT of $\langle e_1^2 \rangle = 3.63 \pm 0.18 \times 10^{-20}\text{V}^2/\text{Hz}$ (or $0.19 \pm 0.04\text{nV}/\sqrt{\text{Hz}}$) for channel 1 (red points) and $\langle e_2^2 \rangle = 3.65 \pm 0.14 \times 10^{-20}\text{V}^2/\text{Hz}$ (or $0.19 \pm 0.04\text{nV}/\sqrt{\text{Hz}}$ for channel 2 (blue points). This value is comparable to world record values; however, for a typical impedance around $R_K/2$ around 10 kΩ, we see that this noise gives a contribution of $\approx 2 \times 10^{-28}\text{A}^2/\text{Hz}$ *i.e.* the same order than the current noise and higher than partition noise is thus not negligible. This justifies *a posteriori* the doubling of the two amplification chains to eliminate this contribution.

2.4.3.4 Calibration with shot noise

Another way to calibrate the amplification chain that is less time consuming but a bit more indirect is to rely on partition noise. Indeed, the partition noise produced at the level of a QPC by a DC bias has been extensively studied [165–168] and measured [169–171] and is now well understood. Starting from the expression of the HBT noise (see equation 2.38) we can show that applying a DC bias V_2^{DC} on input 2 gives an excess current noise:

$$\Delta\overline{S_{33}} = \frac{2e^3 R(1-R)}{h} V_2^{\text{DC}} \left(\coth\left(\frac{eV_2^{\text{DC}}}{2k_B T_{el}} \right) - \frac{2k_B T_{el}}{eV_2^{\text{DC}}} \right). \tag{2.55}$$

When $2k_B T_{el} < eV_2^{\text{DC}}$ we recover the shot noise regime and a noise linear with injected current $e^2 V_2^{\text{DC}}/h$. In the opposite regime, noise is dominated by thermal contributions. We can independently access R with current measurements. Total power in band is computed by replacing $\langle i_0^2 \rangle$ with $\Delta\overline{S_{33}}$ in formula 2.47. Measurements of excess power

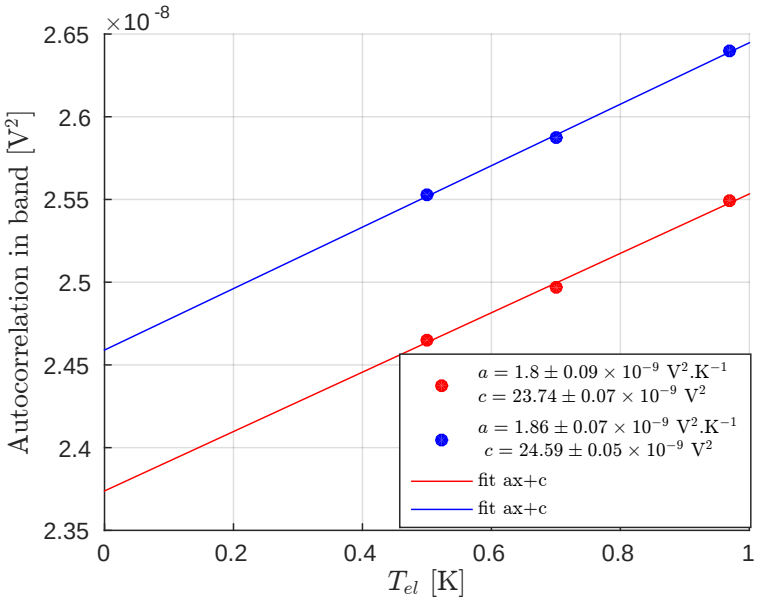

FIGURE 2.13: Autocorrelation power spectrum for each amplification output versus electronic temperature measured on a 50 Ω load. From the offset we can deduce the voltage noise contribution of the HEMT amplifiers.

in band versus V_2^{DC} at $\nu = 2$ (for a different cool down) are plotted in the insert of figure 2.14. From the slope of the fit, we measure the factor $G^2R(1-R)\frac{2e^3}{h}\int |Z(\omega)|^2 d\omega$. If we take the values of G and $Z(\omega)$ determined by the previous calibrations we find it is compatible with $R = 0.25$ which is also the reflection we measure with the current transmission measurement, we thus have a good agreement between different kind of calibration. This calibration enables to cross-check that the gain does not change over long period of time. At $\nu = 2$ we used the value $G = 2187 \pm 100$ which gives a slope for the DC shot noise calibration:

$$a = G^2R(1-R)\frac{2e^3}{h}\int |Z(\omega)|^2 d\omega \tag{2.56}$$

which is equal here to $1.004 \pm 0.028 \times 10^{-4}\mathrm{V}^2/\mathrm{V}$.

Actually, the precise value of G is not critical and only necessary if one wants to determine precisely the effective charge tunneling through the QPC. Indeed, in the HOM experiment, the quantity of interest is a normalized noise Δq where the gain do not appear. Moreover, in chapter 5 we will see that for the tomography protocol, we also normalize all noise measurements directly by the slope measured in the shot noise DC partitioning (factor a in the insert of figure 2.14).

On the main part of figure 2.14, is plotted the shot noise versus $T = 1 - R$ for 3 different values of V_2^{DC} together with a simulation taking into account a 10 mK difference between

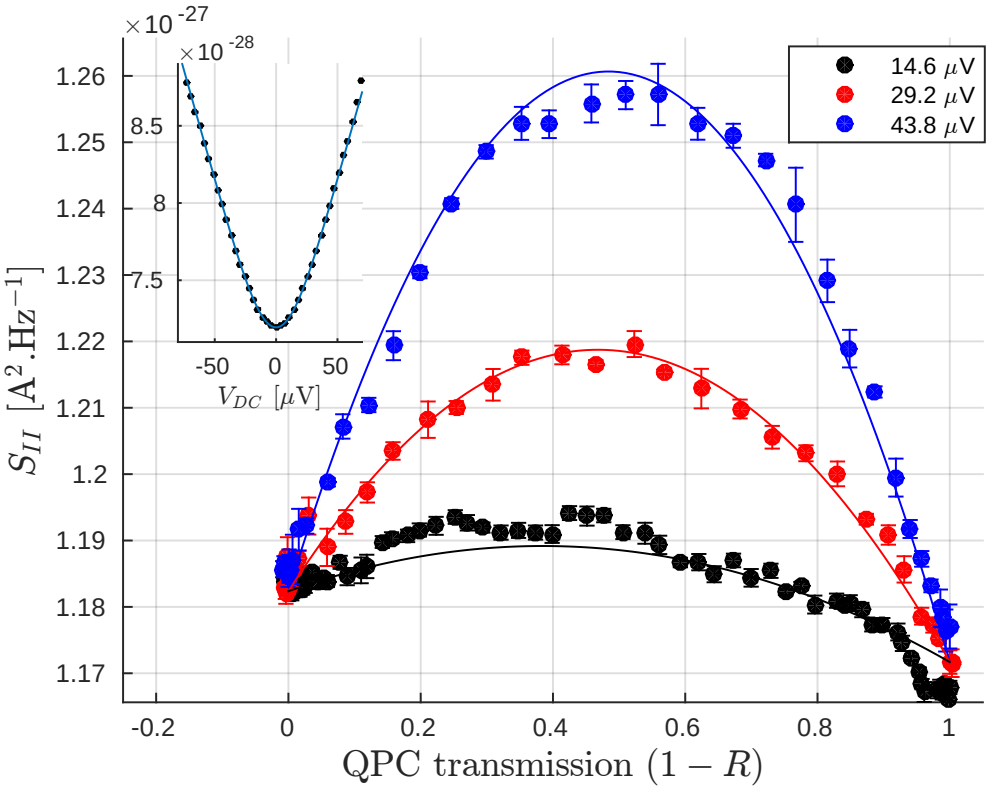

FIGURE 2.14: Shot noise versus QPC transmission $T = 1 - R$ for 3 different bias V_2^{DC} applied to Ohmic contact at filling factor $\nu = 2$. We recover a law in $R(1-R)$. Full line are theoretical models taking into account a 10 mK temperature difference between the two arms (see section 5.2.1 for details). This can be explained by a difference in the way Ohmic contact are thermally anchored on each side. The amplitude of the parabola enables to deduce a total gain G compatible with the one determined with thermal noise calibration. **Insert.** Excess noise versus bias. The full line is a fit using $ax(\coth(x/b) - b/x)$. Parameter $b = 2k_BT_{el}/e$ enables to access the electronic temperature $T_{el} = 94 \pm 1$ mK and a depends both on exact reflection coefficient R and total gain G.

the two arms(see section 5.2.1 for details). We observe that points tend to follow a law $R(1-R)$ apart for the low bias one which has more accidents probably because of disorder.

This procedure also enables us to access the electronic temperature T_{el} with a ± 5 mK precision. For insert data, the deduced electronic temperature is $\approx$ 90 mK. At the beginning of my PhD, the electronic temperature was around 80 mK and deteriorated toward 100 mK at the end (concerns mostly results presented in the last chapter).

Last but not least, this measurement enables to test quickly if the QPC works properly. Indeed, formula 2.55 is valid only when R is independent of energy. All the interpretation of HOM as an overlap of single particle coherence or Wigner overlap falls down if this hypothesis is not valid. When this is not the case, the noise either deviates strongly from this formula and can even have non-monotonic behavior with V^{DC} or it can be seen by

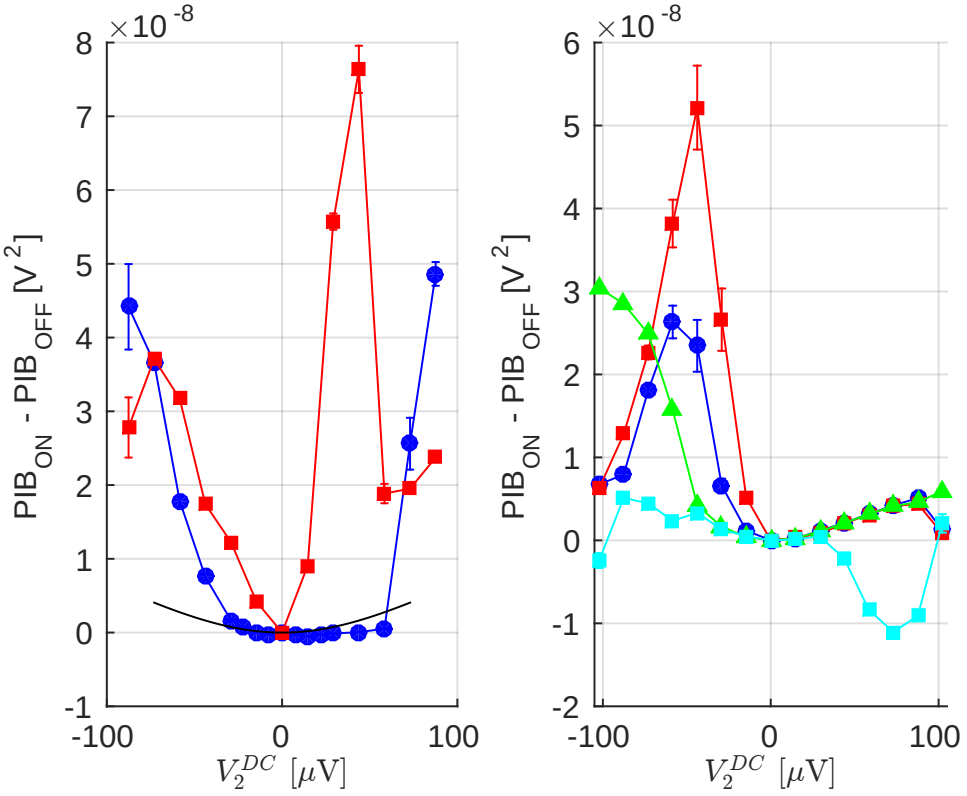

FIGURE 2.15: Pathological noise versus V^{DC} measurements at filling factor 2 for sample S902. **Left.** The black line is a reasonable expectation. For blue curve it seems that high bias activates fluctuators, strongly enhancing noise. For the red curve, these fluctuators appear at even lower bias. **Right.** Four measurement with the same parameters, the only change between these curves is the averaging time and the way V^{DC} is swept (increasing fro red and blue and decreasing for green and cyan). Red and cyan have a time averaging twice longer than blue and green. This shows that the activation of fluctuators depends on the bias integrated over time but also that for this working point has strong hysteresis.

the fitting parameters which are out of reasonable boundaries ($T_{el} > 1$ K for instance). When we find such an odd point we can decide either to change the QPC transmission or move to another magnetic field (but staying on the same Hall plateau) in the hope to recover a better behavior of R. This calibration was therefore done on a daily basis to both check if the QPC is working in an energy independent transmission regime and to monitor the electronic temperature and the gain. Figure 2.15, illustrates what we can measure when the QPC is not working properly either because of hysteresis (right panel) or nonlinearities and activation of fluctuators at high bias (left panel).

2.4.3.5 RF amplitude calibration with noise

The same kind of measurement can be done but with an AC signal on the Ohmic contact instead of a DC one. Comparing this to the previous DC calibration this enables to

determine the voltage amplitude of the drive applied on the Ohmic contact. This will be of great interest for the tomography protocol presented in chapter 5. Going from DC to AC we have to take into account photo assisted effect and excess current partition noise (with only AC bias) becomes [155, 156, 159, 172]:

$$\begin{aligned}\Delta\overline{S_{33}} =& \overline{S_{33}}^{1=OFF,2=ON} - \overline{S_{33}}^{1=OFF,2=OFF} \\ =& \frac{4e^2}{h}R(1-R)\sum_{n=-\infty}^{\infty} J_n^2\left(\frac{eV_2^{\mathrm{AC}}}{\hbar\Omega}\right) n\hbar\Omega \coth\left[\frac{n\hbar\Omega}{2k_BT_{\mathrm{el}}}\right] \\ & - \frac{8e^2}{h}R(1-R)k_BT_{el},\end{aligned} \tag{2.57}$$

where J_n are Bessel functions of the first kind. The slope for the DC shot noise calibration gave access to the product of gain, integrated response of the LC circuit and Fano factor $R(1-R)$. It also enables to access electronic temperature. Thus at the same transparency $1-R$, for a given frequency drive, we have all the ingredients to predict the value of the power in band. We simply need to compute the sum of Bessel functions in the above equation for any amplitude and adjust V_2^{AC} so that the result matches with the measured noise. The numerical sum of Bessel functions is done from $n = -3000$ to $n = 3000$. We checked that this result is not sensitive on this cut off value. A a good rule of thumb to estimate when to stop the sum is to stop at $n_{\max} = \frac{eV_{\max}^{\mathrm{AC}}}{\hbar\Omega}$ where $V_{\max}^{\mathrm{AC}}$ is the maximum amplitude we want to study. This has to be done each time the QPC transmission or the frequency drive are modified. On figure 2.16 is presented such a fit for 4 drive frequencies: 9, 15, 18 and 20 GHz. For clarity, each data higher than 9 GHz are shifted of $4\times10^{-29}\mathrm{A}^2.\mathrm{Hz}^{-1}$. Knowing the amplitude at the output of the generator we can deduce the attenuation down to the Ohmic contact up to $\pm0.5-1$ dB which enables to plot the data versus the amplitude drive on the Ohmic contact (and not on top of the cryostat).

The agreement between data and model is quite good. The red dashed line is calculated with a very low frequency compared to the electronic temperature so as to model an adiabatic "classical" drive. With this, we can see the effect of increasing the frequency drive and the transition from a classical ($hf \ll k_BT_{el}$) to non-classical drive ($hf \gg k_BT_{el}$). Actually, we see very little difference between the classical model and the 9 GHz one although $hf = 37\mu$eV and $k_BTel = 7.8\mu$eV. We will see in chapter 5 how to really characterize a non-classical signal and that a 9 GHz drive is indeed non-classical.

2.4.4 Various improvements

Starting my PhD, I benefited from a fully wired and already functioning cryostat. It is the same cryostat that was used by my predecessors and some components of the

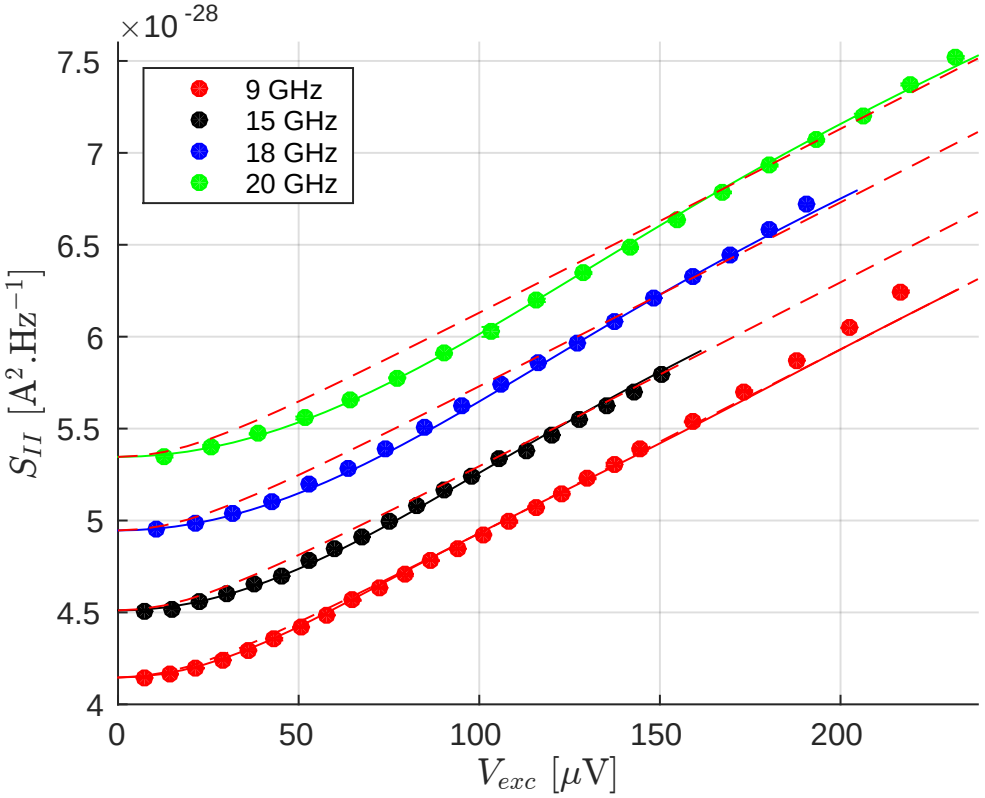

FIGURE 2.16: Current partition noise versus drive amplitude for 4 frequencies (9, 15, 18 and 20 GHz) at zero DC bias. For clarity, each data higher than 9 GHz are shifted of 4×10^{-29}A^2.Hz^{-1}. Full lines correspond to theory of the same color data set, only RF attenuation is left as fitting parameter (gain, QPC transmission and electronic temperature are determined with DC shot noise calibration). Red dashed lines correspond to theory for an adiabatic "classical" drive ($hf \ll k_B T_{el}$), also shifted for comparison, this enables to see the effect of increasing the frequency on partition noise. Agreement with theory is quite good apart from high amplitude points, possibly because of non-negligible heating effects.

circuitry are common to all these works. However, each one of them had to change a bit some other part that his successor had left him, so as to improve it or adapt parts to new sample design.

2.4.4.1 DC lines

Improved thermalisation As far as I am concerned, I first had to improve filtering of the DC lines in particular to filter spurious high frequency parasitic signals not properly filtered by discrete low-pass filter elements. To do so I wrapped 7 Manganin (CuMnNi) wires ($\approx$ 50 cm each) on a copper cylinder anchored at the level of the mixing chamber. The wrapping was done back and forth along the cylinder with a different chirality each way so as to compensate possible eddy (Foucault) currents in the wires. They were glued with a mixture of *Stycast* and copper nano-particles powder. This part was inserted and

soldered in between the sample and the previous last stage thermalisation (copper stripes deposited on Kapton, see [4]). Before this adding, there were two filtering stages of this kind in the fridge. One of them is anchored at the 1K pot stage and the other at the mixing chamber one; however the last one had actually too short copper stripes to thermalise efficiently the DC lines. Indeed, thermalisation length is of the order of ≈ 15 cm at 20 mK and they are only ≈ 2 cm long. Therefore, firmly anchoring the copper cylinder with the wrapped lines not only enhanced filtering but also thermalisation of this DC lines. With the same method we also added a voltage divider on the line V_{bias} going to Ohmic contact (see [107]). The voltage division introduced is $(1.46 \times 10^{-4})^{-1}$.

More DC lines In the beginning of my PhD, we could only use 4 DC lines (V_{g1}, V_{g2}, V_{QPC} and V_{bias}). They were connected on the PCB with shouldered *miniSMP* connectors. We wanted to be able to test samples with a greater number of top gates and also have the ability to address independently each arm of the central QPC so as to be able to find more easily good working points (*e.g.* avoid non-linearity in energy) without having to warm up and cool down the gas each time. This is why we needed to wire more DC lines down to the mixing chamber. Some of them were already there but broken, or not connected to the existing thermalisation setup. For two of these lines I thus used the same method presented in the previous paragraph to thermalise close to the 1K pot. To thermalise and filter close to the mixing chamber, I used a golden box filled with *Ecosorb*, anchored at the mixing chamber stage. Current is transmitted by copper lines embedded in the *Ecosorb*. This also enabled us to use cryogenic biastee (*Marki BTN0040*) to have a better lever arm on the DC voltage applied on top gates. This modifications arrived between chapter 4 and 5. Before that, biastees were at room temperature and the DC part was attenuated like the AC part, so on a range of ± 1 V we could only observe a few peaks shift whereas now we can even totally deplete the dot with only a few hundreds of mV.

To bring more DC lines toward the sample, we used a new kind of PCB designed by Anne Denis with up to twelve possible connections. The only drawbacks of it is that to connect wires to this lines I had to solder thin Manganin wires on a mm^2 scale area. The soldering was not always perfect, rendering it fragile to mechanical stress. Around the end of my PhD, we suspected a transmission noise in our shot-noise data. To better filter the voltage applied on QPC, we soldered an on chip 100 nF CMS capacitor.

Chapter 3

Coulomb interaction in one dimensional chiral systems

"Jt'ai cassé !"

Brice de Nice.

In this section, I will detail the effect of Coulomb interactions on the propagation of charge in the quantum Hall edge channels. First, I will present the plasmon scattering formalism that enables to accurately predict the effect of interactions on the propagation of charge and will also give here a short review of various experiments that already demonstrated these effects with other kind of interferometers, but only with stationary sources. I will then explain how we can characterize these phenomena in an original fashion with the HOM interferometer and finally present measurements that enables to picture the fractionalization of a single electron in the time domain.

3.1 Charge fractionalization

3.1.1 What is it ?

Taking interactions into account in a many-body system is known to be a hard problem in general. This is why the Fermi liquid theory introduced by Lev Landau in 1956 is very powerful and convenient. Indeed, he stated that whatever the strength of the interaction,

low energy excitations of an ensemble of electrons could be treated equivalently as low energy excitations of an ensemble of weakly interacting quasi-particle. There is a one to one adiabatic correspondence between the "bare" electrons and these so-called long lived Landau quasi-particles. They have the same charge, spin and statistics, their mass is simply renormalized [173–175]. This line of reasoning enables to describe a lot of electronic systems and it is so popular that *normal* metals are actually defined by their ability to be described by such a phenomenology and a *non-Fermi liquid* is often synonymous with exoticism. Unfortunately, this convenient way of thinking totally breaks down for one dimensional systems, even for the smallest amount of interaction. Indeed, in a one dimensional interacting system, the Landau quasi-particle is no longer appropriate to describe low energy elementary excitations. However we can still describe the system as a ground state with small energy excitations. New elementary quasi-particles associated to these excitations are non-interacting collective modes (or sound waves), have a linear dispersion relation at low energy and have a bosonic statistic: these are called plasmons [176] and correspond to the excitation of many electron-hole pairs. This model was first introduced by Tomonaga [177] and later developed by Luttinger and Haldane [178–180]. To describe a single electronic excitation in terms of plasmons one needs the help of the now famous bosonisation [181, 182]. It is a non-perturbative theory that is able to make exact predictions for this Tomonaga-Luttinger liquid systems (TLL) in particular concerning dynamical quantities which is what will be of interest for transport experiments.

One remarkable prediction for TLL systems, is the separation between charge and spin degrees of freedom, which leads to a fractionalization of the charge [183–185]. It was observed first in chemically or gated defined wires in GaAs/AlGaAs hetero-structures [186, 187] then with contra-propagating edge channels of the integer quantum Hall effect [188].

Edges of the integer quantum Hall effect are a special kind of Tomonaga-Luttinger liquid since they are chiral *i.e.* excitations propagate in only one way, but they still exhibit collective acoustic modes called edge-magneto plasmons (EMP). They have been studied both with time resolved measurements [189–194] and in the frequency domain [195–199] where it was shown that EMP could be excited with voltage drives in the GHz range. Chirality simplifies the system in the case of integer filling fraction especially at filling factor 2 which has been the most studied both theoretically and experimentally. The essential features of such systems are preserved: spin-charge separation is still predicted [200–204], although the spin mode is trivial here because the channels are spin polarized, we thus simply talk about neutral modes. At $\nu = 2$, for strong interaction, there is one symmetric charge mode and one antisymmetric neutral mode. A sketch is presented on figure 3.1 to illustrate this electron fractionalization. Because of repulsive interedge

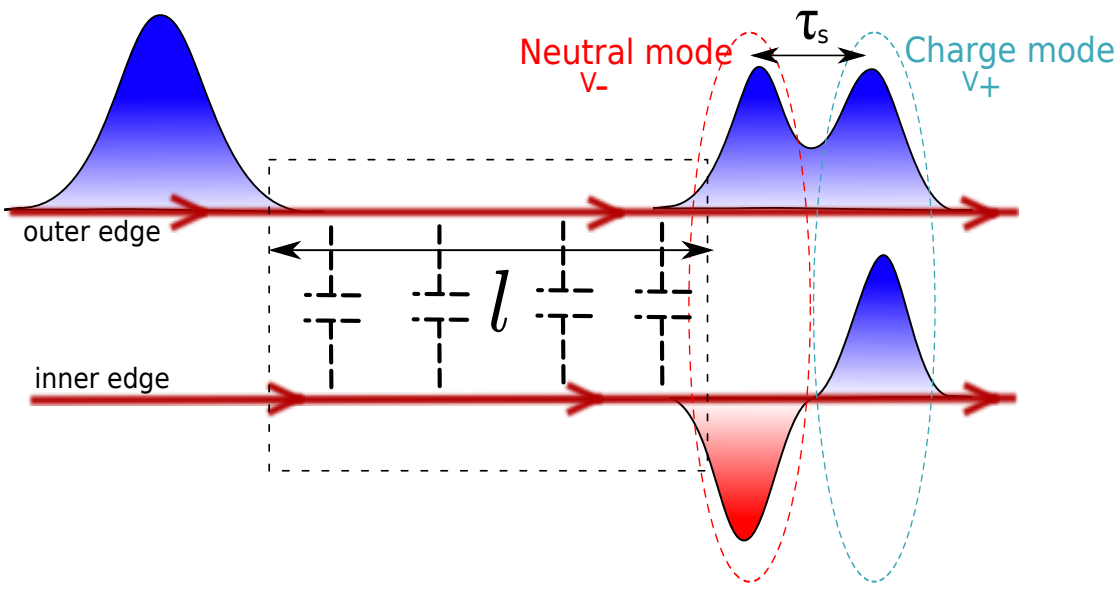

FIGURE 3.1: Sketch of electron fractionalization. Due to inter-channel interaction on propagation length l, an electronic wave packet emitted on the outer edge channel splits in a charge mode (dashed blue oval) propagating at velocity v_- and a neutral mode (red oval) with velocity v_+ separated by time τ_s. The interaction region is represented by a capacitive coupling between the edges in the dashed black box. Negative (positive) charge pulses are represented in blue (red). At the output of the interaction region, the electron on the outer channel has fractionalized in two pulses carrying charge e/2. A dipolar current trace has been generated in the inner channel.

Coulomb interaction, the charge mode has a higher energy and thus propagates with velocity v_+ higher than the antisymmetric neutral mode (or dipolar charge distribution) propagating with velocity v_-. Because of this difference in velocities, a single-electron wave packet generated on the outer edge channel propagating on length l splits in two charge pulses carrying charge e/2 separated by time:

$$\tau_s = \frac{l}{v_-} - \frac{l}{v_+}. \tag{3.1}$$

This process is accompanied by the generation of collective excitations in the inner channel with a dipolar current trace: an electron-like pulse followed by a hole-like one separated by τ_s. This fractionalization of an electron into collective modes has of course dramatic consequences for electronic coherence [201, 202, 205–208] and leads to relaxation in energy [209–212]. Previous experimental studies mainly focused on the Mach-Zehnder interferometer [2, 213–216], or spectroscopy of out-of-equilibrium stationary distribution [55–57, 217].

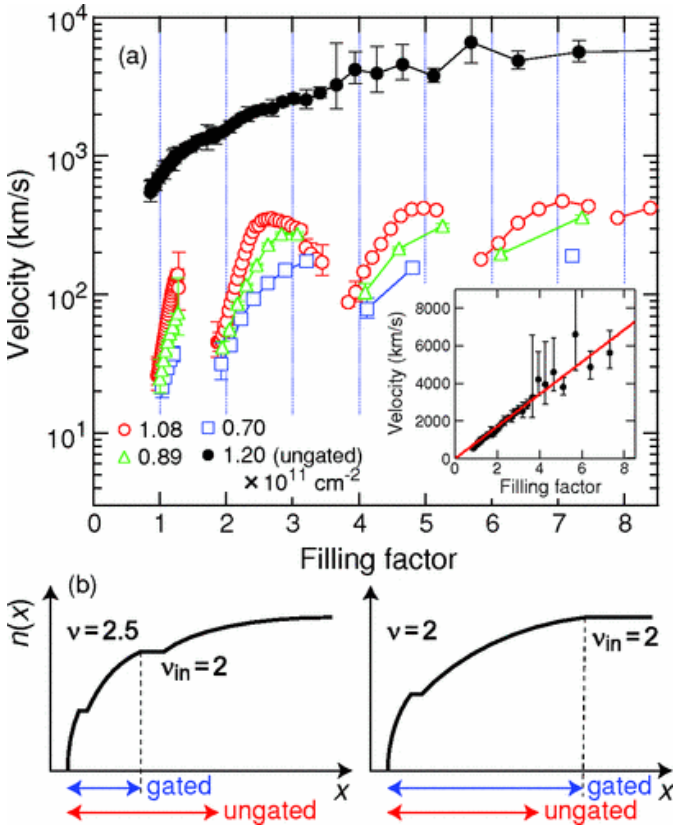

FIGURE 3.2: (Figure extracted from [194])(a) Log-scale plot of the velocity of EMPs in the ungated (solid symbols) and gated (open symbols) regions as a function of ν. Inset shows the linear-scale plot of the velocity in the ungated region. The line is the result of the fitting. (b) Illustration of the density profile $n(x)$ in the edge state and the transverse extent of EMPs in the ungated and gated regions represented by arrows for the bulk filling factors $\nu = 2.5$ and 2.

3.1.2 Edge-magneto plasmons: state of the art

The velocity of the charge mode v_+ could be measured by precise time of flight experiments in reference [194] and was shown to depend strongly on the electromagnetic environment and on magnetic field. Results extracted from the reference are shown in figure 3.2. For chemically etched, ungated electron gases, v_+ goes from $\simeq 5 \times 10^7 \mathrm{m.s}^{-1}$ at high filling factor and decreases to $\simeq 6 \times 10^5 \mathrm{m.s}^{-1}$ at filling factor 1. It is around $\simeq 1 - 2 \times 10^6 \mathrm{m.s}^{-1}$ around filling factor 2. For an electron gas with a large top gate on top of it, screening is increased, so the velocity is reduced by more than one order of magnitude (see color point on figure 3.2). Measured velocities are at minimum $2 \times 10^4 \mathrm{m.s}^{-1}$ at filling factor one and do not go above $5 \times 10^5 \mathrm{m.s}^{-1}$ at high filling factor.

From this, we infer that the exact nature of the modes depends on the detail of the electromagnetic environment. In particular, the outer edge channel being closer to the side gates of the sources (in our configuration), it may have a "bare" velocity lower than

the inner one. Here, by "bare", we mean the Fermi velocity renormalized only by the capacitive coupling to the ground $v = v_F + e^2/(hC_g)$ (see appendix B.1 for details).

The difference between mode velocities could be determined indirectly by analysis of shot-noise induced in the inner edge channel by a independently biased outer edge channel [218–220]. Fano factors compatible with a difference $v_+ - v_- \simeq 5.6 - 6.2 \times 10^4 \mathrm{m.s}^{-1}$ were measured.

One experiment was able to successfully excite independently one edge and thus directly visualized the two eigenmodes [221]. This experiment, developed in our group with the same kind of samples, relied on high frequency admittance measurements and was realized during the PhD of E. Bocquillon and V. Freulon. I will not describe this experiment here, the detailed description of it and their results can be found in their thesis manuscript [3, 107]. In section 3.4, I will use the main theoretical tool developed in their work and apply it to the analysis of the HOM patterns. One of their main result that will interest us is the measurement of the neutral mode velocity $v_- = 4.6 \times 10^4 \mathrm{m.s}^{-1}$ at low frequency (and a smaller one $v_- = 2.3 \times 10^4 \mathrm{m.s}^{-1}$ after 6 GHz) which gives a $\tau_s \simeq 70 - 80$ ps for a similar propagation length around 3 μm. A finite range interaction model was developed and enabled to describe successfully these two regimes. It is demonstrated that at low frequencies, the interaction can be safely approximated by a zero range strong interaction model [221]. Strong interactions mean that the asymmetries between the two bare velocities are negligible compared to the change of velocities imposed by the inter-channel interactions, therefore the eigenmodes are indeed the symmetric charge mode and antisymmetric neutral mode. The smaller velocity appearing at higher frequency could be explained by finite range interaction. Indeed at those frequencies, the EMP's wavelength becomes comparable with the propagation length which affects the electronic density itself affecting charge screening and thus the neutral mode velocity. However this does not impact the strong interaction assumption: charge is still fully transported by the charge mode.

In the group of F. Pierre, thanks to quantum dot energy filtering, they managed to measure the energy distribution of out-of-equilibrium stationary distributions [55–57, 217] and showed that interchannel Coulomb interaction is also responsible for energy relaxation in the outer edge. However, energy is only exchanged between edge channels and does not leak through the rest of the sample. Fujisawa *et al.* managed to bring close together two pairs of counter-propagating edge channels (at $\nu = 2$) and observe long-lived binary spectrum surviving after $5 - 10\mu$m of propagation, indicating negligible energy leakage outside from the edges on those scales [222]. Finally, in a very recently published work Fujisawa *et al.* managed to measure directly in the time domain the fractionalization of charge pulses over large distances (260μm) with time-resolved current

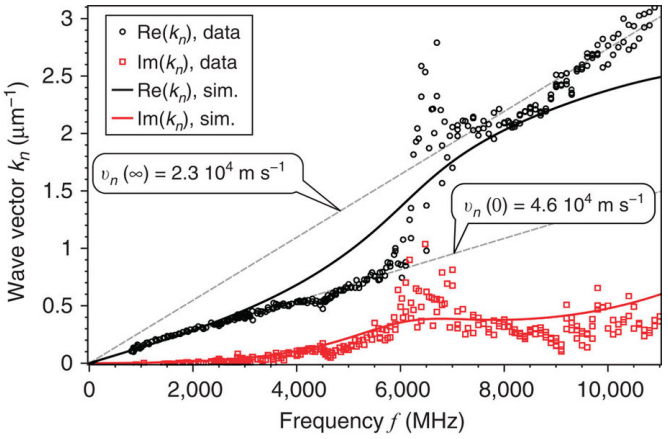

FIGURE 3.3: (Figure extracted from [221]) Real and imaginary parts of the wave vector $k_n(\omega) = \omega/v_n(\omega)$. Re($k_n$) exhibits two non-dispersive regimes: at low frequency ($f < 6$ GHz) $v_n(0) = 4.6 \times 10^4 \text{m.s}^{-1}$ whereas at high frequency ($f \geqslant 7$ GHz) $v_n(\infty) = 2.3 \times 10^4 \text{m.s}^{-1}$. Im($k_n$) $\neq 0$ indicates damping.

measurements [223]. They managed to inject short current pulses at will, on any channel and could thus probe both the charge and the neutral modes. Because they have a really long propagation length, they could also observe the relaxation of the neutral mode due to spin-flip mediated tunneling events. Based on an estimate of their propagation length, they could determine both the charge mode velocity ($v_+ \simeq 4.8 \times 10^5$ m.s^{-1}) and the neutral mode velocity ($v_- \simeq 6.5 \times 10^4$ m.s^{-1}) and their variations with magnetic field or side gate voltage. The results are very similar to ours. Instead of using time-resolved current measurements at 100 ps scale, we will use low frequency noise measurements and because we have shorter propagation length the separation will be less pronounced. However the results are not contradictory.

What happens exactly because of this different velocity mode for a single electron at filling factor $\nu = 2$ was predicted by Degiovannni *et al.* [224] and Wahl *et al.* [225]. In the last reference it was proposed to probe electronic coherence with the HOM interferometer not only the outer channel but also the inner one. This enables to reveal the collective excitations generated in the interaction process. Combined with information of the outer channel, we can directly picture the fractionalization in time domain and establish its relevance for the decoherence and destruction of the quasiparticle, which degrades into the collective modes.

3.2 Experimental measurements

In the following section, I will first present results of the HOM interferometry for outer and inner channels in two different kinds of emission regime for the sources. Data will

be compared with the plasmon scattering formalism that enables to predict exactly the $D = 1$ case, however I will present the formalism later, in section 3.4.

3.2.1 Set up and choice of excitation

The experimental configuration is the same as the one presented in chapter 2. The magnetic field was set at 3.92 T so as to reach a filling factor $\nu = 2$ in the bulk. The emitters are synchronously driven by a periodic square excitation applied on the dot top gates at frequency $\Omega/2\pi = 0.9$ GHz, with a 30 ps rise time. Changing the voltage V_{QPC}, the QPC can be set to partition either the outer or the inner edge channel. The dots are only coupled to the outer edge channel such that the current pulse is generated on the outer channel only. The dot to edge transmission D is used to tune the dot emission time and the dot charge quantization.

Two configurations are studied: at $D = 1$ the dot is perfectly coupled, charge quantization is lost and a classical current pulse (carrying a charge close to e) is generated in the outer channel. By construction, the emission time is as short as possible in this configuration. It provides the minimum temporal extension for the signal and thus the best time resolution. This resolution is limited both by the square pulse rise time ($30-40$ ps) and by the minimum charge relaxation time ($\tau_{RC} = 17$ ps). Another advantage for this configuration is that we directly excite a coherent state which makes calculation with a plasmons scattering theory possible (see 3.4). In the second configuration, $D = 0.3$, charge is quantized and single quasiparticles are emitted in the outer channel. In this regime, the state is a coherent superposition of coherent states and not a simple sum. As we use a periodic square excitation, the electron emission is followed by hole emission corresponding to the dot reloading, with a repetition time $T = 1.10$ ns. It is actually in this configuration that the fate of the Landau quasiparticle is probed. Wigner function in the outer channel associated to these two signals are calculated before propagation and showed on figure 3.4. We have added rebound on the square drive to model imperfections of the RF lines; this issue is discussed in detail in section 3.4.2. This figure illustrates well the complementarity of these two signal: the first one is fully classical (no non classical value in the Wigner function) but has a short temporal extend and is thus suitable to probe fast dynamical events, on the other hand the second state has a wide temporal extend but is much closer to the single quasiparticle on top of a Fermi sea with a well defined energy ($\hbar\omega \approx 30\mu$eV).

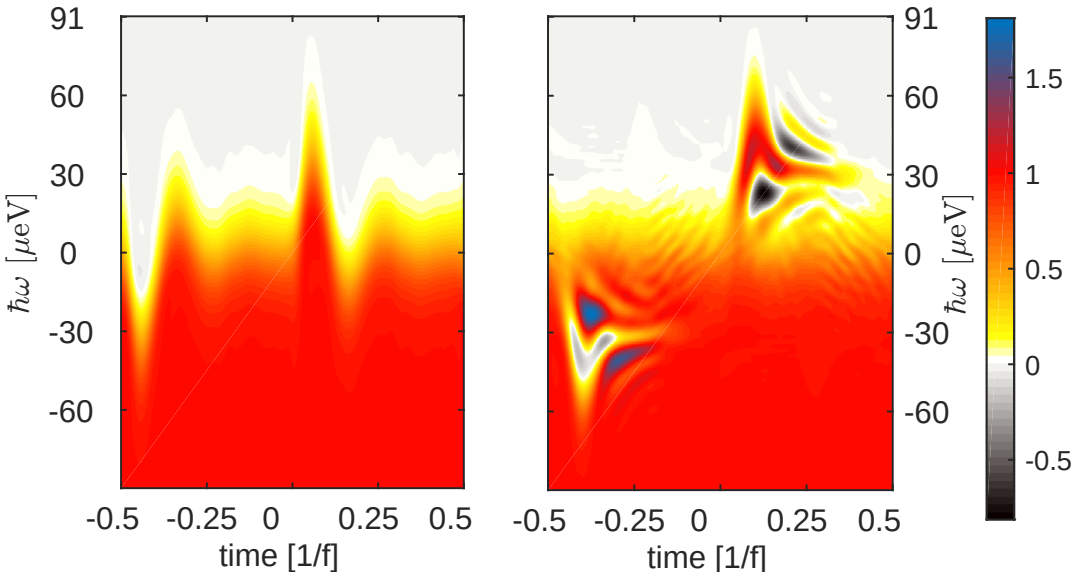

FIGURE 3.4: Wigner functions before propagation created on the outer edge channel in the two different configurations of interest. **Left.** A square drive with a rise time of 40 ps is applied on the top gate at 900 MHz when $D = 1$ with an amplitude of $\simeq 30\mu$V. **Right.** The same square pulse is applied but here $D = 0.3$. The electronic temperature is 90 mK.

3.2.2 Probing temporal width of the dip around $\delta\tau = 0$

Figure 3.5 shows the normalized HOM noise $\Delta q(\tau)$ for $D = 1$ (Fig.3.5.a) and $D \simeq 0.3$ (Fig. 3.5.b), both when the outer (orange points) or the inner (black points) channels are partitioned. From the outer channel partitioning, we probe the evolution of the generated electron pulse during propagation, inner channel partitioning results from the collective excitations generated by the interaction process. First we restrict ourselves to short delay τ. All the traces show a noise reduction (dip), which is reminiscent of two-particle interference. However significant differences are observed in the width of the HOM dips, labeled τ_w, which we estimate using an exponential fit. For $D = 1$, the outer channel dip is roughly twice larger than the inner one: $\tau_w = 80$ ps (outer) versus $\tau_w = 40$ ps (inner). The increased width of the outer channel dip reflects the fractionalization of the current pulse that splits into two pulses of the same sign (see Fig. 3.5c). The smaller width on the inner channel reflects the dipolar current trace (see Fig. 3.5c) and equals the temporal extension of the current pulse of a given sign (electron like or hole like), limited by the excitation pulse rise time.

For larger time delays ($|\tau| \simeq 100$ ps), the inner channel normalized HOM signal shows an overshoot above unity. As predicted in references [9, 225], $\Delta q(\tau) > 1$ occurs at finite temperature when an electron-like pulse collides with a hole-like one. At finite temperature, a hole wave function close to (but below) the Fermi level can have a non-zero overlap with electronic wave functions above the Fermi energy. This is possible

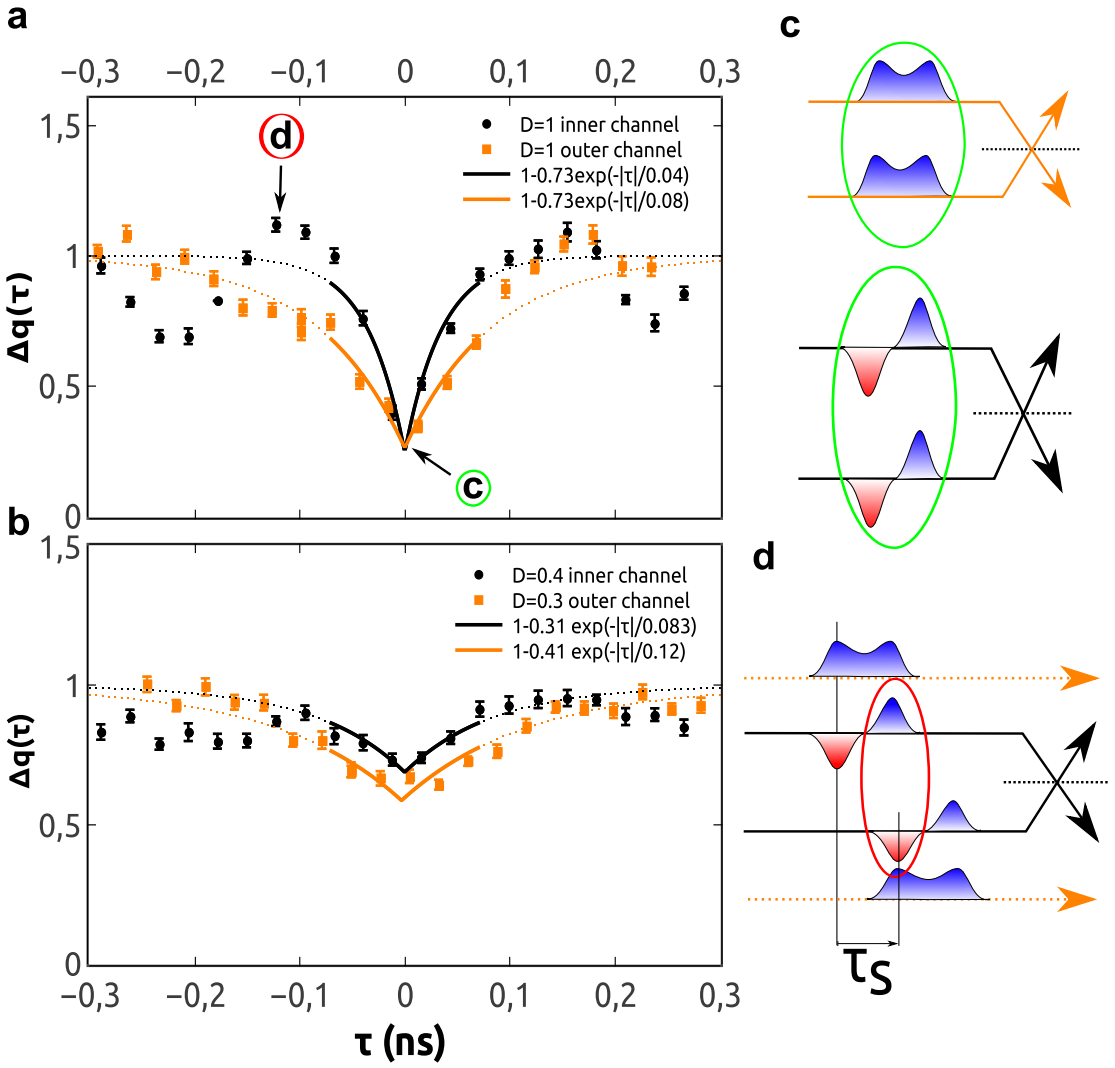

FIGURE 3.5: (**a**) $\Delta q(\tau)$ at $D = 1$ for outer (orange points) and inner (black points) channel partitioning. Error bars on **a** and **b** equal the s.e. of the mean reflecting the statistical dispersion of points. (**b**) $\Delta q(\tau)$ at $D = 0.3$ for outer (orange points) and inner (black points) channel partitioning. Encircled c and d refer to the sketches on **c** and **d**. The black and orange dashed lines on both the panels represent the fits of the dips using the following exponential dependence: $\Delta q(\tau) = 1 - \gamma e^{-|\tau|/\tau_w}$. The extracted values at $D = 1$ are $\gamma = 0.73$ (both for outer and inner channels) and $\tau_w = 40$ ps (inner channel) and $\tau_w = 80$ps (outer channel). At $D = 0.3$, we have $\gamma = 0.41$ and $\tau_w = 120$ ps for the outer channel and $\gamma = 0.31$ and $\tau_w = 83$ ps for the inner one. (**c**) Sketch of current pulses synchronization at $\tau = 0$ for the outer and inner channel partitioning. The outer channels are represented as orange lines, the inner as black lines. Negative (positive) charge pulses are represented by blue (red) colors. Pulses colliding synchronously are emphasized by green circles. (**d**) Sketch of inner and outer channel current pulses when the time delay between the sources is $\tau = \tau_s$. The inner channels (black lines) are partitioned while the outer ones (orange dashed lines) are not.

because the equilibrium Fermi distribution thermally populates states above the Fermi level which can then be depleted by a hole excitation. Thus an interference between an electron-like in input 1 and a Fermi sea combined with a hole-like excitation in input 2 can be thought of as the interference between an electron-like excitation in input 1 and a Fermi sea in input 2 with less occupied state above the Fermi level *i.e.* with a lower temperature for instance. "Lower" refers here to a comparison with the equilibrium Fermi sea distribution in input 2 when source 2 is turned off. Remember now that overlapping electrons give rise to noise reduction, therefore less overlap is synonymous with an increase of noise. Because the hole excitation contributes in reducing the overlap between the electron in input 1 and the Fermi sea in input 2 it diminishes the HOM effect *i.e.* it increases the noise. This can be related to the fact that the HBT noise is actually enhanced while lowering the electronic temperature, because there is less overlap between the electronic excitation in input 1 and the thermal excitations in input 2. This effect was also measured in [62].

This is why we can interpret the overshoot above 1 in the inner channel for $|\tau| \simeq \tau_s \approx 70$ ps, as the electron part of the inner channel current pulse in input 1 colliding with the hole part of the current pulse in input 2 (see sketch on Fig. 3.5d). This contrasts with the monotonic increase of $\Delta q(\tau)$ towards 1 for the outer channel and is a manifestation of the dipole nature of the excitation propagating in the inner edge. When the dot transmission is decreased to $D = 0.3 \pm 0.05$ ($D = 0.4 \pm 0.05$ for inner channel partitioning), we observe the expected increase of the HOM dip width compared with $D = 1$, reflecting the increase in the dot emission time: $\tau_w = 120$ ps (respectively $\tau_w = 80$ ps) for the outer (respectively inner) channel. As predicted in [225], the overshoot above unity disappears.

The dot to edge transmission are slightly different for outer ($D = 0.3$) and inner ($D = 0.4$) channel partitioning. Due to gate coupling, it is hard to tune the dot transmissions to the exact same values when the QPC voltage V_{QPC} is set to partition the outer or the inner channel. In the section 3.3, I detail this experimental difficulty and how I handled it.

3.2.3 Coherent effects at higher time delay τ

Further evidence of fractionalization can be observed on longer time delay $|\tau| \approx T/2$ when electron emission for source 1 is synchronized with hole emission for source 2 (or vice-versa). In this regime, $\Delta q(\tau)$ for $D = 1$, is plotted on figure 3.6 and exhibits again contrasted behaviors for the outer and inner channels. While it monotonically increases above 1 for the outer channel (see fig. 3.6a), as expected for electron/hole collisions, the inner channel shows an additional dip for $|\tau| \approx T/2 - \tau_s$ (see fig. 3.6b). This reveals

again the dipolar nature of the inner current: as the dipoles have opposite signs for electron and hole emission sequences, the electron parts of each dipole are synchronized for $|\tau| = T/2 - \tau_s$ (see sketch on Fig. 3.6d).

A quantitative description of the HOM traces can be obtained (black and orange lines) by simulating (see section 3.4) the propagation of the current pulse in the interaction region. The obtained current traces at the output of the interaction region (black and red dashed lines on fig. 3.13) reproduce the sketch depicted on figure 3.1. The good agreement obtained for the HOM trace supports the above qualitative descriptions of the dips observed at τ_s and $T/2 - \tau_s$ related to charge fractionalization. The additional spurious dip at $|\tau| \approx 350$ ps on the outer channel and $|\tau| \approx 225$ ps on the inner one comes from imperfections of the signal or interaction effects in the dot that we can take into account in our model (see section 3.4.2).

This only showed the charge fractionalization for edge-magneto plasmons. Figure 3.7 presents $\Delta q(\tau)$ at $D \approx 0.3$ in the single electron injection regime, for the full range of time shifts $-T/2 \leq \tau \leq T/2$. The qualitative behavior is similar to that of figure 3.6. In particular, the additional dip for $|\tau| \approx T/2 - \tau_s$ is only observed on the inner channel, which is a hallmark of single electron fractionalization. Compared with $D = 1$, its position is slightly shifted to lower values of $|\tau|$ ($|\tau| \approx 430$ ps), we attribute this difference to the larger width of the emitted current pulse related to the larger emission time.

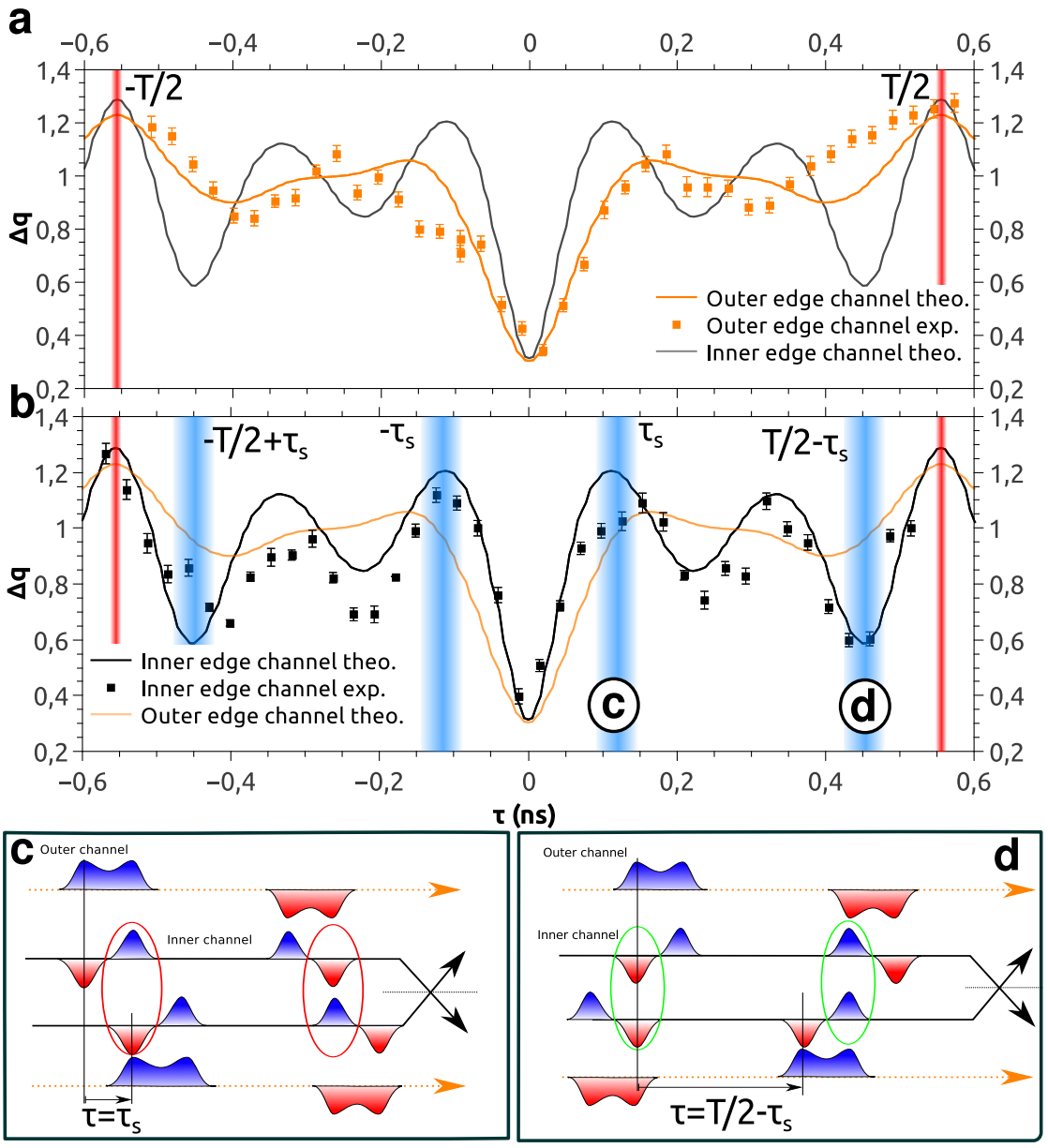

FIGURE 3.6: **a.** $\Delta q(\tau)$ at perfect dot to edge coupling $D = 1$ for outer channel partitioning (orange points). Error bars on both the panels equal the standard error of the mean reflecting the statistical dispersion of points. **b.** $\Delta q(\tau)$ at $D = 1$ for the inner channel partitioning (black points). The orange and black lines on both the panels are simulations for $\Delta q(\tau)$. The vertical red lines correspond to a time delay matching the half-period of the excitation drive: $\tau = \pm T/2$. Encircled c and d refer to the sketches on **c** and **d**. **c** Sketch of current pulses synchronization at $\tau = \tau_s$ for inner channel partitioning. The outer channels are represented as orange lines, the inner as black lines. Negative (positive) charge pulses are represented by blue (red) colours. Pulses colliding synchronously are emphasized by red circles (electron/hole collision in this case). **d** Sketch of current pulses synchronization at $\tau = T/2 - \tau_s$ for inner channel partitioning. Pulses colliding synchronously are emphasized by red circles (electron/electron and hole/hole collisions in this case).

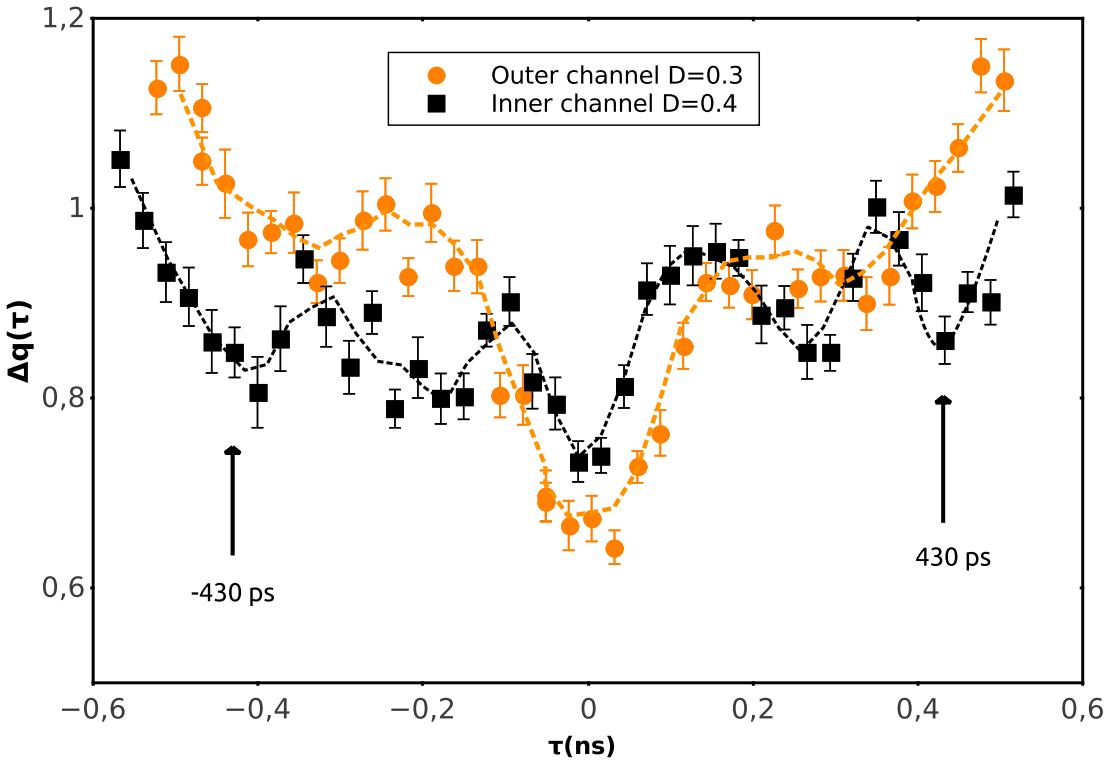

FIGURE 3.7: Full HOM interferometry at low transmission. Inner (black points) and outer (orange points) channels normalized HOM noise for the full range of time delays $-T/2 \leq \tau \leq T/2$. Error bars equal the standard error of the mean reflecting the statistical dispersion of points. The orange and black dashed line represent an interpolation of the data points. The arrows represent the position (averaged on the positive and negative values of τ) of the inner channel HOM dip for $\tau \approx T/2 - \tau_s$.

3.3 Managing electrostatic coupling between the gates

This part is rather technical and might interest starting PhD students who want to learn about subtleties of the simultaneous control of the single electron sources and central QPC. It requires a good comprehension of their functioning which is explained in section 2.2.2.1.

3.3.1 Parasitic coupling between gates

When we measure the first harmonic of the current I_Ω to calibrate the sources, the QPC is fully closed for source 1 but fully open (or at least transmitting the outer edge) for source 2. Between these two situations, V_{QPC} can change by 700 mV. From the situation where we partitioned the inner channel to the one where we partitioned the outer one it can change by 500 mV. This change will affect the electrostatic environment on the source and thus change their effective transmission D. For example, one working point V_{g2} that we might have chosen because it gave the desired D for source 2, with the QPC

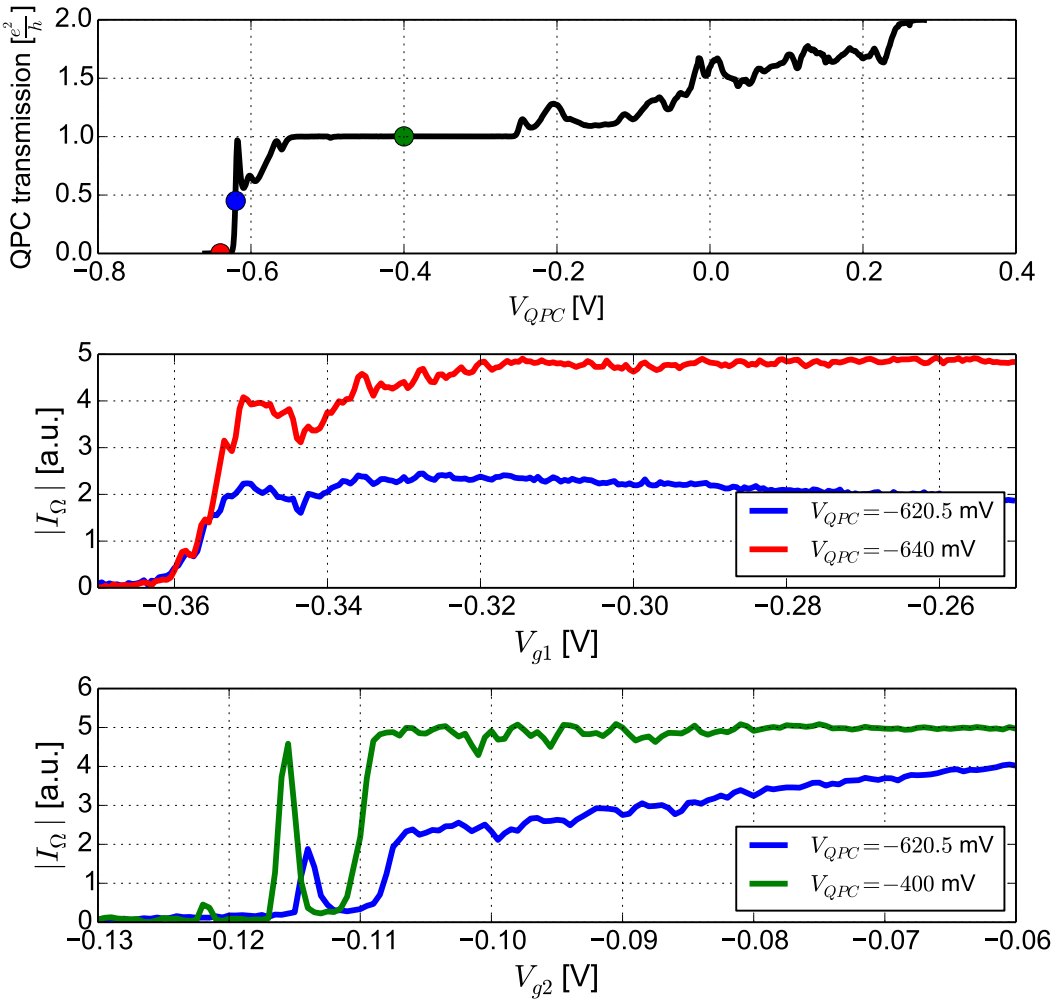

FIGURE 3.8: **Upper.** Transmission of the central QPC as a function of V_{QPC}. The red dot corresponds to the situation where all edge channels are reflected and thus enables to calibrate properly source 1 whereas the green dot corresponds to the situation where we calibrate source 2. The blue dot corresponds to the situation where we partition the outer edge. The color code is the same for the two lower panels. **Middle.** Modulus of the first harmonic of the current coming out of source 1 as a function of V_{g1}. Apart from a homothetic shift in amplitude coherent with a QPC transmission changing from 0 to $\simeq 0.5$, there is no visible change along the x-axis. This is because the induced change on source 1 by a 19.5 mV shift on V_{QPC} is very small.**Lower.** Same thing for source 2 but with different values for V_{QPC}. Here, the change in voltage is larger, so the shift is more visible. We can measure the 1.5 mV shift of the peak for instance. We deduce a coupling of $6.8 \times 10^{-3} V_{g2}.V_{\mathrm{QPC}}^{-1}$.

fully open to send all current to the RF detector, will give a different transmission and escape time when we will change V_{QPC} to partition the outer edge channel. Therefore we need to monitor the transmission of the dot during the HOM experiment. This is not really a problem for $D = 1$ because when dots are open there is a wide range of V_g that do not affect D anymore and a small electrostatic influence from V_{QPC} will not change D.

On figure 3.8, we show a measurement that illustrates the coupling between each source and the central QPC. The larger the difference in values of V_{QPC} between a calibration configuration and a partitioning configuration, the more this coupling is to be compensated carefully. On this figure, we can observe and measure this coupling which manifests as a shift of the x-axis. This shift is too small to be measured for source 1 (middle panel) because the change in V_{QPC} is not so large whereas we can clearly see it for the second source (lower panel). From 3.8, we deduce a coupling between V_{g2} and V_{QPC} of $6.8 \times 10^{-3} V_{g2}.V_{\mathrm{QPC}}^{-1}$. If we assume this coupling to be of the same order of magnitude for V_{g1} it would have given a shift of 0.13 mV. We could then assume that the amplitude of this shift is proportional to V_{QPC} and simply deduce how much we must shift V_{g1} or V_{g2} to get back to any desired value of D.

However, this last hypothesis is actually not valid. This was verified by measuring the shift in transmission of the central QPC for various V_g (see figure 3.9). Equal shift of V_{g2} does not give an equal shift of the transmission on the V_{QPC} axis. Therefore, for both sources, we have to measure the relation I_Ω versus V_g at each partitioning point we used ($V_{\mathrm{QPC}} \simeq -0.1$ V for inner partitioning and $V_{\mathrm{QPC}} \simeq -0.6$ V for outer). This is not precise because at half QPC transmission (for any channel), changing V_g will also affect V_{QPC} in return and thus the total transmitted current through the QPC. This is why we cannot directly compare the complex value I_Ω between two working points V_{QPC}. This explains why on the two lower panels of figure 3.8 the plateaus are not well defined for the two blue curves. Indeed, on these plateau regions ($V_{g1} \in [-0.32V, -0.25V]$ and $V_{g2} \in [-0.108V, -0.06V]$), the current directly coming out of the dot is constant as we vary V_g but because the latter influences back the electrostatic potential on the QPC, it changes R and thus the amount of this current sent to the detector.

3.3.2 The benefit of disorder

If we cannot rely on absolute values of $|I_\Omega|$, it is however possible to use remarkable features of these curves as points of reference. Indeed, the exact shape of $I_\Omega(V_g)$ contains fluctuations coming from electrostatic disorder surrounding the dots. We can observe that some of these features remain from one working point to another, although at a different place on the figure. If the signal is not too low[1], it is possible to find manually where this reference point moved and thus deduce a shift. One might be tempted for instance to use the small Coulomb peaks that easily appear when the amplitude drive is lower or higher than half of the dot level spacing. It is easy to spot them and to measure their shift along the V_g axis in different partitioning situations. This is not what we

[1]The worst situation is when we want to measure $I_{\Omega 1}(V_{g1})$ for the inner channel partitioning.

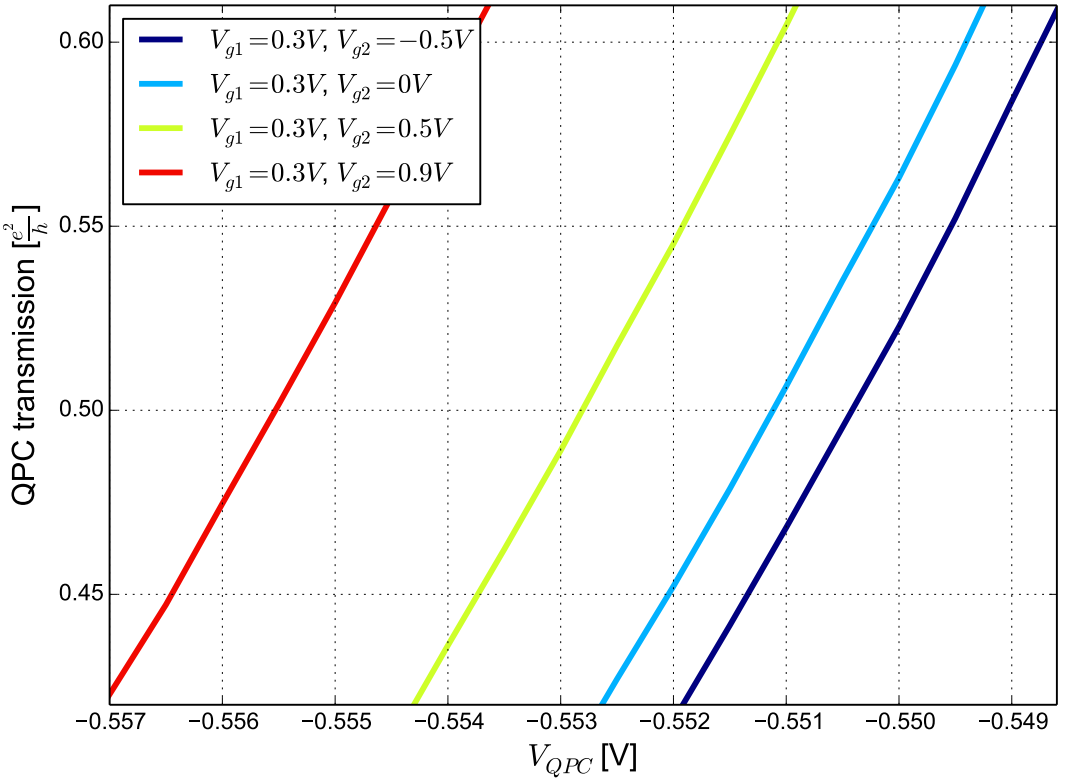

FIGURE 3.9: Zoom of the conductance of the central QPC as a function of V_{QPC} around transmission 0.5. We see that successive decreases of V_{g2} by 500 mV does not shift the curve by the same amount. The last shift of 400 mV (going from V_{g2} = 500 mV to V_{g2} = 900 mV) gives an even larger shift of curve. Thus the coupling between these two gates is not linear.

chose to do because the position of this peak actually has a non trivial dependence on V_g.

Indeed, the local electrostatic potential shift on the source does not only change the transmission D but also the internal chemical potential of the dot μ_{dot}. As we have seen in section 2.2.2.1, μ_{dot} will affect the position of the peak independently of D. Our choice was then to identify the closing of the dot: $D \to 0$. This point is independent of μ_{dot} but can be hard to detect if the signal-to-noise ratio is to small. However, we can partially circumvent this by increasing the excitation amplitude which will not affect the position of the closing. One last drawback of this method is that this feature can be less sharp than a Coulomb peak which makes the measurement less accurate, especially when we measure the closing of source 1 in the inner channel partitioning situation (see figure 3.10). This gives the first correction to apply on V_g to get back to the expected value of D. However this correction will affect in return the relation between the central QPC reflection R and V_{QPC} so we have to measure R back again with the 2 newly corrected values for V_{g1} and V_{g2}. This will give a new working value for V_{QPC} which will shift again

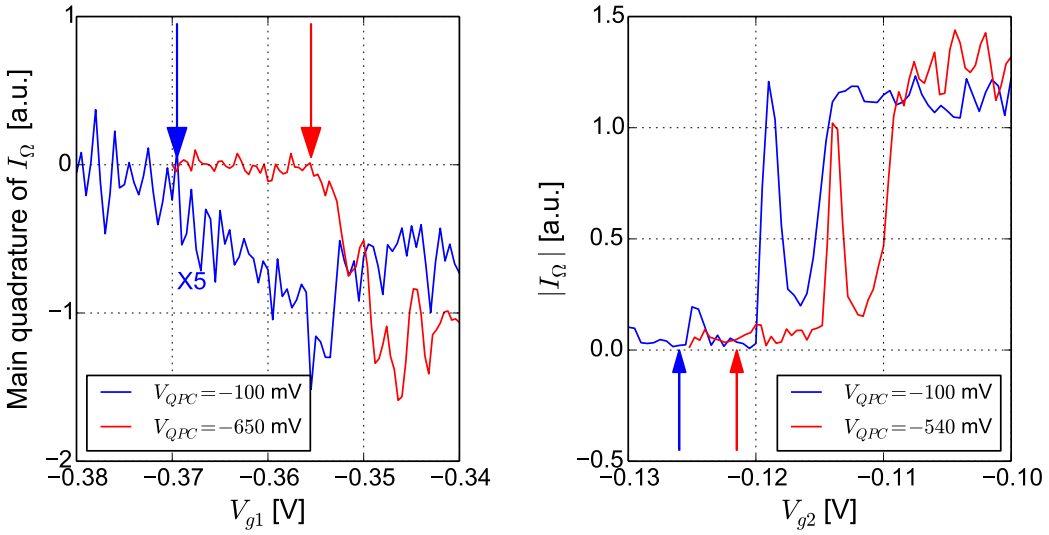

FIGURE 3.10: Illustration of the iterative method first measurements to find a working triplet point $V_{\mathrm{QPC}}, V_{g1}, V_{g2}$. **Left.** Main quadrature of $I_{1\Omega}$ as a function of V_{g1} when the QPC is fully closed (red) and when inner channel is partitioned (blue line is multiplied by 5). The signal is small because almost no current, apart from parasitic coupling, is injected from the dot to the inner edge. Part of this current also comes from capacitive coupling between edges. **Right.** Here the current is large enough so we can plot the modulus of $I_{2\Omega}$ as a function of V_{g2}. Arrows represent V_g values we chose as the closing of the dots. From both figures, we deduce we have to apply a shift of 14 mV for source 1 and 4.5 mV for source 2 to the initial values of V_g corresponding to $D \approx 0.4$.

(but less) V_{g1} and V_{g2} that we will have to measure and compensate. This operation is iterated until convergence. Usually, only a couple of times is enough.

All of these efforts can occasionally be destroyed by global drifts of charge impurities which locally change the electrostatic potential and thus the relations $D(V_g)$ or $R(V_{\mathrm{QPC}})$. Luckily, this drifts are not too frequent on the time scale of an HOM acquisition but force us to regularly check working points of the sources and central QPC and, if need be, go all over this fine tuning process.

This part explained why it was difficult to be precise in the control of D for the inner partitioning situation but not why we could not manage to have the same dot transmission for inner and outer partitioning. This has a more trivial explanation. To insure an injection of holes and electrons symmetric in energy ($\omega_e = -\omega_h$) we lowered the excitation amplitude during the calibration procedure so as to locate Coulomb peaks that appear precisely when the injection is symmetric. As we have seen above, the inner chemical potential is partly independent of the dot transmission. At that time of the experiment we had little control on the dc part of the top gate voltage because we had not set the cryogenic bias-tee yet. Therefore, we had little direct control on μ_{dot} which was then mainly controlled by V_g which also changes D. It appeared that in between the two partitioning situations the electrostatic disorder around the dots changed slightly, thus we

had to choose other peaks of interest. The closest similar transmissions D associated to a peak were not exactly the same from inner ($D \approx 0.4$) to outer partitioning ($D \approx 0.3$).

3.4 Analysis with plasmon scattering formalism

3.4.1 Modeling interactions

In this section we will explain the formalism that helped us to calculate and predict the shape of the current and the HOM figures after a propagation length l, in the case where we directly excite EMPs *i.e.* when the dot is fully open ($D = 1$). This formalism was first introduced in references [202, 210] and fully detailed in the chiral case of filling factor $\nu = 2$ by Ch. Grenier [226], E. Bocquillon [3] and V. Freulon (in french) [107] in their respective thesis manuscript. I will use the main results that concern my measurements.

In this model, there are two incoming currents (one for the outer and one for the inner channel) entering an interacting region (see figure 3.11) and two outgoing currents also corresponding to the outer and inner channels. The outer outgoing channel can be expressed as a linear combination of the two input currents, the same goes for the inner channel. Thus we can describe the interaction region as a scattering matrix. All the details of the interaction model are encoded in this matrix. The first most natural assumption one can make is that the plasmons interact elastically thus the matrix S_{EMP} will not mix frequencies. We can thus focus our reasoning at finite frequency ω without any loss of generality. The relation between outgoing currents after a propagation length l and the incoming ones at position 0 writes:

$$\begin{bmatrix} I_1(\omega, x = l) \\ I_2(\omega, x = l) \end{bmatrix} = S_{EMP}(\omega) \begin{bmatrix} I_1(\omega, x = 0) \\ I_2(\omega, x = 0) \end{bmatrix} = \begin{bmatrix} S_{11} & S_{12} \\ S_{21} & S_{22} \end{bmatrix} \begin{bmatrix} I_1(\omega, x = 0) \\ I_2(\omega, x = 0) \end{bmatrix} \tag{3.2}$$

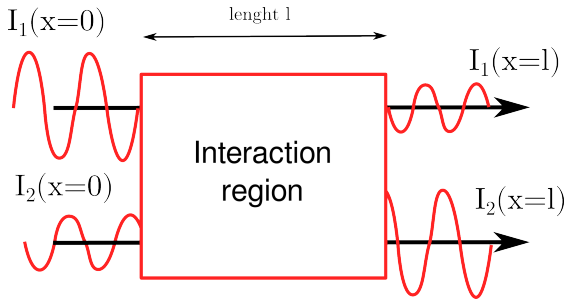

FIGURE 3.11: Scheme of the model. The region where pulses are created is separated from the region in which they interact, itself also separated from the interferometer where the signals are analyzed.

where we labeled 1 the outer edge and 2 the inner one. The fractionalization process can be understood as S_{EMP} having non-zero off-diagonal elements which will mix the currents from both edges. When there is no interaction, a charge injected on the outer edge stays unchanged on it and travels the region with velocity v_1. At $x = l$, all the current injected in the outer edge at $x = 0$ is recovered, therefore $S_{11} = 1$ and $S_{12} = 0$. We can apply the same reasoning for the inner channel and conclude that in the non-interacting case S_{EMP} is the identity (multiplied by $e^{i\frac{\omega l}{v}}$, where v is the bare velocity). On the contrary, in the strong interaction case, the two channels are highly coupled therefore we can guess that the off-diagonal elements will be non negligible. The interaction is also strong enough to blur any asymmetry coming from microscopic disorder so we can safely conclude that in the strong interaction regime $S_{21} = S_{12}$. To find out the correct eigenmodes and eigenvelocities, one has to diagonalize the symmetric matrix S_{EMP}.

To be more quantitative and calculate S_{21}, one has to use bosonisation to express the problem in terms of scattering of bosonic fields ϕ which represents collective modes. The bosonic field ϕ can be expressed as a function of the fermionic one Ψ [227]:

$$\Psi^\dagger(x,t) = \frac{U^\dagger}{\sqrt{2\pi a}} e^{i\sqrt{4\pi}\phi(x,t)}, \tag{3.3}$$

where $U^\dagger$ is an operator which lowers the number of electrons by one to ensure fermionic anitcommutation relations and a is a short distance cutoff. Interactions are easier to treat using ϕ than Ψ. We can decompose the bosonic field as:

$$\phi(x,t) = \frac{-i}{\sqrt{4\pi}} \int_0^\infty \frac{d\omega}{\sqrt{\omega}}\, \hat{b}(\omega) e^{i\omega(x/v_F - t)} - \hat{b}^\dagger(\omega) e^{-i\omega(x/v_F - t)} \tag{3.4}$$

where $\hat{b}(\omega)$ is the annihilation boson field operator at frequency ω and v_F the Fermi velocity. Actually the bosonic modes are easily described by the charge density and the current:

$$\rho(x,t) = \frac{-e}{\sqrt{\pi}} \partial_x \phi(x,t) \tag{3.5}$$

$$i(x,t) = \frac{e}{\sqrt{\pi}} \partial_t \phi(x,t). \tag{3.6}$$

The Hamiltonian on one edge α between position $x = 0$ and $x = l$, writes in the bosonic representation [181, 228]:

$$\mathcal{H}_\alpha = \hbar v_F \int_0^l dx \left(\partial_x \phi_\alpha(x,t)\right)^2 + \frac{e^2}{2\pi} \int_0^l dx \partial_x \phi_\alpha(x,t) u_\alpha(x,t) \tag{3.7}$$

The first term of the equation correspond to free propagation of the bosonic field and the second term to interactions with $u_\alpha(x,t)$, the electric potential in channel α at position x and time t. From this we can deduce the equation of motion (in time or frequency

domain):

$$(\partial_t + v_F\partial_x)\,\phi_\alpha(x,t) = \frac{e\sqrt{\pi}}{h}u_\alpha(x,t) \tag{3.8}$$

$$(i\omega + v_F\partial_x)\,\phi_\alpha(x,\omega) = \frac{e\sqrt{\pi}}{h}u_\alpha(x,\omega), \tag{3.9}$$

where one can recognize on the left-hand side a right moving chiral wave equation at velocity v_F and a source term in the right-hand part. Interactions will be conveyed by this term. Indeed, $u_\alpha(x,t)$ will depend on the electromagnetic environment and in particular on the surrounding distribution of charge ρ. The exact dependence will dictate the physical model for interaction. To implement this model, we state that there is no tunneling from one edge to another, which is valid because the two co-propagating edges have opposite spin polarization and during the 3μm propagation spin flip events are negligible[2]. It can be verified by measuring that there is no noise on a plateau (the outer channel is transmitted perfectly and the inner one reflected). Indeed, if there is tunneling from one edge to another, it induces partitioning and thus shot noise even when channels are perfectly reflected or transmitted. This is not what we observed.

From here, to solve completely the equation of motion, one needs to express u_α in terms of ϕ_α. This is where different kind of microscopic models can be imagined. A few of them have been developed and the corresponding equation of motion derived in [3, 107, 226] and also in appendix B. After some more or less simple algebra, one gets a relation between $\phi_\alpha(l,\omega), \phi_\beta(l,\omega)$ and $\phi_\alpha(0,\omega), \phi_\beta(0,\omega)$ *i.e.* S_{EMP} which, because of relation 3.6, is the same for current I_α and ϕ_α. Based on reference [221] we are going to make the following assumptions to build our scattering matrix:

- The strong interaction regime is achieved.
- The square signal that we use has a fundamental frequency at 0.9 GHz so the dominant harmonics are below 6 GHz, therefore we can restrict ourselves to a short range interaction model because the propagation length from the source to the QPC is smaller than the typical plasmon wavelength.
- There is little dissipation.

Thus we can use the results derived in B.2 to which we add a small dissipation term:

$$S_{11}(\omega) = \frac{1 + e^{i\omega\tau_s - \gamma(\omega)}}{2} \tag{3.10}$$

$$S_{21}(\omega) = \frac{1 - e^{i\omega\tau_s - \gamma(\omega)}}{2}, \tag{3.11}$$

[2]This might be questioned for longer l or if one wants to study this phenomena at $\nu = 3$.

where $\tau_s = l/v_-$ and $\gamma(\omega) = \omega^2\tau_s\tau_r$ is a phenomenological term introduced to model dissipation of EMP. The term $e^{i\omega\tau_s} = e^{i\omega l/v_-}$ shows that the charge injected on the outer channel will, after a fixed propagation length l, oscillate with ω between the two channels. For $\omega = \pi v_-/l$, the charge is completely transferred to the inner channel. According to our HOM experiment (and [221]) we can set $\tau_s = 70$ ps and $\tau_r = 4$ ps. Actually, here we do not use really high frequencies and are thus less sensitive to dissipation. As we will see later, the change induced in the predicted HOM shape, taking dissipation into account or not, is very small and below our resolution (see for instance lower panel of figure 3.13) but we preferred to take it into account in our simulations.

We now have a quantitative way to predict what comes out in the two channels after the interaction region for any input mode $\phi_1(\omega)$ on the outer channel. We must here stress out the fact that it is possible to easily predict the out-coming modes and thus the interference patterns only if we are able to describe our incoming state as a Fourier sum of bosonic modes $\phi(\omega)$. This is the case for $D = 1$ where the top gate is capacitively coupled to the outer edge ($\phi(\omega) \propto V(\omega)$ [226]) and emits a coherent state for plasmons. It is no longer true when we start to pinch the gates V_g. Indeed, as we will see in chapter 4, for $D < 1$ the state at $x = 0$ is a coherent superposition of plasmons and it is less straightforward to describe the state after propagation at $x = l$ in terms of bosonic modes.

Thanks to equation 3.6, we can recover this mode if we know the current intensity at $x = 0$. Because the equation of motion are linear in ω we can predict the outgoing currents for any linear combination of $I_1(\omega)$ coming out of the source. More precisely, we calculate the two output currents after interaction. They are then treated independently as being injected in a non-interacting wire by an Ohmic contact driven with $V(t) = I(t)R_K$. The voltage being known, it is straightforward to compute the coherence functions and the Floquet coefficients c_n (see appendix A.3) coming in both inputs of the beam splitter and thus the full HOM figures and the Wigner functions.

3.4.2 Modeling the exact pulse shape at the sources

3.4.2.1 *Ad Hoc* imperfect square pulse

On the bottom part of figure 3.12, the expected HOM figure for a perfect square voltage applied on the dot at $D = 1$ for both partitioning situations is represented. It does not really look like our results, in particular we observe additional oscillations compared to this prediction. These oscillations can be explained by the imperfect square voltage sequence as the one plotted on the insert of the upper part of the same figure. To drive

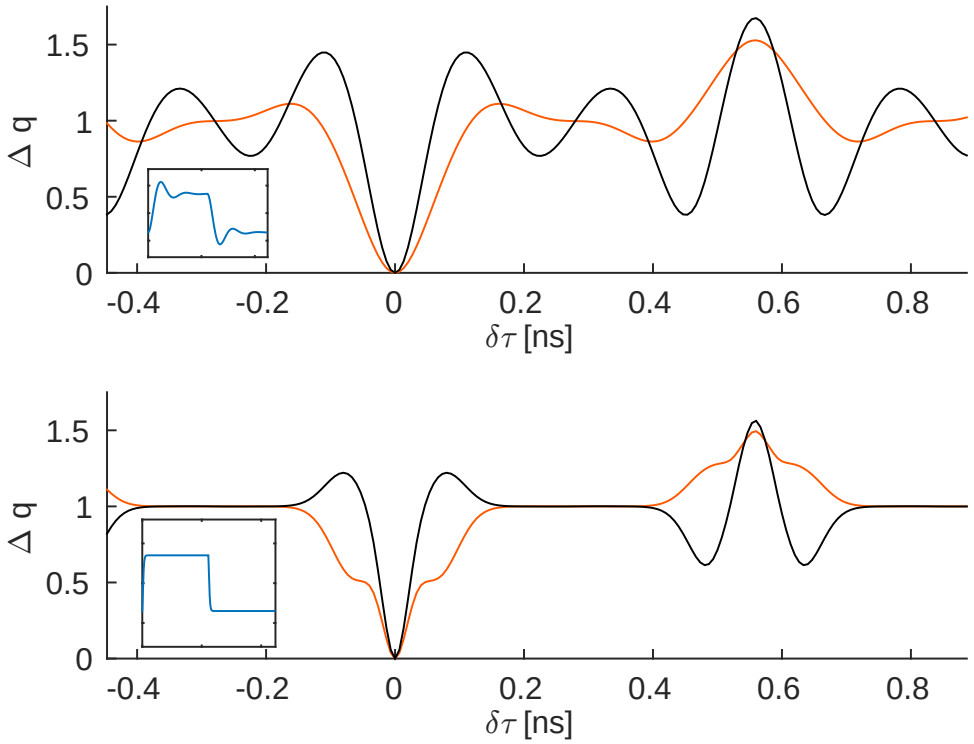

FIGURE 3.12: Comparison of the theoretical HOM figures after interaction for a perfect square (bottom) and the one that fitted best our data (upper). Black lines correspond to inner edge partitioning and orange lines to outer edge partitioning. In the inserts are represented the shape of the square pulses. Both drive sequences are at 0.9 GHz, with an amplitude of 60μV. The electronic temperature is 90 mK.

the dots we used an *Anritsu MT1810A* which has a rise time of 30 ps that is not negligible compared to a half period of 555 ps. The resulting square sequence is not perfect and will influence the current pulse injected in the outer edge channel at $x = 0$. Because at $D = 1$, the top gate is capacitively coupled to the outer edge we can compute this pulse with a simple RC filter:

$$I(\omega) = V(\omega)\frac{i\omega\frac{e^2}{\Delta}}{1 - i\omega\frac{h}{2\Delta}}, \tag{3.12}$$

where the RC time (neglecting interactions in the dot) is $\frac{h}{2\Delta}$ and $\frac{e^2}{\Delta}$ the capacitance between the top gate and the outer edge. Then we can use formula 3.10 to calculate the resulting currents on both edges at $x = l$. We can observe on figure 3.13 that the resulting currents on each channel after interaction have themselves rebounds which explains the ones observed on the HOM figure.

On figure 3.14 the signal coming out of the generator with the same frequency and amplitude used for the HOM experiment is shown. It is compared to the same physical signal after 3 meters of SMA RF cables and to the simulated signal that best fitted our HOM data. The shape of the physical signal does not look at all like a Fourier sum

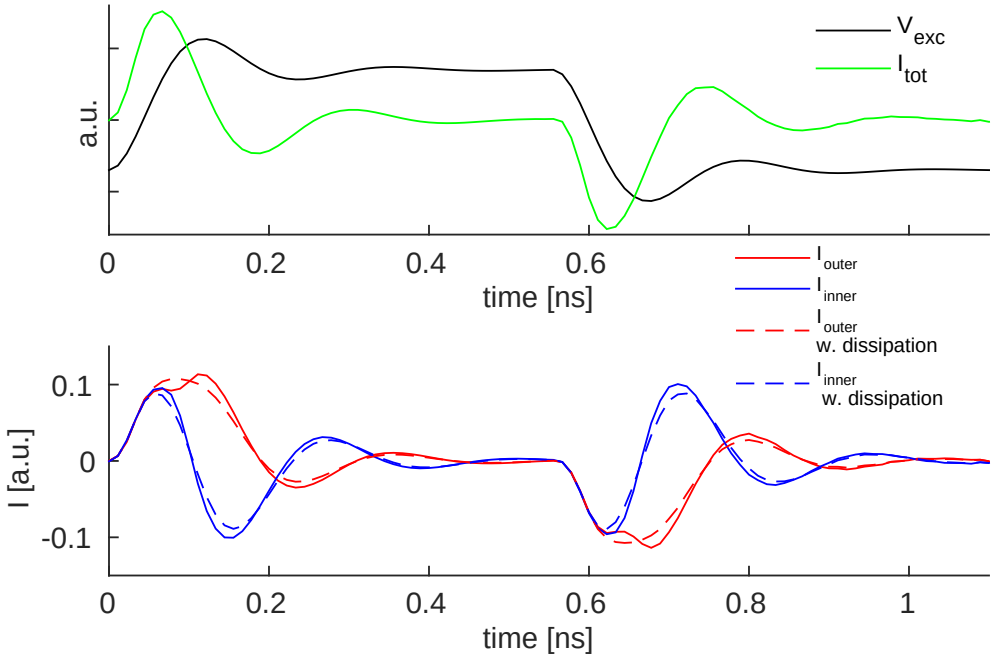

FIGURE 3.13: **Upper.** Voltage drive and total current at the exit of the source that best fitted our data. **Lower.** Resulting current pulses on the outer (red) and inner (blue) channel after interaction with (plain line) or without dissipation (dashed line).

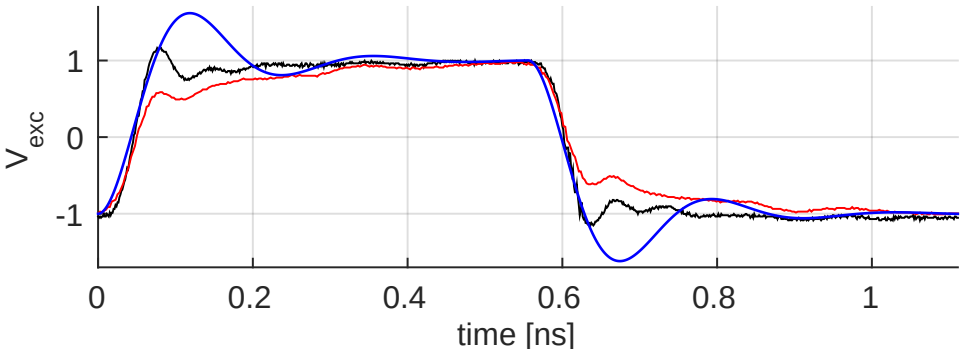

FIGURE 3.14: Measured square sequence at 0.9 GHz coming out of the *Anritsu MT 1810A* in black line. The red line represents the same signal measured after 3 meters of SMA RF cables at room temperature. The blue line corresponds to the imperfect square sequence that gave, after interaction, the best agreement with HOM data on the inner edge channel.

approximation of a square:

$$V(t) = \sum_{n=0}^{N} \frac{4}{\pi(2n+1)} \sin\left((2n+1)\Omega t\right) \tag{3.13}$$

with N a finite integer (typically 3), but rather like a succession of second order responses to a step function with damping, that can thus be modelled (for each half-period) by:

$$V(t) = 2V_{\text{exc}}\left[\left(1 - \frac{e^{-tz\omega_N}}{\sqrt{1-z^2}}\cos\left(t\sqrt{\omega_N^2\left(1-z^2\right)} + \arcsin(-z)\right)\right)\theta(t) - 0.5\right]. \tag{3.14}$$

Here, $\theta(t)$ is the Heaviside function, z controls the damping *i.e.* the amplitude of the extra oscillations and ω_N controls the number of oscillations which is related to the pulse rise time. The parameters that best fitted our HOM data after interactions are $z = 0.35$ and $\omega_N = 5\Omega = 2\pi \times 4.5$ GHz.

Although the agreement with HOM is quite good, the drive sequence does not really match what we observe on top of our cryostat. The black and red lines of figure 3.14 which are closer to a square sequence, cannot account for the observed additional rebounds on the inner edge even when we add numerical filtering to model the loss along the RF cables. We tried also to add random resonances in the model for the RF line but it only caused too much distorted signals with too high and too many rebounds. This *ad hoc* imperfect signal explains well our HOM data but it is hard to justify where those imperfections come from. In the next part we explore a model that can potentially explain these rebounds.

3.4.2.2 Interactions induced current oscillations

It is not really satisfying to account for the observed additional rebounds with unreasonable imperfections of the sources or the RF injection lines. Close to the end of my PhD we became aware of a new study by Litinski *et al.* [229] which solves the non-equilibrium response of an abrupt change of gate voltage on the dot close to $D = 1$ taking electron-electron interactions into account. In particular they show that for strong interactions, the abrupt change in voltage does not emit a single exponential current pulse but rather a series of successive pulses with decaying amplitudes. Indeed, because of interactions in the dot, the admittance of the source, relating the charge dynamics to the applied voltage, is not the one of a simple RC circuit. The effect of interactions on the charge dynamics has also been studied in the opposite regime $D \ll 1$ in references [230, 231]. Büttiker *et al.* also showed that, whatever the transmission of the resistive mode D, the admittance of the capacitor has a universal resistive part of $h/2e^2$ [232]. This universal

quantization is the AC equivalent of the quantization of DC conductance by steps of e^2/h and has been measured in references [1, 233]. However, this theoretical proof was done in the non-interacting case; it was later extended to the interacting case [234**?** –236]. For instance C. Mora and K. Le Hur showed in a non-perturbative approach that this universal value is still valid but only when the AC excitation is lower than Δ [235] which is true in our case. From it they also rewrote the admittance in the case $D = 1$:

$$\mathcal{A}(\omega) = C_g \left(1 - \frac{i\omega\tau_c}{1 - e^{i\omega\tau_f}}\right)^{-1} \tag{3.15}$$

where C_g is the geometric capacitance of the dot and we defined the two time scales of the problem τ_F and $\tau_c = hC_g/e^2$. τ_F corresponds to the time of flight spent in the dot. It is related to the electronic density of states. The lower it is, the higher the density is. On the contrary, τ_c quantifies the Coulomb interaction in the dot. For high ratio of τ_F/τ_c, the Coulomb energy to add an electron is larger than the spacing in energy imposed by confinement.

In all the experiments and calibration presented so far we can only access the total RC time:

$$\tau_{RC} = \frac{1/2}{1/\tau_c + 1/\tau_F}. \tag{3.16}$$

Thanks to the calibration presented in section 2.2.2.3 we can estimate $\tau_{RC} = 17$ ps. To estimate the relative weights of each contribution, or equivalently the ratio τ_F/τ_c one can look at the fine dependence of the escape time with V_{exc} in the non-linear regime. During their respective PhD work, Gwendal Fève and François Parmentier [5, 7] showed that, for similar samples to ours, the charging energy was smaller or equal to the spacing imposed by confinement Δ, conversely it means $\tau_F/\tau_c \lessapprox 1$. In our case, the level spacing is a bit lower (1.4 K instead of 4 K) but the electronic density of the gas is the same ($1.9 \times 10^{11}\text{cm}^{-2}$ for both case) therefore we might expect an increased value for τ_F/τ_c and therefore deviation from the simple RC model.

We applied a fitting procedure on τ_F (τ_c is fixed by equation 3.16 for a fixed value of $\tau_{RC} = 17$ ps). The voltage applied on the dot is chosen with a finite rise time of 30 ps and no rebound ($z = 0.9$, $\omega_N = 11 \times \Omega$). The electronic temperature is 90 mK. With the calculated charge time dependence we can calculate the total current out of the dot and then the two output currents at the level of the QPC (with interaction parameters $\tau_s = 70$ ps and $\tau_r = 4$ ps). Results are presented on figure 3.15. We computed the difference between data and model varying τ_F. This difference has 3 possibly equivalent (but well pronounced) minima at τ_F =136, 201 and 351 ps. However, the latter seems reasonably too high and was not kept. Results are plotted on figure 3.16. Although there is no rebound on the square voltage sequence, these results seems to reproduce

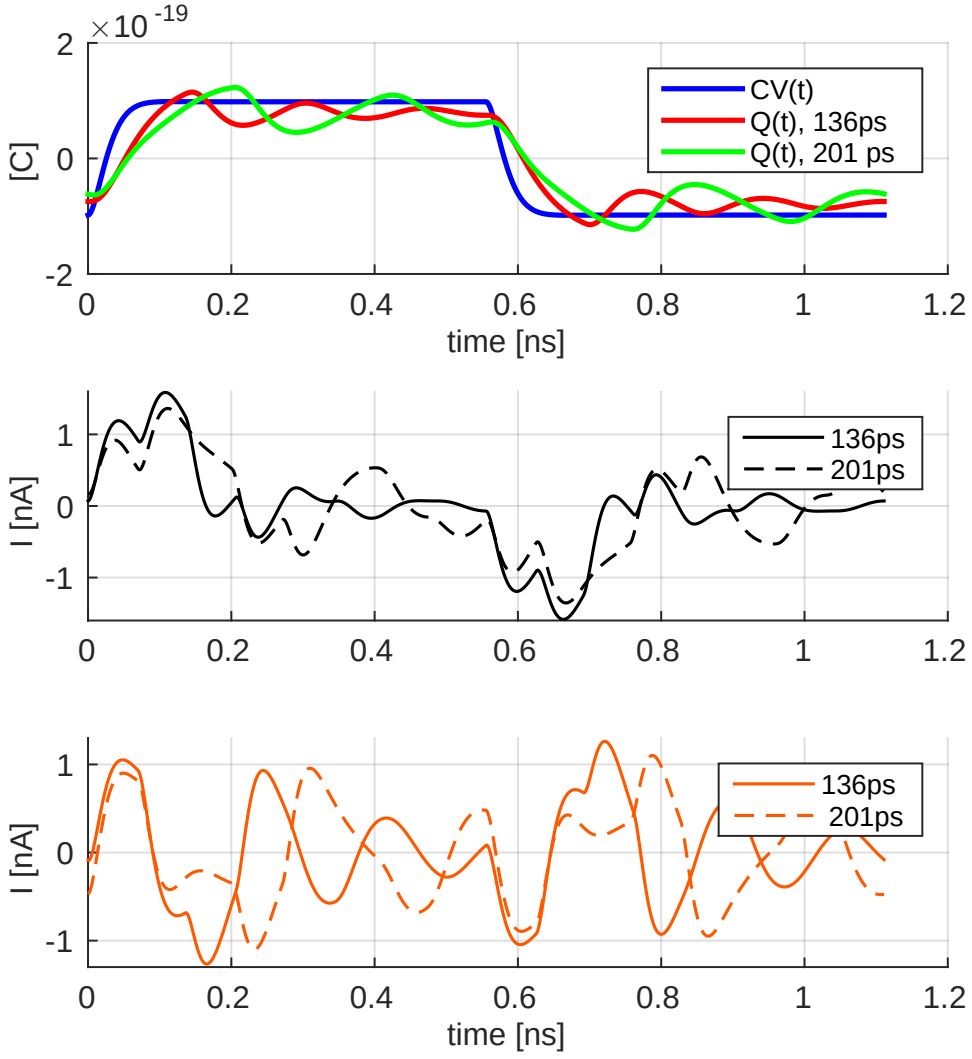

FIGURE 3.15: **Upper** Square pulse applied to the dot (blue) with a rise time of 30 ps ($z = 0.9$, $\omega_N = 11 \times \Omega$) and charge in the dot deduced with the model from [229] with parameters $\tau_{RC} = 17$ ps and $\tau_F = 136$ ps (red) and 201 ps (green). **Middle** Outer currents, after 3 μm interaction length, deduced from the charge evolution in the dot. **Bottom** Inner currents, after 3 μm interaction length, deduced from the charge evolution in the dot.

the additional rebound observed around $|\tau| \approx 250$ ps on the inner channel partitioning situation. For $\tau_F = 136$ ps, the additional rebound appears a bit too early; however the depth of the additional dips at $|\tau| \approx 450$ ps matches better than the other two values of τ_F. For any figure, all electron-hole interference overshoots are always slightly over-estimated. Prediction with $\tau_F = 201$ ps seems to reproduce the slight decrease of noise observed on the outer edge going from $|\tau| \approx 150$ ps to $|\tau| \approx 400$ ps. Overall the agreement is quite good and points out the fact that the ratio τ_F/τ_c is larger than one. Indeed, with this model we could not observe any additional rebound around $|\tau| \approx 200$ ps for $\tau_F < 100$ ps *i.e.* for a purely non-interacting dot. The two values of τ_F (136 and

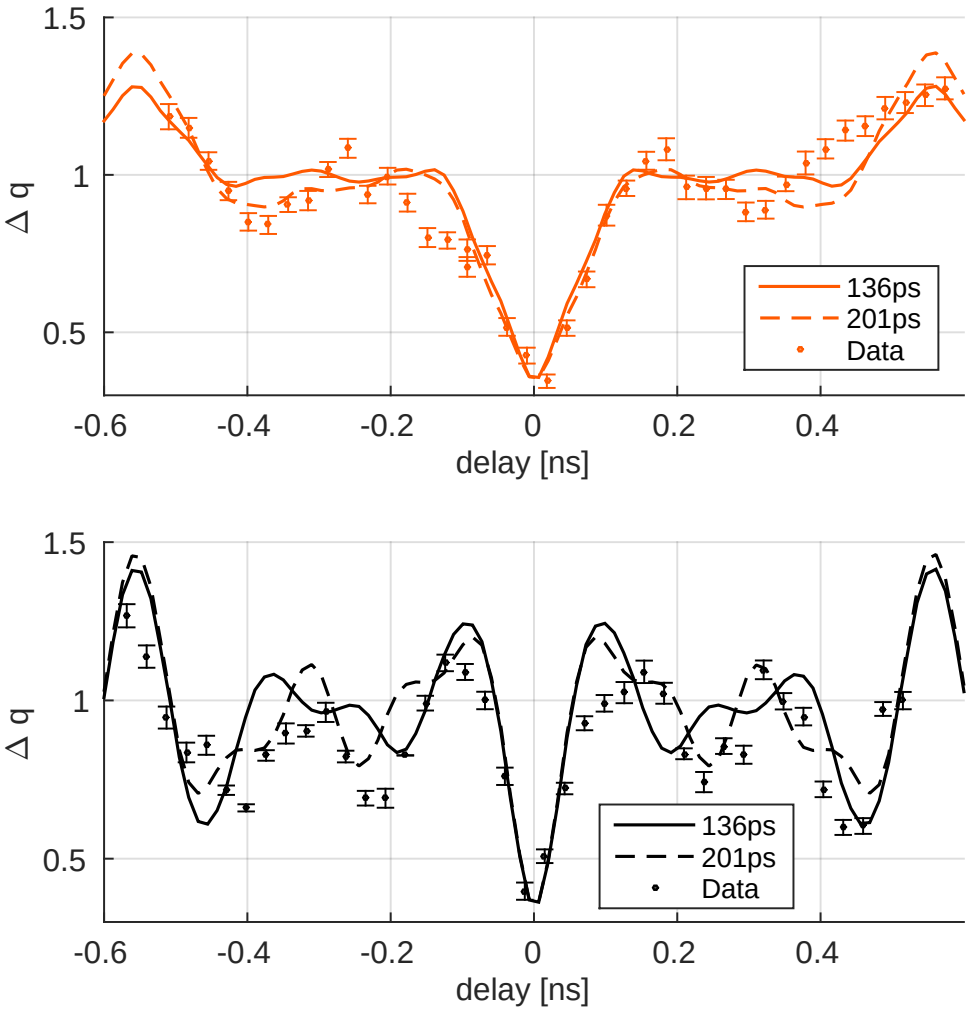

FIGURE 3.16: **Upper** Comparison of HOM figures at 90 mK for outer channel with parameters $\tau_{RC} = 17$ ps, $\tau_F = 136$ ps ($\tau_F/\tau_c = 3$) and 201 ps ($\tau_F/\tau_c = 4.9$). **Bottom** Idem for inner channel partitioning.

201 ps) respectively give a ratio τ_F/τ_c of 3 and 4.9.

This results show that Coulomb interactions in the dot cannot be neglected if one attempts to account for the fine structure of the HOM figure. With this model we have been able to accurately describe the whole interference pattern. The remaining little discrepancies can be explained by slight asymmetries between the two sources which breaks the symmetry of the pattern $\tau \to -\tau$.

3.4.3 Comments on the depth of the dips

Until now I have intendedly been elusive on commenting the depth of the observed dips. If the overlap between the incoming states is perfect we should obtain $\Delta q(\tau = 0) = 0$

which is not what we observed! For instance, on figure 3.5 we observe a dip going to 0.27; we defined a parameter γ to fit with the exponential ($\Delta q(\tau) = 1 - \gamma e^{-\tau/\tau_e}$); γ is actually the visibility of the interference. When no dip is visible, there is no two-particle interference and $\gamma = 0$. When, $\gamma < 1$ there must be decoherence mechanisms at stake to kill the interference pattern. The next chapter is devoted to the exploration of such possible mechanisms; the expert reader may have already guessed that fractionalization is one them. However, we will see that this mechanism cannot account for the loss of visibility at $D = 1$ (others can). In this chapter, to adjust the plotted data with the plasmon scattering theory we had to do the transformation:

$$\Delta q \to 1 + \gamma\,(\Delta q - 1)\,, \tag{3.17}$$

where γ is measured with the depth of the dip ($\gamma = 1 - \Delta q(\tau = 0)$). This transformation has been applied to all the theoretical results presented in this chapter with $\gamma = 0.65$ for both edge partitioning situations.

Conclusion to this chapter

In this chapter we have introduced charge fractionalization which is an effect that appears in all one dimensional systems with interactions. With the HOM interferometer we have addressed this effect in the time domain for two regimes of emission: collision of edge-magneto plasmons ($D = 1$) and collision of single electrons and holes ($D \approx 0.3$) [237]. We extracted from it an interaction strength parameter ($\tau_s = 70$ ps) compatible with previous measurements [221] and revealed the dipolar nature of the excitations created in the inner edge channel. In the $D = 1$ case and with the help of a plasmon scattering theory, we have been able to study the fine details of the interference pattern; in particular we confronted our data with a model taking interactions in the dot into account. The comparison is quite satisfactory, although two values of the ratio of Coulomb energy over confining spacing energy could explain our data. This ratio can be 3 or 4.9.

Chapter 4

Single electron decoherence

"Mais le contexte est plus fort que le concept."

MC Solaar, "La Belle et le Bad Boy".

We finished the previous chapter commenting on the fact that the Pauli dip did not go to 0 at $\tau = 0$. This is a sign that the interference is not perfect and some coherence is lost in the process. In this chapter we are going to study all possible sources for decoherence and determine their relative weights. We will show that Coulomb interactions with the neighboring co-propagating edge channel is the strongest among all. We are going to see the effect of this decoherence mechanism on *single* electron states. The plasmon scattering model we have developed in the previous chapter (see section 3.4) will enable us to describe the loss of visibility in the HOM interference. In contrast to the discussion in the previous chapter, we will here deal with single electron emission and not edge-magneto plasmons. We will first clarify the distinction between the two. This will help us to understand what are the coherent states for plasmons *i.e.* the states not subject to decoherence.

4.1 Quantifying decoherence and its origins

4.1.1 Visibility of the interference

At the end of the previous chapter we introduced the visibility $\gamma = 1 - \Delta q(0)$. This quantity quantifies the visibility of the interference pattern but also the single particle

coherence. Contrary to the case $D = 1$ when the dot is fully open and charge density waves are emitted, in the case $D < 1$ a coherent superposition of those waves are emitted to create a single electron. γ quantifies how much of this coherence is preserved after propagation. In the case of single particle collision, we have shown in section 2.44 that the normalized noise can be written as the overlap of incoming coherence terms:

$$\Delta q(\tau) = 1 - \iint \varphi_1(t)\,\varphi_1^*(t')\,\varphi_2(t)\,\varphi_2^*(t')\;dtdt', \tag{4.1}$$

where φ_i is the wave function of the particle on top of the Fermi sea coming into input i of the QPC. This wave function can be efficiently modeled in the time domain by a truncated exponential function:

$$\varphi(t) = \frac{\theta(t)}{\sqrt{\tau_e}} e^{i\omega_e t} e^{-\frac{t}{2\tau_e}}, \tag{4.2}$$

where $\theta(t)$ is the Heaviside function, $\hbar\omega_e$ the average energy of the particle imposed by the dot level during emission and τ_e is the escape time or time width of the wave packet. With this functions we can compute Δq:

$$\Delta q(\tau) = 1 - \frac{1}{\frac{(\tau_{e,1}+\tau_{e,2})^2}{4\tau_{e,1}\tau_{e,2}} + \tau_{e,1}\tau_{e,2}\left(\omega_{e,1}-\omega_{e,2}\right)^2/\hbar^2} e^{-|\tau|\left(\frac{\theta(\tau)}{\tau_{e,2}}+\frac{\theta(-\tau)}{\tau_{e,1}}\right)}. \tag{4.3}$$

This formula enables us to quantify how the dip changes if the two incident particles are not exactly identical. Two parameters characterize such wave packets and thus indistinguishability can be lost in two different ways which are detailed in the next section. Looking at the different parts $\tau < 0$ and $\tau > 0$ we are thus able to access emission times of the two wave packets. Note that in the case of identical wave packets, we recover $\gamma = 1$ and $\Delta q(\tau) = 1 - e^{-|\tau|/\tau_e}$.

4.1.2 Asymmetries between wave packets

4.1.2.1 Asymmetry in time width

If the emission time is not strictly equal for each source but the energy identical, we have, for $\tau > 0$:

$$\Delta q(\tau) = 1 - \frac{4\tau_{e,1}\tau_{e,2}}{(\tau_{e,1}+\tau_{e,2})^2} e^{-\tau/\tau_{e,2}}, \tag{4.4}$$

and for $\tau < 0$:

$$\Delta q(\tau) = 1 - \frac{4\tau_{e,1}\tau_{e,2}}{(\tau_{e,1}+\tau_{e,2})^2} e^{\tau/\tau_{e,1}}. \tag{4.5}$$

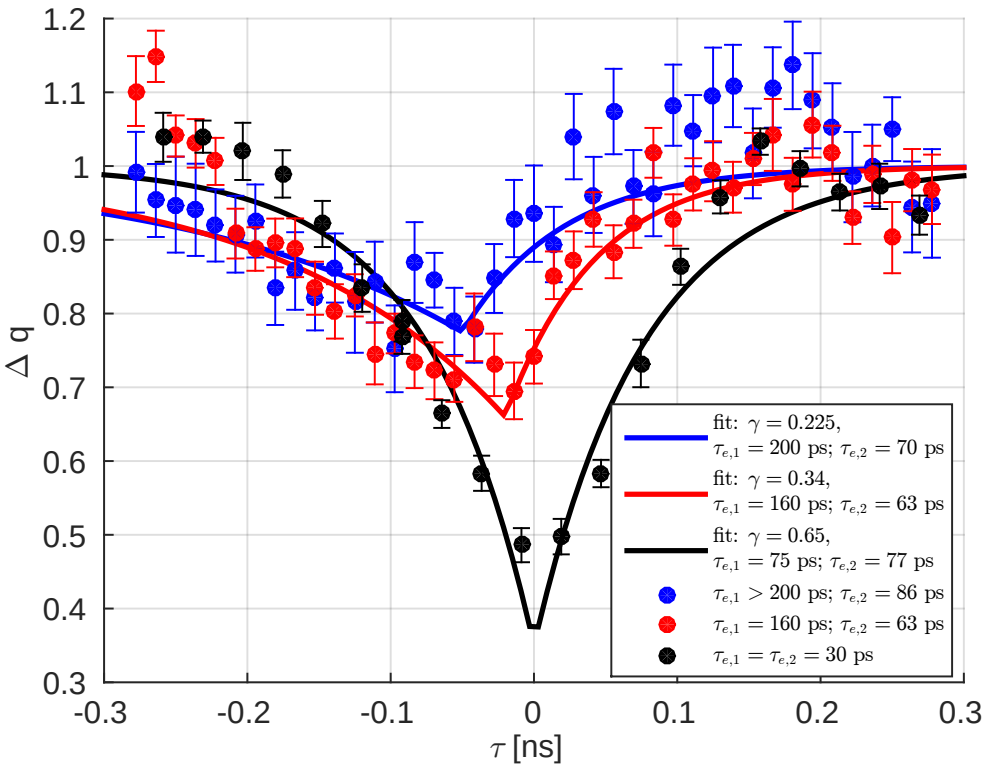

FIGURE 4.1: HOM interference patterns for three different kind of collisions. The black points correspond to wave packet tuned to have the same escape time ($\tau_e = 30$ ps). The blue and red points correspond to asymmetric wave packet interferences (see legend). The escape times given for the data correspond to measurements obtained from the phase delay of the RF current. The dips are fitted with formula 4.3 to which we applied a scaling factor on the visibility factor γ (numbers also in legend) to match the depth. The position in time is slightly shifted to the left for more and more asymmetric situations. For short emission times, the fit gives a much larger time width. This can be explained by fractionalization which splits the wave packet in two.

This can happen because of electrostatic drifts or because the coupling between the gates was not properly compensated (see section 3.3) however it is easier to compensate when we only deal with outer channel partitioning (and not inner). Our typical relative error on the calibration to determine the escape time τ_e is *at worst* around 50% [1]. One can thus calculate that it decreases at most the value of visibility to $\gamma \simeq 0.9$ which does not match the larger visibility loss observed. Indeed, we directly measure the effect of a mismatch in emission time. On figure 4.1, HOM interference patterns for three different kinds of collisions are plotted to check the effect of asymmetric pulses. The first thing to notice is that for short emission times, there is a significant difference between the width extracted from the fit and the escape time determined from the phase delay of the RF current. The broadening of the wave packet can be explained by fractionalization which does not completely split the wave packet in two but simply broadens it because the

[1] This is only for long τ_e; for shorter time it is more around 25%.

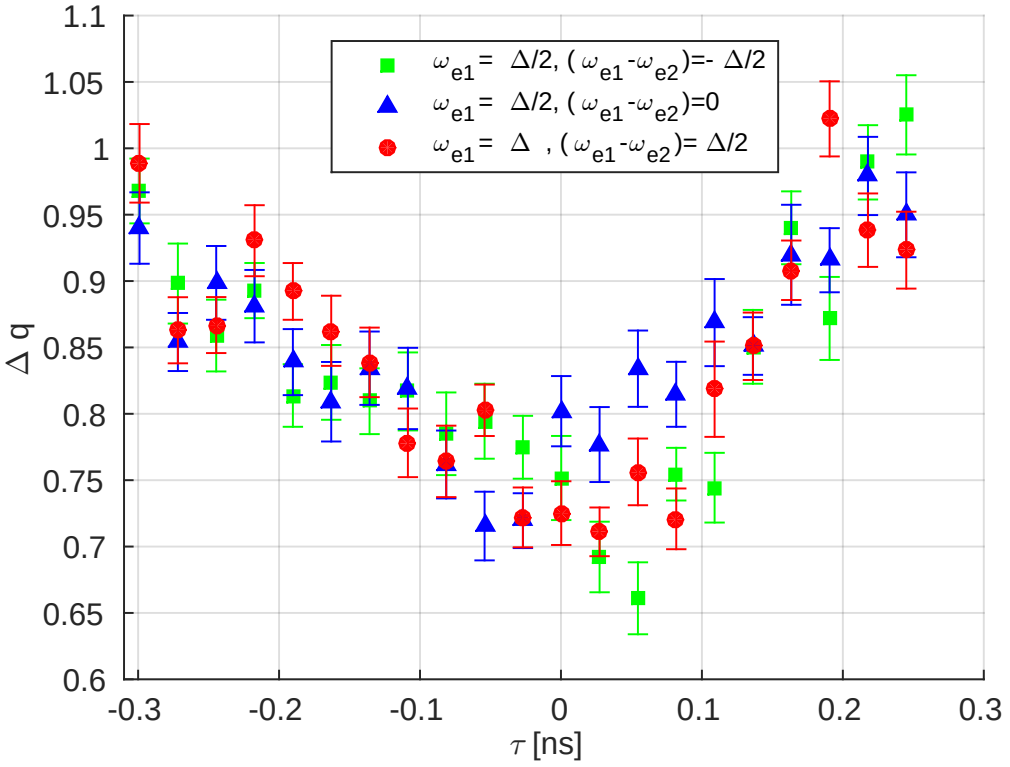

FIGURE 4.2: HOM interference patterns for three different kinds of collisions. For each realization, the two incoming wave packets have different energies. Exponential fits give an emission time around 150 ps (or a bit more for the green one which is slightly asymmetric).

propagation length is too short. For asymmetric situations, apart from an unexplained slight time shift of the x-axis, the agreement between fits and escape time is quite good and the asymmetry of the pattern is visible close to the dip. Another important feature is that the three dips are significantly shallower that one would expect by applying formula 4.3. Indeed, (from more to less symmetric) we measure $\gamma = 0.65$, 0.34 and 0.225 whereas the equation gives respectively 1, 0.81 and 0.76. This suggests that asymmetry on the emission times or even fluctuations of this emission time from one collision to another cannot quantitatively explain the observed loss of visibility.

4.1.2.2 Asymmetry in energy

The same reasons that create asymmetries in emission times can also create asymmetries in the energies at which the particles are emitted. Because of this change in energy the overlap between incoming states will not be perfect and $\gamma \neq 1$. Like in the previous section, we can probe this effect directly. In the case of identical emission time τ_e but

different energy emission, equation 4.3 gives:

$$\Delta q(\tau) = 1 - \frac{e^{-|\tau|/\tau_e}}{1 + \tau_e^2(\omega_{e,1} - \omega_{e,2})^2/\hbar^2}. \tag{4.6}$$

For instance for $\tau_{e1} = \tau_{e2} = \tau_e = 150$ ps we should get a visibility going from 1 to around 0.02 when the energy difference is tuned from 0 to half the dot spacing $\Delta/2 \simeq 60\mu$eV, which is the maximum energy difference we can induce in our setup given the $\Delta-$periodicity in the dot energy. To do so we change the DC bias on the top gates so as to change the inner chemical potential of the dot. In figure 4.2, we tested this prediction and observed that surprisingly, there is no change of visibility. The emission time extracted from fits gives a value around $\tau_e = 150$ ps for the three curves and the visibility seems to be stable around 0.3. It is surprising that this visibility is so low even when the energy is the same but also that it does not vary as we tune the energy mismatch.

The fact that visibility does not vary with energy mismatch may suggest that we do not have a full control on the energy of incident electrons and holes. However this does not seem to affect too dramatically the interference. Of course the visibility is not as "good" as expected but equation 4.3 predicts tinier visibility than what we measure even at maximal energy mismatch.

4.1.3 Electrostatic noise on top gates

Our apparent lack of control on the electron average energy might be attributed to electrostatic fluctuations of the top-gate voltage. To account for this and predict its effect on the visibility a model was developed by Iyoda *et al.* in reference [238]. In this model, the dot is not only coupled to the outer edge channel but also to a generic bosonic bath that models the electrostatic environment. The coupling between the bath and the dot is labeled γ_p and the one between dot and outer edge is labeled $\Gamma = 1/\tau_e$. Starting from a dot filled with one electron at some finite level above the Fermi sea, they use an input-ouput formalism to deduce the evolution in time of the mean occupation number in the dot. Without noise ($\gamma_p = 0$), the dot has a density of states corresponding to a Lorentzian with width Γ. The effect of γ_p is to enlarge this width much like an increase of temperature would do. This parameter γ_p can actually be thought of as an effective electronic temperature in the dot. They then compute the density matrix of the edge channel state; the latter enabling to finally calculate the shape of the HOM dip. Then they predict that the density of states in the dot is a Lorentzian of width $\Gamma + 2\gamma_p$ and

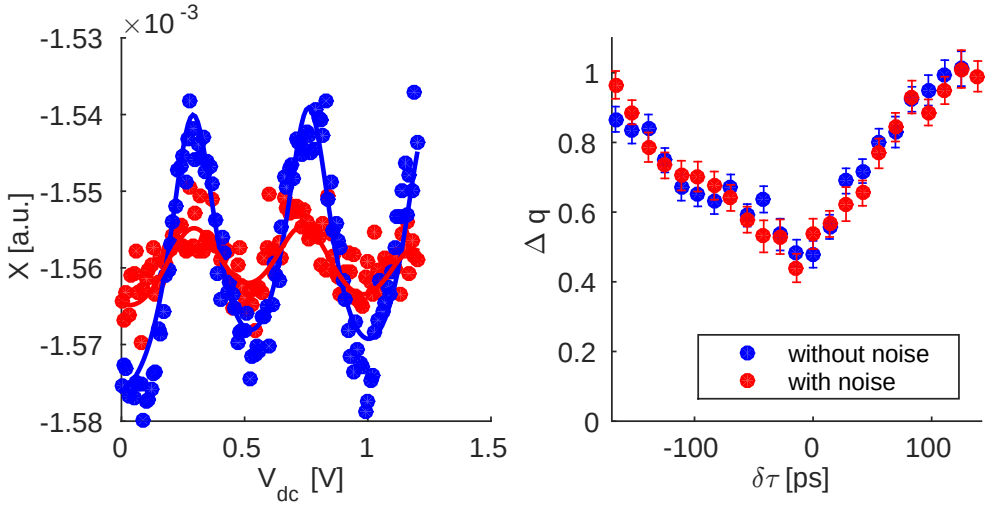

FIGURE 4.3: **Left.** Effect of the artificial noise on one of the quadrature of the RF current. The red curve is the one measured with artificial noise. The amplitude of the drive is 2/3 of $\Delta/2$ so as to be able to observe Coulomb peaks. **Right.** HOM interference with and without artificial on source 2. The emission time are tuned to $\tau_{e1} = \tau_{e2} = 40$ ps but the exponential fit gives $\gamma = 0.56$, $\tau_{e1} = 120$ ps and $\tau_{e2} = 80$ps. There is no significant difference between the two curves.

the visibility of the interference is:

$$\gamma = \frac{\Gamma}{\Gamma + 2\gamma_p}. \tag{4.7}$$

We tested this hypothesis by adding an artificial noise on the top gate voltage over source 2 and measured how it influenced the visibility of the interference. To do so we used the white noise function of a *Agilent 33250A* generator. The noise amplitude was calibrated measuring its effect on the width of the Lorentzian current peaks while varying its top gate DC voltage. The results are presented on the left panel of figure 4.3. We compared the data with a Floquet simulation with $\tau_{e2} = 40$ps. We could model the widening of the peaks by an increase of the effective electronic temperature from 100 mK to ~ 400 mK. Only one quadrature of the RF current is presented here but the same broadening is observed on both. The effect on the interference pattern (see right panel of the same figure) is not visible or at least below our accuracy level.

If the observed visibility loss without artificial noise ($\gamma = 0.6$ at $\tau_e = 40$ ps) was due to a noisy environment, formula 4.7 would have given $\gamma_p = \frac{\gamma^{-1}-1}{2\tau_e} = 2\pi \times (1.3 \pm 0.4)$ GHz. If we choose to rely on exponential fits of the data rather than on the calibration of the source with the measurement of the phase of the RF current the result is a bit different. Indeed, as mentioned in the legend of figure 4.3, exponential fits give 2 different emission times for the sources: $\tau_{e1} = 120$ ps and $\tau_{e2} = 80$ps. Iyoda *et al.* predict that for wave

packets asymetric in time the visibility becomes:

$$\gamma = \frac{2\tau_{e1}^{-1}\tau_{e2}^{-1}}{\frac{1}{2}\left(\tau_{e1}^{-1}+\tau_{e2}^{-1}\right)^2 + 2\gamma_p\left(\tau_{e1}^{-1}+\tau_{e2}^{-1}\right)}. \tag{4.8}$$

This results in $\gamma_p = 2\pi \times (0.50 \pm 0.15)$ GHz. Then, adding artificial noise equivalent to an increase of electronic temperature in the dot from 100 mK to 400 mK adds another contribution to γ_p. The new dephasing rate on source 2 is $\gamma_p' = \gamma_p + k_B T_{el}/\hbar = 2\pi \times 7.6$ GHz (or $2\pi \times 6.8$ GHz with fits). Because this noise is added on one source only, the new visibility becomes:

$$\gamma' = \frac{\Gamma}{\Gamma + \gamma_p + \gamma_p'} = 0.31, \tag{4.9}$$

and we measure $\gamma = 0.56 \pm 0.04$ which would represent a discrepancy of at least 6σ. This discrepancy is even higher with the method using the exponential fits.

We can also analyze the same set of data through Floquet theory and reach to the same conclusion. The blue line on the left panel of figure 4.3 is compatible with the current coming out of one source calculated with Floquet theory with parameters $\tau_e = 40$ ps and a thermal broadening of at most 100 mK. We can then apply a Gaussian averaging of amplitude $\sigma = k_B T_{el} = 100$ mK on the energy of each impinging particle. Convolving formula 4.6 with such a Gaussian distribution, we find $\gamma = 0.8$. Then we increase the amplitude of these fluctuations for one source only toward $\sigma = k_B T_{el} = 400$ mK to find $\gamma = 0.5$. Contrary to Iyoda's model, using Floquet theory and then adding thermal broadening of the emission actually takes into account the $\Delta-$periodicity in energy of the dot which is not the case in their model. We do not obtain the same absolute value than the previous model but we still predict a measurable change of visibility between both situations that is not visible in our data. All this considered, we can rule out the environmental noise dephasing hypothesis as the main reason for decoherence.

4.1.4 Energy dependence of the beam splitter

We usually model the quantum point contact as an energy independent barrier but this is an ideal case which is not always perfectly realized. We try as much as possible to be in this situation but small imperfections can remain. In reference [239], a model is developed to explain the contrast reduction with an energy dependence of the beam-splitter reflection $R(\omega)$. According to this model, the contrast should increase with increasing wave packet length (or with τ_e). However, as we see on figure 4.4 (which will be commented further in details in the next section) we observe clearly the opposite trend. Visibility decreases with the length of wave packets.

4.1.5 Interaction with neighboring channels

One simple (but lengthy) way to test the effect of neighboring channels on decoherence is to add more of them and observe the effect on γ. This is what is plotted on figure 4.4 where data in blue correspond to the evolution of visibility with emission time $\tau_e = \tau_{e1} = \tau_{e2}$ (and equal energy) at filling factor 2 and the red squares are measured at filling factor 3. We observe a quick decrease of γ for both situations although it is more pronounced at $\nu = 3$. To understand the evolution the relation $\gamma(\tau_e)$, we introduce a coherence time τ_c as a phenomenological time scale for decoherence. The excess coherence term becomes $\varphi(t')\varphi^*(t) \to \varphi(t')\varphi^*(t)e^{-|t-t'|/\tau_c}$. Now, only time components (t, t') with $|t - t'| \leq \tau_c$ will interfere whereas longer time component of the coherence will actually be subject to random partitioning. Then we can compute the new visibility starting again from equation 4.1; we get for equal emission times and energies:

$$\gamma = \frac{1}{1 + 2\tau_e/\tau_c}. \tag{4.10}$$

From figure 4.4 we can thus extract two different coherence times: $\tau_c = 60$ ps at $\nu = 3$ and $\tau_c = 98$ ps at $\nu = 2$. On this figure we can observe the decay of coherence terms on a time scale τ_c. Wavepackets larger than this time scale will decompose into several incoherent blocks that will not interfere with each other, leading to a dramatic loss of visibility. The fact that τ_c depends largely on the number of neighboring edge channel is a clear indication that interaction between them is a major ingredient to explain the observed decoherence and thus that it happens during propagation.

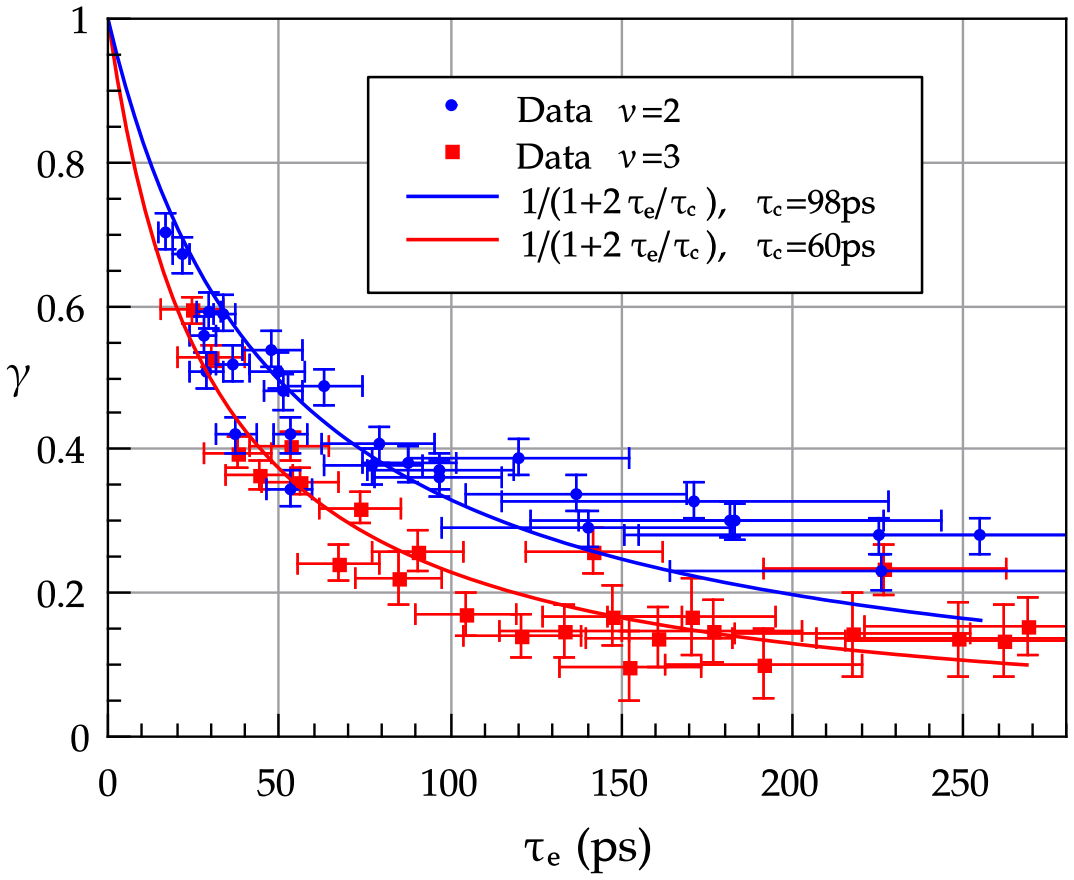

FIGURE 4.4: Evolution of visibility γ as a function of emission time τ_e for $\nu = 2$ (blue dots) and $\nu = 3$ (red squares). The plain lines correspond to the fits by the phenomenological model $\gamma(\tau_e) = (1 + 2\tau_e/\tau_c)^{-1}$.

4.2 Fractionalization of single electrons

Before using our plasmon scattering approach to quantitatively describe the loss of visibility we will establish the difference between edge-magneto plasmons and single particle emission. We will see that the former are actually coherent states.

4.2.1 Injection of plasmons

As we mentioned in the introduction of chapter 3, dealing with interactions in one dimension can be very complicated in the fermionic representation. Bosonisation renders it easier. Emission and propagation are then described in terms of creation and propagation of EMPs which are collective charge excitations of bosonic nature. The situation is even simpler when the dot is perfectly coupled to the outer edge (at $D = 1$). As we have seen already, at $D = 1$, there is a linear relation between the voltage applied on the top gate and the excess charge in the dot area so also between I_ω and V_ω. This relation can

be for instance $I_\omega = iC\omega V_\omega$ in the case of a simple capacitive coupling at low frequency, or the one expressed in equation 3.15. This linearity is always valid at $D = 1$. Solving the equation of motion 3.9 for the plasmon modes we find that it creates a coherent state or, more precisely and because we can excite several frequencies, a product of coherent states [226]. The initial state at $x = 0$ can be written:

$$|\Psi_{\text{in}}\rangle = \bigotimes_{\omega>0} \left[|\alpha_\omega\rangle_1 \otimes |0_\omega\rangle_2\right], \tag{4.11}$$

where the first term of the tensor product correspond to the state in the outer channel and $\bigotimes_{\omega>0} |0_\omega\rangle = |F\rangle$ is the vacuum state for plasmons in the inner edge *i.e.* the Fermi sea (thermal fluctuations are discarded). The tensor product runs over all frequencies that are excited by the drive of the top gate (only one if we use a sine drive at $D = 1$). Here $|\alpha_\omega\rangle = -I_\omega/(e\sqrt{\omega})$ is a coherent state [227], this can be seen by analogy with quantum optics where an oscillating field is also described by a coherent state; here the charge density oscillates.

As a result from interactions, these EMPs are partially transferred to the inner channel at the output of the interaction region (see section 3.4):

$$|\Psi_{\text{out}}\rangle = \bigotimes_{\omega>0} \left[|S_{11}(\omega)\alpha_\omega\rangle_1 \otimes |S_{21}(\omega)\alpha_\omega\rangle_2\right]. \tag{4.12}$$

As seen from the output state, which is still separable, the outer channel does not get entangled with the inner one, this is because we had a coherent input state. A perfect dip $\gamma = 1$ should be observed both for the outer and inner channels as long as the injected currents and interaction parameters are equal in both input of the QPC. This can be understood from gauge transformation arguments. Indeed for classical voltage drives $V_1(t)$ and $V_2(t)$, all the applied voltages can be brought to one input only (for example, 2) by the overall shift $-V_1(t)$. Noise is then obviously suppressed ($\gamma = 1$) for $V_1(t) = V_2(t)$ because there is no potential difference between the two inputs of the QPC for any time t. This is not exactly what we observed in chapter 3 where even at $D = 1$ we observed spurious loss of visibility.

This decoherence at $D = 1$ can be partially explained by the aforementioned mechanism (asymetries, noise, energy dependence of the QPC), to which we can also add a small interaction parameter difference along the two incoming paths toward the QPC (S_{21} not equal for each inputs). It is possible that the remaining sources of decoherence at $D = 1$ are shared between all the above mentioned mechanisms. Indeed, we tried to minimize the dip at $D = 1$ with square pulses by fine tuning the amplitudes and time delays and we could not go below $\Delta q(0) = 0.11$ which suggests some decoherence intrinsic to the

sample (*e.g.* when interactions are not the same in the two input arms of the beam splitter).

To be a bit more precise and so as to be able to compare with the single electron case, we can actually calculate the expected visibility from $|\Psi_{\text{out}}\rangle$. Indeed, the density matrix reads:

$$\hat{\rho}_{\text{out}} = |\Psi_{\text{out}}\rangle\langle\Psi_{\text{out}}| = \bigotimes_{\omega>0} |S_{11}(\omega)\alpha_\omega\rangle\langle S_{11}(\omega)\alpha_\omega|_1 \bigotimes_{\omega>0} |S_{21}(\omega)\alpha_\omega\rangle\langle S_{21}(\omega)\alpha_\omega|_2. \quad (4.13)$$

To measure the outer partition noise we trace out all the other degrees of freedom *i.e.* we take the partial trace on the inner edge part of the density matrix $\hat{\rho}^1_{\text{out}} = Tr_2(\hat{\rho}_{\text{out}})$, we thus recover a pure coherent state (simply multiplied by a complex scalar number $S_{11}(\omega)$) *i.e.* by definition a state not subject to decoherence, thus giving $\gamma = 1$.

4.2.2 Injection of single electron

Here the situation is different because the relation between current and gate voltage is no longer linear thus we do not emit coherent states. The most intuitive representation becomes the electronic one where we can describe the electron with a wave function $\varphi(t)$ like in equation 4.2. However we still need the bosonic representation to treat interactions. Following equation 2.12 and using equations 3.3 and 3.4 to express $\hat{\Psi}^\dagger(x,t)$ as a displacement operator for plasmons, we can write the injection of a single electron state φ_a in the outer edge in terms of plasmons as [226]:

$$|\Psi_{\text{in}}\rangle = |\varphi_a, F\rangle = \left[\int dx\ \varphi_a(x)\Psi^\dagger(x)|F\rangle_1\right] |F\rangle_2 \quad (4.14)$$

$$= \left[\int dx\ \varphi_a(x) \bigotimes_{\omega>0} |\alpha_\omega(x)\rangle_1\right] \bigotimes_{\omega>0} |0_\omega\rangle_2 \quad (4.15)$$

where the coherent states are $\alpha_\omega(x) = e^{-i\omega x/v_F}/\sqrt{\omega}$ [227]. The electron can be described as a coherent superposition of coherent state $\alpha_\omega(x)$ but is still separable between the two edges. However, after propagation length l, the incoming state on the beam splitter writes:

$$|\Psi_{\text{out}}\rangle = \int dx\varphi_a(x) \bigotimes_{\omega>0} \left[|S_{11}(\omega)\alpha_\omega(x)\rangle_1 \otimes |S_{21}(\omega)\alpha_\omega(x)\rangle_2\right]. \quad (4.16)$$

We see that because interactions mix the two edges, the superposition is now on both edges and thus they are entangled (because of the integral sum before the tensor product). After tracing out the environment (inner channel) degrees of freedom, the outer channel coherence is suppressed, corresponding to a strong reduction of visibility. This time the

density matrix in one input after propagation writes:

$$\hat{\rho}_{\text{out}} = \iint dx dx' \varphi_a(x)\varphi_a^*(x') \bigotimes_{\omega>0} |S_{11}(\omega)\alpha_\omega(x)\rangle\langle S_{11}(\omega)\alpha_\omega(x')|_1 \bigotimes_{\omega>0} |S_{21}(\omega)\alpha_\omega(x)\rangle\langle S_{21}(\omega)\alpha_\omega(x')|_2 \tag{4.17}$$

and taking the reduced one for the outer channel we have:

$$\hat{\rho}^1_{\text{out}} = \iint dx dx' \varphi_a(x)\varphi_a^*(x')\mathcal{D}(x,x') \bigotimes_{\omega>0} |S_{11}(\omega)\alpha_\omega(x)\rangle\langle S_{11}(\omega)\alpha_\omega(x')|_1 \tag{4.18}$$

where $\mathcal{D}(x,x')$ is a decoherence function that we can compute. In the continuum limit for ω [227]:

$$\mathcal{D}(x,x') = \exp\left(\int_0^\infty \frac{d\omega}{\omega}|S_{21}(\omega)|^2\left(e^{-i\omega(x-x')/v_F} - 1\right)\right). \tag{4.19}$$

This quantity represents a weight different from unity for coherence terms in equation 4.17 which will finally reduce the total overlap of the two impinging density matrices. Although we have been able to exhibit a relation between interaction parameters and the partial density matrix on the outer channel, it actually reveals harder to compute γ in a fully general case[2]. This is where our collaboration with the team of P. Degiovanni on one side and T. Martin on the other proved to be very fruitful. They managed indeed to compute analytically the coherence at the exit of the interaction region [225, 240]. To do so they used the bosonisation technique and numerical evaluation of the resulting non-perturbative expressions. Degiovanni *et al.* numerically computed the excess electronic coherence function at $T = 0$ K in the Wigner representation [240] and Martin *et al.* managed to compute the coherence at $T = 0.1$ K using quasi-Monte Carlo algorithm with importance sampling [225, 241].

On figure 4.5, the excess Wigner function they computed is plotted for increasing values of the propagation length or equivalently, of τ_s. Here $\Delta W(t,\omega)$ provides a direct visualization of the evolution of the single-electron wave packet under the influence of Coulomb interaction, leading to the destruction of the single electron. For $\tau_s = 0$, $\Delta W(t,\omega)$ corresponds to the Wigner representation of the pure single-electron state (see also figure 2.9). After a short propagation length, $\tau_s = 28$ ps, before the fractionalization in two pulses has occurred, energy relaxes and the spectral weight at ω_e is transferred close to the Fermi energy. The non-classical ripples are also almost completely washed out. On longer propagation length $\tau_s = 70$ ps, the fractionalization in two distinct pulses occurs and can be seen along the temporal axis. As two pulses of charge $e/2$ cannot correspond to a single quasiparticle excitation of the Fermi sea, collective neutral excitations are

[2] The relation $\gamma = 1 - Tr[\hat{\rho}^1]$ is valid only for single particle wave packets well defined above the Fermi sea.

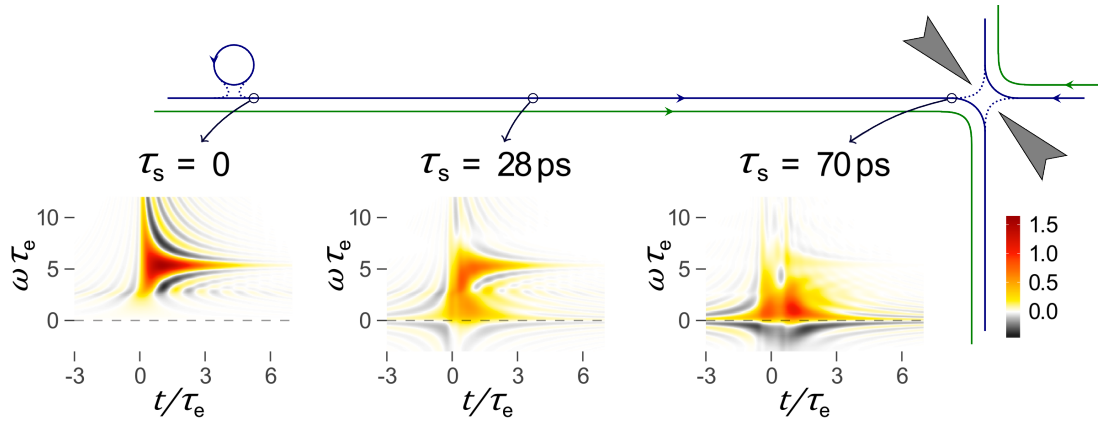

FIGURE 4.5: Wigner representations $\Delta W(t,\omega)$ at $T = 0$K for different propagation lengths $\tau_s = 0, 28$ and 70 ps. The time axis are shifted by time $\tau = l/v_\rho$ to account for the propagation time on length l. For $\tau_s = 0$ ps $\Delta W(t,\omega)$ represents the state emitted in the outer edge channel (blue line) with $\omega_e = 0.7$ K and $\tau_e = 60$ ps. For $\tau_s = 28$ and 70 ps, short range Coulomb interactions between the outer and inner (green line) edge channels are taken into account.

created. This can be seen on $\Delta W(t,\omega)$ by its negative values below the Fermi energy (corresponding to the creation of holes) compensated by an increase of $\Delta W(t,\omega)$ above the Fermi energy (corresponding to the creation of the same number of electrons). The electron is then "destroyed".

4.2.3 Predictions for the HOM patterns

The Hong Ou Mandel noise directly probes the overlap between incoming first order coherence function (or equivalently between Wigner functions), thus with their calculations it was then straightforward to compute the full shape of the dip for any time delay between the sources. The upper-left panel of figure 4.6 presents the data of the HOM traces $\Delta q(\tau)$ for various emission times τ_e together with theoretical predictions at $T = 0$ and $T = 100$ mK, providing an evaluation of the effect of finite temperature on single-electron decoherence. The interaction parameter is set to $\tau_s = 70$ ps. The red, blue, and black curves represent these theoretical predictions taking $\tau_e = 34$, 91, and 147 ps. These values agree within experimental resolution with the values of τ_e extracted from the measurements of the average current. In particular, for the short time $\tau_e = 34$ ps, theoretical predictions capture the broadening of the electronic wave packet by the fractionalization process, which leads to an overestimate by a factor 2 of the emission time extracted from the exponential fit of the dip. However, the resolution is not good enough to observe the predicted side peaks for $\tau_e = 34$ ps at $T = 0.1$ K. The agreement between the data and the predictions is good: once the width of the dip has been chosen to match the data, the values of the contrast also agree. Note that we are able here to fit the full HOM trace using only experimentally measured parameters (emission time

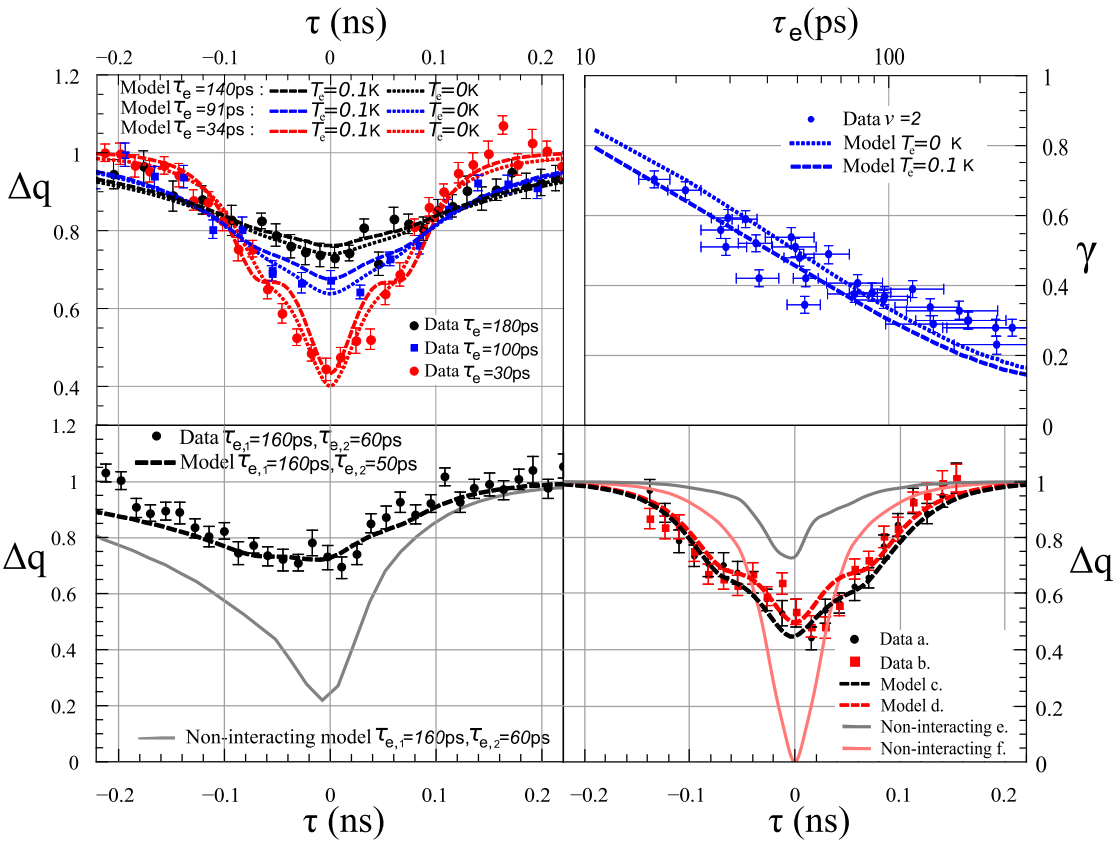

FIGURE 4.6: Data/model comparison. **Upper-left** $\Delta q(\tau)$ for various emission times. Theory accounting for Coulomb interaction is represented by the dotted line ($T = 0$ K) and dashed line ($T = 0.1$ K). **Lower-left**, $\Delta q(\tau)$ for asymmetric emission times. Theory predictions accounting for Coulomb interaction ($T = 0.1$ K) are represented by dashed lines. Predictions of the non-interacting model in blurred black. **Upper-right** contrast γ versus emission time τ_e (in log-linear scale). The dotted ($T = 0$) and dashed ($T = 100$ mK) lines represent theory predictions accounting for Coulomb interaction. **Lower-right** (a) data, $\tau_e = 40$ ps, 400 mK gate noise on dot 2; (b) data, $\tau_e = 40$ ps without gate noise; (c) theory, $T = 0.1$ K, $\omega_{e1} = 0.7$ K, $\omega_{e2} = 0.3$ K, $\tau_e = 40$ ps; (d) theory, $T = 0.1$ K, $\omega_{e1} = \omega_{e2} = 0.7$ K; (e) non-interacting model, $\omega_{e1} = 0.7$ K, $\omega_{e1} = 0.3$ K, $\tau_e = 40$ ps; (f) non-interacting model, $\omega_{e1} = \omega_{e2} = 0.7$ K, $\tau_e = 40$ ps.

τ_e and interaction strength τ_s). The differences between the calculated HOM curves at different temperatures are small, showing a small influence of temperature on single-electron decoherence. This is explained by the electron emission energy $\omega_e > k_B T_{el}$.

Not only is the model able to capture the shape of the HOM dip but it also predicts the full dependence of visibility versus emission time. The comparison with data is shown on the upper-right panel of figure 4.6, theory predicts $\tau_c = 86$ ps at $T_{el} = 100$ mK and $\tau_c = 104$ ps at $T_{el} = 0$ K close to the data. The agreement is quite satisfactory, however for long escape times, data tends to accumulate above the theoretical predictions, in a way similar to what was observed in reference [217]. In our case we might suppose that this in an effect of the time periodicity that becomes comparable with the escape time,

saturating the maximal time length of the wave packet coherence and diverging from a model where single electrons do not overlap from one period to another.

4.2.4 Energy relaxation

To conclude, the theoretical computation also enables us to explain the data shown in section 4.1.2 and 4.1.3. The lower-left panel of figure 4.6 presents the data-model comparison when the emission times of the two sources are detuned. The agreement is also very good, providing the right value for the contrast of two-particle interferences, contrary to the non-interacting predictions (gray line, obtained with equation 4.3).

Remember also that in section 4.1.3 we pointed out the fact that we seemed to have no control on the emission energy or that at least it did not affect the interferences. The lower-right panel of figure 4.6 exhibits the most striking distinctive prediction of the interaction model: the contrast and shape of the HOM trace is almost unchanged when the emission energy of one of the two sources is varied (from 0.7 K to 0.3 K). This behavior is completely different from the non-interacting model predictions (gray and light red lines), for which the contrast varies strongly from 1 to 0.25 when the energies are detuned by 400 mK at $\tau_e = 40$ ps. Surprisingly, in the detuned case, interactions lead to enhancement of the contrast compared to the non-interacting prediction. This restoration of indistinguishability by decoherence is a consequence of the electronic relaxation. We could already see this on the Wigner representation on figure 4.5. At a quantitative level, it can be shown that at long times, the resulting single-electron coherence depends only on the shape of the initial current pulse (here encoded in the duration τ_e) and of the propagation distance, but no longer on the value of its initial injection energy. This erasure effect is a consequence of the entanglement of the electronic degrees of freedom of the outer edge channel with the inner one [240, 242]. Quantitatively confirming this effect is a strong signature of the single-electron decoherence scenario described within the bosonization framework [241].

4.3 Saving single electron

Now that we have confirmed the major role played by Coulomb interactions in the propagation of single electrons in quantum Hall edge channels and quantified how it led both to strong decoherence and relaxation of single particle wave packets, we can use this information to try to improve the setup to maintain some coherence on propagation. Here I am going to expose a few ideas explored during my PhD to try to improve electronic coherence impinging on the beam splitter.

4.3.1 With only one edge channel

The first natural idea one can have is to remove this interacting environment by simply doubling the magnetic field so as to reach filling fraction $\nu = 1$. With only one edge channel, there is no other conductor to lose coherence into and we should be less sensitive to interaction induced decoherence.

We were able to measure dips at $\nu = 1$ ($B \approx 8$T) with the same sample presented in this chapter and the former one. We could measure dips for a square shape drive voltage at different values of transmission D. We did not get a dip going to zero as can be seen on the left panel of figure 4.7. The emission time chosen with the independent current measurement are $\tau_e = 17$ (black points), 50 (red) and 80 ps (blue). The fit with exponentials however gives respectively around 100 ps for the black and red points and around 200 ps for the blue points. This result combined with the observed loss of visibility of the same order than $\nu = 2$ suggests that another decoherence mechanism is also at stage in the $\nu = 1$ system and comes up with a broadening of the wave packet. We can put forward hypothetical explanations for this. First, going to $\nu = 1$ we removed the copropagating edge channel next to the conductor. In the Landauer-Büttiker picture of edge channels, the insulating bulk actually contains closed loop unidimensional conductors that wrap around defect points. They can be though of as isolated neighboring conductors with gapped excitations (defined by their total length) and not connected to a reservoir. Although isolated, this closed loop states contain charges that can interact through Coulomb interactions. This interactions may also destroy the single particle coherence. Another possible explanation could be the coupling with internal acoustic degrees of freedom coming from the finite width of the edge [243] that causes dissipation and thus decoherence. Finally, we cannot expect absolutely no interactions effect as it was shown in reference [221] that interactions are actually long range so we might expect interactions with other kind of nearby conductors.

Although it seems to be a simpler system, other difficulties appear at this filling fraction. First of all, the dots appeared to be more sensitive to electrostatic fluctuations. Indeed, we measured for instance that at a given V_g for one source, the noise created after partition (HBT noise) was not stable enough in time. We suspected that this is due to a lower electronic density in the dot, lowering the quantum capacitance which in turn lowers the charge screening.

Last but not least, we measured, as in reference [244], that a local fractional quantum Hall state forms around the QPC. This was checked in two different ways. On the lower panel of figure 4.7 is plotted the zero bias conductance versus V_{QPC}. Two plateaus at $e^2/3h$ and $e^2/2h$ appear clearly. A third fainter one is also visible at $0.6 \times e^2/h$. These

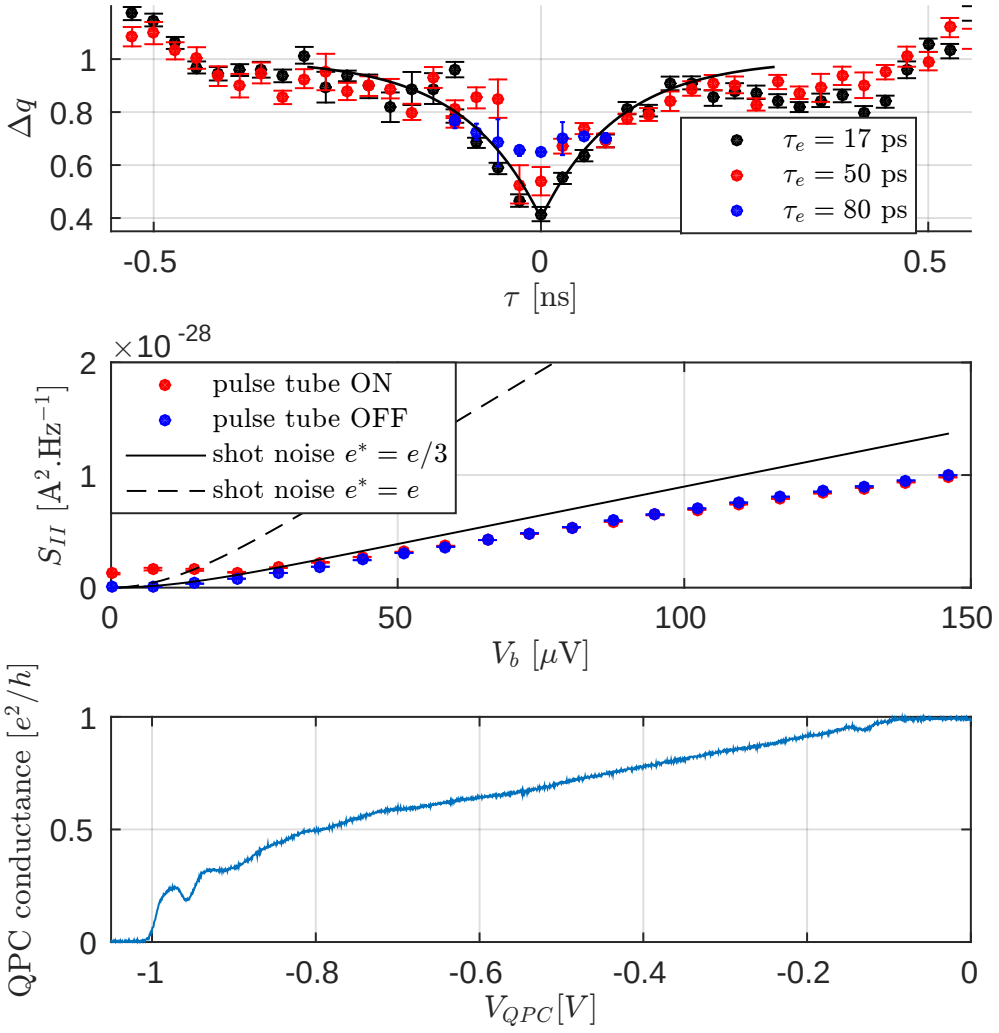

FIGURE 4.7: **Upper.** Normalized noise taken at $\nu = 1$ for different emission times (the blue one has only partial data). **Middle.** Shot noise versus DC bias taken at $\nu = 1$ and $R = 0.45$ with an additional small amplitude 10 GHz signal excitation with and with out pulse tube on. Lines correspond to theoretical expectations for partitioning of electron (dashed line) or quasi-particle of charge $e/3$ (plain line). **Lower.** Measured conductance at $\nu = 1$. A small but clear plateau appears at $\frac{e^2}{3h}$.

structures are reminiscent of fractional quantum Hall edges. In the middle panel, we show the partition noise close to $R = 0.5$. The slope (determined precisely with the calibration detailed in section 2.4.3.2) is not coherent with the tunneling of electrons but rather quasi-particles of effective charge close to $e^* = e/3$ (possibly $e/4$). This is interpreted by the creation of a local fractional quantum Hall droplet at the level of the QPC. Indeed, the voltage applied on the gates locally deplete the electron gas (the density n decreases) so that for the same magnetic field the ratio $\nu = nh/(eB)$ is lowered and can possibly reach a fractional value. This makes the interpretation of the Hong Ou Mandel experiment much more complicated since we deal with a highly correlated many body states whose first order coherence function are not trivial. Lacking both good control on the dot parameters and theoretical predictions to guide us, we decided not to carry on extensively in this direction.

It might be possible to go back to a study of HOM interferences at $\nu = 1$ with lower mobility samples. Indeed, the appearance of fractional quantum Hall phases requires higher mobility than the integer case.

4.3.2 By separating inner and outer edge

4.3.2.1 With top gates

Following the idea developed in reference [57] samples were made with an additional top gate to separate inner and outer edges. The idea being that the strength of the interedge coupling is related to their spatial separation. On the left panel of figure 4.8 is represented a false color SEM picture of this samples. By putting a small negative value on these two arms, it is possible to have a larger spatial separation between the two channels. On the right panel we see it was possible to prevent the inner edge to cross the central QPC even when it is fully open.

Unfortunately, we could not successfully realize an HOM interferometry experiment at $D < 1$ and observe a regain of visibility. This is for several reasons. Adding more gates also means dealing with more parasitic coupling between all these gates. This would not be an unsolvable issue if the sample was stable on time scales longer than the experiment, which was not always the case. We also had some strong hysteresis that did not permit us to use the methods developed in section 3.3.

As can be seen from values of V_{QPC} needed to open the QPC (figure 4.8, right panel), it is naturally closed at 0 V. It seems that compared to previous samples, the added gates lowered the density at the level of the QPC and also possibly the electron mobility thus

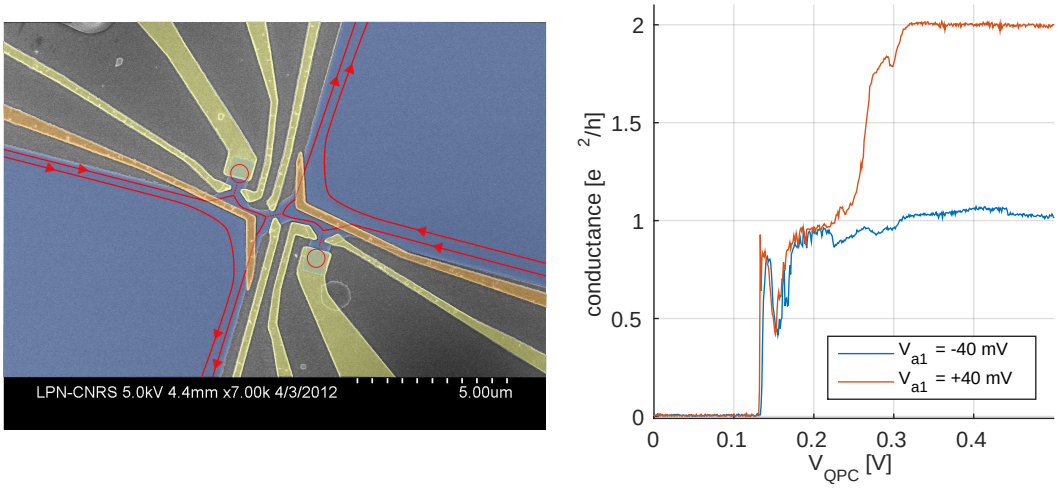

FIGURE 4.8: **Left.** False color SEM picture of a sample from batch S902 with additional top gates (orange) to separate spatially inner and outer edge channels. **Right.** Conductance of the central QPC versus V_{QPC} for two different values of voltage on the left arm. Right arm is set at a very positive value so as to let both edge channels pass. For $V_{a1} = -40$ mV, the inner edge channel cannot pass through the central QPC.

altering the quality of the quantum Hall plateaus. For some samples of the same batch it was impossible to fully open the QPC even with voltage on all gates up to $+1V$.

4.3.2.2 Changing magnetic field at same filling fraction

On a lesser extent we also explored the effect of a change of magnetic field on visibility. In [245] it was shown that even at a fixed filling fraction, the visibility of Mach-Zehnder interferences can be changed with the magnetic field. Furthermore, in reference [246] it was pointed out that it is the filling fraction rather than the magnetic field that really influences the visibility. A complete explanation for this is still lacking and would require to take into account disorder, edge steepness and screening from other compressible areas. However, these experiments point out the role of the magnetic field on the exact shape of the interferometer. One may suspect that changing the magnetic field or filling fraction can alter the separation between inner and outer edge channels thus changing the interchannel interaction strength. We could not find easily, enough magnetic field values that allowed a proper use of the dots (stability, absence of charge impurities, energy independent QPC ...) so we did not carry on in this direction extensively.

Conclusion to this chapter

To conclude, we have analyzed the coherence of single-electron states propagating along a 1D edge channel using HOM interferometry. We observe a strong reduction of the HOM contrast when the width of the emitted single-electron wave packets is increased from which a coherence time $\tau_c = 98$ ps (at $\nu = 2$) can be extracted. Our results are in quantitative agreement with the Coulomb interaction–induced decoherence along propagation, providing direct evidence of the destruction scenario of a single quasiparticle in a 1D conductor. We have explored in detail other possible decoherence mechanisms and (so far) unsuccessful methods to reduce the loss of the single particle coherence.

Chapter 5

Tomography

"Well, I have this weird thing in my head... Like, I get this weird feeling that I'm sweating, but on the inside of my face. And then I get this weird thing where my eyes are all weird, and I can see electricity. Like, I can see green lines going from, like, a light bulb, to all around. And then, I can see that everything is just electrons, colliding, and floating, and playing. And then, I feel like if I just take one deep breath, and then just wish hard enough, I could just vanish, into nothing, like I was before I was born."

Jane, **Louie**, Season 5 Episode 5 *Untitled*

In this chapter we are going to see how the HOM interferometer can be efficiently used to implement a protocol aiming at reconstructing any kind of single particle state or all the single particle information on any many-body state propagating in the quantum Hall edge channels. We are going to use again the Wigner function approach; this protocol enables to directly reconstruct the Wigner function of arbitrary states. We will demonstrate the full generality of this method and what its limits are.

5.1 Protocol

5.1.1 Principle

As we have seen in the previous chapters, our favorite interferometer encodes the overlap between two incoming Wigner functions into out-coming charge fluctuations. If one is able to measure any given overlap between single particle coherence functions, it is therefore very natural to see how to reconstruct any kind of single particle state coming

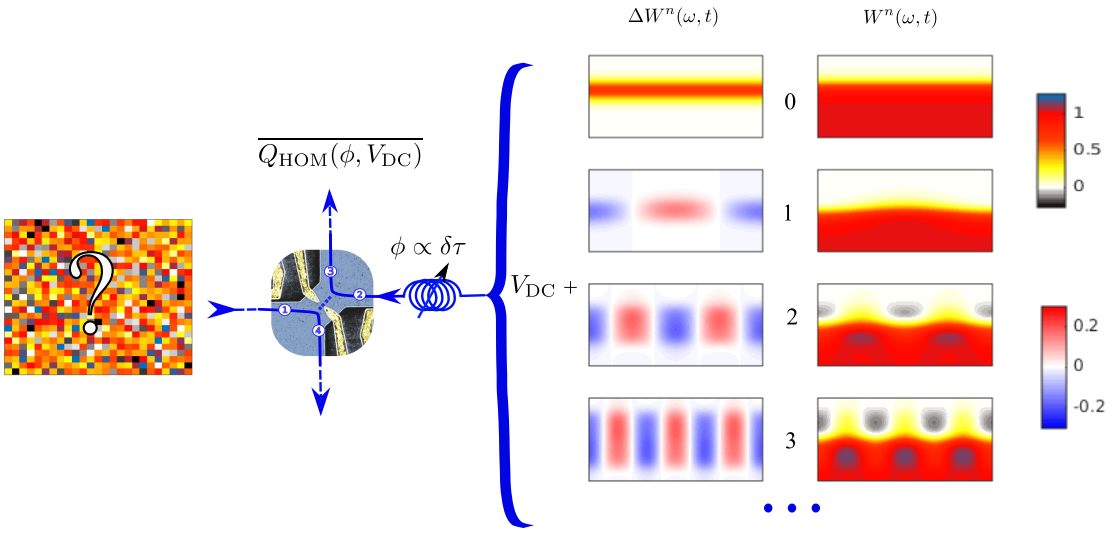

FIGURE 5.1: Scheme of the tomography protocol. An unknown Wigner function is probed by measuring its overlap with Wigner functions sent in the other arm. On the left column are represented the excess Wigner function $\Delta W^n(\omega,t)$ whereas the Fermi sea is added on the right one. Here only the first 4 members of the family (n from 0 to 3) are plotted at 100 mK. For each value of n the overlap is explored in the whole (ϕ, V_{DC}) phase space.

in input 1 $|\varphi\rangle$. If all vectors $|\phi^n\rangle$ coming in input 2 define a basis for your Hilbert space, $|\varphi\rangle$ writes:

$$|\varphi\rangle = \sum_n \langle\phi^n|\varphi\rangle|\phi^n\rangle. \tag{5.1}$$

From this expression it is very clear that measuring all overlaps $\langle\phi^n|\varphi\rangle$ gives you all the information on $|\varphi\rangle$. Actually, as we have mentioned before, Wigner functions contain all single particle information and only this. It does not give any kind of information on many-body correlations. Thus this procedure will not measure the full many-body wave function but only its single particle representation; which is enough for non-interacting many particle systems but not in general.

The idea proposed by Grenier *et al.* [10] is to use a family of small amplitude sine drive excitation oscillating at period multiple of Ω. They are represented on the scheme of figure 5.1 either with (right column) or without (left column) the Fermi sea. At first order they write:

$$W^n(\omega,t)=f(\omega-\omega_{\mathrm{DC}})+\frac{eV_2^{\mathrm{AC}}}{n\hbar\Omega}\cos(n\Omega t+\phi)\left[f(\omega-\omega_{\mathrm{DC}}-n\Omega/2)-f(\omega-\omega_{\mathrm{DC}}+n\Omega/2)\right] \tag{5.2}$$

where $\omega_{\mathrm{DC}} = -eV^{\mathrm{DC}}/\hbar = \mu/\hbar$ and ϕ is the tunable phase difference between signals in both inputs. Basically, time domain information is recovered varying ϕ whereas V^{DC} is changed to capture energy domain information. For $n = 0$, we actually just put a DC bias at the input 2. Contrary to the previous chapters, here the second RF line is not connected to the dot 2 but on the Ohmic contact from which we used to inject only DC

bias; we used a cryogenic bias-tee (*Marki BTN0040*) to be able to inject both AC and DC components on the Ohmic contact.

The choice of Ω has not been commented yet. Here relies the only *a priori* assumption needed to make on the signal to reconstruct: it is $T-$periodic in time ($T = 2\pi/\Omega$). This assumption is not very strong, it implies that we are able to prepare the state with high fidelity at a fixed rate which is anyway the case for almost any other type of mesoscopic measurement[1]. Thus Ω is the rate at which you prepare your unknown state or equivalently it is the signal main Fourier component. In the tomography protocol, increasing n gives information on faster time components.

This choice of probe functions dictates what is the most convenient basis to use for the rest of the discussion. Indeed, if one writes the excess Wigner function:

$$\Delta W_1(\omega, t) = \Delta W_{1,0}(\omega) + \sum_{n' \in \mathbb{Z}^*} \Delta W_{1,n'}(\omega) e^{in'\Omega t}, \tag{5.3}$$

it is then clear that the time averaged overlap between input 1 state ΔW_1 and a probe function W_2^n sent in input 2 will only keep $n' = \pm n$ terms. Thus, W_2^n enables to reconstruct the n^{th} harmonic of ΔW_1 *i.e.* $\Delta W_{1,n}$. Indeed:

$$\overline{Q_{HOM}(\phi, \omega_{\text{DC}})} = -2e^2 \int \frac{d\omega}{2\pi} \overline{\Delta W_1(\omega, t) \Delta W_2^n(\omega, t)} \tag{5.4}$$

$$= -\frac{4e^3 V_2^{\text{AC}}}{\hbar} \int \frac{d\omega}{2\pi} \; |\Delta W_{n,1}(\omega)| \cos(\phi_n(\omega) - \phi) g_n(\omega - \omega_{DC}). \tag{5.5}$$

Where we defined $\phi_n(\omega)$ as:

$$\text{Re}\,(\Delta W_{1,n}(\omega)) \quad = |\Delta W_{1,n}(\omega)| \cos\,(\phi_n(\omega)) \tag{5.6}$$

$$\text{Im}\,(\Delta W_{1,n}(\omega)) \quad = |\Delta W_{1,n}(\omega)| \sin\,(\phi_n(\omega)) \tag{5.7}$$

and

$$g_n(\omega - \omega_{\text{DC}}) = \frac{f(\omega - \omega_{\text{DC}} - n\Omega/2) - f(\omega - \omega_{\text{DC}} + n\Omega/2)}{n\Omega} \tag{5.8}$$

is a kernel function of width $n\hbar\Omega$ and centered on ω_{DC}. We thus get a noise depending on ω_{DC} and that oscillates with ϕ. To change ω_{DC}, we simply change V_{DC} applied on the Ohmic contact which will shift vertically the Wigner functions in input 2. To explore the overlap in the time domain we shift the time delay between the two input $\Delta\tau$ like in a typical HOM experiment. This will shift the Wigner functions in input 2 horizontally. Varying ϕ, we should expect an oscillating signal at frequency $2\pi n\Omega$. To study this

[1] Apart from single shot read-out measurement.

oscillating signal we chose to define the two following quadratures:

$$X_n(\omega_{DC}) = \frac{\overline{Q_{\mathrm{HOM}}}(\pi, \omega_{\mathrm{DC}}) - \overline{Q_{\mathrm{HOM}}}(0, \omega_{\mathrm{DC}})}{2V_2^{\mathrm{AC}}} \tag{5.9}$$

$$Y_n(\omega_{DC}) = \frac{\overline{Q_{\mathrm{HOM}}}(\frac{3\pi}{2}, \omega_{\mathrm{DC}}) - \overline{Q_{\mathrm{HOM}}}(\frac{\pi}{2}, \omega_{\mathrm{DC}})}{2V_2^{\mathrm{AC}}}. \tag{5.10}$$

and we define $\mathcal{A}_n^2 = X_n^2 + Y_n^2$.

For the peculiar case of $n = 0$, we simply apply a dc bias in input 2. Therefore $\Delta W_2^{(0)} = 0$ and we focus on the excess HBT noise which writes:

$$\overline{\Delta Q_{HBT}} = e^2 \int \frac{d\omega}{2\pi} \overline{\Delta W_1(\omega, t)(1 - 2f_{\mu 2}(\omega))}^t. \tag{5.11}$$

There is actually a link between this quantity and the averaged energy density. Indeed, because only ΔW_1 depends on time, taking the derivative of the previous term with respect to V_2^{DC}, one gets:

$$\frac{\partial \overline{\Delta Q_{HBT}}}{\partial V_2^{\mathrm{DC}}} = \frac{2e^3}{h} \int d\omega \; \Delta W_{1,0}(\omega) \frac{-\partial f}{\partial \omega}(\omega - \omega_{DC}) \tag{5.12}$$

which is exactly a convolution of the average energy distribution $\Delta f(\omega) = \Delta W_{1,0}(\omega)$ [2] and a kernel $-\partial f/\partial\omega$ that tends to a Dirac distribution when T_{el} tends to 0. Therefore this part of the protocol is actually just a spectroscopy of the input state 1 much like in references [36, 61].

In both cases ($n = 0$ or $n \neq 0$), we actually only get a convolution of the quantity of interest $\Delta W_{1,n}(\omega)$ with either $g_n(\omega)$ or $-\partial f/\partial\omega$. This kernel are plotted on figure 5.2. We postpone to section 5.3 the discussion on how we exactly deconvolved these quantities and why it is not straightforward when noise is added on the signal after the QPC.

[2] Indeed $\Delta W_{1,0}(\omega)$ encodes the stationary part of ΔW_1 *i.e.* the energy distribution.

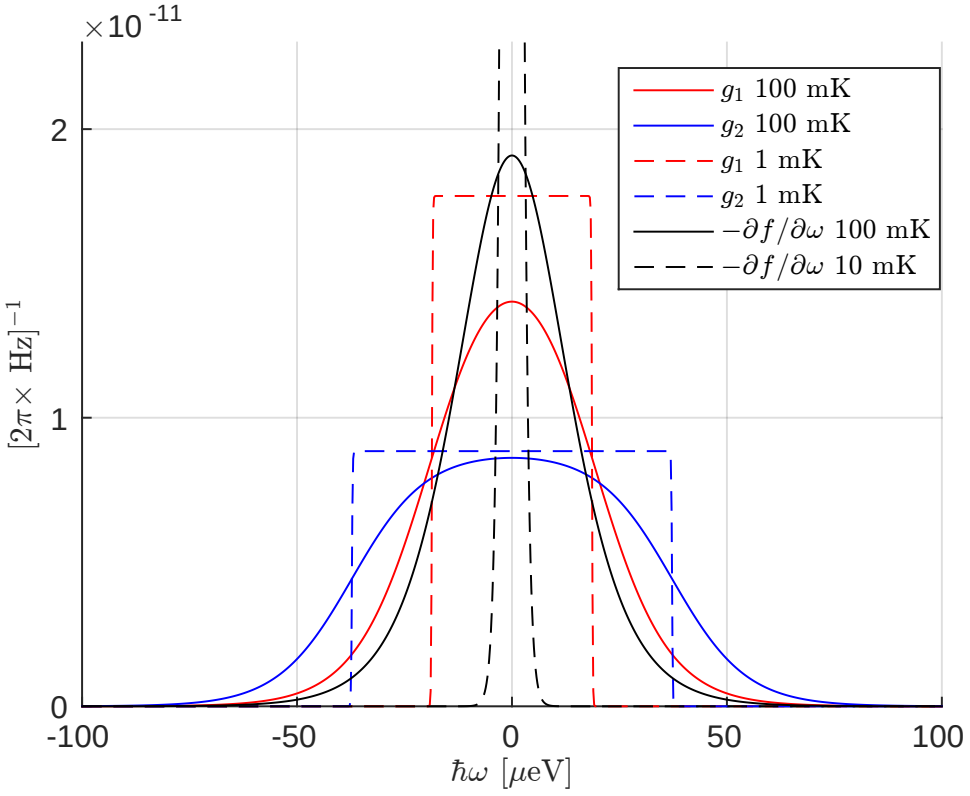

FIGURE 5.2: Plot of a few kernel functions ($-\partial f/\partial\omega$, g_1 and g_2) at different temperatures (1 mK, 10 mK and 100 mK). $-\partial f/\partial\omega$ tends to a Dirac distribution when temperature goes to zero. At 100 mK, the kernel function are smoothed by thermal contributions.

5.2 Results for simple sine drives

5.2.1 Spectroscopy: the n=0 case

Before applying this protocol on the single electron source, we wanted to test it on simpler signals: the dot is set at full transmission $D = 1$ and we only apply a sine drive rather than a square one. Sine drive are ideal candidates for that; indeed, they are simple to create and to characterize independently and theoretical predictions are easy to compute. Moreover, as illustrated on figure 5.3, these signal do not require a lot of steps to be recovered. Indeed, measuring W_n with n only going from 0 to 3 is enough to have a good fidelity for these signals. Another advantage is that Coulomb interactions will not change the signal up to a global complex scalar factor $|S_{11}(\omega)|$. As we have seen in chapter 3, it will just change the global phase of the Wigner function which can be absorbed in the definition of the phase probe. The modulus of this factor can be seen as a renormalization of the excitation drive to a lower value.

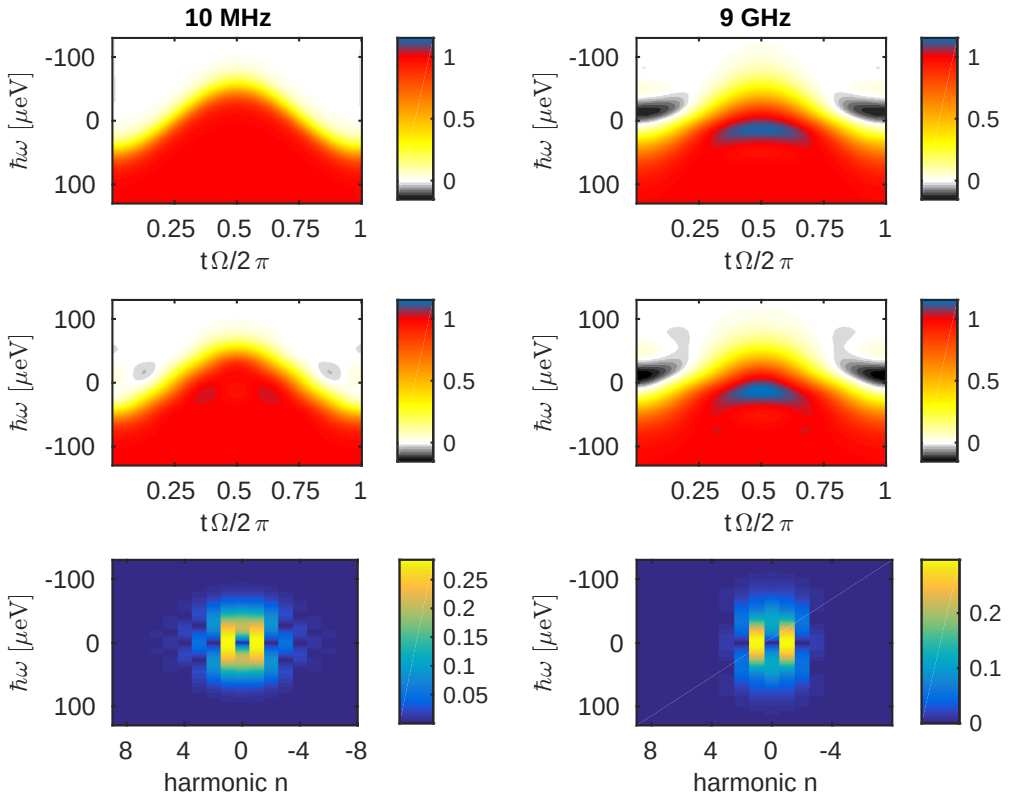

FIGURE 5.3: **Up.** Full Wigner functions at 10 MHz (33μV) and 9 GHz (31μV) at $T_{el} = 90$ mK. **Middle.** Corresponding reconstructed Wigner functions with only 3 harmonics for 10 MHz and 2 harmonics for 9 GHz. **Bottom.** Modulus of corresponding harmonics of Wigner function versus ω. Imaginary part does not exceed 2×10^{-3} so we can fix $\phi_n = 0$ and independent of energy for these drives.

In this section, we will focus first on the part $n = 0$ of the protocol *i.e.* the part that probes the average energy distribution. The procedure is quite standard: for a given V_2^{DC} we measure the noise while the sine drive is on and then again but with the source off (see equation 2.42). We measure $\overline{S}_{33}^{(\mathrm{on,off})} - \overline{S}_{33}^{(\mathrm{off,off})}$ for various V_2^{DC}. This work sets in the general framework of photo-assisted shot-noise which was predicted first by Lesovik *et al.* [155] and then measured in numerous systems such as metallic diffusive wires [156, 247], quantum point contact in GaAs heterostructures [36, 104, 157, 248, 249], tunnel junctions [61, 250–252] and recently in graphene [253]. We applied this procedure for various source drive with different frequencies. For the sake of comparison, we tuned the amplitude of the source drive so as to reach the same value of excess noise $\overline{\Delta S}(V_2^{\mathrm{DC}} = 0)$. This means that although they do not have the same frequency, each of these drives creates the same average number of electron-hole pairs per unit of time.

On figure 5.4, the noise created by each excitation versus the DC bias applied at the other input of the beam splitter is represented. The electronic temperature extracted

from the mere DC shot noise (black curve) is ($T_{el} = 90$ mK). Compared to references [250, 252], we do not see clear change of slope (upper panel), this is mainly because they used a multi-mode, low impedance tunnel junction which enables to maximize the current going through the partitioner and thus shot-noise. This enhances the signal-to-noise ratio. Another advantage of low impedance tunnel junction is that they generate a lower thermal equilibrium noise and produce less Joule heating which enables to use higher RF power and DC bias without heating electrons to much. Despite all, in our case, theory can fully account for this smearing of kinks due to temperature and we see that full lines are in agreement with our experimental results. On the lower panel of figure 5.4, the excess noise is plotted *i.e.* we subtracted the DC contribution to shot-noise (black curve in upper panel) to the other upper panel curves. We see that at $V_2^{\mathrm{DC}} = 0$, the three curves give the same excess noise which means each of the drive creates the same number of particles (electrons and holes) per unit of time. This excess noise then decreases smoothly as we increase $|V_2^{\mathrm{DC}}|$. However, the higher the frequency, the weaker the decrease is. Another way to say this is that the higher the frequency drive, the higher, we need a DC bias to cancel the excess noise. This can be interpreted as due to photo-assisted transport. We also measured the same signal but with excitation at 12 GHz and 15 GHz (not represented for the sake of clarity) which fall as expected in between 9 and 20 GHz.

There are several things to check to be sure what we measure is really a photo-assisted effect. First of all, one could suspect that bringing high power, high frequency signal on a high impedance sample would dissipate heat; not necessary on the Ohmic contact otherwise we would also have this effect with DC biasing but on the surrounding conductors and materials (*e.g.* substrate, bonding pads ...) which in turn would heat the electron gas. Could this heating effect raise the electronic temperature high enough to be responsible for the observed increase of noise at zero bias (between 7 and $10 \times 10^{-10}\mathrm{V}^2$) ? The measured excess noise can be converted into an increase of temperature with the calibration presented in section 2.4.3.3; we obtain $\Delta T_{el} \simeq 4$ mK and we did not see such an increase of the mixing chamber temperature. However this may not rule out heating effects completely. Indeed, below 100 mK electrons do not thermalize well with phonons therefore such a small increase of temperature in the electronic temperature might not be easily detectable by the mixing chamber *RuO* thermometer. Nevertheless, it should give a really different shape to the excess noise versus V_2^{DC} as we see on figure 5.6.

To model heating effects on noise, we suppose that the power is delivered on one contact only and therefore we have two Fermi distributions f_1 and f_2 with different temperatures $T_1 > T_2$ coming on the central QPC which creates some partition noise [10]:

$$\overline{S_{\mathrm{ON,part}}} = R^2\overline{S_{11}} + (1-R)^2\overline{S_{22}} + R(1-R)\overline{Q}, \tag{5.13}$$

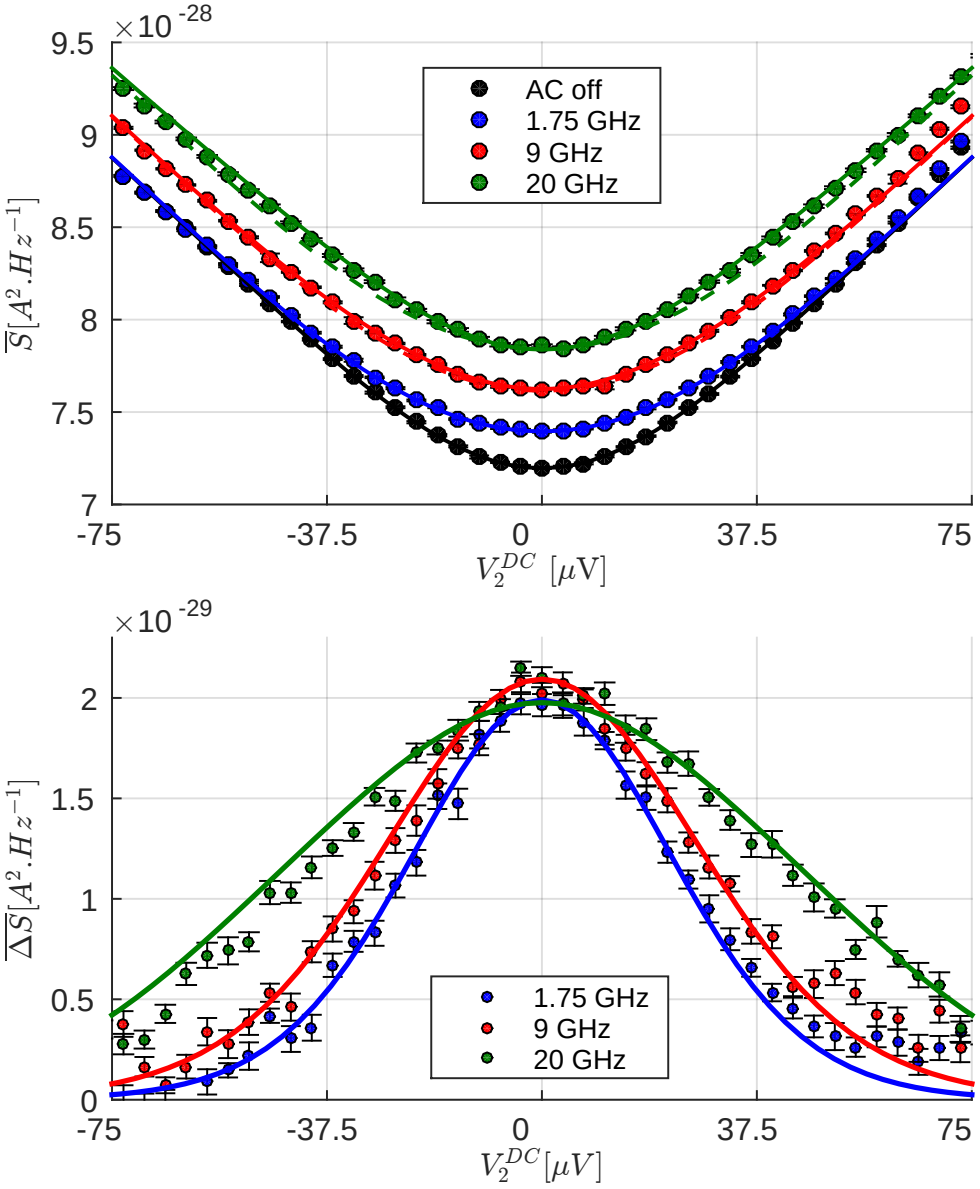

FIGURE 5.4: **Upper.** Low frequency noise with respect to V_2^{DC} for different sine drive excitations (amplitude: 28μV at 1.75 GHz, 31μV at 9 GHz and 40μV at 20 GHz) . For clarity, red and green curves are shifted upward by 2.5×10^{-29} and 4×10^{-29} A^2.Hz^{-1} respectively. Full lines represent theoretical expectations based on photo-assisted shot noise theory. **Lower.** Subtraction by pure DC noise (black curve on the left panel) with theory in plain line. Error bars are standard error to the mean.

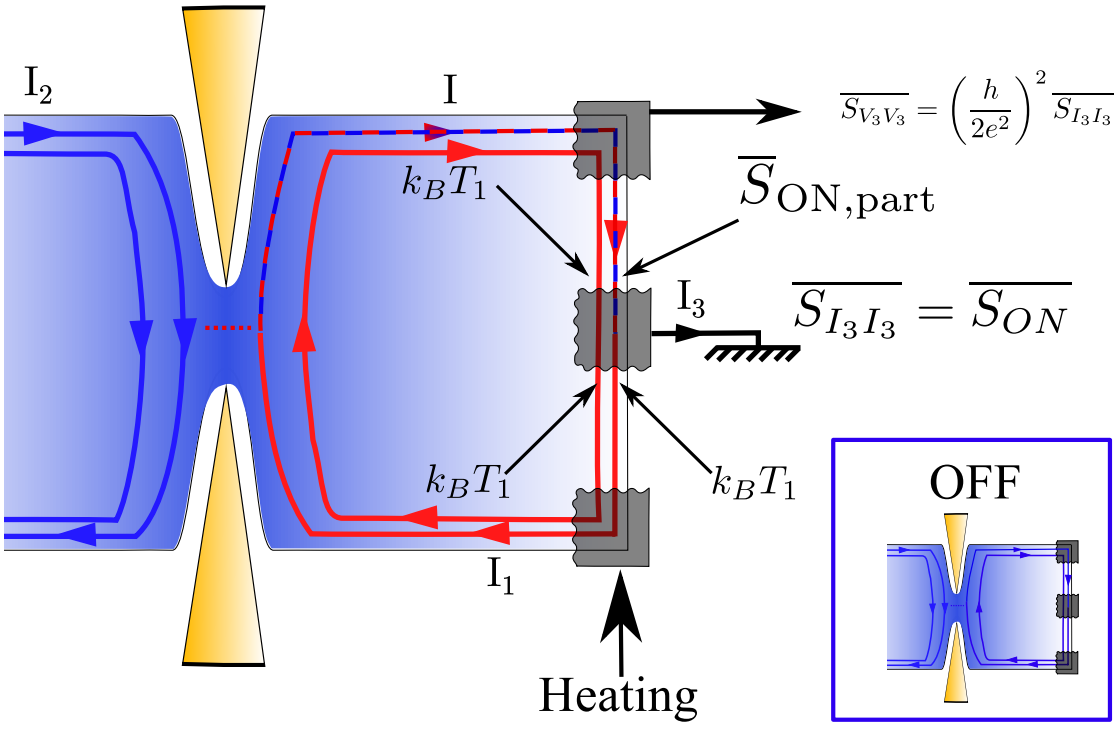

FIGURE 5.5: Scheme of the model to take heating on one side into account. (Insert) When the source is off there is only equilibrium noise and all channels are "cold".

with $S_{11} = \frac{2e^2}{h} k_B T_1$ and $S_{22} = \frac{2e^2}{h} k_B T_2$[3]. We have to add the thermal fluctuations of the fully reflected inner edge and fluctuations of the channels leaving the contact measurement which are also heated (see scheme on figure 5.5).

$$\overline{S_{ON}} = (3+R^2)\overline{S_{11}} + (1-R)^2\overline{S_{22}} + R(1-R)\overline{Q} \tag{5.14}$$

$$\overline{S_{ON}} = \frac{2e^2}{h}\left((3+R^2)k_BT_1 + (1-R)^2 k_BT_2 + R(1-R)\int d\omega\,[f_1 + f_2 - 2f_1f_2]\right). \tag{5.15}$$

When $T_1 = T_2$ we recover $\overline{S_{ON}} = 4k_BT_1\frac{2}{R_K}$ for any R as expected. On figure 5.6 we see that the excess noise produced only by such a heating effect has no to little decrease with respect to V_2^{DC}. The exact temperature increase in one input was left as an adjustable parameter to match the corresponding excess noise. We do not see why heating would be less effective while increasing the DC bias, therefore we can rule out this effect to explain the observed excess noise. We also checked directly that the RF signal did not add non-partition noise simply closing fully the QPC to connect with perfect reflection $R = 1$ the RF input with the Ohmic contact on which the electronic temperature is measured. We did not see an increase larger than $2 \times 10^{-11}\mathrm{V}^2$ *i.e.* 0.08 mK.

[3]The factor 2 comes from the engineer convention that counts positive and negative frequencies.

In a second time, we also have to check that it is not a simple averaging of the DC shot noise curve. Indeed, if there are no photon absorptions, the chemical potential varies adiabatically with a sine shape *i.e.* we can write the Wigner function as $W(\omega, t) = f_{\mu(t)}(\omega)$ and not as a sum of Bessel functions like in equation 2.28. One could suspect that what we observe is simply an averaging effect:

$$\overline{\Delta S}(V_2^{\mathrm{DC}}) = \frac{1}{T}\int_0^T dt\, \left[\overline{S_{\mathrm{OFF}}}\left(V_2^{\mathrm{DC}} + V_2^{\mathrm{AC}}\cos\left(\Omega t\right)\right) - \overline{S_{\mathrm{OFF}}}\left(V_2^{\mathrm{DC}}\right)\right], \tag{5.16}$$

where $T = 2\pi/\Omega$ is the period of the drive. This is what we will call classical (or adiabatic) averaging. This expression should stand only when we do not expect photon absorption event *i.e.* when $\hbar\Omega < k_B T_{el}$. On the other hand, if photon assisted effect occurs, one should get also 5.15 replacing f_1 by $\overline{W_1(\omega, t)}^t$. Therefore using equation 2.28 we recover the analog of Lesovik formula for a 4 terminal geometry [155]:

$$\begin{aligned}
\overline{S_{\mathrm{ON}}}(V_2^{\mathrm{DC}}, V_2^{\mathrm{AC}}) =& \frac{2e^2}{h}\Bigg((3+R^2)4k_BT_1 + (1-R)^2 4k_BT_0 \\
&+R(1-R)\int d\omega \left[f_0 + (1-2f_0)\sum_{n=-\infty}^{\infty}\overline{J_n\left(\frac{2eV_2^{\mathrm{AC}}\cos(\Omega t)}{\hbar\Omega}\right)}^t \frac{1}{e^{\frac{eV_2^{\mathrm{DC}}+\hbar(\omega+n\Omega/2)}{k_BT}}+1}\right]\Bigg) \\
=& \frac{2e^2}{h}\Bigg((3+R^2)4k_BT_1 + (1-R)^2 4k_BT_0 \\
&+R(1-R)\sum_{n=-\infty}^{\infty} J_n^2\left(\frac{eV_2^{\mathrm{AC}}}{\hbar\Omega}\right)\left(eV_2^{\mathrm{DC}} + n\hbar\Omega\right)\left(\coth\left[\frac{eV_2^{\mathrm{DC}} + n\hbar\Omega}{2k_BT_{\mathrm{el}}}\right]\right)\Bigg)
\end{aligned} \tag{5.17}$$

where J_n are the Bessel functions of the first kind. The two models (quantum and adiabatic) are also compared on figure 5.6. For models without heating effects, the amplitude of the drive is adjusted to match the excess noise around $V_2^{\mathrm{DC}} = 0$ V. For models taking heating into account, we choose the increase of electronic temperature so as to match the excess noise on the tails of the curve (at 9 GHz only), where pure PASN should give no excess noise and adjust the amplitude of the drive to match with the data around $V_2^{\mathrm{DC}} = 0$. Because of possible heating effects, it is not clear if we really measure photo-assisted effect at 9 GHz. The effect is however definitely present at 20 GHz (see figure 5.7) where it is clear that neither classical averaging nor heating effects nor a combination of both can quantitatively account for the variation of excess noise with bias. Both at 9 and 20 GHz, the disagreement with the dashed blue line enables us to rule out pure heating effects as an explanation for excess noise. Moreover, the adjusted amplitudes are always close to $\approx 30\mu$V which is in agreement with our estimate of the expected drive amplitudes.

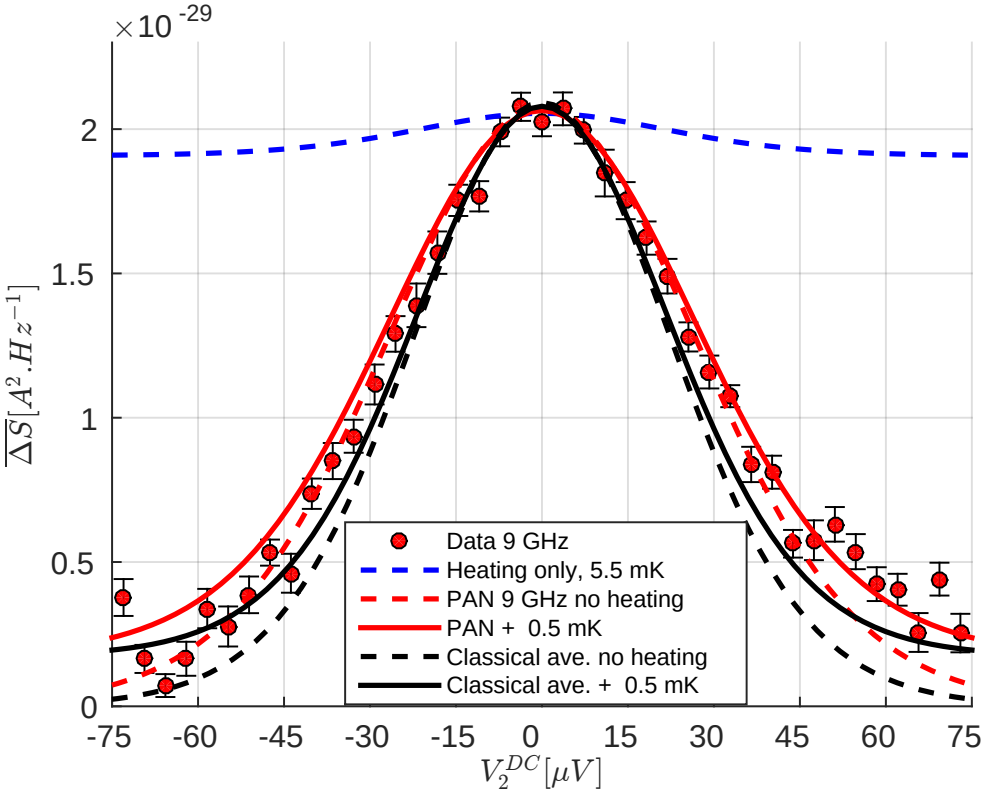

FIGURE 5.6: Comparison of different models with data at 9 GHz. The theoretical result at 100 mK for photo-assisted shot noise is in dashed red line and can be compared to the effect of classical averaging (black dashed line). The amplitude of the drive is let as an adjustable parameter for both. The dashed blue line represents what is expected if all the observed noise was due to heating effect. From its shape we can clearly rule out this effect. A slight increase of temperature is taken into account for the full red and black line.

Photo-assisted effects being hard to observe at 9 GHz although $\hbar\Omega \simeq 4k_BT$ reveals the importance of probing time dependent information. Indeed, as we will see in the following section, combined with data at $n \neq 0$ *i.e.* coherence terms, the Wigner function clearly exhibits non-classical values which are sign for photon absorption events.

Now that we can trust our data, we can derivate $\overline{\Delta Q}$ with respect to V_2^{DC} and then deconvolve by $\frac{\partial f}{\partial \omega}$ with a Wiener filter (see section 5.3) to obtain the energy distribution. The results are presented on figure 5.8. It corresponds to the excess energy distribution: positive values at positive energies correspond to the creation of electrons whereas negative values at negative energies correspond to the creation of holes in the Fermi sea. What can be clearly seen is the difference in energy width of the distribution. The distribution width created by the excitation at 1.75 GHz is mainly governed by eV_{exc} whereas the one at 20 GHz is mainly governed by $\hbar\Omega$. This is a manifestation of photo-assisted effects: 20 GHz photons can create electron-hole pairs with energy up to $eV = hf = 83\mu$eV. We recover the stair case like structure smeared by temperature.

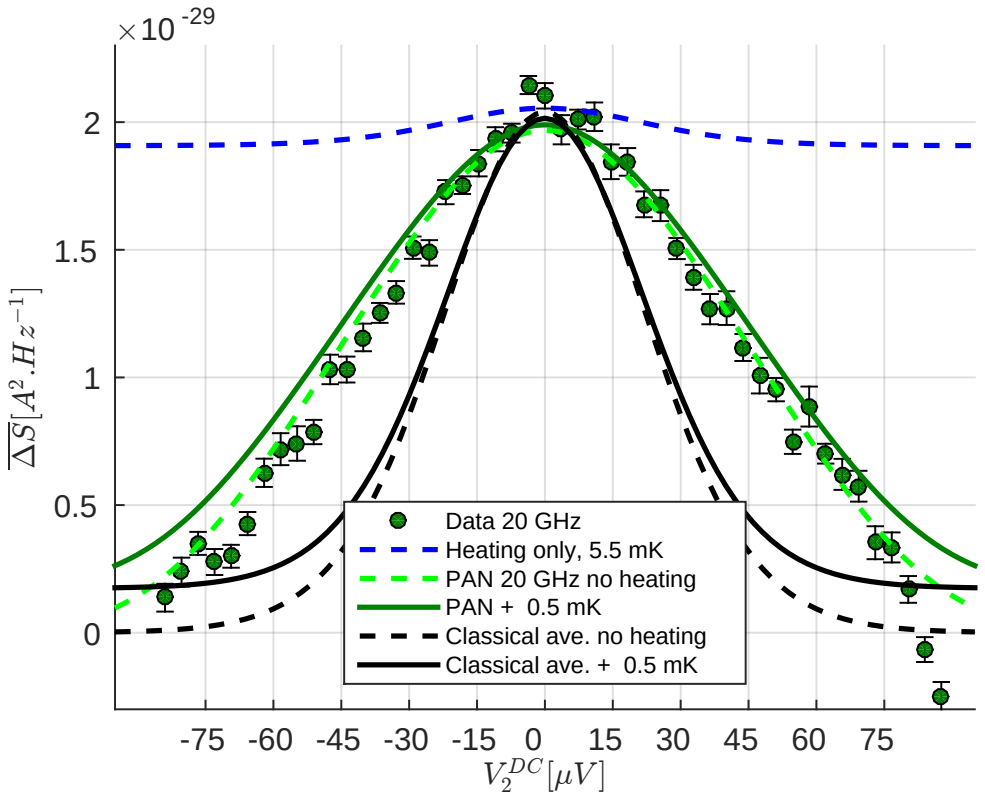

FIGURE 5.7: Comparison of different models with data at 20 GHz. The theoretical result at 100 mK for photo-assisted shot noise is in dashed green line and can be compared to the effect of classical averaging (black dashed line). The amplitude of the drive is let as an adjustable parameter for both. The dashed blue line represents what is expected if all the observed noise was due to heating effect. From its shape we can clearly rule out this effect together with classical averaging effects.

Now we know how to recover energy distribution for any kind of signal but what is more challenging for non-stationary signals is to recover also time domain distribution, this is what we will see in the following section.

5.2.2 Recovering time domain information: $n \neq 0$

Energy distribution is not sufficient to reconstruct completely the electronic wave function of the signal. For non-stationary signal it is crucial to recover off-diagonal coherence terms. As mentioned previously, we add on the probe an excitation drive at pulsation $n\Omega$ with a small amplitude $eV_2^{\mathrm{AC}} < \hbar n\Omega$. The two signals are synchronized and can be delayed with ± 7 ps accuracy thanks to a double output arbitrary waveform generator. We also tested it with a variable mechanical dephaser with a precision $\pm 2ps$ but that did not allow variation of $\delta\tau$ larger than 680 ps. We measured the noise varying $\phi = n\delta\tau\Omega$ over one period or more. An example of such measurement is presented in figure 5.9 for $\Omega/2\pi = 9$ GHz at zero bias for $n = 1$ and $V_2^{\mathrm{DC}} = 35.6\mu$V for $n = 2$. We get an oscillating

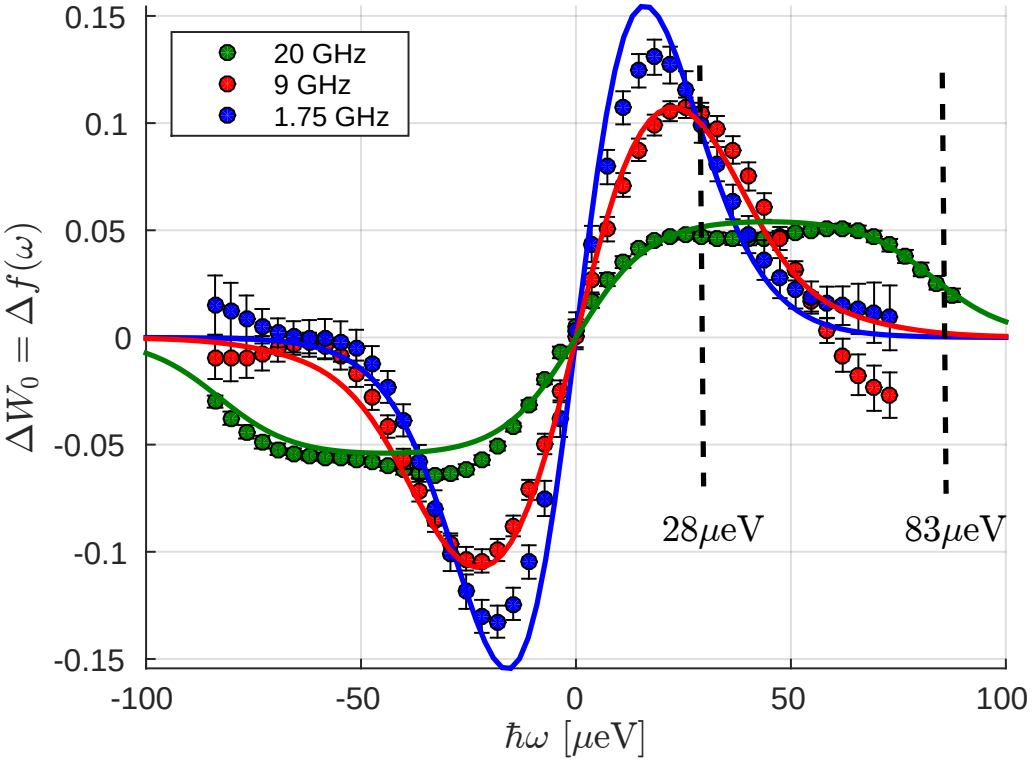

FIGURE 5.8: Results of derivation together with theory. Frequency effect can be clearly seen on the energy width of the distribution. Whereas the width of the low frequency drive is governed by its amplitude (28μV), the one for the 20 GHz drive is governed by $\hbar\Omega/e = 83\mu$V. Error bars are standard error to the mean.

signal at pulsation $n\Omega$. These results tell us that the signal under study has non-zero off-diagonal terms. To reconstruct $\Delta W_n(\omega)$ we use the two quadratures X_n and Y_n defined in equations 5.9 and 5.10. They are equal, up to a amplification factor to:

$$X_n(\omega_{DC}) = \frac{-4e^3}{h} \int d\omega Re(\Delta W_{n,1}(\omega)) g_n(\omega - \omega_{DC}) \tag{5.18}$$

$$Y_n(\omega_{DC}) = \frac{-4e^3}{h} \int d\omega Im(\Delta W_{n,1}(\omega)) g_n(\omega - \omega_{DC}). \tag{5.19}$$

This expressions are only valid if equation 5.2 is valid *i.e.* if we can stop the development of W_2^n at first order in $\frac{eV_2^{\mathrm{AC}}}{n\hbar\Omega}$. We check in section 5.2.3 that we are indeed in a regime where X_n is linear in V_2^{AC}. Conversely, we can also define the polar quantity:

$$\mathcal{A}_n(\omega) e^{i\phi_n(\omega)} = X_n(\omega) + iY_n(\omega). \tag{5.20}$$

As previously done for the spectroscopy procedure, we now measure $X_n(\omega)$ and $Y_n(\omega)$ as a function of ω_{DC}. This will give respectively $Re(\Delta W_n(\omega))$ and $Im(\Delta W_n(\omega))$. For each frequency and each n, we checked that the phase ϕ_n did not vary with V_2^{DC} (*i.e.* with ω). Values of the probe amplitude are summarized on table below. In some cases, we

averaged the results of several tomography steps taken with different probe amplitudes. Once normalized by V_2^{AC}, data gave the same results.

Parameter	10 MHz	9 GHz
V_1 (Source)	$33.0 \pm 2.2\mu V$	$30.9 \pm 1.0\mu V$
$V_2^{n=1}$	$3.0\mu V$ and $5.2\mu V$	$5.9 \pm 0.7\mu V$
$V_2^{n=2}$	$5.2\mu V$, $9.0\mu V$ and $11.9\mu V$	$31.7 \pm 1.8\mu V$
$V_2^{n=3}$	$19.3 \pm 1.6\mu V$	not measured

Actually we cannot really access ϕ_n but only its difference with respect to the phase coming on the probe contact. Increasing n for frequencies in the megahertz range may not change significantly this absolute phase because the signal wavelength is much longer than the propagation length in the cryostat. Indeed, we checked that the relative phase between source and probe did not change while varying n when the source is driven at 10 MHz. However, it is not the case when we apply signals in the gigahertz range. From one n to another the absolute phase on the probe contact changes, shifting the real zero for ϕ_n. Therefore, it makes no sense to combine all $|\Delta W_n|e^{i\phi_n}$. To reconstruct the 9 GHz sine drive Wigner function, we suppose that $\phi_n(\omega) = 0$ for any n and any ω for a sine drive on an Ohmic contact or applied to the top gate in an open dot situation ($D = 1$). This hypothesis is confirmed by Floquet theory and, as mentioned above, we checked it for 10 MHz. At 9 GHz we can only check that ϕ_n does not depend on ω. We will see in section 5.4 how to use the phase measurements at $D = 1$ as phase references to reconstruct more complex phase dependences in particular when $D \neq 1$.

To deconvolve properly ΔW_n from $\mathcal{A}(\omega)e^{i\phi_n(\omega)}$, (or X_n and Y_n) we used a Wiener filter (details for this procedure will be explained in part 5.3). Although it cannot remove all the noise added after the convolution it gives the estimate of $\Delta W_n(\omega)$ with the least error for any ω (not only multiple of $n\hbar\Omega$). Results for sine drives at 10 MHz ($V_{exc} = 33 \pm 2\mu V$) and 9 GHz ($V_{exc} = 31 \pm 1\mu V$) are presented on figure 5.10. Notice that off-diagonal coherence is observed both for the quantum and "classical" signal: even for a mere Fermi sea with an adiabatically oscillating chemical potential there exists off-diagonal coherence in time domain.

It can become quite tedious to apply this procedure for a large number n. We checked with simulations that for these test signals, going up to $n = 3$ is sufficient to reconstruct almost completely the signal (see figure 5.3 for comparison), higher ΔW_n having less weight. For 9 GHz it was difficult to inject enough power at 27 GHz on the probe

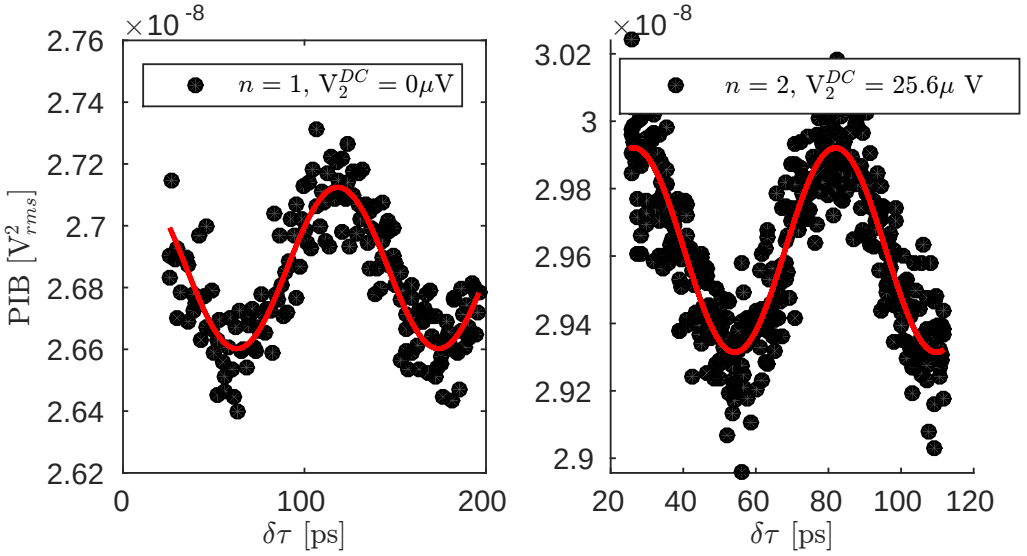

FIGURE 5.9: **Left.** Example of oscillations of $\overline{Q_{HOM}}$ at $V_2^{\mathrm{DC}} = 0\mu$V versus $\delta\tau$ for source and probe signals both at 9 GHz. **Right.** Same source but probe at 18 GHz and $V_2^{\mathrm{DC}} = 35.6\mu$V. As expected, we observe a doubling of the frequency of oscillations with $\delta\tau$. Full lines are fit to extract $\mathcal{A}_n$ and ϕ_n.

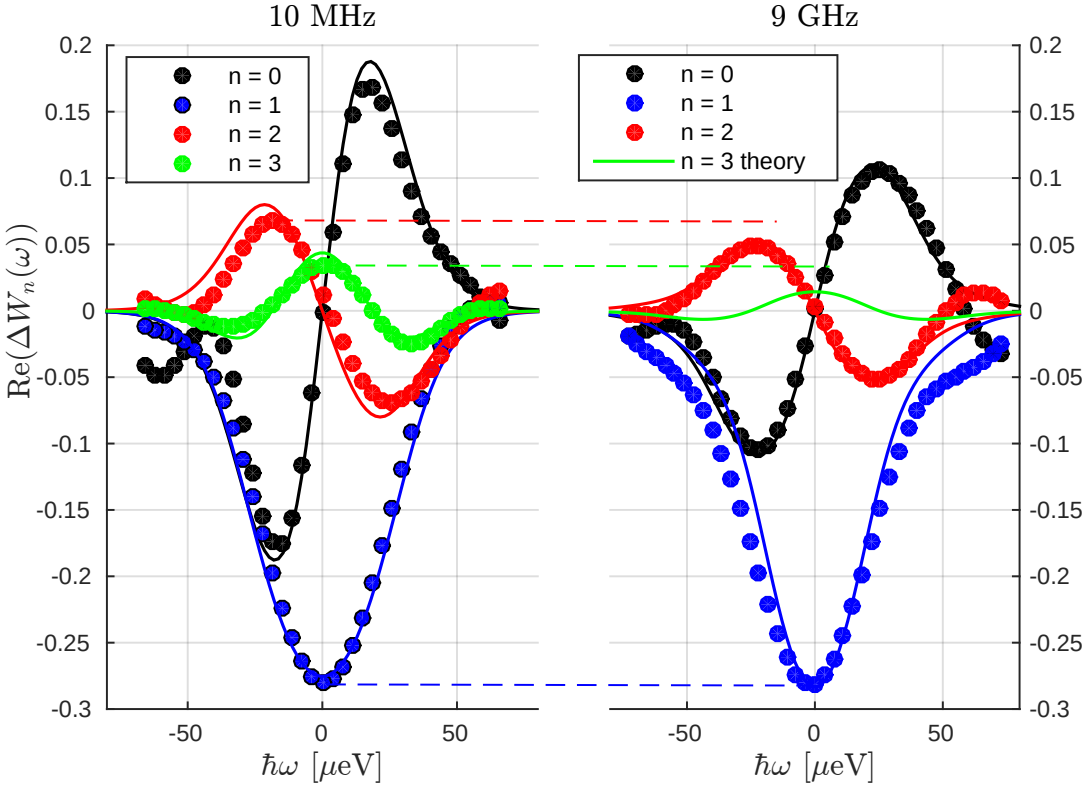

FIGURE 5.10: **Left.** $Re(\Delta W_n(\omega))$ (after deconvolution) for n from 0 to 3 for a sine drive at 10 MHz and $33 \pm 2\mu V$. **Right.** Same results for a sine drive at 9 GHz and $V_{exc} = 31 \pm 1\mu V$. Full lines correspond to theory after deconvolution. Guides for the eyes enable to observe the relative weight of each harmonic. Although $n = 1$ contributions have the same amplitude. The other harmonics have a higher weight for the classical drive.

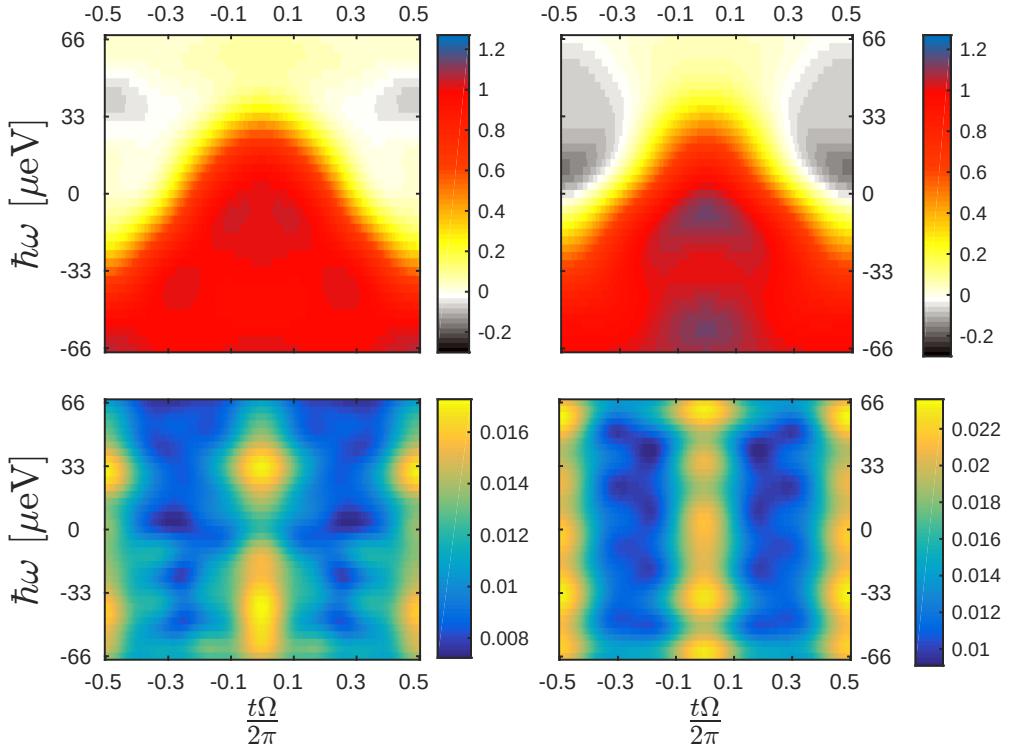

FIGURE 5.11: Reconstructed Wigner functions (**up**) and their standard error to the mean (**low**) for signal at 10 MHz (**left**) and 9 GHz (**right**).

contact and the expected signal was below our detection limit. Results agree well with theoretical model where we calculated numerically overlap between Wigner functions obtained using Floquet scattering formalism.

We can now add all this contributions to reconstruct the full Wigner functions again assuming that for this simple sine drives $\phi_n = 0$ for any n. We actually plot:

$$W_1(\omega, t) = f_{\mu=0} + \Delta W_1(\omega, t) \tag{5.21}$$

$$= f_{\mu=0} + \Delta W_{1,0}(\omega) + 2\sum_{n=1}^{2,3} \mathrm{Re}\left(\Delta W_{1,n}(\omega)\right)\cos(n\Omega t). \tag{5.22}$$

The results are presented on figure 5.11 for 10 MHz and 9 GHz. Error bars are absolute standard error to the mean. They are computed taking the deconvolution process into account. We randomly duplicate each data point 1000 times according to a Gaussian law centered on the value of the data point with a standard deviation corresponding to error bars. Each of these 1000 sets of random $\mathcal{A}_n$ and $\Delta W_{1,0}$ is passed through the deconvolution process. We then obtain a statistical ensemble of Wigner functions from which we can extract a mean value and a standard deviation which is our final error bar.

We notice a quantitative difference between the two reconstructed functions, above error bars. Theoretical expectations are represented on figure 5.3 with or without taking into account the finite number of measured harmonics. Globally there are more deviations from theory at energy far away from the Fermi level. This has two main explanations. First, the QPC is not perfectly energy independent especially at high bias where we suppose we might activate non-linearities. This deviation could already be seen on the spectroscopy. Second, the deconvolution process has some edge effects (which could already be seen on figure 5.10) inducing numerical errors on the estimation of W close to our uppermost and lowest energy values. Finally, another reason for systematic error is the noise added on the signal (actually the noise of the noise) after the beam splitter. The Wiener filter can remove partly its effect but not completely. It insures that the error between our estimate and the real value of ΔW_n is minimal but it cannot be zero.

Despite all these errors we manage to quantitatively discriminate between a classical and a quantum signal. On figure 5.12 we plotted cuts at fixed energy (-11 and $11\mu e$V) of the two functions. The "quantum" signal has significant negative and above one values, which is a mark of non-classical states. We can also clearly see the "classical" signal reaching a plateau at one or zero. These plateaus help to understand why we actually needed more harmonics of W to reconstruct the classical signal. Indeed, a square shape function has a higher harmonic content than an almost sine one. Another way to discuss this difference is in term of number of RF photons. Indeed, for the 10 MHz signal we have $eV_{exc} > \hbar\Omega$ which implies a non negligible fraction of many photon processes, contrary to the 9 GHz case where $\frac{eV_{exc}}{\hbar\Omega} = 0.83$ which implies almost only one photon processes. These multi-photon processes are encoded in $\Delta W_{n\neq 1}$ and it explains why they have higher weights for this particular amplitude V_{exc} at 10 MHz. Going to $eV_{\mathrm{exc}} < \hbar\Omega$ for this frequency would have required too low excitation amplitude ($eV_{\mathrm{exc}} < k_B T$) to be detected with our set up.

5.2.3 Probe characterization

As mentioned at the beginning, this protocol only works if we know perfectly well the probe signal to deconvolve the noise from it. In particular, we have to check that the first order expression of W_2^n (see equation 5.2) is indeed valid. This implies to check that we are in the linear regime where we can assume $eV_2^{\mathrm{AC}} \ll \hbar\Omega$ and thus are able to normalize X_n and Y_n by V_2^{AC}. First we need to know the real amplitude of the drive applied on the Ohmic contact. This is done with the calibration procedure presented in section 2.4.3.5. On figure 5.13 are presented calibrations of the amplitude with noise for 9 and 18 GHz drive.

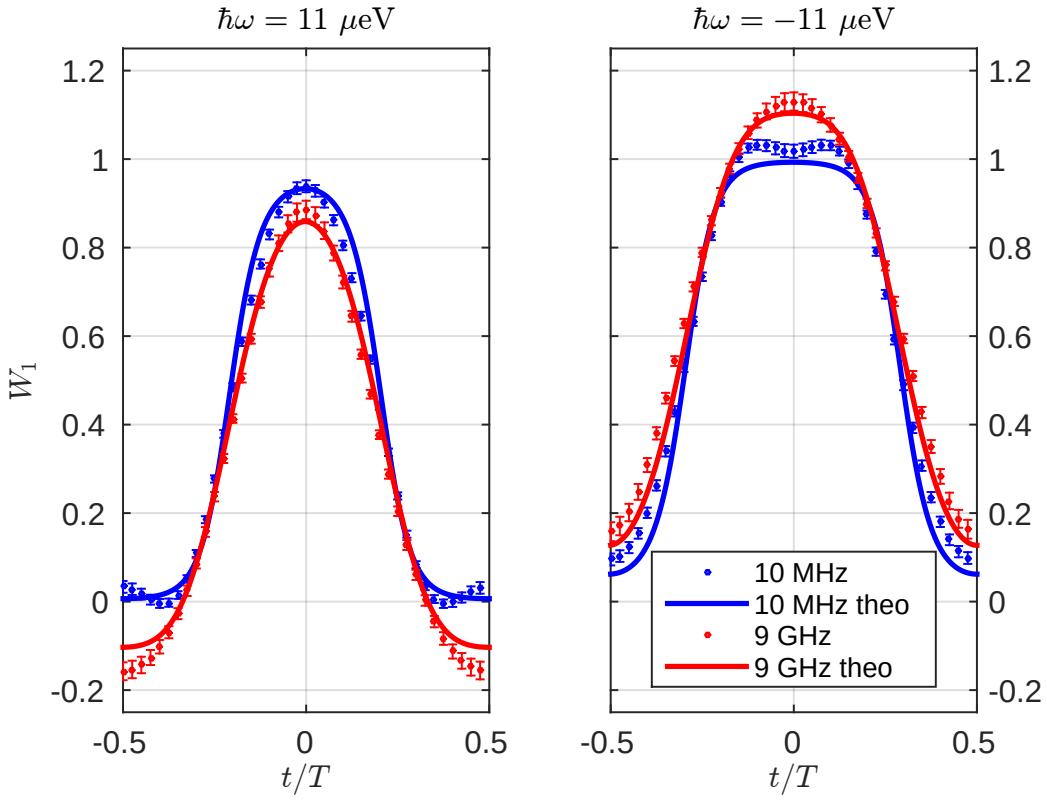

FIGURE 5.12: Cuts at 2 different energies of the two Wigner functions with the theoretical predictions. We clearly see that the classical signal is bounded between classical probability values 0 and 1 whereas the quantum signal has a wider range of values.

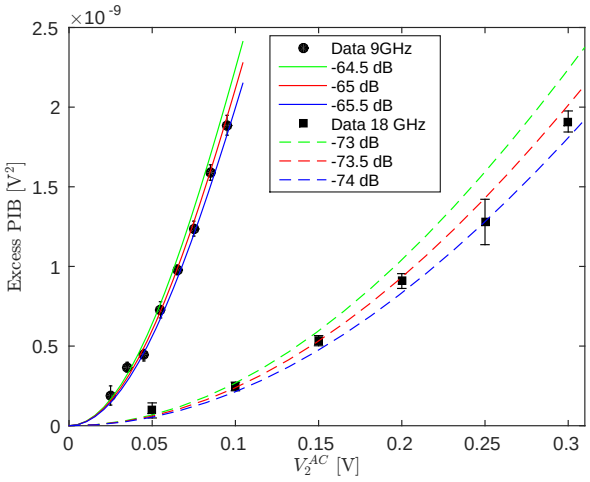

FIGURE 5.13: Excess integrated power versus AC amplitude of the drive for 2 frequencies (9 and 18 GHz), at filling factor 2. Lines correspond to PIB computation with a DC shot noise calibration to determine factor $G^2 \int |Z(\omega)|^2 d\omega R(1-R)$ and electronic temperature, only the attenuation is left as a fitting parameter. From this we deduce the drive amplitude applied on the Ohmic contact.

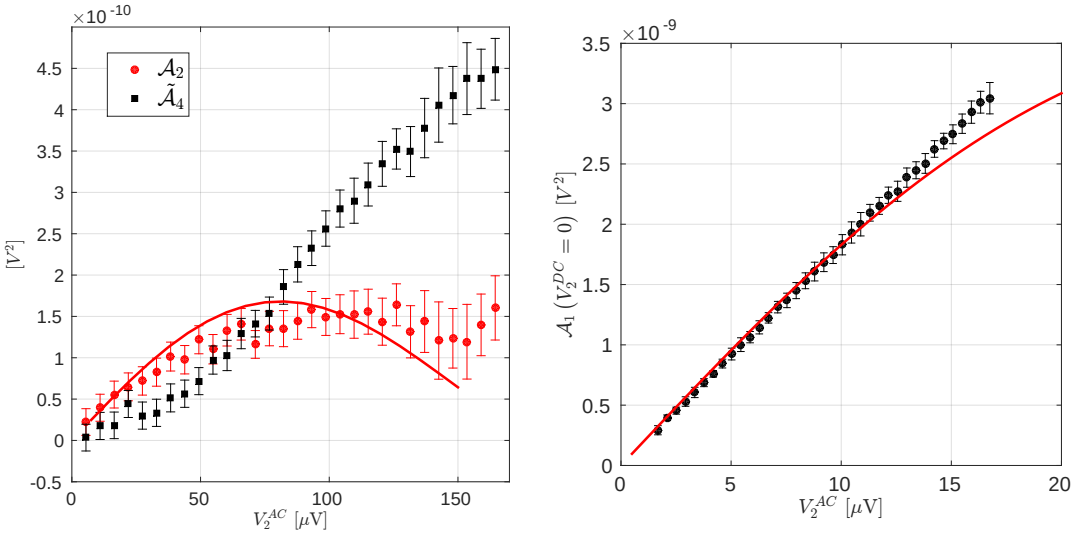

FIGURE 5.14: **Left.** Amplitude of oscillations with $\delta\tau$ at $n = 2$ (*i.e.* $\mathcal{A}_2$) versus V_2^{AC} at fixed $V_2^{\mathrm{DC}} = 29.2\mu$V. (Source at $f = 9$ GHz and amplitude $\simeq 25\mu$V). Theory for $\mathcal{A}_2$ is in full red line. $\mathcal{A}$ is extracted with a fit where the period is imposed. Actually we noticed another oscillation superimposing with twice the frequency so we fitted the noise oscillation with the sum of two sine (one at 18 GHz the other at 36 GHz) and plotted here the deduced two amplitudes. $\tilde{\mathcal{A}}_4$ is this second amplitude. Note that it is not exactly the same as $\mathcal{A}_4$ which would have required to impose only 36 GHz and to be able to calibrate the amplitude of the drive. The appearance of such doubling of oscillation might be due to some nonlinear effects in the mechanical dephaser generating a second harmonic on the probe. This non-linearity is negligible in the regime of the tomography where we imposed $V_2^{\mathrm{AC}} = 32\mu$V on the probe. We still recover a linear behavior for $\mathcal{A}_2$ at low V_2^{AC}. **Right.** Amplitude of oscillations with $\delta\tau$ at $n = 1$ ($\mathcal{A}_1$) versus V_2^{AC} at fixed $V_2^{\mathrm{DC}} = 0\mu$V. Source at 10 MHz with $\simeq 31\mu$V amplitude. $\mathcal{A}$ is extracted with a fit where the period is imposed. Theory is in plain red line. The linear regime is nicely resolved and fits to theory to a large extend.

The linear regime can be checked experimentally simply measuring at a fixed V_2^{DC}, oscillations $\mathcal{A}_n$ versus V_2^{AC}. This is what is plotted on figure 5.14 for data at 9 GHz for $n = 2$. We clearly see a linear regime at low V_2^{AC}; we put ourselves to the higher end of this regime ($V_2^{\mathrm{AC}} \simeq 30\mu$V) so as to maximize the signal-to-noise ratio. On this last figure we see the appearance of a nonlinear phenomena leading to second harmonic generation and therefore to the appearance of another oscillation with twice the frequency. The amplitude of this other oscillation has been labeled $\tilde{\mathcal{A}}_4$ and plotted in black. This oscillation is only parasitic and it is hard to get any relevant information out of it since we hardly know the amplitude of this second harmonic. The only thing that seems clear is that the generation of this second harmonic is not linear in the amplitude V_2^{AC}, probably quadratic and due to the mechanical dephaser. Because we used a relatively small amplitude for V_2^{AC} at $n = 2$ for 9 GHz, it is reasonable, as we have done since the beginning, to neglect this effect at small V_2^{AC}. For comparison, a similar set of data is represented on figure 5.14 for $n = 1$ at 10 MHz.

We have seen here the basic principle and typical results of this protocol however we will

see in the following part that going from $-\frac{\partial\overline{\Delta Q_{HOM}}}{\partial V_{DC}}$ to $\Delta W_{1,0}$ or from $\mathcal{A}_n$ to $\Delta W_{1,n}$ is actually not that straightforward; especially when noise is added by the measurement apparatus from the QPC up to the spectrum analyzer.

5.3 How to properly deconvolve a noisy signal: the Wiener filter

5.3.1 The problem

We are in the case where the quantity we observe $\widetilde{\Delta W_n}(\omega)$ can be modeled as a convolution of the signal we want: $\Delta W_n(\omega)$, with an *apparatus function* $g_n(\omega)$ which is known *a priori*. This apparatus function adds an independent stationary noise $b(\omega)$ of power spectrum density $\Gamma_b(\tilde{\omega})$:

$$\widetilde{\Delta W_n}(\omega_{DC}) = \int_{-\infty}^{+\infty} \Delta W_n(\omega) g_n(\omega_{DC} - \omega) d\omega + b(\omega_{DC}), \tag{5.23}$$

where $\tilde{\omega}$ is the conjugate variable of ω with respect to the Fourier transformation TF. We are looking for a complex filter function $H(\tilde{\omega})$ such that:

$$\Delta W_n(\omega) = TF^{-1}\left[H^*(\tilde{\omega})\, TF\left[\widetilde{\Delta W_n}(\tilde{\omega})\right]\right]. \tag{5.24}$$

Without any noise, the solution is obvious: $H = G(\tilde{\omega}) = TF(g_n(\omega))$ is the complex transfer function corresponding to the filter $g_n(\omega)$. In our case we know analytically g_n so it is easy to compute:

$$\Delta W_n(\omega) = TF^{-1}\left[\frac{TF[\widetilde{\Delta W_n}](\tilde{\omega})}{G(\tilde{\omega})}\right]. \tag{5.25}$$

However, because $\Gamma_b(\tilde{\omega}) \neq 0$, the numerator of this expression will converge to finite value at high $\tilde{\omega}$ whereas the denominator will converge exponentially to zero, therefore the whole expression will diverge at high $\tilde{\omega}$. Thus, if one is not cautious, the deconvolved signal will have giant unphysical rapid oscillations. On one hand, one needs to set a cut-off on H at high $\tilde{\omega}$ to prevent this; on the other hand if this cut-off is too low, the resulting deconvolution might miss physical features varying rapidly with ω *i.e.* there will be too much averaging. How to find the optimal cut-off?

5.3.2 The solution

The answer to this question was found by Norbert Wiener in the 40's [254] and writes:

$$H(\tilde{\omega}) = \frac{G^*(\tilde{\omega})}{|G(\tilde{\omega})|^2(\tilde{\omega}) + \frac{\Gamma_b(\tilde{\omega})}{\Gamma_W(\tilde{\omega})}} = \frac{1}{G(\tilde{\omega})}\frac{1}{1+\rho^{-1}(\tilde{\omega})}, \tag{5.26}$$

where Γ_W is the power density spectrum of ΔW and we have introduced the signal-to-noise ratio:

$$\rho(\tilde{\omega}) = \frac{|G(\tilde{\omega})|^2\Gamma_W(\tilde{\omega})}{\Gamma_b(\tilde{\omega})}. \tag{5.27}$$

If the signal-to-noise ratio tends toward infinity, one does not need any cut-off. Because noise is non zero, it is impossible to perfectly recover ΔW_n but this solution insures that the error between the estimate $\widehat{\Delta W_n}$ and the real function ΔW_n will be minimal. It is a filter commonly used to remove noise prior to signal detection in audio recordings, sismographs, images or even to help gravitational wave detection. This filter is easy to compute when you can measure independently Γ_b and Γ_W but it is not our situation. Indeed, apart from its $T-$ periodicity we assume nothing on W. Thus, I had to implement a method to circumvent this problem. This is what is presented in the rest of this section.

First we construct the Wiener filter:

$$H_a(\tilde{\omega}) = \frac{G^*(\tilde{\omega})}{|G(\tilde{\omega})|^2 + a/\left|\Delta\widetilde{\mathcal{W}}(\tilde{\omega})\right|^2} \tag{5.28}$$

where $\Delta\widetilde{\mathcal{W}}(\tilde{\omega})$ is the Fourier transform of $\Delta\widetilde{W}(\omega)$. The deconvolved signal *i.e.* the estimator of the quantity of interest (not strictly equal to ΔW_n):

$$\widehat{\Delta W_n}(\omega, a) = TF^{-1}\left[H_a \times \Delta\widetilde{\mathcal{W}}(\tilde{\omega})\right]. \tag{5.29}$$

The error on the estimated value $e(\omega) = \Delta W_n(\omega) - \widehat{\Delta W_n}(\omega)$, will vary with the parameter a, which plays the same role as $\rho^{-1}(\omega)$ the inverse of a signal-to-noise ratio. In the situation $a = 0$, the filter is merely the inverse of the apparatus function and only gives a proper reconstruction when the noise is absent, otherwise it adds huge unphysical oscillations. Conversely, the situation $a \gg 1$ (low signal-to-noise ratio) corresponds to an over-filtering which tends to smooth and damp too much the resulting signal. To the limit $a \to +\infty$, the result is a flat constant.

To optimize the value of a, one needs to find the appropriate balance between those two regimes. To do so, we constructed two quantities that have opposite trends with a:

$$\mathcal{N}_1(a) = \sqrt{\frac{\int \left| \frac{\partial \widehat{\Delta W_n}}{\partial \omega}(\omega, a) \right|^2 d\omega}{\int \left| \frac{\partial \widehat{\Delta W_n}}{\partial \omega}(\omega, 0) \right|^2 d\omega}} \tag{5.30}$$

$$\mathcal{N}_2(a) = \sqrt{\frac{\int \left(\widetilde{\Delta W_n} - \widehat{\Delta W_n} \otimes g_n \right)^2 d\omega}{\int \widetilde{\Delta W_n}^2}}. \tag{5.31}$$

The first quantity is decreasing from 1 to 0 with increasing a; it quantifies if there are too many unphysical oscillations added by the filter. The second one goes from 0 to 1 with increasing a and quantifies if the filter is over-smoothing data or not. The higher $\mathcal{N}_1$ is, the higher unphysical oscillations are added by the deconvolution. The higher $\mathcal{N}_2$, the smoother the deconvolution gets. A balance is to be found between this two regimes *i.e.* we need to find a value of a that minimizes both $\mathcal{N}_1$ and $\mathcal{N}_2$. On the left panel of figure 5.15 is represented on a log-log scale $\mathcal{N}_1$ versus $\mathcal{N}_2$ for one set of data (10 MHz, $n = 1$) but the trend is the same for all n. On this plot, we clearly identify the over-smoothed regime and the regime where there is not enough filtering (too many oscillations). The optimal value a is to be found in the circled area, however there are actually several inflexion points in this area which renders the minimization criteria non-trivial and more difficult to find. We implemented a procedure so as to determine systematically for each data set the most appropriate value of a.

First we tried to approach this value evaluating the deconvolution results by eye. As sketch on figure 5.16, the good point is roughly located on the last plateau of $\mathcal{N}_1$ and before the plateau reaching $\mathcal{N}_2 = 1$. We thus established the following procedure : we start to decrease a from a high value (such that $\mathcal{N}_2(a) = 1$) and after leaving the plateau of $\mathcal{N}_2$, we searched numerically for the first inflexion point in $log(\mathcal{N}_1)$ *i.e.* we evaluated the first cancellation of $\partial^2 ln(\mathcal{N}_1)/\partial a^2$ while decreasing a. This gives the red diamond point on figure 5.15.

This procedure is *ad hoc* and even seems a bit arbitrary but there are several ways to check the rationality of it. For instance on the lower panel of figure 5.16, we can check that applying a second time the convolution g_n to the estimator $\widehat{\Delta W_n}$ we get back to the raw data. It is not the case for a too high value of a (black and green curves). In other words, for a too high, data are too much deteriorated. We can quantify this by imposing an *ad hoc* limit $\mathcal{N}_2 \lesssim 0.1$ which is actually reasonable because it corresponds to

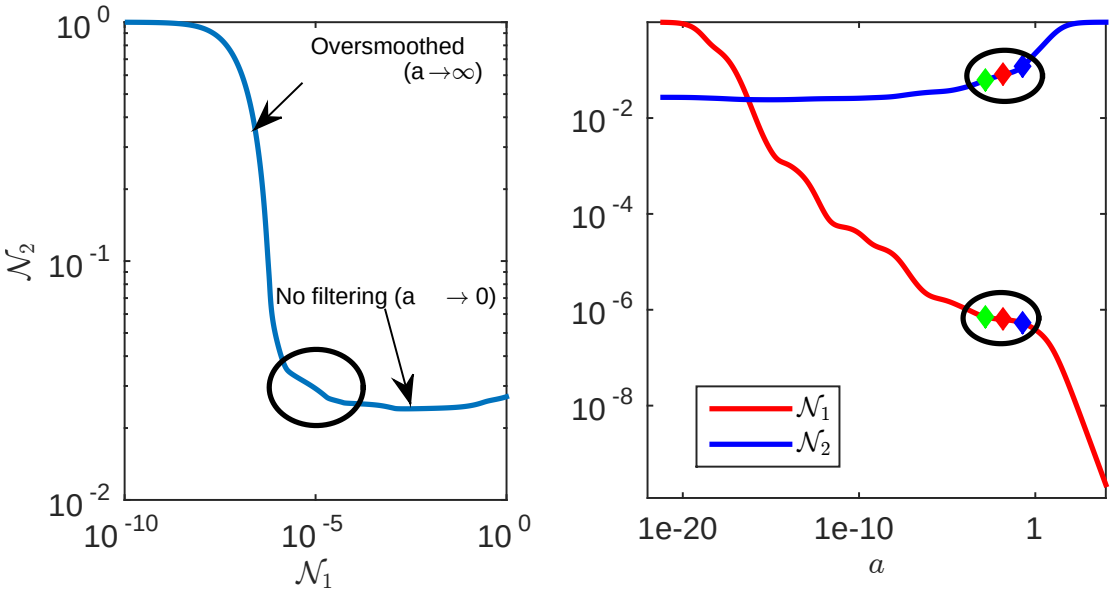

FIGURE 5.15: **Left.** Example of $\mathcal{N}_2$ versus $\mathcal{N}_1$ varying a for data $n = 1$ at 10 MHz. The appropriate filtering corresponds to a point in the circled area. **Right.** $\mathcal{N}_1$ and $\mathcal{N}_2$ versus a for same data. The appropriate filtering corresponds to the red diamond point ($a = 1.18 \times 10^{-2}$). The green diamond corresponds to an under-filtered choice ($a = 10^{-3}$) and blue diamond to an over-smoothed choice ($a = 1.35 \times 10^{-1}$).

the typical order of the relative error on raw data. Indeed, we consider the deterioration is not significant if reconvolved data $\widehat{\Delta W_n} \otimes g_n$ are still within the error bars. For some reason, it appeared that for every set of data on which we applied this procedure, finding the first cancellation point of $\partial^2 ln(\mathcal{N}_1)/\partial a^2$ while decreasing a is enough because it always corresponds to a value of a for which $\mathcal{N}_2 \lesssim 0.1$.

Conversely, we need a criteria to exclude *under-smoothed* choice. On the upper panel of figure 5.16 blue and cyan curves clearly show unphysical oscillations and correspond indeed to a too small value of a.

Actually, to control that the relative uncertainty on a does not influence much the final result we constructed a Monte-Carlo exploration of each data set. That is to say that we constructed multiple set of Wigner functions out of data and parameter a that could vary according to a Gaussian law. For the raw noise data, center of the Gaussian density function is determined by the average value of the noise and the standard deviation by standard error to the mean. For a: the density of $ln(a)$ is chosen as a Gaussian function; center is determined by: $\partial^2 ln(\mathcal{N}_1)/\partial a^2 = 0$ and standard deviation by $\sigma_{ln(a)} = 1.22$. This concentrates most of the value of a on the plateau between the blue and green diamonds on figure 5.15. We thus have a reproducible and traceable method to deconvolve the signal. This method generates a set of (typically 1000) Wigner functions (or only partial

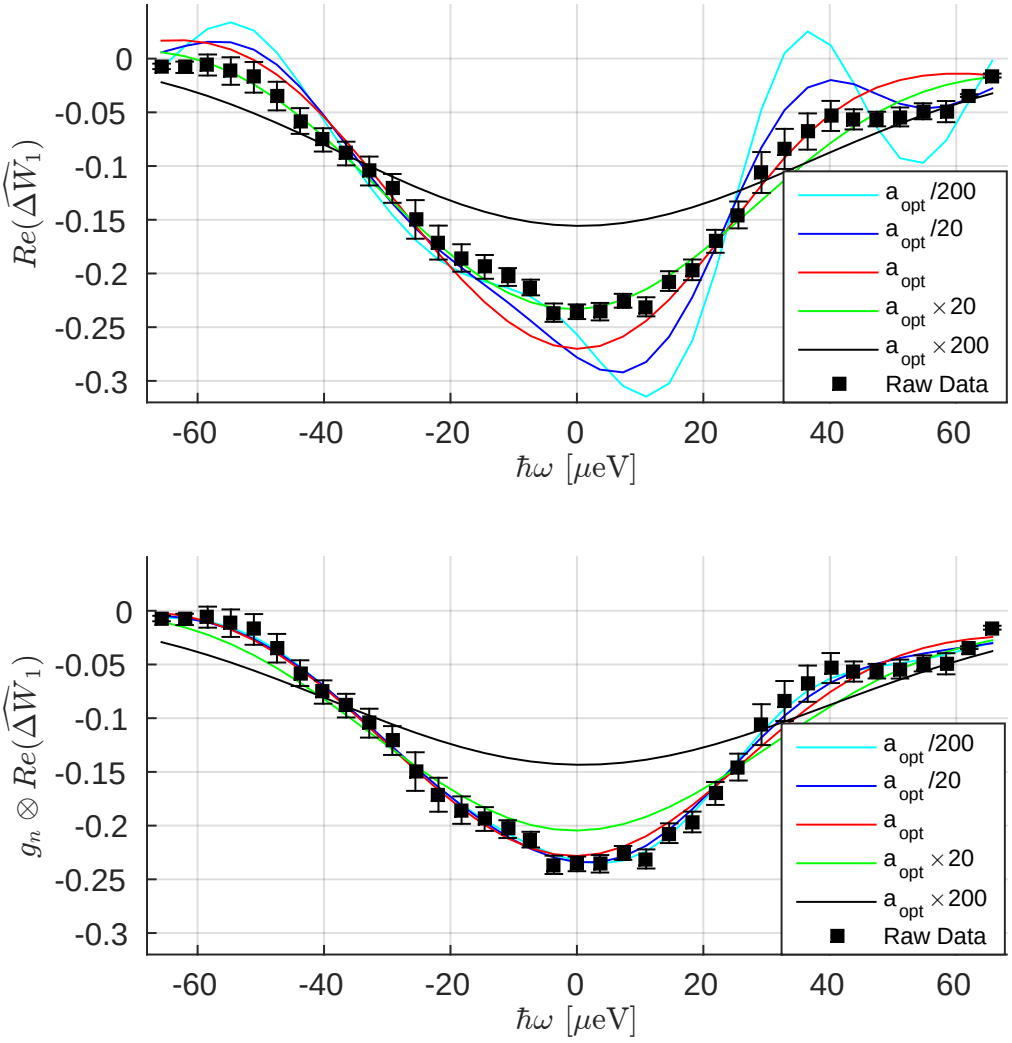

FIGURE 5.16: **Upper.** Results of different inverse filtered data (10 MHz, $n = 1$) for 5 different values of a. a_{opt} corresponds to the first cancellation of $\partial^2 ln(\mathcal{N}_1)/\partial a^2$ while decreasing a (see main text). **Lower.** Results of different inverse filtered data to which we reapplied the kernel g_n. Not recovering raw data (green and black lines) is a sign for over-smoothing.

harmonics ΔW_n) of which we take the average and calculate the standard deviation for error bars. Any error bars on deconvolved data or Wigner functions presented in this chapter are determined through this method. We see that the method works relatively well and does not add too much errors to the signal.

Stating that we do not know anything on ΔW is actually exaggerated. Indeed, for simple test signals like what will be presented in the following part, we do not expect any surprises and we can compute all ΔW_n. Theoretically we can thus calculate Γ_W, measure Γ_b and deduce ρ. In the next section, we compare deconvolution using two Wiener filters constructed differently and show that they give relatively the same result.

5.3.3 Wiener deconvolution with guess on the signal-to-noise ratio

With Floquet theory, it is possible to compute the expected harmonics $\Delta W_n(\omega)$. As mentioned previously, for a sine drive at $D = 1$, interactions will only have the effect of renormalizing the drive amplitude. Because we used shot noise to calibrate the amplitude of the source and shot noise depends on what comes at the level of the QPC after interactions, the method presented in section 2.4.3.5 actually gives us access to this renormalized amplitude. With drive frequency and electronic temperature, we know all the parameters to compute exactly the Wigner function incoming at the level of the QPC. Therefore we are also able to compute $\Gamma_W(\tilde{\omega})$. To compute ρ in equation 5.26 we also need Γ_b. We assume white Gaussian noise with standard deviation corresponding to error bars (before deconvolution). All error bars on the raw data are not strictly identical but of the same order of magnitude so we take their average to define Γ_b.

This procedure is actually a bit odd: we use our perfect knowledge of the incoming state to improve a filtering method that is used to infer information on the incoming state. If we already know everything on the incoming state, why would we need a tomography protocol with a Wiener filter? Actually we did this to test the method presented in the previous section. If the two methods give similar results, this means that they both use roughly the same signal-to-noise ratio as a cut-off in the Wiener filter and confirms the interest of the method presented previously.

To go further in this verification, we also calculated ρ with approximations of the exact theoretical ΔW_n. To do so we fit the raw data at $n > 0$ with a Gaussian function multiplied by a polynomial expression of order $n - 1$ and because we obtain an analytical formula we can simply deconvolve it with the inverse of a Fourier transform (see equation 5.24). The resulting function is used to compute an approximation of $\Gamma_W(\tilde{\omega})$ and thus an approximation of ρ. For $n = 0$, we fit the data with a Gaussian function, then derivate it and then deconvolve it. Figure 5.17 shows the results of the deconvolution (for $n = 3$ of 10 MHz) for all these methods and compares it to the method with no guess (blue line) presented in the previous section. The comparison was done for all n and all frequencies, we checked that each time the three methods give roughly the same result which confirms the relevance of the "no guess" method (method 1 on the figure).

5.3.4 Relevance of the Wiener filter and comparison with the Leviton tomography

The Wiener deconvolution procedure is of fundamental importance for the protocol to be fully general. Indeed, contrary to the Leviton tomography [104] it enables us to

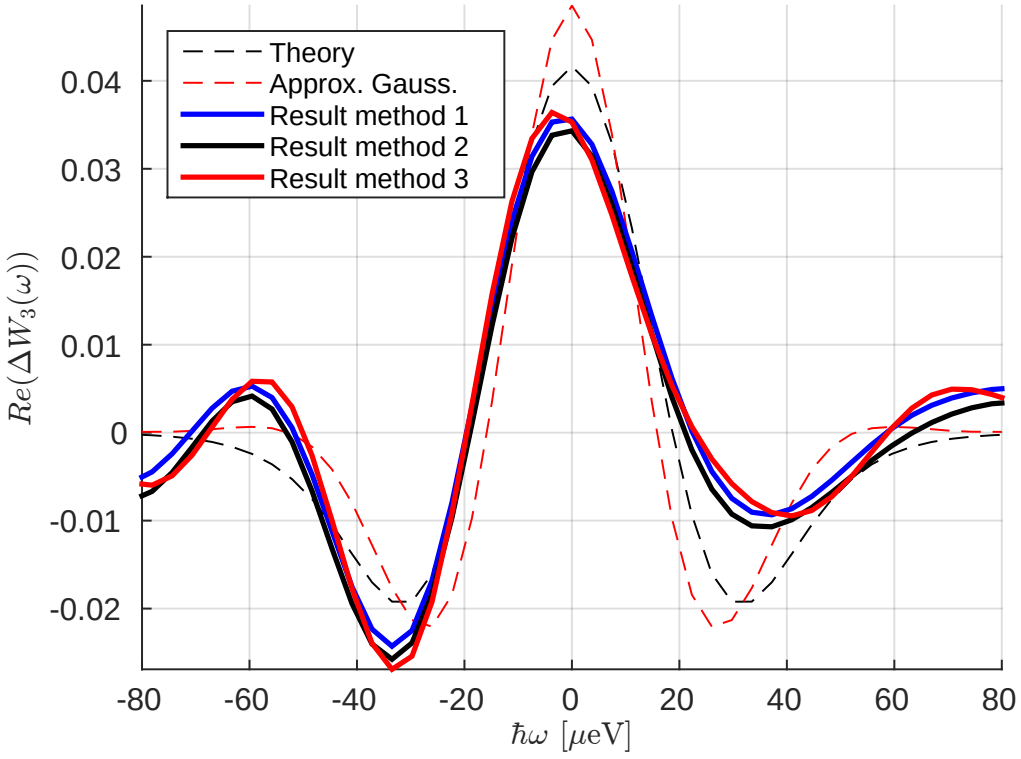

FIGURE 5.17: Deconvolution results for $n = 3$ of the 10 MHz drive. Method 1 corresponds to the method without any guess (see previous section). Method 2 uses Floquet theory (black dashed line) for a guess and method 3 uses an approximation of data with Gaussian functions which are then deconvolved analytically (red dashed line); here at $n = 3$ we used $f(x) = 0.05(1 - \frac{x^2}{21\times10^{-6}}) \exp(-(\frac{x}{28\times10^{-6}})^2)$ with $x = \hbar\omega/e$. As we see, all three methods give relatively the same result.

free ourselves from the projection of our noise results onto the c_n (or p_n) coefficients (probability to absorb or emit n photons). This projection has of course the advantage to reduce the uncertainty on the reconstructed signal. However, like a filter, it cannot capture all possible electronic signals. Indeed, it only enables to reconstruct signals that are created by the excitation of an Ohmic contact with a voltage drive. More precisely, it makes sense to use this formalism only when the first order coherence function writes:

$$\mathcal{G}^{(e)}(t, t') = \exp\left(\frac{ie}{\hbar}\int_{t'}^{t} V(\tau')d\tau'\right)\mathcal{G}_{F_\mu}(t - t') \tag{5.32}$$

or equivalently when the Wigner function writes:

$$W(\omega, t) = \sum_{(n_+,n_-)\in\mathbb{Z}^2} c_{n_+}[V_{\mathrm{AC}}]c_{n_-}[V_{\mathrm{AC}}]^* e^{2\pi i(n_- - n_+)ft} f_\mu\left(\omega - (n_+ + n_-)\Omega/2\right). \tag{5.33}$$

This is only a peculiar class of signal. For the mesoscopic capacitor in the single particle injection regime or GHz single electron pumps, the Wigner function cannot be described that way. What is more, we see that for the analysis to be feasible, we have to restrict

ourselves to a few photon processes, so that only a few n are retained. In reference [104] they fitted 3 curves, each with a four parameters model. These parameters are linear combinations of the c_n. In principle one should take into account all n but in the low amplitude regime they could restrain to a few of them, keeping only the first c_n with n in the range $[0, 3]$. For high amplitude $V_{\mathrm{AC}} \gtrsim hf/e$ this is not valid anymore. In particular, this makes it impossible to measure adiabatic signals ($eV_{\mathrm{AC}} \gg k_B T \gg hf$).

To conclude this comparison, our system is a 4 terminal geometry with a real space propagation between the source and the interferometer contrary to the Leviton which is created and measured at the exact same place. This makes our system more sensitive to interactions and lowers the signal-to-noise ratio but enables us to address interesting electron-electron interaction problems in the framework of electron quantum optics.

5.4 Wigner function coming out of the single electron source: a first attempt

5.4.1 Choice of parameters

This protocol is particularly relevant when applied to reconstruct non-stationary signals created with a time dependent scatterer. At $D \simeq 0.2 - 0.3$, corresponding to a well defined single electron wave packet above the Fermi sea, the current was too low to create enough measurable partition noise. We had to find a compromise between having a well defined single electron state and enough current. Working at 3.5 GHz, we chose a value of $D \simeq 0.7$ which corresponds for this frequency to the beginning of the decrease of current on a plot $\langle I \rangle$ versus V_g (see section 2.2.2.1). We actually set the magnetic field at a lower value to reach only $\nu = 3$, this is because we had trouble to find a stable working point for the source at $\nu = 2$ (drifts in electrostatic environment). This stability was recovered going to $\nu = 3$ but it comes with a lower signal-to-noise ratio. Indeed, the impedance of the gas is lower and thus the current-to-voltage conversion ($S_{VV} = \frac{R_K^2}{\nu^2} S_{II}$) less efficient.

For this cool down, even at $\nu = 3$, we observed long time drifts of the dot parameters. Since measurements could last several days, we had to implement an automatic feedback loop to be sure we stayed as fixed as possible around the same value of D. To do so it was easier to lower the excitation amplitude so as to see the appearance of peaks in the current versus gate voltage. We chose a value of $V_{\mathrm{exc}} \simeq 52\mu\mathrm{V}$ corresponding to half dot spacing and applied a sine drive (easier to calibrate in amplitude) at 3.5 GHz. The theoretical Wigner function for this set of parameters is presented on figure 5.18 for $T_{el} = 100$ mK. We clearly see the effect of the time dependent scatterer that adds

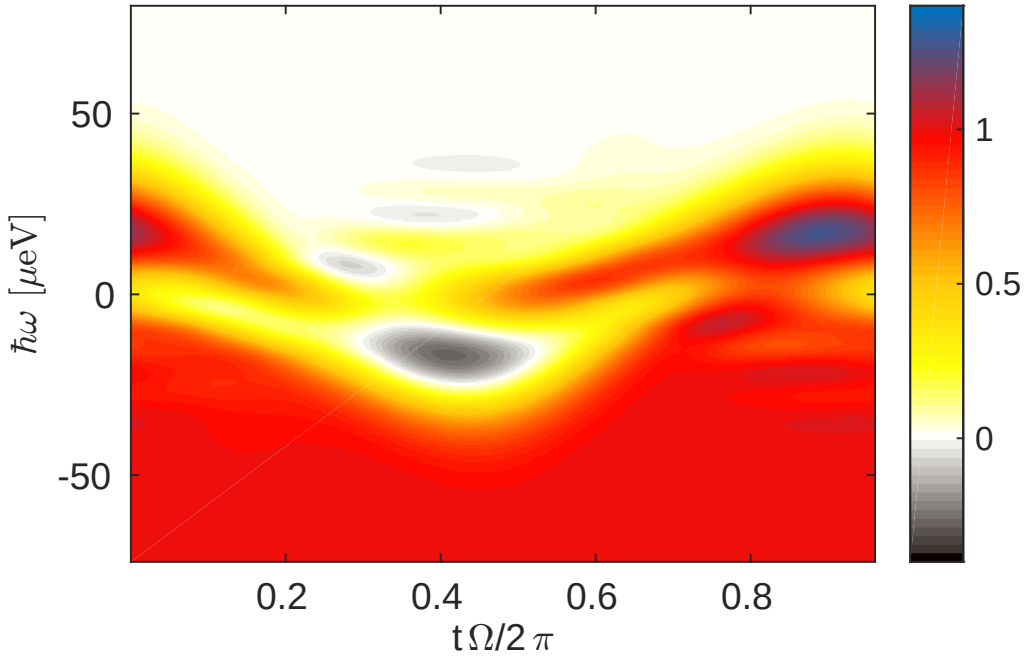

FIGURE 5.18: Theoretical Wigner function before interactions ($\Omega/2\pi = 3.5$ GHz). Parameters of injection were determined with RF current measurements and the amplitude of the drive with noise measurements.

stronger negativities and values above one to the signal compared to the situation $D = 1$. However, we are not in a regime of single particle injection.

The protocol for this back-action loop is the following. We applied a small amplitude modulation on the dot potential at 1.033 kHz and measured the derivative of its response (first harmonic) with a Lock-in (*Zurich instrument HFLI*). Thus a current peak is observed as a cancellation point. This makes it easy to implement a proximity criteria for the feedback loop to compensate drifts of the dot potential.

5.4.2 Phases calibration

As mentioned previously, we might expect the phase of $\Delta W_{1,n}$ to vary with n and with energy ω. For each n, we will use the phase ϕ_n determined in the same set of parameters but at $D = 1$ as the origin of phases. To do so, for each n, we set ourselves at an energy that maximizes the noise oscillations with $\delta\tau$ and fit them to determine amplitude and phase. As mentioned in the previous section, we checked that ϕ_n does not vary with energy at $D = 1$. Results are summarized in the following table:

n	ϕ_n $(D = 1)$
1	$\pi/2 \pm \pi/50$
2	$2\pi/5 \pm \pi/25$
3	2.06 ± 0.36 rad

This origin of phase now being properly calibrated, we can measure all harmonics of W_1 when the source is pinched at $D = 0.7$ and driven at 3.5 GHz. We did not have time to go beyond $n = 3$ although it is clear that for this kind of signal it is not enough to reconstruct the full Wigner function. We checked with Floquet scattering theory that, for this amplitude of drive, harmonics 3, 4 and 5 at $D = 0.7$ are of the same order of magnitude than $n = 3$ for $D = 1$ (but $n = 4$ and 5 are negligible at $D = 1$). The amplitude and phase of each ΔW_n is represented on figure 5.19. Up to some differences, results are relatively close to what is measured at $D = 1$. The first difference concerns $\Delta W_{0,1} = \Delta f$ which has slightly higher weight at higher energies compared to $D = 1$. This is in agreement with the effect of a reduced transmission D. Indeed in the limit of small transmissions, the injected electron has a well defined energy and Δf has a really peaked shape around the average energy (see figure 2.9 for instance). Thus in an intermediate regime we expect to reduce weights at energies below the dot energy level. We also observe a global phase shift of $\approx \pi/4$ for $n = 2$. Floquet theory without interactions indeed predicts a non-zero phase but also a non-monotonic phase relation with ω (that we cannot observe). The fact that ΔW_3 is really small is also quite surprising. We are currently working with the theory group of Pascal Degiovanni to try to predict the effect of interactions on the Wigner harmonics ΔW_n and compare it to these results. The fact that we are not in a single electron injection regime renders calculation more complicated because of many-body effects. Finally, we cannot really combine all these harmonics to reconstruct a full Wigner that makes sense. We need to measure more harmonics to recover a meaningful function: these are only preliminary results.

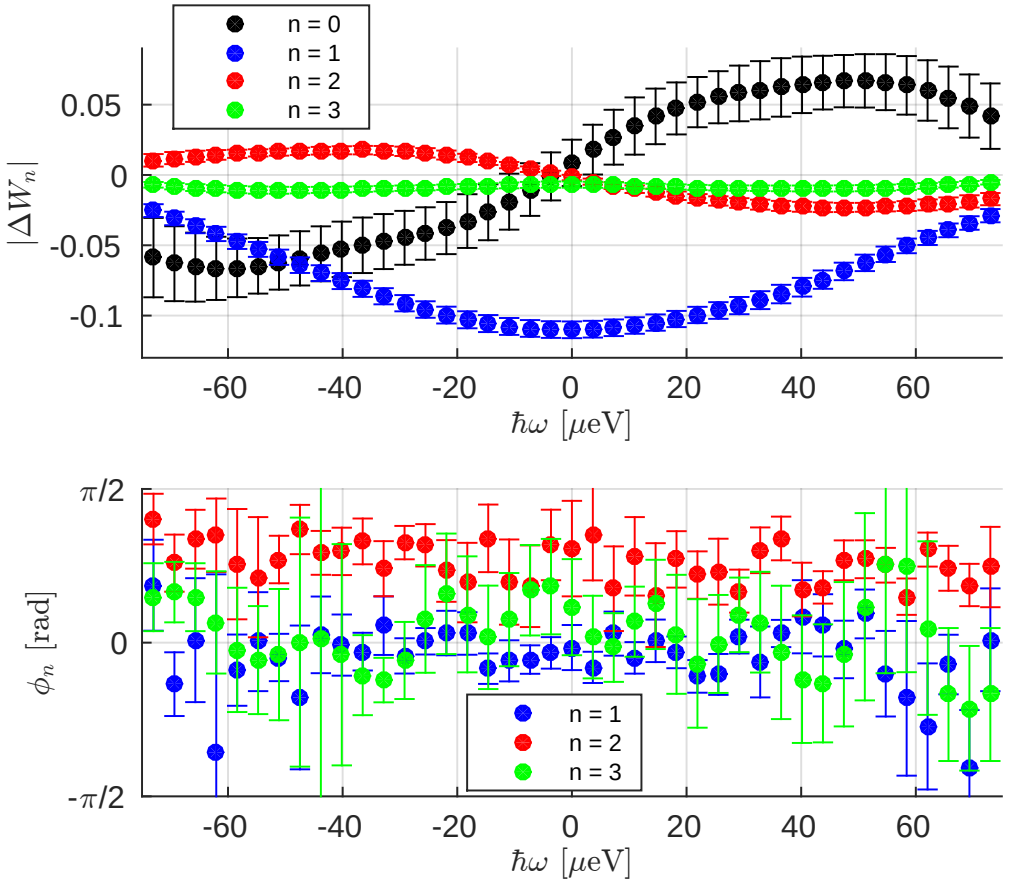

FIGURE 5.19: Measured modulus of $\Delta W_{1,n}$ (**up**) and difference of phase with $D = 1$ case (**down**) for n from 0 to 3 with the dot pinched at $D = 0.7$ and driven at 3.5 GHz with $V_{\text{exc}} = 52\mu$V. Negative modulus corresponds to a phase shift of π (we restricted ϕ_n to $[-\pi/2; \pi/2]$).

Conclusion to this chapter

In this chapter, I have presented a universal tomography protocol aiming at reconstructing the Wigner functions of any arbitrary propagating electronic state *i.e.* any arbitrary electronic signal. For this protocol to be general, I had to design a Wiener filter and a method to estimate the tuning parameter of this filter. We successfully applied this protocol to reconstruct the Wigner functions of two simple states and from it, we quantitatively established the difference between the two. We were able to observe strong negativities and values above one in the Wigner function of the non-classical photo-assisted signal but also the classicality of the adiabatic drive. Using this protocol, we then presented promising preliminary results on the reconstruction of the Wigner function of a more exotic state when the transparency of the dot is not one.

Chapter 6

Conclusion

6.1 Summary

In this manuscript, I presented two experiments relying on two-particle interferences. The first one enabled to observe the fractionalization of a single electron into two collective modes. We observed the decoherence and relaxation induced by this phenomenon. In a second part, I showed we could use the interferometer to realize tomography of single electron states.

In the first part of this work, we used the electronic analog of the Hong Ou Mandel interferometer to study a complex many-body problem which is the role of interactions on a single particle in a one dimensional system. Because of interactions and low dimensionality, a single electron injected in a quantum Hall edge channel decomposes on collective bosonic modes. This splitting happens on short time scales but the HOM interferometer enables a great precision in the time domain. We could measure the shape in the time domain of short current pulses containing one or few electrons and observe their separation in two after propagation over 3 μm in the outer edge channel at filling factor two. On the inner edge we could observe the dipole structure created by this interaction mechanism and measure a time scale τ_s defining an interaction strength parameter coherent with previous frequency admittance measurements done on this sample [221]. This confirmed the hypothesis of strong and short range Coulomb interactions (for frequencies below 6 GHz). From the detailed analysis of the pulse shape we could also probe the influence of Coulomb interactions in the dot used to inject single electron excitations (not only in between propagation channels).

Focusing then in the regime where we injected exactly particles one by one. We explored the evolution of the single electron coherence with respect to the temporal width

of the emitted wavepacket and could extract from it a characteristic coherence time. We measured this coherence time at filling factor two and three. Together with other cross check experiments we could show that Coulomb interaction in between edge channels is the main responsible for single electron decoherence. Comparing quantitatively our results with a bosonisation model we established the relevance of this effect and could provide a fully predictive picture of the decoherence mechanism without any adjustable parameters. We described this life and death scenario in terms of electronic Wigner functions. From this we showed that during propagation, single electron states decompose on the two edges which then get entangled. We also showed that this decoherence is accompanied by strong relaxation in energy in the outer edge.

From the observation that this interferometer can work as an accurate signal analyzer we decided to extend its use. Following ideas developed by Grenier *et al.* [10] we started to implement a tomography protocol aiming at reconstructing the full Wigner function of any arbitrary propagating state. This protocol has many analogies with what has been done for the leviton source [104] but is more general in the sense that it can be used to process any signals and not just signals created by a drive on an Ohmic contact. We first tested this protocol on simple sine drives at different frequencies applied on an open dot so as to establish the difference between classical and "quantum" drives. In this regime, the sources only emitted coherent collective states also called edge-magneto plasmons which are different from single electron states. Doing so we measured photon-assisted shot noise of sine drives up to 20 GHz while varying the DC bias. This enabled us to recover the energy distribution of the analyzed signal *i.e.* population terms, but the protocol aims further.

With it we could indeed recover coherence terms of a classical signal at 10 MHz and of a non-adiabatic drive at 9 GHz. With a Wiener filter we reconstructed the best estimate of the total Wigner function. We could quantitatively establish a difference between the two signals and strong non-classicalities were visible for the 9 GHz signal. We then applied this protocol to reconstruct the excitation coming out of a pinched dot which starts to have quantization effects. The measurements in this regime of injection are longer because we need a higher number of harmonics to recompose the Wigner function. For the moment, we only have partial results and could not reconstruct such a Wigner function. We are also currently working with our collaborators in the group of Pascal Degiovanni to decompose the signal measured in the close dot situation as a sum of single electron-hole pair excitation and to characterize their correlations and overlap between successive periods T.

6.2 Outlook

The natural following of this work will be to pursue the tomography of single electronic states with more resolution. Because of inter-channel interactions it is not obvious to detect something significantly different from a Fermi sea excited with a sine drive. This is why we designed new samples with 2 pairs of single electron sources placed symmetrically from each side of the QPC. One of this pair has a shorter propagation length toward the QPC and the other a longer one. This would enable a direct comparison during the same cool down of two different propagation lengths.

Rather than isolating the inner channel from the outer one we could, like in reference [214], gap the excitations of the inner one by closing it on himself. If the loop is small enough, the induced gap is higher than the energy of injected electron and relaxation is forbidden because no electron-hole pairs with energy lower than this gap can be excited in the inner edge. Our collaborators in Lyon are currently working on a quantitative description of this system in terms of Wigner functions.

Doing this experiments, it was often tempting to go to fractional filling factors. With our samples we could easily reach $\nu = 2/3$ and there have been theoretical predictions on what one could expect in terms of photon assisted shot noise [37, 255–259] in particular at $\nu = 2/3$ [84] where noise measurements versus temperature could enable to discriminate between still debated different quasi-particle models [260]. We have made a few attempts in this direction but faced experimental difficulties. In particular, injecting RF signal through Ohmic contact led to significant heat dissipation probably because of a higher impedance mismatch.

We have introduced the Hong Ou Mandel interferometer explaining how bosons and fermions manifested a different behavior in this experiment. One then might be tempt to probe directly the quantum statistic of anyons which has never been done unambiguously. There have been predictions for collisions of out-of-equilibrium distributions of anyons [119] but actually it seems that to probe quantum statistics directly, 2 partitioners, rather than one, are needed [261].

Appendix A

Computation of coherence function within Floquet formalism

A.1 Definition and properties

Time domain

$$\{\hat{\psi}(t'), \hat{\psi}^\dagger(t)\} = \delta(t - t') \tag{A.1}$$

$$\mathcal{G}^{(e)}(t, t') = \left\langle \hat{\psi}^\dagger(t')\hat{\psi}(t) \right\rangle \tag{A.2}$$

where $\langle ... \rangle$ is the average on the quantum state and $\mathcal{G}^{(h)}$ is the hole coherence function. The Floquet decomposition gives:

$$\mathcal{G}(t, t') = \sum_n \mathcal{G}_n(t - t')e^{-in\Omega\frac{t+t'}{2}} = \sum_n \mathcal{G}_n(\tau)e^{-in\Omega\bar{t}}. \tag{A.3}$$

Energy domain

$$\tilde{\mathcal{G}}^{(e)}(\omega, \omega') = \left\langle \hat{c}^\dagger(\omega')\hat{c}(\omega) \right\rangle . \tag{A.4}$$

We define the Fourier transform:

$$\mathcal{G}_n^{(e)}(\tau) = \int d\omega e^{-i\omega\tau/\hbar}\tilde{\mathcal{G}}_n^{(e)}(\omega). \tag{A.5}$$

Properties

$$\tilde{\mathcal{G}}^{(e)}(\omega, \omega') = \sum_n \tilde{\mathcal{G}}_n^{(e)}\Big(\frac{\omega + \omega'}{2}\Big)\delta(\omega' - \omega + n\hbar\Omega). \tag{A.6}$$

$$\mathcal{G}^{(e)}(t, t') = \mathcal{G}^{(e)^*}(t', t) \tag{A.7}$$

Setting $\Delta\mathcal{G}^{(e)} = \mathcal{G}^{(e)} - \mathcal{G}_F^{(e)}$ as the excess coherence fucntion with respect to the Fermi sea coherence $\mathcal{G}_F^{(e)}$, we get:

$$\mathcal{G}_n^{(e)}(\tau) = \mathcal{G}_{-n}^{(e)^*}(-\tau) \tag{A.8}$$

$$\tilde{\mathcal{G}}_n^{(e)}(\omega) = \tilde{\mathcal{G}}_{-n}^{(e)*}(\omega) \tag{A.9}$$

A.2 Coherence of a single electron on top of a Fermi sea

We consider a single electron wave packet $|\varphi_e\rangle$ well defined above the Fermi sea at $T_{el} = 0$ K *i.e.* there is no overlap with $|F_\mu\rangle$. $|\varphi_e\rangle$ is defined the following way:

$$|\varphi_e\rangle = \int d\omega\ \varphi_e(\omega)\hat{c}^\dagger(\omega)|F_\mu\rangle. \tag{A.10}$$

We want to calculate:

$$\begin{aligned}\tilde{\mathcal{G}}^{(e)}(\omega,\omega') &= \left\langle \varphi_e \left| \hat{c}^\dagger(\omega')\hat{c}(\omega) \right| \varphi_e \right\rangle \\ &= \iint d\omega_1 d\omega_2 \varphi_e^*(\omega_1)\varphi_e(\omega_2) \left\langle F_\mu \left| \hat{c}(\omega_1)\hat{c}^\dagger(\omega')\hat{c}(\omega)\hat{c}^\dagger(\omega_2) \right| F_\mu \right\rangle ,\end{aligned} \tag{A.11}$$

applying Wick's theorem (at $T = 0$ K):

$$\begin{aligned}\tilde{\mathcal{G}}^{(e)}(\omega,\omega') &= \iint d\omega_1 d\omega_2 \varphi_e^*(\omega_1)\varphi_e(\omega_2) \left\langle F_\mu \left| \hat{c}(\omega_1)\hat{c}^\dagger(\omega') \right| F_\mu \right\rangle \left\langle F_\mu \left| \hat{c}(\omega)\hat{c}^\dagger(\omega_2) \right| F_\mu \right\rangle \\ &+ \iint d\omega_1 d\omega_2 \varphi_e^*(\omega_1)\varphi_e(\omega_2) \left\langle F_\mu \left| \hat{c}(\omega_1)\hat{c}^\dagger(\omega_2) \right| F_\mu \right\rangle \left\langle F_\mu \left| \hat{c}^\dagger(\omega')\hat{c}(\omega) \right| F_\mu \right\rangle \\ &= \iint d\omega_1 d\omega_2 \varphi_e^*(\omega_1)\varphi_e(\omega_2)(1 - f_\mu(\omega'))\delta(\omega_1 - \omega')(1 - f_\mu(\omega))\delta(\omega_2 - \omega) \\ &+ \langle\varphi_e|\varphi_e\rangle \left\langle F_\mu \left| \hat{c}^\dagger(\omega')\hat{c}(\omega) \right| F_\mu \right\rangle \\ &= \varphi_e^*(\omega')\varphi_e(\omega) + \tilde{\mathcal{G}}_F^{(e)}(\omega,\omega'),\end{aligned} \tag{A.12}$$

so $\Delta\tilde{\mathcal{G}}^{(e)}(\omega,\omega') = \varphi_e^*(\omega')\varphi_e(\omega)$ contains all the information on the added single particle wave packet.

A.3 Coherence out of the mesoscopic capacitor

In this section, we will use the scattering matrix formalism developed in [7] to show the main formula used in the matlab code to compute the coherence out of the dot. The source is considered as a time dependent scatterer that converts the input mode $\hat{\Psi}_{in}(t)$

into ouput mode $\hat{\Psi}_{out}(t)$:

$$\hat{\Psi}_{out}(t) = \int dt' U(t,t')\hat{\Psi}_{in}(t'), \tag{A.13}$$

where $U(t,t')$ is the Floquet scattering matrix. One can show that for a dot transparency $D = d^2$, transit time $\tau_f = \frac{h}{\Delta}$ and with an applied drive voltage $V_{\rm dc} + V_{\rm exc}(t)$, this matrix writes:

$$\begin{aligned} U(t,t') &= r\delta(t-t') - \sum_{q=1}^{\infty} d^2 r^{q-1} e^{-\frac{ie}{\hbar}\left(V_{\rm dc} q\tau_F + \int_{t'}^{t} dt_1 V_{\rm exc}(t_1)\right)} \delta(t-t'-q\tau_F) \\ &= r\delta(\tau) - \sum_{q=1}^{\infty} d^2 r^{q-1} e^{-\frac{ie}{\hbar}V_{\rm dc} q\tau_F}\delta(\tau - q\tau_F) e^{-\frac{ie}{\hbar}\int_{\bar{t}-\tau/2}^{\bar{t}+\tau/2} dt_1 V_{\rm exc}(t_1)} \end{aligned} \tag{A.14}$$

where q represents the "number of turn" made by the electron before tunneling out of the dot. To compute more easily this matrix we write it in Floquet formalism:

$$U(t,t') = \sum_m U_m(\tau) e^{-im\Omega\bar{t}}. \tag{A.15}$$

To do this decomposition we need to Fourier transform the exponential term in A.14:

$$c_n = \frac{1}{\mathcal{T}} \int_0^{\mathcal{T}} d\bar{t} e^{in\Omega\bar{t}} e^{-\frac{ie}{\hbar}\int_0^{\bar{t}} dt_1 V_{\rm exc}(t_1)} \tag{A.16}$$

$$e^{-\frac{ie}{\hbar}\int_0^{\bar{t}} dt_1 V_{\rm exc}(t_1)} = \sum_n c_n e^{-in\Omega\bar{t}}. \tag{A.17}$$

Knowing :

$$\sum_n c_n c_{n-m}^* = \delta_{m,0}, \tag{A.18}$$

we have :

$$e^{-\frac{ie}{\hbar}\int_{\bar{t}-\tau/2}^{\bar{t}+\tau/2} dt_1 V_{\rm exc}(t_1)} = \sum_{n,m} c_n c_{n-m}^* e^{-im\Omega\bar{t}} e^{-i(n+\frac{m}{2})\Omega q\tau_F}. \tag{A.19}$$

According to A.15, we have:

$$U_m(\tau) = \sum_n c_n c_{n-m}^* \left[r\delta(\tau) - d^2 \sum_{q=1}^{\infty} r^{q-1} e^{-i\left(\frac{e}{\hbar}V_{\rm dc} + (n+\frac{m}{2})\Omega\right)q\tau_F} \delta(\tau - q\tau_F) \right] \tag{A.20}$$

Coefficients c_n are equal to p_n coefficients in reference [36]. They are easy to compute numerically when one knows $V_{\rm exc}(t)$. They correspond to the probability for the electronic state to absorb ($n > 0$) or emit ($n < 0$) n photons at frequency $\Omega/2\pi$. Finally to get a

coherence function in energy domain we simply apply:

$$U_m(\omega) = \int d\tau e^{i\tau\omega} U_m(\tau) \tag{A.21}$$

$$= \sum_n c_n c^*_{n-m} \left[r - d^2 \sum_{q=1}^{\infty} r^{q-1} e^{-\frac{iq\tau_F}{\hbar}\left(eV_{\rm dc}-\omega+(n+\frac{m}{2})\hbar\Omega\right)} \right] \tag{A.22}$$

$$= \sum_n c_n c^*_{n-m} \left[\frac{r - e^{-\frac{i\tau_F}{\hbar}\left(eV_{\rm dc}-\omega+(n+\frac{m}{2})\hbar\Omega\right)}}{1 - re^{-\frac{i\tau_F}{\hbar}\left(eV_{\rm dc}-\omega+(n+\frac{m}{2})\hbar\Omega\right)}} \right]. \tag{A.23}$$

This is how we compute $U_m(\omega)$ from parameters D, $V_{\rm dc}$, $V_{\rm exc}(t)$, Ω, T_{el} and Δ. Instead of converting back to $U(t,t')$, we prefer to calculate directly the output mode in energy. On one hand:

$$\tilde{\mathcal{G}}^{(e)}(\omega,\omega') = f(\omega)\delta(\omega-\omega'), \tag{A.24}$$

and on the other :

$$\begin{aligned} \hat{c}_{out}(\omega) &= \int dt e^{i\omega t} \hat{\Psi}_{out}(t) \\ &= \int d\tau \sum_m U_m(\tau) \hat{c}_{in}(\omega - m\hbar\Omega) e^{i(\omega - \frac{m}{2}\hbar\Omega)\tau/\hbar}. \end{aligned} \tag{A.25}$$

Finally :

$$\hat{c}_{out}(\omega) = \sum_m U_m(\omega - \frac{m}{2}\hbar\Omega)\hat{c}_{in}(\omega - m\hbar\Omega). \tag{A.26}$$

from it we can directly compute the coherence function:

$$\begin{aligned} \tilde{\mathcal{G}}^{(e)}_{out}(\omega,\omega') &= \left\langle \hat{c}_{out}(\omega')\hat{c}_{out}(\omega) \right\rangle \\ &= \sum_{m,m'} U^*_{m'}(\omega' - \frac{m'}{2}\hbar\Omega) U_m(\omega - \frac{m}{2}\hbar\Omega) f(\omega - m\hbar\Omega)\delta(\omega - \omega' - (m-m')\hbar\Omega). \end{aligned} \tag{A.27}$$

It is interesting to express directly the Floquet coefficient $\tilde{\mathcal{G}}^{(e)}_n(\omega)$, indeed, they are also equal to Floquet coefficients of the Wigner function $W_n(\omega)$; according to A.6:

$$\tilde{\mathcal{G}}^{(e)}_n(\omega) = \sum_p U^*_p \left(\omega - \frac{p+n}{2}\hbar\Omega\right) U_{p+n}\left(\omega - \frac{p}{2}\hbar\Omega\right) f\left(\omega - \left(p + \frac{n}{2}\right)\hbar\Omega\right), \tag{A.28}$$

or equivalently:

$$\tilde{\mathcal{G}}^{(e)}_n(\omega) = \sum_m U^*_{m-n}\left(\omega - \frac{m}{2}\hbar\Omega\right) U_m\left(\omega - \frac{m-n}{2}\hbar\Omega\right) f\left(\omega - \left(m - \frac{n}{2}\right)\hbar\Omega\right), \tag{A.29}$$

The first step of the Matlab code is to compute $U_n(\omega)$ as a matrix. One dimension of the matrix correspond to n index and the other is a discretization of the energy axis ω from -3Δ to 3Δ. This cut-off in energy set some constrains on the set of parameter we can use (frequency, dot spacing, drive amplitude and temperature) but it is not a real issue when we use realistic typical values for our experiment. The same is done for f. We benefit from the fact that Matlab is efficient in calculating matrix product. Thus we obtain the coherence functions as matrices. One advantage of Floquet decomposition is that we actually manipulate $\tilde{\mathcal{G}}_n^{(e)}(\omega)$ instead of $\tilde{\mathcal{G}}^{(e)}(\omega,\omega')$ and thus we only have to discretize (and thus lose precision) on one energy axis, the other being already quantized by Floquet theory (but without loss of precision).

A.4 Noise computation

The interference term in the noise reads:

$$Q(t,t') = e^2\left(\mathcal{G}_1^{(e)}\left(t,t'\right)\left(\delta\left(t-t'\right) - \mathcal{G}_2^{(e)^*}(t,t')\right) + \mathcal{G}_2^{(e)}(t,t')\left(\delta(t-t') - \mathcal{G}_1^{(e)^*}(t,t')\right)\right). \tag{A.30}$$

However we only access the low frequency noise which is (factor 2 comes from an "engineer" convention):

$$\overline{Q}(\Omega_M) = 2\int d\tau\ \overline{Q(t,t')}^{\bar{t}} e^{i\Omega_M\tau} \tag{A.31}$$

with the measurement frequency $\Omega_M \to 0$. One can show that:

$$\int d\tau\ \overline{\mathcal{G}_1^{(e)}(t,t')\left(\delta(t-t') - \mathcal{G}_2^{(e)}(t',t)\right)}^{\bar{t}} e^{i\Omega_M\tau} \to \sum_n \int d\omega\ \tilde{\mathcal{G}}_{n,1}^{(e)}(\omega)\left(\delta_{n,0} - \tilde{\mathcal{G}}_{n,2}^{(e)*}(\omega)\right). \tag{A.32}$$

which gives:

$$\overline{Q}(0) = 2e^2\sum_n \int d\omega \tilde{\mathcal{G}}_{n,1}^{(e)}\left(\omega\right)\left(\delta_{n,0} - \tilde{\mathcal{G}}_{n,2}^{(e)*}\left(\omega\right)\right) + \tilde{\mathcal{G}}_{n,2}^{(e)}\left(\omega\right)\left(\delta_{n,0} - \tilde{\mathcal{G}}_{n,1}^{(e)*}\left(\omega\right)\right). \tag{A.33}$$

This correspond to the total low frequency interference term to which we need to remove the Fermi sea contribution:

$$\overline{Q_{F_\mu}}(0) = 2e^2\int d\omega\left(f_{\mu 1}\left(\omega\right)\left(1 - f_{\mu 2}\left(\omega\right)\right) + 1 \leftrightarrow 2\right). \tag{A.34}$$

We thus have all the ingredients to compute excess noise at any temperature for any excitation.

A.4.1 Hanbury Brown & Twiss case

Here we suppose that source 2 is off so we have:

$$\tilde{\mathcal{G}}^{(e)}_{n,2}(\omega) = \delta_{n,0} f_{\mu 2}(\omega). \tag{A.35}$$

So we are left with

$$\begin{aligned}\overline{\Delta Q_{HBT1}} =& 2e^2 \sum_n \int d\omega \left(\Delta\tilde{\mathcal{G}}^{(e)}_{n1}(\omega)\delta_{n,0}(1 - f_{\mu 2}(\omega)) + \delta_{n,0} f_{\mu 2}(\omega)(-\Delta\tilde{\mathcal{G}}^{(e)*}_{n1}(\omega)) \right) \\ =& 2e^2 \int d\omega \left(\Delta\tilde{\mathcal{G}}^{(e)}_{0,1}(\omega)(1 - 2f_{\mu 2}(\omega)) \right).\end{aligned} \tag{A.36}$$

Here, the code simply sums up on the energy direction the $\Delta\tilde{\mathcal{G}}^{(e)}(\omega)$ matrix column corresponding to $n = 0$.

$\Delta\mathcal{G}^{(e)}_{n=0}$ counts occupation in energy. Indeed, terms with $n = 0$ correspond to stationary terms over one period *i.e.* stationary terms on any time scale. Another way to express this is to express the occupation in energy $\rho(\omega)$ with A.6:

$$\rho(\omega) = \left\langle \hat{c}^\dagger(\omega)\hat{c}(\omega) \right\rangle = \mathcal{G}^{(e)}_{n=0}(\omega). \tag{A.37}$$

Therefore, $\overline{\Delta Q_{HBT1}}$ enables to count out of equilibrium excitations. When temperature is low enough compare to energy of excitations we can consider $(1 - 2f_\mu)$ as a simple weight -1 for $\omega < 0$ and 1 for $\omega > 0$. In the canonical injection regime, we emit one hole well defined below μ_2 and one electron above it, that counts as 2. The process is repeated at frequency f so HBT noise will count an average of $2f$ particles per unit of time. Therefore:

$$\overline{\Delta Q_{HBT1}} = 4e^2 f \tag{A.38}$$

A.4.2 Hong, Ou & Mandel case

Here both sources are on, we can decompose ΔQ as:

$$\overline{\Delta Q} = \overline{\Delta Q_{HBT1}} + \overline{\Delta Q_{HBT2}} + \overline{\Delta Q_{HOM}}, \tag{A.39}$$

so that:

$$\overline{\Delta Q_{HOM}} = -2e^2 \sum_n \int d\omega \left(\Delta\mathcal{G}^{(e)}_{n1}(\omega)\Delta\mathcal{G}^{(e)*}_{n2}(\omega) + \Delta\mathcal{G}^{(e)}_{n2}(\omega)\Delta\mathcal{G}^{(e)*}_{n1}(\omega) \right) \tag{A.40}$$

Here in the Matlab code, we first use the dot product to compute the matrices corresponding to the two terms in between brackets above. Then, we calculate the sum on both matrix's dimensions which correspond to the sum over n and the integral over energy.

We can interpret $\overline{\Delta Q_{HOM}}$ as an overlap of single particle wave packet. Using A.12, we can write for a temperature low enough compared to energy of excitations:

$$\begin{aligned}
\overline{\Delta Q_{HOM}} &= -2e^2 \int d\tau \; \overline{\Delta \mathcal{G}_1^{(e)}(t,t')\Delta \mathcal{G}_2^{(e)}(t',t) + \Delta \mathcal{G}_1^{(e)}(t',t)\Delta \mathcal{G}_2^{(e)}(t,t')}^{\bar{t}} && \text{(A.41)} \\
&= -4e^2 f \int d\tau \; \overline{\varphi_{e,1}^*(t')\varphi_{e,1}(t)\varphi_{e,2}^*(t)\varphi_{e,2}(t')}^{\bar{t}} + c.c. && \text{(A.42)} \\
&= -8e^2 f \, |\langle \varphi_{e,1} | \varphi_{e,2} \rangle|^2 \, , && \text{(A.43)}
\end{aligned}$$

Combining A.38 and A.43 we get in the low temperature limit:

$$\Delta q = \frac{\overline{\Delta Q}}{\overline{\Delta Q_{HBT1}} + \overline{\Delta Q_{HBT2}}} = 1 - |\langle \varphi_{e,1} | \varphi_{e,2} \rangle|^2 \, . \qquad \text{(A.44)}$$

Appendix B

Different models for plasmon scattering theory

B.1 Intra-channel interaction only

Here, we disregard any interaction between the two channels. In channel alpha, the potential is defined with respect to the ground reference. We can model this by a distributed capacitive coupling to the ground C_g. Then we simply have:

$$u_\alpha(x,\omega) = \frac{\rho(x,\omega)}{C_g} = \frac{-e}{C_g\sqrt{\pi}}\partial_x\phi_\alpha(x,\omega), \tag{B.1}$$

then the equation of motion on channel α becomes:

$$\left(i\omega + v_F\partial_x\right)\phi_\alpha(x,\omega) = \frac{-e^2}{hC_g}\partial_x\phi_\alpha(x,\omega), \tag{B.2}$$

which simply solves in:

$$\phi_\alpha(l,\omega) = \phi_\alpha(0,\omega)e^{i\frac{\omega l}{v_F+\frac{e^2}{hC_g}}}. \tag{B.3}$$

We see here that screening renormalizes the velocity. We recover qualitatively the difference of velocities for charge mode between gated and ungated samples of reference [194]. Indeed, bringing a metallic gate close to the edges can be seen as a increasing the capacitance toward the ground which then lower velocities. On the other hand, in the ungated gas, the potential in the edges is poorly screened ($C_g \to 0$) which increases renormalized velocities. Note that the Fermi velocity is the minimal velocity one can obtain (and not the maximum).

B.2 Short-range interaction

This is the most discussed model in the literature. The potentials u_α are calculated with the inverse of the distributed capacitance matrix $\boldsymbol{C}$ which relates $u_\alpha(x)$ and $\rho_\alpha(x)$ at same position x only: it means that the interaction has a zero length range.

$$\begin{bmatrix}\rho_1(\omega,\,x)\\ \rho_2(\omega,\,x)\end{bmatrix} = \begin{bmatrix}C_{g1}+C & -C\\ -C & C_{g2}+C\end{bmatrix}\begin{bmatrix}u_1(\omega,\,x)\\ u_2(\omega,\,x)\end{bmatrix}, \tag{B.4}$$

where C is the capacitance per unit length between the two channels and C_{gi} the capacitance per unit length between ground and channel i. One then has to diagonalize $\boldsymbol{\mathcal{V}} = v_F\boldsymbol{Id} + \frac{e^2}{h}\boldsymbol{C}^{-1}$ to find the new eigenmodes $\phi_\pm$ for the bosonic field and the new eigenvelocities $v_\pm$:

$$\begin{bmatrix}\phi_+\\ \phi_-\end{bmatrix} = \begin{bmatrix}\cos(\theta/2) & \sin(\theta/2)\\ \sin(\theta/2) & -\cos(\theta/2)\end{bmatrix}\begin{bmatrix}\phi_1\\ \phi_2\end{bmatrix} \tag{B.5}$$

$$v_\pm = v_F + \frac{e^2}{h}\frac{C_{g1}+C_{g2}+2C \mp \sqrt{4C^2+(C_{g1}-C_{g2})^2}}{2\left(C_{g1}C_{g2}+C\left(C_{g1}+C_{g2}\right)\right)}, \tag{B.6}$$

with

$$\sin(\theta/2) = \frac{2C}{\sqrt{2\left[(C_{g1}-C_{g2})^2+4C^2\right]+2(C_{g1}-C_{g2})\sqrt{(C_{g1}-C_{g2})^2+4C^2}}}. \tag{B.7}$$

The equation of motion simply solves in $\phi_\pm(l,\,\omega) = e^{i\omega l/v_\pm}\phi_\pm(0,\,\omega)$. One has to do the inverse basis transformation to recover the scattering matrix elements:

$$S_{11}(\omega) = \frac{e^{i\omega l/v_+}+e^{i\omega l/v_-}}{2} + \cos\theta\frac{e^{i\omega l/v_+}-e^{i\omega l/v_-}}{2} \tag{B.8}$$

$$S_{21}(\omega) = \sin\theta\frac{e^{i\omega l/v_+}-e^{i\omega l/v_-}}{2} \tag{B.9}$$

with:

$$\cos\theta = \frac{C_{g1}-C_{g2}}{\sqrt{4C^2+(C_{g1}-C_{g2})^2}}. \tag{B.10}$$

In the strong interaction limit, the ratio $\frac{C_{g1}}{C}$ and $\frac{C_{g2}}{C}$ tends to zero or equivalently $\theta \to \pi/2$ so these expressions simplifies and we recover the two so called charge and neutral mode, ϕ_ρ and ϕ_n respectively. The charge mode is the symmetric charge distribution and the neutral one the anti-symmetric one, as given by the expression:

$$\phi_+ \to \phi_\rho(\omega) = \frac{1}{\sqrt{2}}\left(\phi_1(\omega)+\phi_2(\omega)\right) \tag{B.11}$$

$$\phi_- \to \phi_n(\omega) = \frac{1}{\sqrt{2}}\left(\phi_1(\omega)-\phi_2(\omega)\right). \tag{B.12}$$

In this configuration the velocities become:

$$v_+ \to v_\rho = v_F + \frac{e^2}{h}\frac{2}{C_{g1} + C_{g2}} \tag{B.13}$$

$$v_- \to v_n = v_F + \frac{e^2}{h}\frac{1}{2C} \tag{B.14}$$

Here capacitance are divided by a unit length so the previous expression is homogeneous. Finally one gets the scattering matrix elements:

$$S_{11}(\omega) = \frac{1+e^{i\omega l/v_-}}{2} \tag{B.15}$$

$$S_{21}(\omega) = \frac{1-e^{i\omega l/v_-}}{2}. \tag{B.16}$$

Bibliography

[1] G. Fève, A. Mahé, J.-M. Berroir, T. Kontos, B. Plaçais, C. Glattli, A. Cavanna, B. Etienne, and Y. Jin, An On-Demand Coherent Single Electron Source, *Science 316 (2007) 1169*, May 2007, doi: 10.1126/science.1141243. 0.1, 1.5, 1.7.1, 3.4.2.2

[2] P. Roulleau, F. Portier, P. Roche, A. Cavanna, G. Faini, U. Gennser, and D. Mailly, Direct Measurement of the Coherence Length of Edge States in the Integer Quantum Hall Regime, *Phys. Rev. Lett.*, 100:126802, Mar 2008, doi: 10.1103/PhysRevLett.100.126802. 0.2.1.1, 1.2, 3.1.1

[3] E. Bocquillon, Electron quantum optics in quantum Hall edge channels, Theses, Université Pierre et Marie Curie - Paris VI, November 2012. 3, 2, 2.2.2.1, 3.1.2, 3.4.1, 3.4.1

[4] J. Gabelli, Evidence of quantum coherence in dynamical electronic transport, Theses, Université Pierre et Marie Curie - Paris VI, January 2006. 0.2.1.3, 1.1, 2, 2.4.4.1

[5] G. Fève, Quantization of the AC current : the quantum dot as a subnanosecond single electron source, Theses, Université Pierre et Marie Curie - Paris VI, November 2006. 2, 2.2.2.1, 3.4.2.2

[6] A. Mahé, Bruit de charge d'une source d'électrons uniques subnanoseconde., Theses, Université Pierre et Marie Curie - Paris VI, November 2009. 2, 2.2.2.2

[7] F. Parmentier, Short-time Hanbury-Brown and Twiss correlation of a single-electron beam in ballistic conductors, Theses, Université Pierre et Marie Curie - Paris VI, November 2010. 0.2.1.3, 2, 2.2.2.1, 2.2.2.2, 2.2.2.3, 2.7, 2.3.2.4, 3.4.2.2, A.3

[8] S. E. Nigg and M. Büttiker, Quantum to classical transition of the charge relaxation resistance of a mesoscopic capacitor, *Phys. Rev. B*, 77:085312, Feb 2008, doi: 10.1103/PhysRevB.77.085312. 0.2.1.3, 2.2.2.1

[9] T. Jonckheere, J. Rech, C. Wahl, and T. Martin, Electron and hole Hong-Ou-Mandel interferometry, *Phys. Rev. B*, 86:125425, Sep 2012, doi: 10.1103/PhysRevB.86.125425. 0.3, 2.3.3, 3.2.2

[10] C. Grenier, R. Hervé, E. Bocquillon, F. D. Parmentier, B. Plaçais, J. M. Berroir, G. Fève, and P. Degiovanni, Single-electron quantum tomography in quantum Hall edge channels, *New Journal of Physics*, 13(9):093007, 2011. 0.4, 1.7.3, 1.7.4, 2.3, 1, 2.3.1, 5.1.1, 5.2.1, 6.1

[11] I. Yang, W. Kang, L. N. Pfeiffer, K. W. Baldwin, K. W. West, E.-A. Kim, and E. Fradkin, Quantum Hall line junction with impurities as a multislit Luttinger liquid interferometer, *Phys. Rev. B*, 71:113312, Mar 2005, doi: 10.1103/PhysRevB.71.113312. 1.2

[12] i. m. c. Kurdak, A. M. Chang, A. Chin, and T. Y. Chang, Quantum interference effects and spin-orbit interaction in quasi-one-dimensional wires and rings, *Phys. Rev. B*, 46:6846–6856, Sep 1992, doi: 10.1103/PhysRevB.46.6846. 1.2

[13] J. A. Katine, M. J. Berry, R. M. Westervelt, and A. C. Gossard, Determination of the electronic phase coherence time in one-dimensional channels, *Phys. Rev. B*, 57:1698–1702, Jan 1998, doi: 10.1103/PhysRevB.57.1698. 1.2

[14] R. Landauer, Spatial Variation of Currents and Fields Due to Localized Scatterers in Metallic Conduction, *IBM Journal of Research and Development*, 1(3):223–231, July 1957, ISSN 0018-8646, doi: 10.1147/rd.13.0223. 1.3, 2.2.1

[15] B. J. van Wees, H. van Houten, C. W. J. Beenakker, J. G. Williamson, L. P. Kouwenhoven, D. van der Marel, and C. T. Foxon, Quantized conductance of point contacts in a two-dimensional electron gas, *Phys. Rev. Lett.*, 60:848–850, Feb 1988, doi: 10.1103/PhysRevLett.60.848. 1.3, 1.2, 2.2.1

[16] D. A. Wharam, T. J. Thornton, R. Newbury, M. Pepper, H. Ahmed, J. E. F. Frost, D. G. Hasko, D. C. Peacock, D. A. Ritchie, and G. A. C. Jones, One-dimensional transport and the quantisation of the ballistic resistance, *Journal of Physics C: Solid State Physics*, 21(8):L209, 1988. 1.3, 2.2.1

[17] A. Yacoby, M. Heiblum, V. Umansky, H. Shtrikman, and D. Mahalu, Unexpected Periodicity in an Electronic Double Slit Interference Experiment, *Phys. Rev. Lett.*, 73:3149–3152, Dec 1994, doi: 10.1103/PhysRevLett.73.3149. 1.4, 1.3

[18] J. P. Pekola, O.-P. Saira, V. F. Maisi, A. Kemppinen, M. Möttönen, Y. A. Pashkin, and D. V. Averin, Single-electron current sources: Toward a refined definition of the ampere, *Reviews of Modern Physics*, 85(4):1421–1472, October 2013, ISSN 0034-6861, doi: 10.1103/RevModPhys.85.1421. 1.5

[19] J. Splettstoesser, M. Moskalets, and M. Büttiker, Two-Particle Nonlocal Aharonov-Bohm Effect from Two Single-Particle Emitters, *Phys. Rev. Lett.*, 103:076804, Aug 2009, doi: 10.1103/PhysRevLett.103.076804. 1.5, 1.7.4

[20] L. Chirolli, V. Giovannetti, R. Fazio, and V. Scarani, Time-bin entanglement of quasiparticles in semiconductor devices, *Phys. Rev. B*, 84:195307, Nov 2011, doi: 10.1103/PhysRevB.84.195307.

[21] Y. Sherkunov, N. d'Ambrumenil, P. Samuelsson, and M. Büttiker, Optimal pumping of orbital entanglement with single-particle emitters, *Phys. Rev. B*, 85:081108, Feb 2012, doi: 10.1103/PhysRevB.85.081108.

[22] F. Brange, O. Malkoc, and P. Samuelsson, Subdecoherence Time Generation and Detection of Orbital Entanglement in Quantum Dots, *Phys. Rev. Lett.*, 114:176803, Apr 2015, doi: 10.1103/PhysRevLett.114.176803.

[23] P. P. Hofer, D. Dasenbrook, and C. Flindt, On-demand entanglement generation using dynamic single-electron sources, *Physica Status Solidi B.*, Dec 2016, ISSN 1521-3951, doi: 10.1002/pssb.201600582. 1.5

[24] L. J. Geerligs, V. F. Anderegg, P. A. M. Holweg, J. E. Mooij, H. Pothier, D. Esteve, C. Urbina, and M. H. Devoret, Frequency-locked turnstile device for single electrons, *Phys. Rev. Lett.*, 64:2691–2694, May 1990, doi: 10.1103/PhysRevLett.64.2691. 1.5.1

[25] L. P. Kouwenhoven, A. T. Johnson, N. C. van der Vaart, C. J. P. M. Harmans, and C. T. Foxon, Quantized current in a quantum-dot turnstile using oscillating tunnel barriers, *Physical Review Letters*, 67(12):1626–1629, September 1991, ISSN 0031-9007, doi: 10.1103/PhysRevLett.67.1626.

[26] H. Pothier, P. Lafarge, C. Urbina, D. Esteve, and M. H. Devoret, Single-Electron Pump Based on Charging Effects, *EPL (Europhysics Letters)*, 17(3):249, 1992. 1.5.1

[27] A. Fujiwara, K. Nishiguchi, and Y. Ono, Nanoampere charge pump by single-electron ratchet using silicon nanowire metal-oxide-semiconductor field-effect transistor, *Applied Physics Letters*, 92(4):042102, 2008, doi: 10.1063/1.2837544. 1.5.1

[28] B. Kaestner, V. Kashcheyevs, S. Amakawa, M. D. Blumenthal, L. Li, T. J. B. M. Janssen, G. Hein, K. Pierz, T. Weimann, U. Siegner, and H. W. Schumacher, Single-parameter nonadiabatic quantized charge pumping, *Phys. Rev. B*, 77:153301, Apr 2008, doi: 10.1103/PhysRevB.77.153301. 1.5.1

[29] S. P. Giblin, S. J. Wright, J. D. Fletcher, M. Kataoka, M. Pepper, T. J. B. M. Janssen, D. A. Ritchie, C. A. Nicoll, D. Anderson, and G. A. C. Jones, An accurate high-speed single-electron quantum dot pump, *New Journal of Physics*, 12(7):073013, 2010. 1.5.1

[30] Giblin S.P., Kataoka M., Fletcher J.D., See P., Janssen T.J.B.M., Griffiths J.P., Jones G.A.C., Farrer I., and Ritchie D.A., Towards a quantum representation of the ampere using single electron pumps, *Nature Communications*, 3:930, jul 2012, doi: 10.1038/ncomms1935. 1.5.1

[31] J. D. Fletcher, P. See, H. Howe, M. Pepper, S. P. Giblin, J. P. Griffiths, G. A. C. Jones, I. Farrer, D. A. Ritchie, T. J. B. M. Janssen, and M. Kataoka, Clock-Controlled Emission of Single-Electron Wave Packets in a Solid-State Circuit, *Physical Review Letters*, 111(21):216807, November 2013, ISSN 0031-9007, doi: 10.1103/PhysRevLett.111.216807. 1.5.1, 1.7.1

[32] J. Waldie, P. See, V. Kashcheyevs, J. P. Griffiths, I. Farrer, G. A. C. Jones, D. A. Ritchie, T. J. B. M. Janssen, and M. Kataoka, Measurement and control of electron wave packets from a single-electron source, *Phys. Rev. B*, 92:125305, Sep 2015, doi: 10.1103/PhysRevB.92.125305. 1.5.1, 1.7.1

[33] G. Yamahata, S. P. Giblin, M. Kataoka, T. Karasawa, and A. Fujiwara, Gigahertz single-electron pumping in silicon with an accuracy better than 9.2 parts in 107, *Applied Physics Letters*, 109(1):013101, 2016, doi: 10.1063/1.4953872. 1.5.1

[34] D. M. T. van Zanten, D. M. Basko, I. M. Khaymovich, J. P. Pekola, H. Courtois, and C. B. Winkelmann, Single Quantum Level Electron Turnstile, *Phys. Rev. Lett.*, 116:166801, Apr 2016, doi: 10.1103/PhysRevLett.116.166801. 1.5.1

[35] J. Keeling, I. Klich, and L. S. Levitov, Minimal Excitation States of Electrons in One-Dimensional Wires, *Phys. Rev. Lett.*, 97:116403, Sep 2006, doi: 10.1103/PhysRevLett.97.116403. 1.5.2

[36] J. Dubois, T. Jullien, F. Portier, P. Roche, A. Cavanna, Y. Jin, W. Wegscheider, P. Roulleau, and D. C. Glattli, Minimal-excitation states for electron quantum optics using levitons., *Nature*, 502(7473):659–63, October 2013, ISSN 1476-4687, doi: 10.1038/nature12713. 1.5, 1.5.2, 1.5.2, 1.7.2, 5.1.1, 5.2.1, A.3

[37] J. Rech, D. Ferraro, T. Jonckheere, L. Vannucci, M. Sassetti, and T. Martin, Minimal Excitations in the Fractional Quantum Hall Regime, *Phys. Rev. Lett.*, 118:076801, Feb 2017, doi: 10.1103/PhysRevLett.118.076801. 1.5.2, 6.2

[38] Hermelin Sylvain, Takada Shintaro, Yamamoto Michihisa, Tarucha Seigo, Wieck Andreas D., Saminadayar Laurent, Bauerle Christopher, and Meunier Tristan, Electrons surfing on a sound wave as a platform for quantum optics with flying electrons, *Nature*, 477(7365):435–438, sep 2011, ISSN 0028-0836, doi: 10.1038/nature10416. 1.5.3

[39] McNeil R. P. G., Kataoka M., Ford C. J. B., Barnes C. H. W., Anderson D., Jones G. A. C., Farrer I., and Ritchie D. A., On-demand single-electron transfer between distant quantum dots, *Nature*, 477(7365):439–442, sep 2011, ISSN 0028-0836, doi: 10.1038/nature10444. 1.5.3

[40] B. Bertrand, S. Hermelin, S. Takada, M. Yamamoto, S. Tarucha, A. Ludwig, W. A. D., C. Bäuerle, and T. Meunier, Fast spin information transfer between distant quantum dots using individual electrons, *Nat Nano*, 11(8):672–676, aug 2016, ISSN 1748-3387, doi: 10.1038/nnano.2016.82. 1.6, 1.5.3

[41] B. Bertrand, S. Hermelin, P.-A. Mortemousque, S. Takada, M. Yamamoto, S. Tarucha, A. Ludwig, A. D. Wieck, C. Bäuerle, and T. Meunier, Injection of a single electron from static to moving quantum dots, *Nanotechnology*, 27(21): 214001, 2016. 1.6

[42] K. v. Klitzing, G. Dorda, and M. Pepper, New Method for High-Accuracy Determination of the Fine-Structure Constant Based on Quantized Hall Resistance, *Phys. Rev. Lett.*, 45:494–497, Aug 1980, doi: 10.1103/PhysRevLett.45.494. 1.6

[43] J. Guillemette, S. S. Sabri, B. Wu, K. Bennaceur, P. E. Gaskell, M. Savard, P. L. Lévesque, F. Mahvash, A. Guermoune, M. Siaj, R. Martel, T. Szkopek, and G. Gervais, Quantum Hall Effect in Hydrogenated Graphene, *Phys. Rev. Lett.*, 110: 176801, Apr 2013, doi: 10.1103/PhysRevLett.110.176801. 1.6

[44] M. O. Goerbig, Quantum Hall Effects, *ArXiv e-prints*, September 2009. 1.6

[45] Ji Yang, Chung Yunchul, Sprinzak D., Heiblum M., Mahalu D., and Shtrikman Hadas, An electronic Mach-Zehnder interferometer, *Nature*, 422(6930):415–418, mar 2003, ISSN 0028-0836, doi: 10.1038/nature01503. 1.6

[46] E. V. Deviatov, A. Ganczarczyk, A. Lorke, G. Biasiol, and L. Sorba, Quantum Hall Mach-Zehnder interferometer far beyond equilibrium, *Phys. Rev. B*, 84:235313, Dec 2011, doi: 10.1103/PhysRevB.84.235313.

[47] E. Weisz, H. K. Choi, I. Sivan, M. Heiblum, Y. Gefen, D. Mahalu, and V. Umansky, An electronic quantum eraser, *Science*, 344(6190):1363–1366, 2014, ISSN 0036-8075, doi: 10.1126/science.1248459.

[48] B. Karmakar, D. Venturelli, L. Chirolli, V. Giovannetti, R. Fazio, S. Roddaro, L. N. Pfeiffer, K. W. West, F. Taddei, and V. Pellegrini, Nanoscale Mach-Zehnder interferometer with spin-resolved quantum Hall edge states, *Phys. Rev. B*, 92: 195303, Nov 2015, doi: 10.1103/PhysRevB.92.195303.

[49] N. Hiyama, M. Hashisaka, and T. Fujisawa, An edge-magnetoplasmon Mach-Zehnder interferometer, *Applied Physics Letters*, 107(14):143101, 2015, doi: 10.1063/1.4932111. 1.6

[50] G. Gabrielse, D. Hanneke, T. Kinoshita, M. Nio, and B. Odom, New Determination of the Fine Structure Constant from the Electron g Value and QED, *Phys. Rev. Lett.*, 97:030802, Jul 2006, doi: 10.1103/PhysRevLett.97.030802. 1.7

[51] Tektronik, Techniques for extending real-time oscilloscope bandwidth, Technical report, 2013, URL `http://literature.cdn.keysight.com/litweb/pdf/5989-8794EN.pdf?id=1464210`. 1.7.1

[52] R. Thalineau, A. D. Wieck, C. Bäuerle, and T. Meunier, Using a two-electron spin qubit to detect electrons flying above the Fermi sea, *ArXiv e-prints*, March 2014. 1.7.1

[53] M. Kataoka, N. Johnson, C. Emary, P. See, J. P. Griffiths, G. A. C. Jones, I. Farrer, D. A. Ritchie, M. Pepper, and T. J. B. M. Janssen, Time-of-Flight Measurements of Single-Electron Wave Packets in Quantum Hall Edge States, *Phys. Rev. Lett.*, 116:126803, Mar 2016, doi: 10.1103/PhysRevLett.116.126803. 1.7.1, 1.8

[54] N. Johnson, J. D. Fletcher, D. A. Humphreys, P. See, J. P. Griffiths, G. A. C. Jones, I. Farrer, D. A. Ritchie, M. Pepper, T. J. B. M. Janssen, and M. Kataoka, Ultrafast Voltage Sampling using Single-Electron Wavepackets, *ArXiv e-prints*, October 2016. 1.7.1

[55] C. Altimiras, H. le Sueur, U. Gennser, A. Cavanna, D. Mailly, and F. Pierre, Non-equilibrium edge-channel spectroscopy in the integer quantum Hall regime, *Nature Physics*, 6(1):34–39, October 2009, ISSN 1745-2473, doi: 10.1038/nphys1429. 1.7.1, 3.1.1, 3.1.2

[56] H. le Sueur, C. Altimiras, U. Gennser, A. Cavanna, D. Mailly, and F. Pierre, Energy Relaxation in the Integer Quantum Hall Regime, *Phys. Rev. Lett.*, 105: 056803, Jul 2010, doi: 10.1103/PhysRevLett.105.056803.

[57] C. Altimiras, H. le Sueur, U. Gennser, A. Cavanna, D. Mailly, and F. Pierre, Tuning Energy Relaxation along Quantum Hall Channels, *Phys. Rev. Lett.*, 105:226804, Nov 2010, doi: 10.1103/PhysRevLett.105.226804. 1.7.1, 3.1.1, 3.1.2, 4.3.2.1

[58] A. M. Robinson and V. I. Talyanskii, Shot Noise in the Current of a Surface Acoustic-Wave-Driven Single-Electron Pump, *Phys. Rev. Lett.*, 95:247202, Dec 2005, doi: 10.1103/PhysRevLett.95.247202. 1.7.2

[59] N. Maire, F. Hohls, B. Kaestner, K. Pierz, H. W. Schumacher, and R. J. Haug, Noise measurement of a quantized charge pump, *Applied Physics Letters*, 92(8): 082112, 2008, doi: 10.1063/1.2885076. 1.7.2

[60] J. Keeling, A. V. Shytov, and L. S. Levitov, Coherent Particle Transfer in an On-Demand Single-Electron Source, *Phys. Rev. Lett.*, 101:196404, Nov 2008, doi: 10.1103/PhysRevLett.101.196404. 1.7.2

[61] J. Gabelli and B. Reulet, Shaping a time-dependent excitation to minimize the shot noise in a tunnel junction, *Phys. Rev. B*, 87:075403, Feb 2013, doi: 10.1103/PhysRevB.87.075403. 1.7.2, 5.1.1, 5.2.1

[62] E. Bocquillon, F. D. Parmentier, C. Grenier, J.-M. Berroir, P. Degiovanni, D. C. Glattli, B. Plaçais, A. Cavanna, Y. Jin, and G. Fève, Electron Quantum Optics: Partitioning Electrons One by One, *Phys. Rev. Lett.*, 108:196803, May 2012, doi: 10.1103/PhysRevLett.108.196803. 1.7.2, 3.2.2

[63] M. Moskalets, P. Samuelsson, and M. Büttiker, Quantized Dynamics of a Coherent Capacitor, *Phys. Rev. Lett.*, 100:086601, Feb 2008, doi: 10.1103/PhysRevLett.100.086601. 1.7.2

[64] M. Albert, C. Flindt, and M. Büttiker, Accuracy of the quantum capacitor as a single-electron source, *Phys. Rev. B*, 82:041407, Jul 2010, doi: 10.1103/PhysRevB.82.041407.

[65] T. Jonckheere, T. Stoll, J. Rech, and T. Martin, Real-time simulation of finite-frequency noise from a single-electron emitter, *Phys. Rev. B*, 85:045321, Jan 2012, doi: 10.1103/PhysRevB.85.045321.

[66] M. Moskalets, Noise of a single-electron emitter, *Phys. Rev. B*, 88:035433, Jul 2013, doi: 10.1103/PhysRevB.88.035433. 1.7.2

[67] A. Mahé, F. D. Parmentier, E. Bocquillon, J.-M. Berroir, D. C. Glattli, T. Kontos, B. Plaçais, G. Fève, A. Cavanna, and Y. Jin, Current correlations of an on-demand single-electron emitter, *Phys. Rev. B*, 82:201309, Nov 2010, doi: 10.1103/PhysRevB.82.201309. 1.7.2, 2.3.3

[68] F. D. Parmentier, E. Bocquillon, J.-M. Berroir, D. C. Glattli, B. Plaçais, G. Fève, M. Albert, C. Flindt, and M. Büttiker, Current noise spectrum of a single-particle emitter: Theory and experiment, *Phys. Rev. B*, 85:165438, Apr 2012, doi: 10.1103/PhysRevB.85.165438. 1.7.2

[69] F. Battista, M. Moskalets, M. Albert, and P. Samuelsson, Quantum Heat Fluctuations of Single-Particle Sources, *Phys. Rev. Lett.*, 110:126602, Mar 2013, doi: 10.1103/PhysRevLett.110.126602. 1.7.2

[70] M. Moskalets and G. Haack, Heat and charge transport measurements to access single-electron quantum characteristics, *physica status solidi (b)*, 254(3):1600616–n/a, 2017, ISSN 1521-3951, doi: 10.1002/pssb.201600616, 1600616.

[71] M. Moskalets, Single-particle emission at finite temperatures, *ArXiv e-prints*, February 2017. 1.7.2

[72] F. Battista, F. Haupt, and J. Splettstoesser, Energy and power fluctuations in ac-driven coherent conductors, *Phys. Rev. B*, 90:085418, Aug 2014, doi: 10.1103/PhysRevB.90.085418. 1.7.2

[73] R. B. Laughlin, Anomalous Quantum Hall Effect: An Incompressible Quantum Fluid with Fractionally Charged Excitations, *Phys. Rev. Lett.*, 50:1395–1398, May 1983, doi: 10.1103/PhysRevLett.50.1395. 1.7.2

[74] S. B. Isakov, T. Martin, and S. Ouvry, Conductance and Shot Noise for Particles with Exclusion Statistics, *Phys. Rev. Lett.*, 83:580–583, Jul 1999, doi: 10.1103/PhysRevLett.83.580. 1.7.2

[75] de-Picciotto R., Reznikov M., Heiblum M., Umansky V., Bunin G., and Mahalu D., Direct observation of a fractional charge, *Nature*, 389(6647):162–164, sep 1997, ISSN 0028-0836, doi: 10.1038/38241. 1.7.2

[76] L. Saminadayar, D. C. Glattli, Y. Jin, and B. Etienne, Observation of the $e/3$ Fractionally Charged Laughlin Quasiparticle, *Phys. Rev. Lett.*, 79:2526–2529, Sep 1997, doi: 10.1103/PhysRevLett.79.2526. 1.7.2

[77] Y. C. Chung, M. Heiblum, and V. Umansky, Scattering of Bunched Fractionally Charged Quasiparticles, *Phys. Rev. Lett.*, 91:216804, Nov 2003, doi: 10.1103/PhysRevLett.91.216804. 1.7.2

[78] Dolev M., Heiblum M., Umansky V., Stern Ady, and Mahalu D., Observation of a quarter of an electron charge at the $\nu = 5/2$ quantum Hall state, *Nature*, 452 (7189):829–834, apr 2008, ISSN 0028-0836, doi: 10.1038/nature06855. 1.7.2

[79] A. Bid, N. Ofek, M. Heiblum, V. Umansky, and D. Mahalu, Shot Noise and Charge at the 2/3 Composite Fractional Quantum Hall State, *Phys. Rev. Lett.*, 103:236802, Dec 2009, doi: 10.1103/PhysRevLett.103.236802. 1.7.2

[80] D. Ferraro, A. Braggio, N. Magnoli, and M. Sassetti, Charge tunneling in fractional edge channels, *Phys. Rev. B*, 82:085323, Aug 2010, doi: 10.1103/PhysRevB.82.085323. 1.7.2

[81] M. Carrega, D. Ferraro, A. Braggio, N. Magnoli, and M. Sassetti, Anomalous Charge Tunneling in Fractional Quantum Hall Edge States at a Filling Factor $\nu = 5/2$, *Phys. Rev. Lett.*, 107:146404, Sep 2011, doi: 10.1103/PhysRevLett.107.146404. 1.7.2

[82] M. Dolev, Y. Gross, Y. C. Chung, M. Heiblum, V. Umansky, and D. Mahalu, Dependence of the tunneling quasiparticle charge determined via shot noise measurements on the tunneling barrier and energetics, *Phys. Rev. B*, 81:161303, Apr 2010, doi: 10.1103/PhysRevB.81.161303. 1.7.2

[83] D. Ferraro, A. Braggio, N. Magnoli, and M. Sassetti, Finite-frequency noise for edge states at a filling factor $\nu = 2/5$, *Physica Scripta*, 2012(T151):014025, 2012. 1.7.2

[84] D. Ferraro, M. Carrega, A. Braggio, and M. Sassetti, Multiple quasiparticle Hall spectroscopy investigated with a resonant detector, *New Journal of Physics*, 16(4): 043018, 2014. 1.7.2, 6.2

[85] M. Carrega, D. Ferraro, A. Braggio, N. Magnoli, and M. Sassetti, Spectral noise for edge states at the filling factor $\nu = 5/2$, *New Journal of Physics*, 14(2):023017, 2012. 1.7.2

[86] A. Braggio, M. Carrega, D. Ferraro, and M. Sassetti, Finite frequency noise spectroscopy for fractional Hall states at $\nu = 5/2$, *Journal of Statistical Mechanics: Theory and Experiment*, 2016(5):054010, 2016. 1.7.2

[87] G. Haack, M. Moskalets, and M. Büttiker, Glauber coherence of single-electron sources, *Phys. Rev. B*, 87:201302, May 2013, doi: 10.1103/PhysRevB.87.201302. 1.7.3, 2.3

[88] M. Moskalets, First-order correlation function of a stream of single-electron wave packets, *Phys. Rev. B*, 91:195431, May 2015, doi: 10.1103/PhysRevB.91.195431. 1.7.3

[89] É. Thibierge, D. Ferraro, B. Roussel, C. Cabart, A. Marguerite, G. Fève, and P. Degiovanni, Two-electron coherence and its measurement in electron quantum optics, *Phys. Rev. B*, 93:081302, Feb 2016, doi: 10.1103/PhysRevB.93.081302. 1.7.3, 1.7.4, 2.3.2.2

[90] D. Ferraro, A. Feller, A. Ghibaudo, E. Thibierge, E. Bocquillon, G. Fève, C. Grenier, and P. Degiovanni, Wigner function approach to single electron coherence in quantum Hall edge channels, *Phys. Rev. B*, 88:205303, Nov 2013, doi: 10.1103/PhysRevB.88.205303. 1.7.3, 2.3, 2.3.2.1, 2.3.2.4

[91] L. S. Levitov, H. Lee, and G. B. Lesovik, Electron counting statistics and coherent states of electric current, *Journal of Mathematical Physics*, 37(10):4845–4866, 1996, doi: 10.1063/1.531672. 1.7.3

[92] Y. V. Nazarov and M. Kindermann, Full counting statistics of a general quantum mechanical variable, *The European Physical Journal B - Condensed Matter and Complex Systems*, 35(3):413–420, 2003, ISSN 1434-6036, doi: 10.1140/epjb/e2003-00293-1.

[93] P. P. Hofer and A. A. Clerk, Negative Full Counting Statistics Arise from Interference Effects, *Phys. Rev. Lett.*, 116:013603, Jan 2016, doi: 10.1103/PhysRevLett.116.013603.

[94] D. Dasenbrook and C. Flindt, Dynamical Scheme for Interferometric Measurements of Full-Counting Statistics, *Phys. Rev. Lett.*, 117:146801, Sep 2016, doi: 10.1103/PhysRevLett.117.146801.

[95] P. P. Hofer, Quasi-probability distributions for observables in dynamic systems, *ArXiv e-prints*, February 2017. 1.7.3

[96] M. Albert, C. Flindt, and M. Büttiker, Distributions of Waiting Times of Dynamic Single-Electron Emitters, *Phys. Rev. Lett.*, 107:086805, Aug 2011, doi: 10.1103/PhysRevLett.107.086805. 1.7.3

[97] M. Albert, G. Haack, C. Flindt, and M. Büttiker, Electron Waiting Times in Mesoscopic Conductors, *Phys. Rev. Lett.*, 108:186806, May 2012, doi: 10.1103/PhysRevLett.108.186806.

[98] K. H. Thomas and C. Flindt, Electron waiting times in non-Markovian quantum transport, *Phys. Rev. B*, 87:121405, Mar 2013, doi: 10.1103/PhysRevB.87.121405.

[99] L. Rajabi, C. Pöltl, and M. Governale, Waiting Time Distributions for the Transport through a Quantum-Dot Tunnel Coupled to One Normal and One Superconducting Lead, *Phys. Rev. Lett.*, 111:067002, Aug 2013, doi: 10.1103/PhysRevLett.111.067002.

[100] D. Dasenbrook, C. Flindt, and M. Büttiker, Floquet Theory of Electron Waiting Times in Quantum-Coherent Conductors, *Phys. Rev. Lett.*, 112:146801, Apr 2014, doi: 10.1103/PhysRevLett.112.146801.

[101] G.-M. Tang, F. Xu, and J. Wang, Waiting time distribution of quantum electronic transport in the transient regime, *Phys. Rev. B*, 89:205310, May 2014, doi: 10.1103/PhysRevB.89.205310.

[102] K. H. Thomas and C. Flindt, Waiting time distributions of noninteracting fermions on a tight-binding chain, *Phys. Rev. B*, 89:245420, Jun 2014, doi: 10.1103/PhysRevB.89.245420.

[103] M. Albert and P. Devillard, Waiting time distribution for trains of quantized electron pulses, *Phys. Rev. B*, 90:035431, Jul 2014, doi: 10.1103/PhysRevB.90.035431. 1.7.3

[104] T. Jullien, P. Roulleau, B. Roche, a. Cavanna, Y. Jin, and D. C. Glattli, Quantum tomography of an electron, *Nature*, 514(7524):603–607, October 2014, ISSN 0028-0836, doi: 10.1038/nature13821. 1.9, 1.7.4, 2.3.2.1, 5.2.1, 5.3.4, 5.3.4, 6.1

[105] P. Samuelsson and M. Büttiker, Quantum state tomography with quantum shot noise, *Physical Review B*, 73(4):041305, January 2006, ISSN 1098-0121, doi: 10.1103/PhysRevB.73.041305. 1.7.4

[106] M. Vanević, J. Gabelli, W. Belzig, and B. Reulet, Electron and electron-hole quasiparticle states in a driven quantum contact, *Phys. Rev. B*, 93:041416, Jan 2016, doi: 10.1103/PhysRevB.93.041416. 1.7.4, 2.3.2.3

[107] V. Freulon, Decoherence of single electron wavepackets in the edge channels of the integer quantum Hall effect, Theses, Ecole Normale Supérieure, October 2014. 2, 2.4.1, 2.4.2, 2.4.4.1, 3.1.2, 3.4.1, 3.4.1

[108] C. K. Hong, Z. Y. Ou, and L. Mandel, Measurement of subpicosecond time intervals between two photons by interference, *Phys. Rev. Lett.*, 59:2044–2046, Nov 1987, doi: 10.1103/PhysRevLett.59.2044. 2.1.1

[109] S. Ol'khovskaya, J. Splettstoesser, M. Moskalets, and M. Büttiker, Shot Noise of a Mesoscopic Two-Particle Collider, *Phys. Rev. Lett.*, 101:166802, Oct 2008, doi: 10.1103/PhysRevLett.101.166802. 2.1.1, 2.3.3

[110] Heeres Reinier W., Kouwenhoven Leo P., and Zwiller Valery, Quantum interference in plasmonic circuits, *Nat Nano*, 8(10):719–722, oct 2013, ISSN 1748-3387, doi: 10.1038/nnano.2013.150. 2.1.2

[111] G. Di Martino, Y. Sonnefraud, M. S. Tame, S. Kéna-Cohen, F. Dieleman, i. m. c. K. Özdemir, M. S. Kim, and S. A. Maier, Observation of Quantum Interference in the Plasmonic Hong-Ou-Mandel Effect, *Phys. Rev. Applied*, 1:034004, Apr 2014, doi: 10.1103/PhysRevApplied.1.034004. 2.1.2

[112] Fakonas James S., Lee Hyunseok, Kelaita Yousif A., and Atwater Harry A., Two-plasmon quantum interference, *Nat Photon*, 8(4):317–320, apr 2014, ISSN 1749-4885, doi: 10.1038/nphoton.2014.40. 2.1.2

[113] A. M. Kaufman, B. J. Lester, C. M. Reynolds, M. L. Wall, M. Foss-Feig, K. R. A. Hazzard, A. M. Rey, and C. A. Regal, Two-particle quantum interference in tunnel-coupled optical tweezers, *Science*, 345(6194):306–309, 2014, ISSN 0036-8075, doi: 10.1126/science.1250057. 2.1.2

[114] Lopes R., Imanaliev A., Aspect A., Cheneau M., Boiron D., and Westbrook C. I., Atomic Hong-Ou-Mandel experiment, *Nature*, 520(7545):66–68, apr 2015, ISSN 0028-0836, doi: 10.1038/nature14331. 2.1.2

[115] Toyoda Kenji, Hiji Ryoto, Noguchi Atsushi, and Urabe Shinji, Hong–Ou–Mandel interference of two phonons in trapped ions, *Nature*, 527(7576):74–77, nov 2015, ISSN 0028-0836, doi: 10.1038/nature15735. 2.1.2

[116] J. Li, M.-T. Zhou, B. Jing, X.-J. Wang, S.-J. Yang, X. Jiang, K. Mølmer, X.-H. Bao, and J.-W. Pan, Hong-Ou-Mandel Interference between Two Deterministic Collective Excitations in an Atomic Ensemble, *Phys. Rev. Lett.*, 117:180501, Oct 2016, doi: 10.1103/PhysRevLett.117.180501. 2.1.2

[117] Liu R. C., Odom B., Yamamoto Y., and Tarucha S., Quantum interference in electron collision, *Nature*, 391(6664):263–265, jan 1998, ISSN 0028-0836, doi: 10.1038/34611. 2.1.2

[118] E. Bocquillon, V. Freulon, J.-M. Berroir, P. Degiovanni, B. Plaçais, A. Cavanna, Y. Jin, and G. Fève, Coherence and Indistinguishability of Single Electrons Emitted by Independent Sources, *Science*, 339(6123):1054–1057, 2013, ISSN 0036-8075, doi: 10.1126/science.1232572. 2.1.2

[119] B. Rosenow, I. P. Levkivskyi, and B. I. Halperin, Current Correlations from a Mesoscopic Anyon Collider, *Phys. Rev. Lett.*, 116:156802, Apr 2016, doi: 10.1103/PhysRevLett.116.156802. 2.1.2, 6.2

[120] D. Ferraro, J. Rech, T. Jonckheere, and T. Martin, Nonlocal interference and Hong-Ou-Mandel collisions of single Bogoliubov quasiparticles, *Phys. Rev. B*, 91:075406, Feb 2015, doi: 10.1103/PhysRevB.91.075406. 2.1.2

[121] R. Landauer, Electrical resistance of disordered one-dimensional lattices, *Philosophical Magazine*, 21(172):863–867, 1970, doi: 10.1080/14786437008238472. 2.2.1

[122] M. Büttiker, Four-Terminal Phase-Coherent Conductance, *Phys. Rev. Lett.*, 57:1761–1764, Oct 1986, doi: 10.1103/PhysRevLett.57.1761. 2.2.1

[123] G. Haack, M. Moskalets, J. Splettstoesser, and M. Büttiker, Coherence of single-electron sources from Mach-Zehnder interferometry, *Phys. Rev. B*, 84:081303, Aug 2011, doi: 10.1103/PhysRevB.84.081303. 2.3

[124] R. J. Glauber, The Quantum Theory of Optical Coherence, *Phys. Rev.*, 130:2529–2539, Jun 1963, doi: 10.1103/PhysRev.130.2529. 2.3

[125] G. Floquet, Sur les équations différentielles linéaires à coefficients périodiques, *Annales scientifiques de l'École Normale Supérieure*, 12:47–88, 1883. 2.3.1

[126] M. Moskalets and M. Büttiker, Floquet scattering theory of quantum pumps, *Phys. Rev. B*, 66:205320, Nov 2002, doi: 10.1103/PhysRevB.66.205320. 2.3.1

[127] M. Moskalets and M. Büttiker, Floquet scattering theory for current and heat noise in large amplitude adiabatic pumps, *Phys. Rev. B*, 70:245305, Dec 2004, doi: 10.1103/PhysRevB.70.245305. 2.3.1

[128] E. Wigner, On the Quantum Correction For Thermodynamic Equilibrium, *Phys. Rev.*, 40:749–759, Jun 1932, doi: 10.1103/PhysRev.40.749. 2.3.2.1

[129] J. Ville, Théorie et Applications de la Notion de Signal Analytique, *Câbles et Transmission*, 21:61–74, 1948. 2.3.2.1

[130] *The Wigner distribution: theory and application in signal processing*, Elsevier Science, w. mecklenbräuker franz hlawatsch edition, October 1997, ISBN 9780444888563. 2.3.2.1

[131] M. Hillery, R. O'Connell, M. Scully, and E. Wigner, Distribution functions in physics: Fundamentals, *Physics Reports*, 106(3):121–167, April 1984, ISSN 03701573, doi: 10.1016/0370-1573(84)90160-1. 2.3.2.1

[132] E. C. G. Sudarshan, Equivalence of Semiclassical and Quantum Mechanical Descriptions of Statistical Light Beams, *Phys. Rev. Lett.*, 10:277–279, Apr 1963, doi: 10.1103/PhysRevLett.10.277. 2.3.2.1

[133] R. J. Glauber, Coherent and Incoherent States of the Radiation Field, *Phys. Rev.*, 131:2766–2788, Sep 1963, doi: 10.1103/PhysRev.131.2766. 2.3.2.1

[134] K. Husimi, Some Formal Properties of the Density Matrix, *Proceedings of the Physico-Mathematical Society of Japan. 3rd Series*, 22(4):264–314, 1940. 2.3.2.1

[135] K. Nemoto and B. C. Sanders, Superpositions of SU (3) coherent states via a nonlinear evolution, *Journal of Physics A: Mathematical and General*, 34(10): 2051, 2001. 2.3.2.1

[136] D. T. Smithey, M. Beck, M. G. Raymer, and A. Faridani, Measurement of the Wigner distribution and the density matrix of a light mode using optical homodyne tomography: Application to squeezed states and the vacuum, *Physical Review Letters*, 70(9):1244–1247, March 1993, ISSN 0031-9007, doi: 10.1103/PhysRevLett.70.1244. 2.3.2.1

[137] G. Breitenbach, S. Schiller, and J. Mlynek, Measurement of the quantum states of squeezed light, *Nature*, 387(6632):471–475, May 1997, ISSN 0028-0836, doi: 10.1038/387471a0. 2.3.2.1

[138] A. I. Lvovsky, H. Hansen, T. Aichele, O. Benson, J. Mlynek, and S. Schiller, Quantum State Reconstruction of the Single-Photon Fock State, *Physical Review Letters*, 87(5):050402, July 2001, ISSN 0031-9007, doi: 10.1103/PhysRevLett.87.050402.

[139] P. Bertet, A. Auffeves, P. Maioli, S. Osnaghi, T. Meunier, M. Brune, J. M. Raimond, and S. Haroche, Direct Measurement of the Wigner Function of a One-Photon Fock State in a Cavity, *Physical Review Letters*, 89(20):200402, October 2002, ISSN 0031-9007, doi: 10.1103/PhysRevLett.89.200402.

[140] A. Ourjoumtsev, R. Tualle-Brouri, and P. Grangier, Quantum Homodyne Tomography of a Two-Photon Fock State, *Phys. Rev. Lett.*, 96:213601, Jun 2006, doi: 10.1103/PhysRevLett.96.213601. 2.3.2.1

[141] Deleglise Samuel, Dotsenko Igor, Sayrin Clement, Bernu Julien, Brune Michel, Raimond Jean-Michel, and Haroche Serge, Reconstruction of non-classical cavity field states with snapshots of their decoherence, *Nature*, 455(7212):510–514, sep 2008, ISSN 0028-0836, doi: 10.1038/nature07288. 2.3.2.1

[142] M. Hofheinz, H. Wang, M. Ansmann, R. C. Bialczak, E. Lucero, M. Neeley, A. D. O'Connell, D. Sank, J. Wenner, J. M. Martinis, and A. N. Cleland, Synthesizing arbitrary quantum states in a superconducting resonator., *Nature*, 459(7246):546–9, May 2009, ISSN 1476-4687, doi: 10.1038/nature08005. 2.3.2.1

[143] C. Eichler, D. Bozyigit, C. Lang, L. Steffen, J. Fink, and A. Wallraff, Experimental State Tomography of Itinerant Single Microwave Photons, *Physical Review Letters*, 106(22):220503, June 2011, ISSN 0031-9007, doi: 10.1103/PhysRevLett.106.220503.

[144] F. Mallet, M. A. Castellanos-Beltran, H. S. Ku, S. Glancy, E. Knill, K. D. Irwin, G. C. Hilton, L. R. Vale, and K. W. Lehnert, Quantum State Tomography of an Itinerant Squeezed Microwave Field, *Phys. Rev. Lett.*, 106:220502, Jun 2011, doi: 10.1103/PhysRevLett.106.220502.

[145] L. Bretheau, P. Campagne-Ibarcq, E. Flurin, F. Mallet, and B. Huard, Quantum dynamics of an electromagnetic mode that cannot contain N photons, *Science*, 348 (6236):776–779, May 2015, ISSN 0036-8075, doi: 10.1126/science.1259345. 2.3.2.1

[146] T. J. Dunn, I. A. Walmsley, and S. Mukamel, Experimental Determination of the Quantum-Mechanical State of a Molecular Vibrational Mode Using Fluorescence Tomography, *Physical Review Letters*, 74(6):884–887, February 1995, ISSN 0031-9007, doi: 10.1103/PhysRevLett.74.884. 2.3.2.1

[147] D. Leibfried, D. M. Meekhof, B. E. King, C. Monroe, W. M. Itano, and D. J. Wineland, Experimental Determination of the Motional Quantum State of a Trapped Atom, *Physical Review Letters*, 77(21):4281–4285, November 1996, ISSN 0031-9007, doi: 10.1103/PhysRevLett.77.4281. 2.3.2.1

[148] C. Kurtsiefer, T. Pfau, and J. Mlynek, Measurement of the Wigner function of an ensemble of helium atoms, *Nature*, 386(6621):150–153, March 1997, ISSN 0028-0836, doi: 10.1038/386150a0. 2.3.2.1

[149] T. Tilma, M. J. Everitt, J. H. Samson, W. J. Munro, and K. Nemoto, Wigner Functions for Arbitrary Quantum Systems, *Phys. Rev. Lett.*, 117:180401, Oct 2016, doi: 10.1103/PhysRevLett.117.180401. 2.3.2.1

[150] W. R. Frensley, Wigner-function model of a resonant-tunneling semiconductor device, *Phys. Rev. B*, 36:1570–1580, Jul 1987, doi: 10.1103/PhysRevB.36.1570. 2.3.2.1

[151] N. C. Kluksdahl, A. M. Kriman, D. K. Ferry, and C. Ringhofer, Self-consistent study of the resonant-tunneling diode, *Phys. Rev. B*, 39:7720–7735, Apr 1989, doi: 10.1103/PhysRevB.39.7720.

[152] P. Bordone, M. Pascoli, R. Brunetti, A. Bertoni, C. Jacoboni, and A. Abramo, Quantum transport of electrons in open nanostructures with the Wigner-function formalism, *Phys. Rev. B*, 59:3060–3069, Jan 1999, doi: 10.1103/PhysRevB.59.3060.

[153] C. Jacoboni and P. Bordone, The Wigner-function approach to non-equilibrium electron transport, *Reports on Progress in Physics*, 67(7):1033, 2004. 2.3.2.1

[154] B. Roussel, C. Cabart, G. Fève, E. Thibierge, and P. Degiovanni, Electron quantum optics as quantum signal processing, *physica status solidi (b)*, pages 1600621–n/a, 2017, ISSN 1521-3951, doi: 10.1002/pssb.201600621, 1600621. 2.3.2.2

[155] G. B. Lesovik and L. S. Levitov, Noise in an ac biased junction: Nonstationary Aharonov-Bohm effect, *Phys. Rev. Lett.*, 72:538–541, Jan 1994, doi: 10.1103/PhysRevLett.72.538. 2.3.2.3, 2.4.3.5, 5.2.1, 5.2.1

[156] R. J. Schoelkopf, A. A. Kozhevnikov, D. E. Prober, and M. J. Rooks, Observation of "Photon-Assisted" Shot Noise in a Phase-Coherent Conductor, *Phys. Rev. Lett.*, 80:2437–2440, Mar 1998, doi: 10.1103/PhysRevLett.80.2437. 2.4.3.5, 5.2.1

[157] L.-H. Reydellet, P. Roche, D. C. Glattli, B. Etienne, and Y. Jin, Quantum Partition Noise of Photon-Created Electron-Hole Pairs, *Phys. Rev. Lett.*, 90:176803, Apr 2003, doi: 10.1103/PhysRevLett.90.176803. 2.3.2.3, 5.2.1

[158] V. Kashcheyevs and P. Samuelsson, Classical-to-quantum crossover in electron on-demand emission, *ArXiv e-prints*, January 2017. 2.3.2.3

[159] M. H. Pedersen and M. Büttiker, Scattering theory of photon-assisted electron transport, *Phys. Rev. B*, 58:12993–13006, Nov 1998, doi: 10.1103/PhysRevB.58.12993. 2.3.2.4, 2.4.3.5

[160] Hanbury Brown, R. and Twiss, R. Q., Correlation between Photons in two Coherent Beams of Light, *Nature*, 177(4497):27–29, jan 1956, doi: 10.1038/177027a0. 2.3.3

[161] T. Jullien, Mesoscopic few-electron voltage pulse source, Theses, Université Paris Sud - Paris XI, April 2014. 2.3.3

[162] Y. Jin, Q. Dong, A. Cavanna, U. Gennser, L. Couraud, and C. Ulysse, "Ultra-low noise HEMTs for deep cryogenic low-frequency and high-impedance readout electronics, in *2014 12th IEEE International Conference on Solid-State and Integrated Circuit Technology (ICSICT)*, pages 1–4, Oct 2014, doi: 10.1109/ICSICT.2014.7021379. 2.4.1

[163] J. B. Johnson, Thermal Agitation of Electricity in Conductors, *Phys. Rev.*, 32:97–109, Jul 1928, doi: 10.1103/PhysRev.32.97. 2.4.2

[164] H. Nyquist, Thermal Agitation of Electric Charge in Conductors, *Phys. Rev.*, 32:110–113, Jul 1928, doi: 10.1103/PhysRev.32.110. 2.4.2

[165] G. B. Lesovik, Excess quantum noise in 2D ballistic point contacts, *JETP Letters*, 49(9):592, 1989. 2.4.3.4

[166] M. Büttiker, Scattering theory of thermal and excess noise in open conductors, *Phys. Rev. Lett.*, 65:2901–2904, Dec 1990, doi: 10.1103/PhysRevLett.65.2901.

[167] M. Büttiker, Scattering theory of current and intensity noise correlations in conductors and wave guides, *Phys. Rev. B*, 46:12485–12507, Nov 1992, doi: 10.1103/PhysRevB.46.12485.

[168] T. Martin and R. Landauer, Wave-packet approach to noise in multichannel mesoscopic systems, *Phys. Rev. B*, 45:1742–1755, Jan 1992, doi: 10.1103/PhysRevB.45.1742. 2.4.3.4

[169] M. Reznikov, M. Heiblum, H. Shtrikman, and D. Mahalu, Temporal Correlation of Electrons: Suppression of Shot Noise in a Ballistic Quantum Point Contact, *Phys. Rev. Lett.*, 75:3340–3343, Oct 1995, doi: 10.1103/PhysRevLett.75.3340. 2.4.3.4

[170] A. Kumar, L. Saminadayar, D. C. Glattli, Y. Jin, and B. Etienne, Experimental Test of the Quantum Shot Noise Reduction Theory, *Phys. Rev. Lett.*, 76:2778–2781, Apr 1996, doi: 10.1103/PhysRevLett.76.2778.

[171] M. Henny, S. Oberholzer, C. Strunk, T. Heinzel, K. Ensslin, M. Holland, and C. Schönenberger, The Fermionic Hanbury Brown and Twiss Experiment, *Science*, 284(5412):296–298, 1999, ISSN 0036-8075, doi: 10.1126/science.284.5412.296. 2.4.3.4

[172] L.-H. Bize-Reydellet, Bruit quantique électronique et photons micro-ondes, Theses, Université Pierre et Marie Curie - Paris VI, June 2003. 2.4.3.5

[173] D. P. Landau, The theory of the Fermi liquid, *Zh. Eksp. Teor. Fiz.*, 30:1058–1064, 1956. 3.1.1

[174] D. P. Landau, Oscillations in a Fermi liquid, *Zh. Eksp. Teor. Fiz.*, 32:59–66, 1957.

[175] D. P. Landau, On the theory of a Fermi liquid, *Zh. Eksp. Teor. Fiz.*, 35:97–103, 1958. 3.1.1

[176] C. L. Kane and M. P. A. Fisher, Transport in a one-channel Luttinger liquid, *Phys. Rev. Lett.*, 68:1220–1223, Feb 1992, doi: 10.1103/PhysRevLett.68.1220. 3.1.1

[177] S.-i. Tomonaga, Remarks on Bloch's Method of Sound Waves applied to Many-Fermion Problems, *Progress of Theoretical Physics*, 5(4):544–569, 1950, doi: 10.1143/ptp/5.4.544. 3.1.1

[178] J. Luttinger, An exactly soluble model of a Many-Fermion System, *Journal of mathematical physics*, 4(9):1154–1162, 1963, doi: 10.1063/1.1704046. 3.1.1

[179] F. D. M. Haldane, 'Luttinger liquid theory' of one-dimensional quantum fluids. I. Properties of the Luttinger model and their extension to the general 1D interacting spinless Fermi gas, *Journal of Physics C: Solid State Physics*, 14(19):2585, 1981.

[180] A. M. Chang, Chiral Luttinger liquids at the fractional quantum Hall edge, *Rev. Mod. Phys.*, 75:1449–1505, Nov 2003, doi: 10.1103/RevModPhys.75.1449. 3.1.1

[181] J. von Delft and H. Schoeller, Bosonization for beginners — refermionization for experts, *Annalen der Physik*, 7(4):225–305, 1998, ISSN 1521-3889, doi: 10.1002/(SICI)1521-3889(199811)7:4<225::AID-ANDP225>3.0.CO;2-L. 3.1.1, 3.4.1

[182] D. Sénéchal, An introduction to bosonization, *eprint arXiv:cond-mat/9908262*, August 1999. 3.1.1

[183] I. Safi and H. J. Schulz, Transport in an inhomogeneous interacting one-dimensional system, *Phys. Rev. B*, 52:R17040–R17043, Dec 1995, doi: 10.1103/PhysRevB.52.R17040. 3.1.1

[184] K.-V. Pham, M. Gabay, and P. Lederer, Fractional excitations in the Luttinger liquid, *Phys. Rev. B*, 61:16397–16422, Jun 2000, doi: 10.1103/PhysRevB.61.16397.

[185] K.-I. Imura, K.-V. Pham, P. Lederer, and F. Piéchon, Conductance of one-dimensional quantum wires, *Phys. Rev. B*, 66:035313, Jul 2002, doi: 10.1103/PhysRevB.66.035313. 3.1.1

[186] Steinberg Hadar, Barak Gilad, Yacoby Amir, Pfeiffer Loren N., West Ken W., Halperin Bertrand I., and Le Hur Karyn, Charge fractionalization in quantum wires, *Nat Phys*, 4(2):116–119, feb 2008, ISSN 1745-2473, doi: 10.1038/nphys810. 3.1.1

[187] Y. Jompol, C. J. B. Ford, J. P. Griffiths, I. Farrer, G. A. C. Jones, D. Anderson, D. A. Ritchie, T. W. Silk, and A. J. Schofield, Probing Spin-Charge Separation in a Tomonaga-Luttinger Liquid, *Science*, 325(5940):597–601, 2009, ISSN 0036-8075, doi: 10.1126/science.1171769. 3.1.1

[188] H. Kamata, N. Kumada, M. Hashisaka, K. Muraki, and T. Fujisawa, Fractionalized wave packets from an artificial Tomonaga-Luttinger liquid, *Nature nanotechnology*, 9(3):177–181, mar 2014, ISSN 1748-3387, doi: 10.1038/nnano.2013.312. 3.1.1

[189] R. C. Ashoori, H. L. Stormer, L. N. Pfeiffer, K. W. Baldwin, and K. West, Edge magnetoplasmons in the time domain, *Phys. Rev. B*, 45:3894–3897, Feb 1992, doi: 10.1103/PhysRevB.45.3894. 3.1.1

[190] N. B. Zhitenev, R. J. Haug, K. v. Klitzing, and K. Eberl, Time-resolved measurements of transport in edge channels, *Phys. Rev. Lett.*, 71:2292–2295, Oct 1993, doi: 10.1103/PhysRevLett.71.2292.

[191] G. Ernst, R. J. Haug, J. Kuhl, K. von Klitzing, and K. Eberl, Acoustic Edge Modes of the Degenerate Two-Dimensional Electron Gas Studied by Time-Resolved Magnetotransport Measurements, *Phys. Rev. Lett.*, 77:4245–4248, Nov 1996, doi: 10.1103/PhysRevLett.77.4245.

[192] G. Sukhodub, F. Hohls, and R. J. Haug, Observation of an Interedge Magnetoplasmon Mode in a Degenerate Two-Dimensional Electron Gas, *Phys. Rev. Lett.*, 93:196801, Nov 2004, doi: 10.1103/PhysRevLett.93.196801.

[193] H. Kamata, T. Ota, K. Muraki, and T. Fujisawa, Voltage-controlled group velocity of edge magnetoplasmon in the quantum Hall regime, *Phys. Rev. B*, 81:085329, Feb 2010, doi: 10.1103/PhysRevB.81.085329.

[194] N. Kumada, H. Kamata, and T. Fujisawa, Edge magnetoplasmon transport in gated and ungated quantum Hall systems, *Phys. Rev. B*, 84:045314, Jul 2011, doi: 10.1103/PhysRevB.84.045314. 3.1.1, 3.2, 3.1.2, B.1

[195] S. J. Allen, H. L. Störmer, and J. C. M. Hwang, Dimensional resonance of the two-dimensional electron gas in selectively doped GaAs/AlGaAs heterostructures, *Phys. Rev. B*, 28:4875–4877, Oct 1983, doi: 10.1103/PhysRevB.28.4875. 3.1.1

[196] V. I. Talyanskii, A. V. Polisski, D. D. Arnone, M. Pepper, C. G. Smith, D. A. Ritchie, J. E. Frost, and G. A. C. Jones, Spectroscopy of a two-dimensional electron gas in the quantum-Hall-effect regime by use of low-frequency edge magnetoplasmons, *Phys. Rev. B*, 46:12427–12432, Nov 1992, doi: 10.1103/PhysRevB.46.12427.

[197] J. Gabelli, G. Fève, T. Kontos, J.-M. Berroir, B. Placais, D. C. Glattli, B. Etienne, Y. Jin, and M. Büttiker, Relaxation Time of a Chiral Quantum $R-L$ Circuit, *Phys. Rev. Lett.*, 98:166806, Apr 2007, doi: 10.1103/PhysRevLett.98.166806.

[198] M. Hashisaka, K. Washio, H. Kamata, K. Muraki, and T. Fujisawa, Distributed electrochemical capacitance evidenced in high-frequency admittance measurements on a quantum Hall device, *Phys. Rev. B*, 85:155424, Apr 2012, doi: 10.1103/PhysRevB.85.155424.

[199] I. V. Andreev, V. M. Muravev, D. V. Smetnev, and I. V. Kukushkin, Acoustic magnetoplasmons in a two-dimensional electron system with a smooth edge, *Phys. Rev. B*, 86:125315, Sep 2012, doi: 10.1103/PhysRevB.86.125315. 3.1.1

[200] H. C. Lee and S.-R. Eric Yang, Spin-charge separation in quantum Hall edge liquids, *Phys. Rev. B*, 56:R15529–R15532, Dec 1997, doi: 10.1103/PhysRevB.56.R15529. 3.1.1

[201] E. V. Sukhorukov and V. V. Cheianov, Resonant Dephasing in the Electronic Mach-Zehnder Interferometer, *Phys. Rev. Lett.*, 99:156801, Oct 2007, doi: 10.1103/PhysRevLett.99.156801. 3.1.1

[202] I. P. Levkivskyi and E. V. Sukhorukov, Dephasing in the electronic Mach-Zehnder interferometer at filling factor $\nu = 2$, *Phys. Rev. B*, 78:045322, Jul 2008, doi: 10.1103/PhysRevB.78.045322. 3.1.1, 3.4.1

[203] E. Berg, Y. Oreg, E.-A. Kim, and F. von Oppen, Fractional Charges on an Integer Quantum Hall Edge, *Phys. Rev. Lett.*, 102:236402, Jun 2009, doi: 10.1103/PhysRevLett.102.236402.

[204] L. Chirolli, F. Taddei, R. Fazio, and V. Giovannetti, Interactions in Electronic Mach-Zehnder Interferometers with Copropagating Edge Channels, *Phys. Rev. Lett.*, 111:036801, Jul 2013, doi: 10.1103/PhysRevLett.111.036801. 3.1.1

[205] K. Le Hur, Electron fractionalization-induced dephasing in Luttinger liquids, *Phys. Rev. B*, 65:233314, Jun 2002, doi: 10.1103/PhysRevB.65.233314. 3.1.1

[206] K. Le Hur, Dephasing of Mesoscopic Interferences from Electron Fractionalization, *Phys. Rev. Lett.*, 95:076801, Aug 2005, doi: 10.1103/PhysRevLett.95.076801.

[207] K. Le Hur, Electron lifetime in Luttinger liquids, *Phys. Rev. B*, 74:165104, Oct 2006, doi: 10.1103/PhysRevB.74.165104.

[208] S. Ngo Dinh, D. A. Bagrets, and A. D. Mirlin, Analytically solvable model of an electronic Mach-Zehnder interferometer, *Phys. Rev. B*, 87:195433, May 2013, doi: 10.1103/PhysRevB.87.195433. 3.1.1

[209] A. M. Lunde, S. E. Nigg, and M. Büttiker, Interaction-induced edge channel equilibration, *Phys. Rev. B*, 81:041311, Jan 2010, doi: 10.1103/PhysRevB.81.041311. 3.1.1

[210] P. Degiovanni, C. Grenier, G. Fève, C. Altimiras, H. le Sueur, and F. Pierre, Plasmon scattering approach to energy exchange and high-frequency noise in $\nu = 2$ quantum Hall edge channels, *Phys. Rev. B*, 81:121302, Mar 2010, doi: 10.1103/PhysRevB.81.121302. 3.4.1

[211] D. L. Kovrizhin and J. T. Chalker, Equilibration of integer quantum Hall edge states, *Phys. Rev. B*, 84:085105, Aug 2011, doi: 10.1103/PhysRevB.84.085105.

[212] I. P. Levkivskyi and E. V. Sukhorukov, Energy relaxation at quantum Hall edge, *Phys. Rev. B*, 85:075309, Feb 2012, doi: 10.1103/PhysRevB.85.075309. 3.1.1

[213] I. Neder, M. Heiblum, Y. Levinson, D. Mahalu, and V. Umansky, Unexpected Behavior in a Two-Path Electron Interferometer, *Phys. Rev. Lett.*, 96:016804, Jan 2006, doi: 10.1103/PhysRevLett.96.016804. 3.1.1

[214] P.-A. Huynh, F. Portier, H. le Sueur, G. Faini, U. Gennser, D. Mailly, F. Pierre, W. Wegscheider, and P. Roche, Quantum Coherence Engineering in the Integer Quantum Hall Regime, *Phys. Rev. Lett.*, 108:256802, Jun 2012, doi: 10.1103/PhysRevLett.108.256802. 6.2

[215] A. Helzel, L. V. Litvin, I. P. Levkivskyi, E. V. Sukhorukov, W. Wegscheider, and C. Strunk, Counting statistics and dephasing transition in an electronic Mach-Zehnder interferometer, *Phys. Rev. B*, 91:245419, Jun 2015, doi: 10.1103/PhysRevB.91.245419.

[216] I. Gurman, R. Sabo, M. Heiblum, V. Umansky, and D. Mahalu, Dephasing of an electronic two-path interferometer, *Phys. Rev. B*, 93:121412, Mar 2016, doi: 10.1103/PhysRevB.93.121412. 3.1.1

[217] S. Tewari, P. Roulleau, C. Grenier, F. Portier, A. Cavanna, U. Gennser, D. Mailly, and P. Roche, Robust quantum coherence above the Fermi sea, *Phys. Rev. B*, 93:035420, Jan 2016, doi: 10.1103/PhysRevB.93.035420. 3.1.1, 3.1.2, 4.2.3

[218] I. Neder, Fractionalization Noise in Edge Channels of Integer Quantum Hall States, *Phys. Rev. Lett.*, 108:186404, May 2012, doi: 10.1103/PhysRevLett.108.186404. 3.1.2

[219] M. Milletarì and B. Rosenow, Shot-Noise Signatures of Charge Fractionalization in the $\nu = 2$ Quantum Hall Edge, *Phys. Rev. Lett.*, 111:136807, Sep 2013, doi: 10.1103/PhysRevLett.111.136807.

[220] H. Inoue, A. Grivnin, N. Ofek, I. Neder, M. Heiblum, V. Umansky, and D. Mahalu, Charge Fractionalization in the Integer Quantum Hall Effect, *Phys. Rev. Lett.*, 112:166801, Apr 2014, doi: 10.1103/PhysRevLett.112.166801. 3.1.2

[221] Bocquillon E., Freulon V., Berroir J-.M, Degiovanni P., Plaçais B., Cavanna A., Jin Y., and Fève G., Separation of neutral and charge modes in one-dimensional chiral edge channels, *Nature Communications*, 4:1839, may 2013, doi: 10.1038/ncomms2788. 3.1.2, 3.3, 3.4.1, 3.4.1, 3.4.3, 4.3.1, 6.1

[222] K. Washio, R. Nakazawa, M. Hashisaka, K. Muraki, Y. Tokura, and T. Fujisawa, Long-lived binary tunneling spectrum in the quantum Hall Tomonaga-Luttinger liquid, *Phys. Rev. B*, 93:075304, Feb 2016, doi: 10.1103/PhysRevB.93.075304. 3.1.2

[223] Hashisaka M., Hiyama N., Akiho T., Muraki K., and Fujisawa T., Waveform measurement of charge- and spin-density wavepackets in a chiral Tomonaga-Luttinger liquid, *Nat Phys*, 13(6):559–562, jun 2017, ISSN 1745-2481, doi: 10.1038/nphys4062. 3.1.2

[224] C. Grenier, J. Dubois, T. Jullien, P. Roulleau, D. C. Glattli, and P. Degiovanni, Fractionalization of minimal excitations in integer quantum Hall edge channels, *Phys. Rev. B*, 88:085302, Aug 2013, doi: 10.1103/PhysRevB.88.085302. 3.1.2

[225] C. Wahl, J. Rech, T. Jonckheere, and T. Martin, Interactions and Charge Fractionalization in an Electronic Hong-Ou-Mandel Interferometer, *Phys. Rev. Lett.*, 112:046802, Jan 2014, doi: 10.1103/PhysRevLett.112.046802. 3.1.2, 3.2.2, 4.2.2

[226] C. Grenier, Electronic quantum optics, Theses, Ecole normale supérieure de lyon - ENS LYON, June 2011. 3.4.1, 3.4.1, 3.4.1, 4.2.1, 4.2.2

[227] P. Degiovanni, C. Grenier, and G. Fève, Decoherence and relaxation of single-electron excitations in quantum Hall edge channels, *Phys. Rev. B*, 80:241307, Dec 2009, doi: 10.1103/PhysRevB.80.241307. 3.4.1, 4.2.1, 4.2.2, 4.2.2

[228] T. Giamarchi, *Quantum Physics in One Dimension*, Oxford University Press, 2003, ISBN 0-19-852500-1. 3.4.1

[229] D. Litinski, P. W. Brouwer, and M. Filippone, The Interacting Mesoscopic Capacitor Out of Equilibrium, *ArXiv e-prints*, December 2016. 3.4.2.2, 3.15

[230] J. Splettstoesser, M. Governale, J. König, and M. Büttiker, Charge and spin dynamics in interacting quantum dots, *Phys. Rev. B*, 81:165318, Apr 2010, doi: 10.1103/PhysRevB.81.165318. 3.4.2.2

[231] L. D. Contreras-Pulido, J. Splettstoesser, M. Governale, J. König, and M. Büttiker, Time scales in the dynamics of an interacting quantum dot, *Phys. Rev. B*, 85: 075301, Feb 2012, doi: 10.1103/PhysRevB.85.075301. 3.4.2.2

[232] M. Büttiker, H. Thomas, and A. Prêtre, Mesoscopic capacitors, *Physics Letters A*, 180(4):364–369, 1993, ISSN 0375-9601, doi: 10.1016/0375-9601(93)91193-9. 3.4.2.2

[233] J. Gabelli, G. Fève, J.-M. Berroir, B. Plaçais, A. Cavanna, B. Etienne, Y. Jin, and D. C. Glattli, Violation of Kirchhoff's Laws for a Coherent RC Circuit, *Science*, 313(5786):499–502, 2006, ISSN 0036-8075, doi: 10.1126/science.1126940. 3.4.2.2

[234] Y. I. Rodionov, I. S. Burmistrov, and A. S. Ioselevich, Charge relaxation resistance in the Coulomb blockade problem, *Phys. Rev. B*, 80:035332, Jul 2009, doi: 10.1103/PhysRevB.80.035332. 3.4.2.2

[235] Mora Christophe and Le Hur Karyn, Universal resistances of the quantum resistance-capacitance circuit, *Nat Phys*, 6(9):697–701, sep 2010, ISSN 1745-2473, doi: 10.1038/nphys1690. 3.4.2.2

[236] M. Filippone, K. Le Hur, and C. Mora, Giant Charge Relaxation Resistance in the Anderson Model, *Phys. Rev. Lett.*, 107:176601, Oct 2011, doi: 10.1103/PhysRevLett.107.176601. 3.4.2.2

[237] V. Freulon, A. Marguerite, J.-M. J.-M. Berroir, B. Plaçais, a. Cavanna, Y. Jin, and G. Fève, Hong-Ou-Mandel experiment for temporal investigation of single-electron fractionalization, *Nature Communications*, 6:6854, January 2015, ISSN 2041-1723, doi: 10.1038/ncomms7854. 3.4.3

[238] E. Iyoda, T. Kato, K. Koshino, and T. Martin, Dephasing in single-electron generation due to environmental noise probed by Hong-Ou-Mandel interferometry, *Phys. Rev. B*, 89:205318, May 2014, doi: 10.1103/PhysRevB.89.205318. 4.1.3

[239] D. Marian, E. Colomés, and X. Oriols, Time-dependent exchange and tunneling: detection at the same place of two electrons emitted simultaneously from different sources, *Journal of Physics: Condensed Matter*, 27(24):245302, 2015. 4.1.4

[240] D. Ferraro, B. Roussel, C. Cabart, E. Thibierge, G. Fève, C. Grenier, and P. Degiovanni, Real-Time Decoherence of Landau and Levitov Quasiparticles in Quantum Hall Edge Channels, *Phys. Rev. Lett.*, 113:166403, Oct 2014, doi: 10.1103/PhysRevLett.113.166403. 4.2.2, 4.2.4

[241] A. Marguerite, C. Cabart, C. Wahl, B. Roussel, V. Freulon, D. Ferraro, C. Grenier, J.-M. Berroir, B. Plaçais, T. Jonckheere, J. Rech, T. Martin, P. Degiovanni, A. Cavanna, Y. Jin, and G. Fève, Decoherence and relaxation of a single electron in a one-dimensional conductor, *Phys. Rev. B*, 94:115311, Sep 2016, doi: 10.1103/PhysRevB.94.115311. 4.2.2, 4.2.4

[242] A. M. Lunde and S. E. Nigg, Statistical theory of relaxation of high-energy electrons in quantum Hall edge states, *Phys. Rev. B*, 94:045409, Jul 2016, doi: 10.1103/PhysRevB.94.045409. 4.2.4

[243] D. B. Chklovskii, B. I. Shklovskii, and L. I. Glazman, Electrostatics of edge channels, *Phys. Rev. B*, 46:4026–4034, Aug 1992, doi: 10.1103/PhysRevB.46.4026. 4.3.1

[244] M. Hashisaka, T. Ota, K. Muraki, and T. Fujisawa, Shot-Noise Evidence of Fractional Quasiparticle Creation in a Local Fractional Quantum Hall State, *Phys. Rev. Lett.*, 114:056802, Feb 2015, doi: 10.1103/PhysRevLett.114.056802. 4.3.1

[245] P. Roulleau, F. Portier, P. Roche, A. Cavanna, G. Faini, U. Gennser, and D. Mailly, Noise Dephasing in Edge States of the Integer Quantum Hall Regime, *Phys. Rev. Lett.*, 101:186803, Oct 2008, doi: 10.1103/PhysRevLett.101.186803. 4.3.2.2

[246] L. V. Litvin, A. Helzel, H.-P. Tranitz, W. Wegscheider, and C. Strunk, Edge-channel interference controlled by Landau level filling, *Phys. Rev. B*, 78:075303, Aug 2008, doi: 10.1103/PhysRevB.78.075303. 4.3.2.2

[247] A. A. Kozhevnikov, R. J. Schoelkopf, and D. E. Prober, Observation of Photon-Assisted Noise in a Diffusive Normal Metal–Superconductor Junction, *Phys. Rev. Lett.*, 84:3398–3401, Apr 2000, doi: 10.1103/PhysRevLett.84.3398. 5.2.1

[248] J. Dubois, T. Jullien, C. Grenier, P. Degiovanni, P. Roulleau, and D. C. Glattli, Integer and fractional charge Lorentzian voltage pulses analyzed in the framework of photon-assisted shot noise, *Phys. Rev. B*, 88:085301, Aug 2013, doi: 10.1103/PhysRevB.88.085301. 5.2.1

[249] Jompol Y., Roulleau P., Jullien T., Roche B., Farrer I., Ritchie D. A., and Glattli D. C., Detecting noise with shot noise using on-chip photon detector, *Nature Communications*, 6:6130, jan 2015, doi: 10.1038/ncomms7130. 5.2.1

[250] J. Gabelli and B. Reulet, Dynamics of Quantum Noise in a Tunnel Junction under ac Excitation, *Phys. Rev. Lett.*, 100:026601, Jan 2008, doi: 10.1103/PhysRevLett.100.026601. 5.2.1

[251] G. Gasse, C. Lupien, and B. Reulet, Observation of Squeezing in the Electron Quantum Shot Noise of a Tunnel Junction, *Physical Review Letters*, 111(13):136601, September 2013, ISSN 0031-9007, doi: 10.1103/PhysRevLett.111.136601.

[252] G. Gasse, L. Spietz, C. Lupien, and B. Reulet, Observation of quantum oscillations in the photoassisted shot noise of a tunnel junction, *Phys. Rev. B*, 88:241402, Dec 2013, doi: 10.1103/PhysRevB.88.241402. 5.2.1

[253] F. D. Parmentier, L. N. Serkovic-Loli, P. Roulleau, and D. C. Glattli, Photon-Assisted Shot Noise in Graphene in the Terahertz Range, *Phys. Rev. Lett.*, 116: 227401, Jun 2016, doi: 10.1103/PhysRevLett.116.227401. 5.2.1

[254] N. Wiener, *Extrapolation, Interpolation, and Smoothing of Stationary Time Series*, Wiley and Sons, 1949. 5.3.2

[255] E. Iyoda and T. Fujii, Analysis of Shot Noise at Finite Temperatures in Fractional Quantum Hall Edge States, *Journal of the Physical Society of Japan*, 80(7):073709, 2011, doi: 10.1143/JPSJ.80.073709. 6.2

[256] G. Campagnano, O. Zilberberg, I. V. Gornyi, D. E. Feldman, A. C. Potter, and Y. Gefen, Hanbury Brown–Twiss Interference of Anyons, *Phys. Rev. Lett.*, 109: 106802, Sep 2012, doi: 10.1103/PhysRevLett.109.106802.

[257] O. Shtanko, K. Snizhko, and V. Cheianov, Nonequilibrium noise in transport across a tunneling contact between $\nu = \frac{2}{3}$ fractional quantum Hall edges, *Phys. Rev. B*, 89:125104, Mar 2014, doi: 10.1103/PhysRevB.89.125104.

[258] M. Carrega, D. Ferraro, A. Braggio, and M. Sassetti, Finite frequency noise for Laughlin state investigated by a resonant circuit, *Journal of Physics: Conference Series*, 568(5):052005, 2014.

[259] S. Takei, B. Rosenow, and A. Stern, Noise due to neutral modes in the $\nu = 2/3$ fractional quantum Hall state, *Phys. Rev. B*, 91:241104, Jun 2015, doi: 10.1103/PhysRevB.91.241104. 6.2

[260] R. Sabo, I. Gurman, A. Rosenblatt, F. Lafont, D. Banitt, J. Park, M. Heiblum, Y. Gefen, V. Umansky, and D. Mahalu, A New Paradigm for Edge Reconstruction in Fractional Quantum Hall States, *ArXiv e-prints*, March 2016. 6.2

[261] E.-A. Kim, M. Lawler, S. Vishveshwara, and E. Fradkin, Signatures of Fractional Statistics in Noise Experiments in Quantum Hall Fluids, *Phys. Rev. Lett.*, 95: 176402, Oct 2005, doi: 10.1103/PhysRevLett.95.176402. 6.2

Résumé : Cette thèse est dédiée à l'analyse de signaux électriques quantiques dans les canaux de bords de l'effet Hall quantique. En particulier, j'ai utilisé l'analogue électronique de l'interféromètre de Hong, Ou et Mandel pour réaliser des expériences d'interférométrie à deux particules. En entrée de l'interféromètre sont placées des sources d'électrons uniques qui permettent l'injection contrôlée d'excitation ne contenant qu'une seule particule. Les canaux de bords guident ces excitations jusqu'à l'interféromètre. Il s'agit d'un contact ponctuel quantique qui agit comme une lame semi-réfléchissante pour les électrons. On mesure en sortie les fluctuations basse fréquence du courant. Cela nous permet de mesurer le recouvrement entre les fonctions d'onde à un électron émises à chaque entrée. Grâce à cette mesure de recouvrement, j'ai pu caractériser à des échelles de temps sub-nanoseconde, le rôle des interactions Coulombienne sur la propagation de l'électron unique. J'ai pu montrer que ces interactions étaient la source principale de la décohérence du paquet d'onde mono-électronique et qu'elles décomposent l'électron sur des modes collectifs. C'est une manifestation de la fractionalisation de l'électron qui apparaît dans les systèmes uni-dimensionnel en interactions. Grâce à cet interféromètre, j'ai pu aussi implémenter un protocole de tomographie qui permet de reconstruire toute les informations à une particule de n'importe quel signal émis dans le canal de bord. Ce travail permet d'étudier finement des courants non-classiques.

Mots clefs : Physique mésoscopique, optique quantique électronique, effet Hall quantique, source d'électrons uniques, bruits de courant, fractionalisation, imagerie de fonctions de Wigner.

Abstract : This thesis is dedicated to processing of quantum electronic signals in the edge channels of the integer quantum Hall effect. In particular, I used the electronic analogue of the Hong, Ou and Mandel interferometer to realize two particle interference measurements. The interferometer consists of a quantum point contact (QPC) that acts as an electronic beam-splitter. The inputs are fed by single electron sources whose single particle excitations are guided toward the QPC by quantum Hall edge channels. We measure low frequency current noise in one of the output to measure overlaps of first order coherence functions. With this interferometer I could characterize on short time scales the role of Coulomb interactions on single electron propagation. I could show that interactions are the main source of decoherence of the single particle wave packet and that the electron decomposes into collective modes. This is due to fractionalisation which is a hallmark of interacting unidimensional systems. Thanks to this interferometer I could also implement a universal tomography protocol to dissect all single particle information of any arbitrary current. This enables the study of non-classical propagating state.

Keywords: Mesoscopic physics, electron quantum optics, quantum Hall effect, single electron source, current fluctuations, fractionalisation, Wigner function tomography